AN EXPERIMENTAL STUDY ON STATIC AND DYNAMIC BEHAVIOUR OF MODEL PILE FOUNDATIONS

A THESIS SUBMITTED TO
THE GRADUATE SCHOOL OF NATURAL AND APPLIED SCIENCES
OF
MIDDLE EAST TECHNICAL UNIVERSITY

BY

YEŞİM SEMA ÜNSEVER

IN PARTIAL FULFILLMENT OF THE REQUIREMENTS
FOR
THE DEGREE OF DOCTOR OF PHILOSOPHY
IN
CIVIL ENGINEERING

FEBRUARY 2015

Approval of the thesis:

AN EXPERIMENTAL STUDY ON STATIC AND DYNAMIC BEHAVIOUR OF MODEL PILE FOUNDATIONS

submitted by **YEŞİM SEMA ÜNSEVER** in partial fulfillment of the requirements for the degree of **Doctor of Philosophy in Civil Engineering Department, Middle East Technical University** by,

Prof. Dr. Gülbin Dural Ünver _____
Dean, Graduate School of **Natural and Applied Sciences**

Prof. Dr. Ahmet Cevdet Yalçıner _____
Head of Department, **Civil Engineering**

Prof. Dr. M. Yener Özkan _____
Supervisor, **Civil Engineering Dept., METU**

Examining Committee Members:

Prof. Dr. Erdal Çokça _____
Civil Engineering Dept., METU

Prof. Dr. M. Yener Özkan _____
Civil Engineering Dept., METU

Prof. Dr. Tatsunori Matsumoto _____
Civil Engineering Dept., Kanazawa University, Japan

Prof. Dr. Kemal Önder Çetin _____
Civil Engineering Dept., METU

Prof. Dr. Celal Karpuz _____
Mining Engineering Dept., METU

Date: 18.02.2015

I hereby declare that all information in this document has been obtained and presented in accordance with academic rules and ethical conduct. I also declare that, as required by these rules and conduct, I have fully cited and referenced all material and results that are not original to this work.

Name, Last Name: Yeşim Sema Ünsever

Signature:

ABSTRACT

AN EXPERIMENTAL STUDY ON STATIC AND DYNAMIC BEHAVIOUR OF MODEL PILE FOUNDATIONS

Ünsever, Yeşim Sema

Ph.D., Department of Civil Engineering

Supervisor: Prof. Dr. M. Yener Özkan

February 2015, 253 pages

When the subsoil beneath a structure is weak to carry the loads from the superstructure, use of piled foundations is one of the widely employed alternatives. These types of foundations may also be subjected to transient or cyclic lateral loads arising from earthquake, wind, etc. Detailed case histories of dynamically loaded pile foundations are not too many in the literature. In this study, a series of static cyclic horizontal load tests and 1-g shaking table tests on various model foundations, such as piled raft, pile group, full raft, small raft, capped pile and single pile were performed in dry sand. In dynamic tests, the response of the pile foundations was investigated under cyclic loadings with variable frequencies. After testing stage, finite element software, PLAXIS 3D was used for few setups to have a deeper understanding of the behavior of the piled raft.

The results showed that the raft has a significant effect on reducing the settlements and transmitting vertical load through the raft which causes stress increment in the soil. This stress increment causes to increase the amount of load carried by piles. Also, the behavior of the piled raft is affected considerably by the

interaction of the piles and the raft, which leads to the conclusion that it is not plausible to assess the behavior of the piled raft by examining the components individually.

Keywords: piled raft, vertical load test, static cyclic load test, shaking table test, numerical modelling

ÖZ

MODEL KAZIKLI TEMELLERİN STATİK VE DİNAMİK DAVRANIŞI ÜZERİNE DENEYSEL BİR ÇALIŞMA

Ünsever, Yeşim Sema
Doktora, İnşaat Mühendisliği Bölümü
Tez Yöneticisi: Prof. Dr. M. Yener Özkan

Şubat 2015, 253 sayfa

Bir yapının oturduğu zeminin yapıdan gelecek düşey yükleri taşıma açısından yetersiz olduğu durumlarda, kazıklı temel kullanımı yaygın bir alternatiftir. Ayrıca, bu tip temeller deprem, rüzgâr gibi geçici ya da tekrarlı yatay etkilerden dolayı yüklemelere de maruz kalabilirler. Kazıklı temellerin dinamik yükler altındaki davranışını anlayabilmek için gereksinim duyulan zemin-kazık yapılarının dinamik tepkileri konusunda mevcut vaka analizleri sayısı literatürde çok fazla değildir. Bu çalışmada, kuru kum içerisinde bulunan temel modelleri; kazıklı radye, grup radye, radye temel, tekli ve radyeli kazık için yatay yükleme ve 1-g sarsma tablası deneyleri yapılmıştır. Dinamik deneylerde kazıklı temel modelinin farklı frekanslara sahip sinüs dalgaları altındaki sismik tepkileri araştırılmıştır. Test aşamasından sonra, kazıklı temel davranışını daha detaylı anlamak amacıyla sonlu elemanlar yazılımı, PLAXIS 3D kullanılmıştır.

Elde edilen sonuçlara göre, oturmaları azaltmada ve uygulanan düşey yükleri zemine iletmede radyenin belirgin bir etkisi bulunmaktadır. Zemine iletilen düşey yükler, zeminde gerilim artışına neden olmaktadır, bu gerilim artışı da kazıkların

taşıdığı yük miktarını artırmaktadır. Ayrıca, kazıklı temel davranışını kazıkları ve temeli ayrı ayrı inceleyerek tahmin etmek gerçekçi bir yaklaşım değildir, çünkü kazıklı temellerin davranışı, kazık ve radye etkileşiminden fazlasıyla etkilenmektedir.

Anahtar Kelimeler: kazıklı temel, düşey yükleme, statik çevrimsel yatay yükleme, sarsma tablası deneyi, nümerik modelleme

To my parents and my sister, Ayça,

My beloved husband, Ümit,

Without whose love and support this wouldn’t have been possible.

ACKNOWLEDGMENTS

I would like to express my sincere gratitude to my supervisor Prof. Dr. M. Yener Özkan for his support, guidance, advice, encouragement and insight throughout our studies. His patience helped me overcome many difficulties and finished this dissertation. I would like to also thank Prof. Dr. Kemal Önder Çetin and Prof. Dr. Celal Karpuz for serving on various examining committees.

I am grateful to Prof. Dr. Tatsunori Matsumoto for his support and advice during this research. I also thank for his suggestions and comments which increased the technical quality of this dissertation. It was a pleasure to work with him during my studies in Kanazawa University. I would also like to express my gratitude to Mr. Shinya Shimono and Dr. Phan Ta Le for their cooperation during my experiments.

I would like to thank to my friends Gülşah Aytekin, Burcu Taşan Cılız, Aysu Özsoy, Abdullah Sandıkkaya, Raluca Musat, Yasemin İlkay, Aslı Arıkan, Ayşe Arat, Canan Bozdoğan, Esin Şişman and Pınar Kasımoğlu for their friendship and I deeply appreciate their belief in me.

I would like to express my heart-felt gratitude to my parents Sevim-Cumali Ünsever and my sister Ayça Ünsever for their love and continuous support. I warmly appreciate their encouragement, unyielding patience and understanding throughout my life.

My deepest thank belongs to my dearest husband, Ümit Taner Yüksekol. None of this would have been possible without his love, patience and understanding. I am thankful to him for his confidence in me, support, encouragement and being in my life.

TABLE OF CONTENTS

ABSTRACT v
ÖZ vii
ACKNOWLEDGMENTS x
TABLE OF CONTENTS xi
LIST OF TABLES xiv
LIST OF FIGURES xv
CHAPTERS
1. INTRODUCTION 1
1.1 General 1
1.2 Objective and Scope 3
2. LITERATURE REVIEW 5
2.1 Response of Pile Foundations under Seismic Loading 7
2.1.1 Analysis of single pile 8
2.1.2 Analysis of pile group 9
2.2 Modelling of Pile Foundations under Dynamic Loads 12
2.2.1 Physical modelling 12
2.2.2 Previous studies on the behavior of pile foundations 15
2.2.3 Previous studies on pile foundations by finite element analysis 34
3. VERTICAL AND STATIC CYCLIC LOAD TESTS ON MODEL FOUNDATIONS 49
3.1 Introduction 49
3.2 Preparations of Experiments 50
3.2.1 Model piles 50
3.2.2 Calibration of instruments 53
3.2.3 Model ground and the soil box 57
3.3 Similitude of the model pile 65
3.4 Model Foundations 66

3.4.1 Single pile (SP) 66
3.4.2 Full raft (FR) 67
3.4.3 Piled raft (PR) 67
3.4.4 Pile group (PG) 68
3.4.5 Small raft (SR) 69
3.4.6 Capped pile (CP) 69
3.5 Vertical Loading Tests and Results 70
3.5.1 Single pile (SP) and Capped pile (CP) 71
3.5.2 Small raft (SR) and Full raft (FR) 76
3.5.3 Piled raft (PR) 79
3.6 Static Cyclic Horizontal Loading Tests and Results 85
3.6.1 Capped Pile (CP) Tests with/without Vertical Loading 87
3.6.2 Full Raft (FR) and Small Raft (SR) Tests 98
3.6.3 Piled Raft (PR) and Pile Group (PG) Tests 104
3.7 Conclusions 131
4. SHAKING TABLE TESTS ON MODEL FOUNDATIONS 135
4.1 Introduction 135
4.2 Preparation of the Experiments 135
4.2.1 Model foundation and model ground 135
4.2.2 Calibrations of the instruments 137
4.3 Shaking Table Tests and Results 140
4.3.1 Shaking table test of the table alone 141
4.3.2 Shaking table test of the model ground alone 142
4.3.3 Piled raft (PR) and Pile group (PG) models under the sinusoidal wave of 20 Hz frequency 145
4.3.4 Full Raft (FR) model under a sinusoidal wave of 20 Hz frequency 165
4.3.5 Piled raft (PR) model under a sinusoidal wave of 5 Hz frequency 173
4.3.6 Comparison of PR model responses under static cyclic horizontal load test and dynamic test with a sinusoidal wave of 5 Hz frequency 182
4.4 Conclusions 185

5. NUMERICAL ANALYSES OF MODEL FOUNDATIONS UNDER VERTICAL AND STATIC HORIZONTAL LOADING 189
5.1 Introduction 189
5.2 Selection of Constitutive Model 189
5.3 Triaxial Tests and Results 193
5.4 Numerical Modelling of the Experiments 196
5.5 Comparison of Experimental and Analytical Results 200
5.5.1 Vertical load tests 200
5.5.2 Horizontal load test of piled raft and pile group 215
5.6 Conclusions 234
6. SUMMARY, CONCLUSIONS AND RECOMMENDATIONS 235
6.1 Summary 235
6.2 Conclusions 236
6.2.1 Conclusions regarding static test results and finite element analyses 236
6.2.2 Conclusions regarding dynamic test results 240
6.3 Recommendations for Future Studies 242
REFERENCES 243
CURRICULUM VITAE 251

LIST OF TABLES

TABLES

Table 2.1 Scale Factors for Shaking Table Test (Iai, 1989). 13
Table 3.1 Properties of the pipe pile. 51
Table 3.2 Summary of the calibration factors. 57
Table 3.3 Strength parameters .of the Silica sand #6. 60
Table 3.4 Physical properties of Silica sand # 6. 61
Table 3.5 Summary of similitude law for scale ratio, λ=30 (Iai, 1989) 66
Table 3.6 Summary of vertical loads applied on FR and SR during static cyclic load test experiments. 98
Table 4.1 Summary of the calibration factors of the instrumentations. 140
Table 4.2 Average amplification factors. 142
Table 5.1 Material properties of the sand. 195
Table 5.2 Material properties of the pile and the raft. 199

LIST OF FIGURES

FIGURES

Figure 2.1 Pile-structure idealization (Prakash, 1981). 6
Figure 2.2 Typical *p* - *y* curves (Coduto, 1994). 9
Figure 2.3 3D Model for analysis of pile foundations (Finn, 2005). 12
Figure 2.4 Load-deflection curves for single pile (Rollins et al., 2005). 17
Figure 2.5 Cracks and deformation of the piles (Tamura et al., 1999). 19
Figure 2.6 Test setup for 4 single piles, loaded by different loads 21
Figure 2.7 Experiment setup of the piled raft and raft alone (Horikoshi et al., 2003a)..... 22
Figure 2.8 Comparison of horizontal load-displacement relationship of piled raft (Horikoshi et al., 2003b). 23
Figure 2.9 Test setup for static horizontal load test (Matsumoto et al., 2004a).... 24
Figure 2.10 Proportions of (a) horizontal (b) vertical carried by piles 26
Figure 2.11 Large scale shaking table model for case 2 (Kagawa et al., 2004).... 27
Figure 2.12 *p* - *y* curves for (a) single pile (b) 2 × 4 group pile (Roy et al., 2004). 28
Figure 2.13 Single pile model and the instrumentation (Su and Li, 2006). 29
Figure 2.14 Layout for model tests (a) Vertical pile (b) Inclined pile 30
Figure 2.15 a) 1*g* Physical model geometry b) axi-symmetric numerical simulation with one quarter of the model c) boundary conditions of numerical simulation (Baziar et al., 2009). 31
Figure 2.16 Composite ground with rigid piles (Song and Wu, 2009). 32
Figure 2.17 Test setup for static cyclic horizontal load test..... 34
Figure 2.18 Load-settlement relationship of piled-raft elements 35
Figure 2.19 Comparison of pile load-settlement behavior of single pile..... 36
Figure 2.20 Lateral stiffness of the single pile with and without mass..... 37

Figure 2.21 Measured and calculated hysteresis loops (a) 2*D* above ground in dense sand (b) 2D above ground in loose sand (c) 6D above ground in dense sand (d) 6*D* above ground in loose sand (Hutchinson et al., 2005). 39
Figure 2.22 3D Finite element mesh of single pile (Ramachandran, 2005). 40
Figure 2.23 Soil-pile model of the experiment (Cubrinovski et al., 2005)..... 41
Figure 2.24 The instrumented model and the finite element mesh for the single pile (Finn, 2005). 42
Figure 2.25 Finite element mesh of the model (Kasali et al., 2006). 43
Figure 2.26 Load deflection behavior (Poulos et al., 2011). 45
Figure 2.27 Lateral load deflection behavior of the midpoint of the raft 46
Figure 2.28 Finite element mesh for the analysis (a) 3D view (b) Plan view 47
Figure 3.1 Arrangement of vertical and shear strain gauges. 51
Figure 3.2 Test setup for bending test of pile before covering. 52
Figure 3.3 (a) Covering the pile with special glue; “hard rock” and sand (b) hard rock material and the apparatus. 52
Figure 3.4 Preparation of the 3 piles (a) before covering (b) after covering. 53
Figure 3.5 Calibration of right and left load cells..... 54
Figure 3.6 Calibration of right and left vertical dial gauges. 55
Figure 3.7 Cone penetration apparatus calibration test. 56
Figure 3.8 Horizontal and vertical strain graph of the rode..... 56
Figure 3.9 Sieve test results of sand. 58
Figure 3.10. Relationship between the elastic constraint modulus, E_c, with effective vertical stress, σ_v’. 59
Figure 3.11 Effective mean stress, *p’* versus deviatoric stress, *q*. 61
Figure 3.12 The Laminar box (a) drawing (b) photo. 62
Figure 3.13 CPT results of PR test with locations. 63
Figure 3.14 CPT results of PG test with locations. 64
Figure 3.15 CPT results of all four tests. 64
Figure 3.16 Design of the full raft. 67
Figure 3.17 Design of 3-pile piled raft or 3-pile pile group. 68
Figure 3.18 Design of the small raft. 69

Figure 3.19 Design of the capped pile. 70
Figure 3.20 Test setup for SP model (a) drawing (b) photo of the experiment. ... 72
Figure 3.21 Vertical loading capacity of SP and CP..... 73
Figure 3.22 Comparison of SP and the pile component of CP. 74
Figure 3.23 Load-settlement relationship obtained from vertical loading of CP.. 75
Figure 3.24 Proportion of vertical load carried by each component of CP..... 75
Figure 3.25 Axial force distributions along the pile (a) SP (b) CP, where *w*/*D* is normalized settlement of the pile. 76
Figure 3.26 Test setup for FR model (a) drawing (b) photo of the experiment.... 77
Figure 3.27 Vertical loading capacity of SR and FR. 78
Figure 3.28 Load supported by components of CP with loads of SR and SP..... 79
Figure 3.29 Test setup for PR model (a) drawing (b) photo of the experiment.... 80
Figure 3.30 Load-settlement relationship obtained from vertical loading test of PR..... 81
Figure 3.31 Proportion of vertical load carried by each component..... 82
Figure 3.32 Vertical loading capacity of 3 × SP and 3 piles of PR. 82
Figure 3.33 Comparison of SP, pile component of CP and each pile component of PR..... 83
Figure 3.34 Axial force distribution along each pile (a) P1 (b) P2 (c) P3. 84
Figure 3.35 Approximate method to estimate shear forces and lateral soil resistance, generated on the pile..... 87
Figure 3.36 Test setup for horizontal loading of CP with vertical loading (a) drawing (b) photo of the experiment..... 88
Figure 3.37 Horizontal load on the pile vs. normalized displacement (a) with vertical loading (b) without vertical loading..... 89
Figure 3.38 Vertical displacement of the small raft during cyclic horizontal loading displacement (a) with vertical loading (b) without vertical loading. 90
Figure 3.39 Inclination of the small raft during cyclic horizontal loading (a) with vertical loading (b) without vertical loading..... 90

Figure 3.40 Percentage of horizontal load carried by single pile vs. normalized horizontal displacement (a) with vertical loading (CP-V) (b) without vertical loading (CP-N). 92
Figure 3.41 (a) Bending moment (b) shear force (c) lateral ground resistance on each pile node vs. normalized horizontal displacement with vertical loading 93
Figure 3.42 (a) Bending moment (b) shear force (c) lateral ground resistance on each pile node vs. normalized horizontal displacement without vertical loading (CP-N). 94
Figure 3.43 (a) Bending moment (b) shear force (c) lateral ground reaction distribution of the pile with vertical loading (CP-V)..... 96
Figure 3.44 (a) Bending moment (b) shear force (c) lateral ground reaction distribution of the pile without vertical loading (CP-N)..... 97
Figure 3.45 Axial force distribution of CP-V..... 98
Figure 3.46 Test setup for FR model (a) drawing (b) photo of the experiment. ... 99
Figure 3.47 Horizontal load-displacement relationships of vertical loading for SR. 100
Figure 3.48 Horizontal load-displacement relationship of vertical loading for FR. 101
Figure 3.49 Horizontal load vs. vertical load relationships for SR. 102
Figure 3.50 Horizontal load vs. vertical load relationships for FR. 102
Figure 3.51 Horizontal stiffness vs. average contact pressure. 103
Figure 3.52 Horizontal stiffness per unit area vs. average contact pressure. 103
Figure 3.53 Test setup for PR model (a) drawing (b) photo of the experiment. . 105
Figure 3.54 Test setup for PG model (a) drawing (b) photo of the experiment. . 106
Figure 3.55 Horizontal load vs. normalized horizontal displacement relationship of PR and PG models. 107
Figure 3.56 Zoom in initial loading stages of PR and PG models. 108
Figure 3.57 Horizontal load at each pile vs. normalized horizontal displacement of PR and PG. 109
Figure 3.58 Vertical displacement of the raft during cyclic horizontal loading of PR and PG. 110

Figure 3.59 Inclination of the raft during cyclic horizontal loading of PR and PG. 111
Figure 3.60 Load sharing between the 3 piles and the raft during cyclic horizontal loading of PR. 112
Figure 3.61 Percentage of horizontal load carried by 3 piles vs. normalized horizontal displacement of PR. 112
Figure 3.62 Percentage of vertical load carried by 3 piles vs. normalized horizontal displacement of PR. 113
Figure 3.63 Bending moments on each pile node (a) P1 (b) P2 (c) P3 in PR model. 114
Figure 3.64 Bending moments on each pile node (a) P1 (b) P2 (c) P3 in PG model. 115
Figure 3.65 Shear force on each pile node (a) P1 (b) P2 (c) P3 in PR model..... 116
Figure 3.66 Shear force on each pile node (a) P1 (b) P2 (c) P3 in PG model. ... 117
Figure 3.67 Lateral ground resistance on each pile node (a) P1 (b) P2 (c) P3 in PR model..... 118
Figure 3.68 Lateral ground resistance on each pile node (a) P1 (b) P2 (c) P3 in PG model..... 119
Figure 3.69 Bending moment distribution of each pile (a) P1 (b) P2 (c) P3 in PR. 121
Figure 3.70 Bending moment distribution of each pile (a) P1 (b) P2 (c) P3 in PG. 122
Figure 3.71 Shear force distribution of each pile (a) P1 (b) P2 (c) P3 in PR..... 123
Figure 3.72 Shear force distribution of each pile (a) P1 (b) P2 (c) P3 in PG. 124
Figure 3.73 Lateral ground resistance at each pile (a) P1 (b) P2 (c) P3 in PR. .. 125
Figure 3.74 Lateral ground resistance at each pile (a) P1 (b) P2 (c) P3 in PG. .. 126
Figure 3.75 Axial force distribution during horizontal loading (a) PR and (b) PG. 128
Figure 3.76 Axial force distribution at each pile along the pile length..... 129
Figure 3.77 Axial force distribution at each pile along the pile length..... 130
Figure 4.1 Model foundation (3-pile piled raft or 3-pile pile group). 136

Figure 4.2 Calibration of vertical laser displacement transducers; LDT-R and LDT-L. 138
Figure 4.3 Calibration of horizontal laser displacement transducers; LDT-1 and LDT-2. 138
Figure 4.4 Calibration of accelerometers; ACC-1 and ACC-2. 139
Figure 4.5 Amplification factor vs. frequency graph. 141
Figure 4.6 Test setup for model ground alone (a) drawing (b) photo. 143
Figure 4.7 Model ground without foundation test result. 144
Figure 4.8 Acceleration vs. time graph at depth, z = 100 mm for input motion having f = 6 Hz. 145
Figure 4.9 Acceleration vs. time graph at depth, z = 100 mm for input motion having f = 20 Hz. 145
Figure 4.10 Test setup for PR model (a) drawing (b) photo of the experiment. . 148
Figure 4.11 Test setup for PG model (a) drawing (b) photo of the experiment. . 149
Figure 4.12 Input motion, measured at the bottom of the laminar box 150
Figure 4.13 Acceleration responses measured at the raft and at the mid-height of the mass (a) PR (b) PG. 151
Figure 4.14 Zoom in acceleration response measured at the raft and at the mid-height of the mass with input motion (a) PR (b) PG. 152
Figure 4.15 Measured accelerations at depth, z = 100 mm (or 80 mm), between the piles (a) PR (b) PG. 153
Figure 4.16 Measured accelerations at depth, z = 100 mm (or 80 mm), outside of the piles (a) PR (b) PG. 154
Figure 4.17 Measured accelerations at the ground surface (a) PR (b) PG. 154
Figure 4.18 Horizontal load-displacement relationships (a) PR and (b) PG. 156
Figure 4.19 Horizontal load carried by each pile (a) PR and (b) PG. 157
Figure 4.20 Vertical load carried by each pile (a) PR and (b) PG. 158
Figure 4.21 Vertical displacement of the raft for (a) PR and (b) PG. 159
Figure 4.22 Inclination of the raft for (a) PR and (b) PG 160
Figure 4.23 Percentage of horizontal load carried by 3 piles during shaking of PR. 161

Figure 4.24 Percentage of vertical load carried by 3 piles during shaking of PR. 161
Figure 4.25 Distribution of (a) bending moment (b) shear force (c) lateral ground resistance along each pile shaft of PR, where $H = \pm 50$ N. 163
Figure 4.26 Distribution of (a) bending moment (b) shear force (c) lateral ground resistance along each pile shaft of PG, where $H = \pm 50$ N. 164
Figure 4.27 Distribution of axial force along each pile shaft of (a) PR and (b) PG, where $H = \pm 50$ N. 165
Figure 4.28 Test setup for FR model (a) drawing (b) photo of the experiment. . 166
Figure 4.29 Input motion measured at the bottom of the laminar box 168
Figure 4.30 Acceleration responses measured at the raft and at the mid-height of the mass (a) FR, $V = 497$ N (b) FR, $V = 198$ N. 168
Figure 4.31 Zoom in acceleration response measured at the raft and at the mid-height of the mass with input motion (a) FR, $V = 497$ N (b) FR, $V = 198$ N. 169
Figure 4.32 Measured accelerations at the ground surface 170
Figure 4.33 Horizontal load-displacement relationship of (a) FR, $V = 497$ N (b) FR, $V = 198$ N. 171
Figure 4.34 Settlement of full raft with 198 N vertical loading (FR, $V = 198$ N). 172
Figure 4.35 Inclination of full raft with 198 N vertical loading (FR, $V = 198$ N). 172
Figure 4.36 Input motion measured at the bottom of the laminar box for PR-5 Hz. 173
Figure 4.37 Acceleration responses measured at the raft and at the mid-height of the mass for PR-5 Hz. 174
Figure 4.38 Zoom in acceleration response measured at the raft and at the mid-height of the mass with input motion for PR-5 Hz. 175
Figure 4.39 Measured acceleration at depth, $z = 100$ mm, between the piles for PR-5 Hz. 176
Figure 4.40 Measured acceleration at depth, $z = 100$ mm, outside of the piles for PR-5 Hz. 176

Figure 4.41 Measured acceleration at the ground surface for PR-5 Hz. 176
Figure 4.42 Horizontal load-normalized horizontal displacement relationship of PR -5 Hz. 177
Figure 4.43 Horizontal load carried by each pile for PR-5 Hz. 178
Figure 4.44 Axial force carried by each pile for PR-5 Hz. 178
Figure 4.45 Settlement of the raft for PR-5 Hz. 179
Figure 4.46 Inclination of the raft for PR-5 Hz. 179
Figure 4.47 Percentage of horizontal load carried by 3 piles for PR-5 Hz. 180
Figure 4.48 Percentage of vertical load carried by 3 piles for PR-5 Hz. 180
Figure 4.49 Distribution of (a) bending moment (b) shear force along each pile shaft of PR - 5 Hz frequency test, where $H = \pm 50$ N. 181
Figure 4.50 Distribution of axial force along each pile shaft of PR - 5 Hz frequency test, where $H = \pm 50$ N. 182
Figure 4.51 Comparison of total horizontal load on PR between 5 Hz frequency dynamic test and static cyclic test. 183
Figure 4.52 Comparison of horizontal load carried by 3 piles between 5 Hz frequency dynamic test and static cyclic test. 183
Figure 4.53 Comparison of vertical load carried by 3 piles between 5 Hz frequency dynamic test and static cyclic test. 184
Figure 4.54 Comparison of inclination of the raft between 5 Hz frequency dynamic test and static cyclic test. 184
Figure 4.55 Comparison of bending moment, shear force, lateral ground resistance and axial force between 5 Hz dynamic test and static cyclic test. 185
Figure 5.1 Hyperbolic stress-strain relationship for a standard drained triaxial test (Schanz et al., 1999). 193
Figure 5.2 Deviatoric stress q vs. axial strain ε_a. 194
Figure 5.3 Volumetric strain ε_{vol} vs. axial strain ε_a. 195
Figure 5.4 Finite element mesh of the piled raft model for vertical loading test. 197
Figure 5.5 Finite element mesh of the piled raft model for horizontal loading test. 197
Figure 5.6 Mechanism of hybrid elements (Kimura and Zhang, 2000). 198

Figure 5.7 Finite element mesh of the single pile model for vertical loading test. 200
Figure 5.8 Single pile model in detail. 201
Figure 5.9 Vertical load-pile head settlement relationship of the single pile..... 202
Figure 5.10 Distribution of axial forces along the single pile shaft. 203
Figure 5.11 Mean stress contours for single pile vertical loading analysis. 204
Figure 5.12 Finite element mesh of the full raft model for vertical loading test. 205
Figure 5.13 Raft model in detail. 206
Figure 5.14 Load- settlement relationships of the full raft. 206
Figure 5.15 Mean stress contours for full raft vertical loading analysis. 207
Figure 5.16 Vertical load- settlement relationship of the piled raft. 208
Figure 5.17 Load sharing of 3 piles and the raft under vertical loading. 209
Figure 5.18 Vertical loads at edge and center piles. 210
Figure 5.19 Mean stress contours for piled raft vertical loading analysis. 211
Figure 5.20 Distribution of axial forces along each pile shaft (P1, P2 and P3).. 213
Figure 5.21 Distribution of shaft resistance along each pile (P1, P2 and P3)..... 214
Figure 5.22 Total displacement contours of piled raft under vertical loading. ... 215
Figure 5.23 Finite element mesh of the pile group model for static horizontal loading test. 216
Figure 5.24 Horizontal load-normalized horizontal displacement relationship of (a) PR (b) PG..... 218
Figure 5.25 Vertical load-displacement relationships of (a) PR (b) PG. 220
Figure 5.26 Shear load-displacement relationships of (a) PR (b) PG. 221
Figure 5.27 Mean stress contours for horizontal loading analysis (a) PR (b) PG. 222
Figure 5.28 Proportion of horizontal load carried by the raft. 224
Figure 5.29 Proportion of vertical load carried by the raft. 224
Figure 5.30 Bending moment distribution along each pile shaft (P1, P2 and P3) for piled raft..... 227
Figure 5.31 Bending moment distribution along each pile shaft (P1, P2 and P3) for pile group..... 228

Figure 5.32 Shear force distribution along each pile shaft (P1, P2 and P3) for piled raft. 229
Figure 5.33 Shear force distribution along each pile shaft (P1, P2 and P3) for pile group. 230
Figure 5.34 Axial force distribution along each pile shaft (P1, P2 and P3) for piled raft. 231
Figure 5.35 Axial force distribution along each pile shaft (P1, P2 and P3) for pile group. 232
Figure 5.36 Total displacement contours under horizontal loading (a) PR (b) PG. 233

CHAPTER 1

INTRODUCTION

1.1 General

If the soil strength beneath a superstructure is not sufficient to carry the loads from the structure, a common solution is to increase the depth of foundation to transfer the loads to stronger soil layers by using pile foundations. In Turkey, pile foundations are used widely for high-rise buildings, and these foundations may be subjected to horizontal loading such as earthquakes, winds, etc. in their lifetime since Turkey is located on an active earthquake zone. In recent years, piled raft foundations have been used extensively to reduce average and/or differential settlement of building foundations e.g. Poulos and Davis (2005), Yamashita et al. (2011a), Yamashita et al. (2011b), Yamashita (2012), Katzenbach and Leppla (2013). Although the application of piled raft foundations is increasing, their use in civil engineering structures such as bridges is limited, except in Germany (Hetch and Dürwang, 2001). Foundation area and number of piles of bridge pier foundations are generally smaller than that of building foundations and dead load from the superstructure on unit area of the foundation of a bridge pier is relatively larger compared to building foundations. Therefore, to predict the behavior of a bridge foundation subjected to combination of vertical load, horizontal load and over-turning moment should be cautiously considered in design.

In the design of piled raft foundations, the main concerns are estimation of settlement and load sharing between piles and the raft. When the additional capacity provided by the raft element of the piled raft is considered in designs, the required number of piles could be reduced (Poulos et al., 2011). Moreover, the raft has an effect of transferring the applied pressure to the soil, which can increase the

lateral stresses in the soil and therefore the ultimate load capacity of the piles also increase (Katzenbach et al., 1998).

Number of experimental studies on horizontal loading of pile foundations were reported, e.g. Shibata et al. (1989), Murono et al. (1997), Tokimatsu and Suzuki (2004), Tokimatsu et al. (2005), Ishizaki et al. (2012). Behavior of model pile foundations in dry or saturated grounds subjected to static or dynamic (seismic) loading were investigated in these studies, where the piles are end bearing piles, which means that model piles are fixed to the bottom of the soil containers.

Moreover, field monitoring of piled raft foundations were carried out in Japan, e.g. Yamada et al. (2001), Yamashita et al. (2012) and Yamashita (2012). In these field works, the piles are sat on a firm bearing strata and traditional design concept of pile group is still adopted predominantly even though pile foundations are piled raft foundations in reality. As the raft effect is not taken into account in the traditional design approach, it does not reflect the actual behavior of piled raft. This approach may be attributed to the fact that the knowledge about behavior of piled rafts subjected to combination of vertical load and shaking (dynamic load) is still limited even today. The field monitoring data show that the pile raft foundations are stable even against severe earthquakes such as Hyogoken-Nambu Earthquake in 1995 and Tohoku Pacific Earthquake in 2011.

In order to widen the application of piled rafts, their behavior when supported by friction piles needs to be understood and a pertinent design approach needs to be established. Centrifuge modelling of piled rafts in dry sand ground subjected to static and dynamic (shaking) horizontal loading were carried out by Horikoshi et al. (2003a, 2003b). Similar experiments were carried out by Matsumoto et al. (2004a, 2004b, 2010) at 1-g field. The results of these experimental study show that piled raft foundation is stable compared to pile groups when subjected to static or dynamic horizontal loading.

Nevertheless, the design framework of piled rafts subjected to horizontal loading has not been fully established (Matsumoto, 2013).

1.2 Objective and Scope

In this study, in order to throw further sight into the behavior of piled raft foundations under vertical and horizontal loading, a series of vertical load tests, cyclic horizontal load tests and shaking table tests on a 3-pile piled raft model were carried out in dry sand model ground at 1-g field. Load tests of the components of the piled raft model, such as full raft and single pile, were also carried out to investigate their interactions in the piled raft. A FEM software, PLAXIS 3D (Plaxis, 2013), was used for numerical modelling of the load tests. The hardening soil model (Schanz et al., 1999) was employed in modelling the sand based on the triaxial CD compression test results, while elastic model was used for piled raft, single pile or raft model.

The following sections describe the essential structuring in each chapter. The study presented here is composed of six chapters.

Chapter 1 reviews the basic literature, major contributions and outline of the dissertation.

Chapter 2 summarizes the literature survey of static and dynamic experimental studies and studies on finite element analyses of piled raft foundations.

Chapter 3 describes the test setup for vertical and static cyclic horizontal load tests in dry sand, laboratory test results on dry sand to define its basic properties and the preparation of the model foundations. The equipment and laboratory procedures are also discussed. All model foundations e.g. piled raft, pile group, single pile, capped pile and full raft are introduced in this chapter. It covers the main differences between the piled raft and pile group under vertical and static

cyclic horizontal loading. It also emphasizes the effect of existence of vertical loading on the response of model foundations under horizontal loading.

Chapter 4 discusses the behavior of piled raft and pile group under the combination of vertical loading and dynamic loading. The resonant frequency of the model ground is assessed as 20 Hz. Model foundation experiments were carried out under sinusoidal waves with two different frequencies; 20 Hz and 5 Hz. 5 Hz test results on piled raft are compared with the static cyclic test results at the end of the chapter.

Chapter 5 presents the finite element analyze results for vertical and monotonic horizontal loading conditions using finite element software, Plaxis 3D (2013). Determination of the soil model utilizing the CD triaxial test results on model ground and the selection of the material parameters of the sand are also included. This chapter presents a comparison of experimental and numerical results.

Chapter 6 summarizes the experimental and numerical results and main findings of this study. Recommendations for further research are also suggested.

CHAPTER 2

LITERATURE REVIEW

When the subsoil beneath a structure is too weak to carry the loads from the structure, the depth of foundation is increased to transfer the load to the stronger soil layers by using pile foundations. These types of foundations may also be subjected to transient or cyclic lateral loads arising from earthquake, wind, wave, blast, impact or machine loading. Therefore, pile foundations located on soft soils may amplify ground motions and structures can be faced with serious problems.

It has been a common seismic design practice to accept the total lateral load applied to a pile foundation as a base shear computed in the dynamic analysis of the superstructure.

A practical solution for soil-pile interaction under dynamic loads was stated by Prakash and Chandrasekaran (1980; cited in Prakash, 1981). The idealization of pile-structure system is shown in Figure 2.1. In this analysis,

-the system is assumed to be one dimensional

-pile is divided into a convenient number of segments whose masses are concentrated at the center

-the modulus of the soil is assumed to be either constant or variable with depth

-the mass of the superstructure is concentrated at the pile tap.

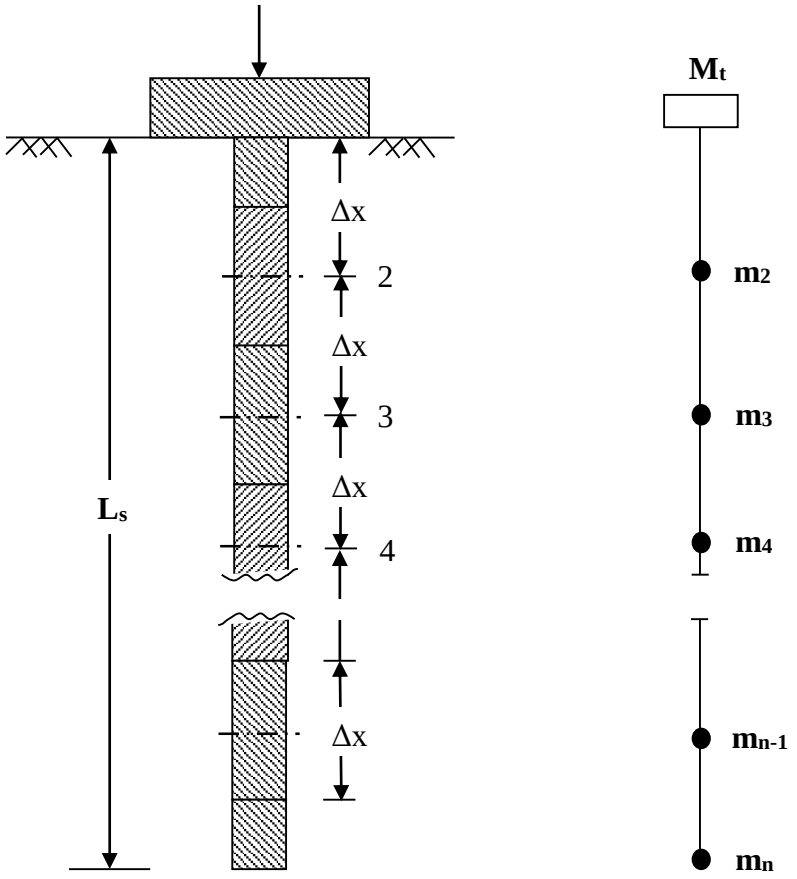

Figure 2.1 Pile-structure idealization (Prakash, 1981).

There are three techniques to solve the soil-pile-superstructure interaction. First one assumes the soil as a continuum with linear elastic properties. Second one represents the soil and the pile by using finite element technique which allows the usage of variable soil-pile properties. Third one uses lumped masses, springs, and dashpots to represent soil-pile system that allows the variation of depth and nonlinearity of soil properties (Prakash, 1981).

However, dynamic response of soil-pile structures provided in case histories are very few to examine the validation of these methods. In order to solve such difficulties, centrifuge or shaking table model tests are used to obtain data under

controlled conditions. Centrifuge tests provide a better understanding of complex behavior since it satisfies the gravitational stress field in the prototype. On the other hand, shaking table tests have an advantage of well controlled large amplitude motions and easier experimental measurements to investigate the qualitative behavior of the model.

2.1 Response of Pile Foundations under Seismic Loading

During an earthquake, the forces in pile foundations can be investigated in two parts: first one is the resistance of the piles to the soil motions and the second one is the response of the piles to the forces generated by vibration of the super structure. These forces can be called as kinematic-interaction and inertial-interaction forces, respectively (Kaynia and Mahzooni, 1996, Castelli and Maugeri, 2009).

Commonly used procedure for seismic design of piles may consider the inertial-interaction forces and neglect the kinematic-interaction forces. Therefore, the piles are designed for the inertial forces in the structure obtained from its dynamic analysis. There are many researches supporting that phenomenon. However, another research based on shaking table test results indicates that the kinematic-interaction forces should not be ignored since they can induce damage by itself (Mizuno et al., 1984; cited in Kaynia and Mahzooni, 1996). It is stated that the kinematic interaction has large contribution to the seismic shear forces and bending moments in the piles except the frequencies close to the natural frequency of the soil-structure system, which means that at these frequencies, close to the natural frequency of the system, inertial interaction may be significantly larger than kinematic interaction. Also it is stated that, contribution of kinematic interaction is higher in layered soils, having significant stiffness contrast (Kaynia and Mahzooni, 1996, Irshad and Akhtar, 2006). Moreover, kinematic interaction of pile forces is strongly effected from pile’s rigidity and pile’s spacing in a pile

group. Castelli and Maugeri (2009) are also stated that ignoring the kinematic interaction can cause to underestimate the maximum moments at the pile head.

2.1.1 Analysis of single pile

The most common approach to analyze the single pile is using Winkler springs and dashpots to simulate the soil stiffness and damping, while the pile is modeled as beam. The springs may be elastic or non-linear (Finn, 2005):

Elastic springs: The origin of this method is based on the paper of Chang (1937), which discusses the lateral pile loading tests. He presents a method that the interaction of soil and pile are represented by elastic springs and the spring constant is assumed to be constant or change as a function of depth. It can be approximated by the following formula:

$$k_x = \delta . E_s(z) \tag{2.1}$$

where k_x is the stiffness of the continuously distributed spring, $E_s(z)$ is the Young's modulus of the soil as a function of depth, z, and δ is a coefficient depends on the type of soil profile, the type of head loading and the relative stiffness of the pile with respect to soil (Gazetas and Dobry, 1984). Discrete spring stiffness from Equation 2.1 can be obtained by multiplying it with the tributary area of one spring (spacing between two adjacent springs).

Non-linear springs: The response of foundations under dynamic loading is actually nonlinear. The modulus of soil decreases with strain, which causes to decrease the soil stiffness (Finn, 2005). Therefore, nonlinear springs are used instead of elastic springs by specified curves called *p* - *y* curves where *p* is the lateral soil resistance per unit length of the foundation and *y* is the lateral deflection (Reese et al., 1974). Typical *p* - *y* curves are shown in Figure 2.2.

Curve “A” shows ductile behavior which may occur in soft clays and sands and Curve “B” shows brittle behavior, which may occur in stiff clay (Coduto, 1994).

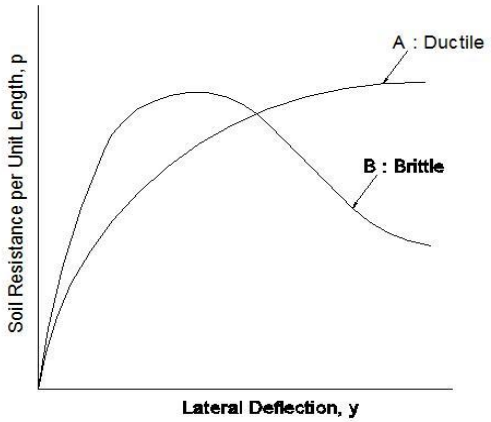

Figure 2.2 Typical *p* - *y* curves (Coduto, 1994).

The *p* - *y* method is calibrated from full scale load tests and it considers many variables:

- Any non-linear load deflection curve
- Variation of the nonlinear load deflection curve with depth
- Variation in the foundation stiffness with depth
- Elastic-plastic flexural behavior in the foundation

This method considers not only the compression between foundation and soil, but also the shear friction on the two adjacent sides (Coduto, 1994).

2.1.2 Analysis of pile group

The response of pile groups with closely spaced piles is different from the response of a single pile because of the over-lapping displacement fields of individual single piles in the group. This means group resistance is less than the

sum of the individual pile resistance. There are some procedures to define the response of the group of piles under dynamic loading:

Elasticity based solution: In this method, the sum of the response of each pile is calculated by assuming each of the piles as a single pile and then interaction factor is applied. The interaction factor considers the horizontal movement of one pile as a result of loading of another pile. It is expressed as the ratio of the displacement of the pile due to the adjacent one to the displacement of the pile due to its own loading. Although, it seems to be an easy procedure to determine the response of pile group, it is difficult to extend it to non-linear condition which is the actual behavior of the soil. Also, it is difficult to solve the system under seismic or dynamic loads with this method (Poulos and Davis, 1980).

Wave propagation based solution: This method uses the wave propagation theory to compute the interaction factor between piles under dynamic loads. In other words, the vibration of each pile causes an additional displacement of the adjacent pile due to wave propagation. In this procedure, vibrating pile is called as active pile and the adjacent pile is called as passive pile. For piles under axial loading, the interaction factor can be calculated as (Morse and Ingard, 1968; cited in Ramachandran, 2005):

$$\alpha_v(S) \approx \left(\frac{d}{2S}\right)^{0.5} exp\left(\frac{-\beta\omega S}{V_s}\right) exp\left(\frac{-i\omega S}{V_s}\right) \tag{2.2}$$

where $\alpha_v(s)$ is the pile interaction factor, s is the pile spacing, d is the pile diameter, β is the soil damping, ω is the angular frequency of the input loading, V_s is the shear wave velocity in the soil medium and $i = \sqrt{-1}$. This procedure can be used for dynamic loadings; however nonlinear effects are limited with the calculation of the response of single piles. Therefore, the effect of soil non-linearity on pile to pile interaction cannot be considered (Dobry and Gazetas, 1988; cited in Ramachandran, 2005).

P-multipliers solution: This method is the extension of Winkler model with nonlinear springs. The nonlinear response of each spring is presented by a *p* - *y* curve. At the same horizontal displacement, a pile in a group resists smaller horizontal load than a single pile, because of group effect, which is defined by *P* - multipliers. *P*-multipliers (reduction factor), which is proposed by Brown et al. (1988), applied to the *p*-term of *p* - *y* curve of a single pile to obtain the behavior of the piles in the group. *P*-multipliers are assumed to be constant with depth, but it can be changed according to the row position in the group. Therefore, it can be said that *P*-multiplier depends on the number of piles, pile spacing and position in the group, soil type, pile type and load level (Zhang et al., 1999, Rollins et al., 1998; cited in Castelli and Maugeri, 2009). *P*-multipliers in the literature are estimated from static or cyclic load tests; therefore it could be better to validate them by dynamic tests or back analyses. Although this method is widely used and applicable to software, it is difficult to analyze large pile groups under dynamic loads since it requires extensive modelling and considerable analysis time (Ramachandran, 2005).

Finite element analyses: Another approach is using the finite element method which involves 2D/3D modelling of the pile and soil continuum and assigning appropriate material models to represent the nonlinear behavior of the soil. In the analysis, instead of using the full three dimensional wave equations, finite element continuum analysis can be performed with the assumption of the pile foundation responses are the shear stresses on vertical and horizontal planes and the normal stresses in the direction of shaking. These basic assumptions of simplified 3D analysis are shown in Figure 2.3. As it is seen in the figure, the soil is modelled using 3D finite elements and the pile is modelled using beam or block elements (Finn, 2005).

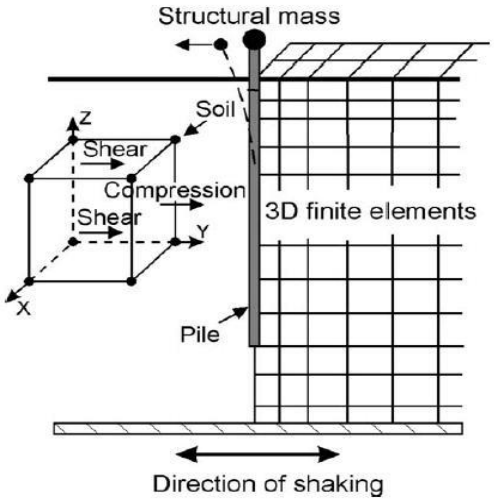

Figure 2.3 3D Model for analysis of pile foundations (Finn, 2005).

2.2 Modelling of Pile Foundations under Dynamic Loads

2.2.1 Physical modelling

In physical modelling, the behavior of the prototype is investigated with a smaller model which has more rapid response and closer control. In the model, the effects of the parameters can be investigated by changing one parameter and taking others constant. An important issue is how the results of the model can be translated to the prototype behavior. Since the material behavior is commonly nonlinear and the interaction between several materials should also be taken into account, dimensional analysis can be performed by using Buckingham pi theorem. This theorem helps to satisfy the same safety margin between the prototype and the model by keeping dimensionless parameters constant. In fact, this can be possible if gravitational acceleration, g which is a fundamental parameter for most of the geotechnical problems can be increased artificially by the help of geotechnical centrifuge equipment. However, in shaking table test, it cannot be

possible to keep all the dimensionless parameters constant, in other words to scale gravitational acceleration (Iai, 1989, Wood, 2004).

The related scaling factors for 1-g shaking table test are summarized in Table 2.1. Stiffness (shear modulus) of a soil is a difficult concept since the soil has nonlinear behavior. The small strain stiffness which controls the dynamic response is dependent on the effective stress level, σ in a form of σ^{α}. The exponent, α (dependency of the stiffness to the stress level) might be of the order of 0.5 for sands and 1.0 for clays according to the results of experimental studies (Iai, 1989, Wood, 2004).

Table 2.1 Scale Factors for Shaking Table Test (Iai, 1989).

Quantity	**General**	**Scale factors for 1g**	**For sand (α=0.5)**
Length	n_l	1/n	1/n
Mass density	n_p	1	1
Acceleration	n_g	1	1
Stiffness	n_G	$1/n^{\alpha}$	$1/n^{1/2}$
Stress	$n_p n_g n_l$	1/n	1/n
Force	$n_p n_g n_l^3$	$1/n^3$	$1/n^3$
Strain	$n_p n_g n_l / n_G$	$1/n^{1-\alpha}$	$1/n^{1/2}$
Displacement	$n_p n_g n_l^2 / n_G$	$1/n^{2-\alpha}$	$1/n^{3/2}$
Time	$n_l (n_p/n_G)^{1/2}$	$1/n^{1-\alpha/2}$	$1/n^{3/4}$
Velocity	$n_g n_l (n_p/n_G)^{1/2}$	$1/n^{1-\alpha/2}$	$1/n^{3/4}$
Frequency	$(n_G/n_p)^{1/2}/n_l$	$n^{1-\alpha/2}$	$1/n^{3/4}$
Shear wave velocity	$(n_G/n_p)^{1/2}$	$1/n^{\alpha/2}$	$1/n^{1/4}$
Bending rigidity of pile	$n_G . n_l^4$	$1/n^{4+\alpha}$	$1/n^{9/2}$
Longitudinal rigidity of pile	$n_G . n_l^2$	$1/n^{2+\alpha}$	$1/n^{5/2}$

The similitude law is derived by considering some approximations such as (Iai, 1989);

(1) Soil skeleton is assumed as continuous medium

(2) Deformation should be small to satisfy the equilibrium equation

(3) Strain of the soil skeleton is assumed as small.

For a pile under lateral loading, dimensionless parameter that describes the relative pile-soil stiffness is $G.L^4/E.I$, where shear stiffness of soil is G, length of the pile is L, and flexural rigidity of the pile is $E.I$. Therefore, if this dimensionless parameter remains the same for prototype and model, correct physical modelling can be obtained. This gives the following equation,

$$n_E.n_I = n_G.n_L^4 \tag{2.3}$$

where n_E, n_I, n_L and n_G are the scaling factors for Young's modulus, moment of inertia, length of the pile and shear modulus of the soil, respectively (Wood, 2004).

According to Meyerhof (1976; cited in Prakash and Sharma, 1990), which has the same concept with the above argument about pile-soil interaction, the stiffness of the pile is given with the formula, $K_r = E_p.I_p/E_h.L^4$ where E_p, I_p and L are the modulus of elasticity, moment of inertia and length of the pile and E_h is the average horizontal soil modulus along the pile. The same formula has been introduced as pile-flexibility factor by Poulos and Davis, 1980.

On the other hand, when dynamic soil-structure interaction is considered, the effect of natural frequencies should also be taken into account. So, it is also required to satisfy the following formula;

$$n_{ps}.n_A = n_p.n_L^2 \tag{2.4}$$

where n_{ps} and n_A are the scaling factors for density and area for the pile, respectively, and n_p is the scaling factor for density of the soil. It is difficult to satisfy both conditions in 1-g shaking table test since the requirements are conflicted and therefore both equations cannot be applied simultaneously (Wood, 2004).

2.2.2 Previous studies on the behavior of pile foundations

In recent years, a few case histories monitored the soil-structure interaction. The effectiveness of piled raft foundation was monitored and reported by Yamashita et al. (2011a), Yamashita et al. (2011b), Yamashita et al. (2014)., etc.

One of the examples is piled raft foundation in Osaka that subjected to Hyogoken-Nanbu earthquake (Yamashita et al., 2011a). After the earthquake, all the monitored parameters such as settlement, axial force of piles, load proportion between pile and raft remains the same as before the earthquake. Another field monitoring study was performed by Yamashita et al. (2012), which shows the advantage of base-isolated system. The monitored data also did not change in this case which proves that both structure and foundation are quite stable. Yamashita et al. (2014) has studied on the field monitoring of piled raft that focusing on load sharing and settlement before and after a strong earthquake. The ratios of the axial load carried by the piles to the effective stress were between 67 % - 85 % and 57 % - 82 % before and after the earthquake according to the position of the pile, respectively.

Moreover, Yamada et al. (2001) investigated the behavior of 12 stories building with two stories basement. During construction by top-down method, temporary piles and soil cement pile wall were placed to support the upper structure until the basement slab was constructed. Therefore, although the foundation of the building was designed as a raft, it behaved as the piled raft foundation due to the temporary piles, which remained there after the construction. The proportion of the load,

carried by the raft was estimated as 61 % at the time of the completion of the building and one and half years after the completion of the building, it became 55 % - 58 %. 2 years after the completion of the building, the 1995 Hyogoken-Nambu Earthquake hit the building, where the maximum ground surface acceleration was measured about 200 gal. However, the proportion of load sharing did not change before and after the earthquake.

Full-scale tests were also performed to investigate the *p*-multipliers and the pile spacing effects on laterally loaded pile groups (Rollins et al., 2005, 2006). For this purpose, 3 × 3, 3 × 4 and 3 × 5 pile groups with different pile spacing and a single pile having the same properties with the piles in the groups were tested. Soil profile consisted of stiff clay with sand layers, and water level was 1.0 m below the ground surface. 15 cycles were applied to each configuration, it was seen that as the number of static cycling increases stiffness reduction occurs both in the group and single pile models (Figure 2.4). This might be because of gap generation at small displacements. In other words, after the first cycle, the primary resistance of the system was due to the pile strength only until the gap was closed. The maximum moment also increased about 14 % – 30 % at 15th cycle for a given load. The increase of the maximum moment might due to the soil softening, which causes larger bending at the same load. Measured data was compared with LPILE software program, which predicts measurements quite good. Moreover, statnamic load test was applied on series of pile groups at field. It was observed that dynamic resistance is 50 % - 75 % larger than static resistance. In addition, dynamic test curves enclosed larger loops than the static tests, which points out significant damping that was estimated between 30 % - 40 % from simplified single-degree-of-freedom analyses.

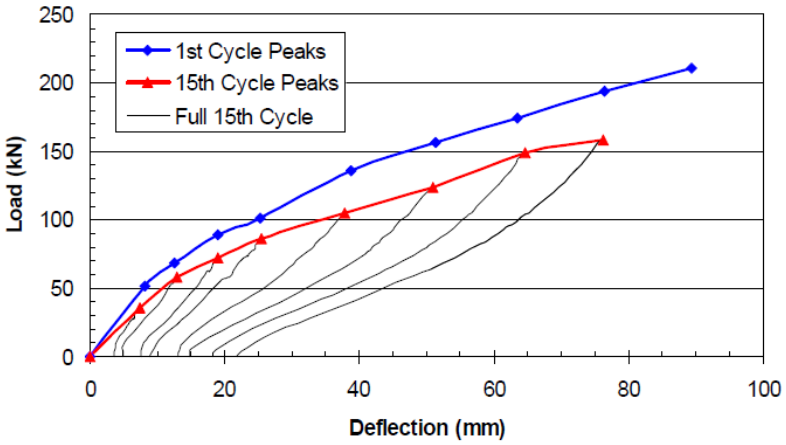

Figure 2.4 Load-deflection curves for single pile (Rollins et al., 2005).

Although field tests give good information, it is difficult to control the factors that affect the results, whereas model tests allow sensitivity analyses since it is repeatable. Model tests are also useful to determine the effects of parameters of both soil and structure and the behavior of the system when it is difficult to predict such properties due to the lack of case studies. There are mainly two types of model tests; centrifuge test and shaking table test. The main difference between these two tests is; centrifuge test is performed under higher gravitational field whereas shaking table test is performed under 1-g gravitational field. Important developments on shaking table tests and centrifuge tests make possible to investigate soil-structure interaction, liquefaction and so on.

Most of the models are constructed much smaller than the prototype since it is easier to control source of observations and gives results more rapidly. However, there are some points to be considered in detail; the boundary conditions shall be well defined and well controlled and the size of the model shall be as large as possible. Another important issue is when the soil mass is shaken, the energy due to shear waves can be reflected through the boundaries. It can be avoided by using a laminar box, composed of infinitesimal rings or rectangular steel frames that are able to move relative to each other (Wood et al., 2002). Also, soil-structure

interaction effects shall be considered in shaking table test in order to avoid getting too conservative information (Konagai and Ahsan, 2002).

It was stated that centrifuge and shaking table tests cannot reflect all the features of the prototype, but they give information about performance of the model. Seismic loading of a foundation system may depend on many features, such as building-foundation vibration patterns, soil-foundation interaction, soil behavior, etc. These types of tests are also used to validate the numerical codes (Romo et al., 2000).

In the literature, there are considerable amount of experiments performed on different configurations of model foundations in dry or saturated grounds to understand the behavior of piles under vertical loading and lateral loading (static and dynamic). Some of the model test experiments on the behavior of pile foundations are summarized as follows:

McVay et al. (1995) was carried out lateral loading test of single pile and free-head 3 × 3 pile groups with 3*D* and 5*D* spacing at two different densities of sand (D_r =33 % and 55 %) by centrifuge tests. They aimed to study on group efficiency and *p*-multipliers. The model was scaled up to 1/45 of the prototype. Calculated lateral load-deflection curve of single pile was in good agreement with the prototype response. They also concluded that shadowing effect (group interaction effect) of a group pile depends on pile spacing and soil density. 3*D* and 5*D* spacing models had constant efficiencies of approximately 0.74 and 0.93 for most displacements, respectively.

In the study of Tamura et al. (1999), the behavior and failure mechanism of four reinforced concrete piles in saturated sand with a relative density of 60 % was conducted by shaking table test during soil liquefaction. The concrete piles' diameter was 15 cm and the length was 6 m. Tests were performed on the soil-pile-structure system whose heads (rigid connection) and tips were attached to the

structural model and laminar shear box, respectively. The input motion was a synthesized ground motion with variable amplitudes. It was indicated that bending moments at the pile head occur due to the forces transferred from the superstructure (inertial forces) initially, then deformation progress to the middle part of the pile as a result of soil deformation (kinematic forces) (Figure 2.5). It was also concluded that, the response acceleration is smaller than the input motion when liquefaction occurs.

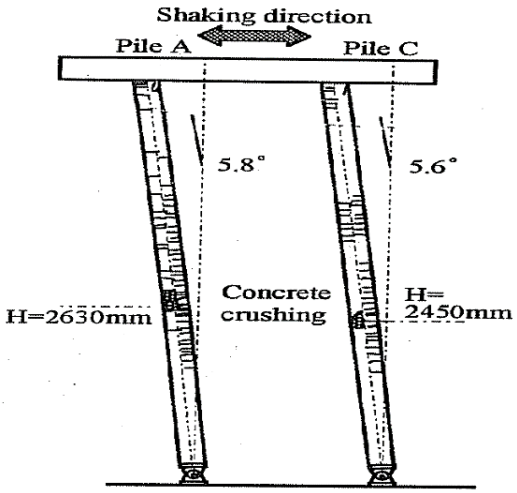

Figure 2.5 Cracks and deformation of the piles (Tamura et al., 1999).

Zhang et al. (1999) was studied on the lateral response of the single pile and 3 × 3 to 7 × 3 pile groups. It was concluded that maximum bending moments on pile do not depend on group size, but depends on the pile position within the group. They also compared the response of pile groups in loose (D_r = 36 %) and medium dense (D_r = 55 %) sand. It was seen that moments and shear forces are about 20 % larger in medium sand for the lead row piles.

Boulanger et al. (1999) performed centrifuge experiments on single piles with 9 different earthquakes as input motion. The soil profile was saturated soft clay layer, underlined by medium dense sand. The superstructure masses were placed at the top of the piles. They used the results of experiments to evaluate the performance of dynamic *p* - *y* analysis method by GeoFEAP (Bray et al., 1995; cited in Boulanger et al., 1999). It was stated that the analyses results were in reasonable agreement with the experiment results considering the earthquake motions covered in this study.

Meymand et al. (2000) conducted experiments on the behavior of single piles with different inertial conditions under dynamic loading by 1-g shaking table. The model soil was cohesive soil and the pile was an aluminum tube, end bearing pile. In the experiment, the same single pile with 4 different head masses were tested under the scaled version of Loma Prieta Earthquake (Figure 2.6). The results showed that the heavily loaded piles (S1, S2 and S3) are dominated by inertial interaction, whereas lightly loaded pile (S4) is dominated by kinematic interaction. Moreover, in order to check the performance of the laminar box, free field test results were simulated with SHAKE 91 (Idriss and Sun, 1992). The agreement of the experiment and analyses results confirmed the validity of the box to reflect the free field conditions, which means model boundary conditions were minimized.

Wu et al. (2002) has studied soil–single pile behavior in dry sand under variable loading conditions and variable input motions using multi-directional 4.0 m × 4.0 m shaking table and 1.5 m × 2.0 m laminar box with a height of 2.0 m. First, free field test was performed with dry sand to check the shaking table performance under different excitations (scaled earthquake records). It was observed that the boundary condition effect increases with the increase of excitations, but the range of the increment is not so large. Secondly, two identical single, reinforced concrete piles with different masses were tested in the same soil profile as the free field test, under earthquake waves including El Centro wave and Kobe wave with

different amplitudes. It was observed that the frequency of the soil profile get far away from the frequency of the system, as the acceleration response of the structure decreases. Also, it was concluded that inertial interaction of the system becomes larger with increasing the excitation intensities.

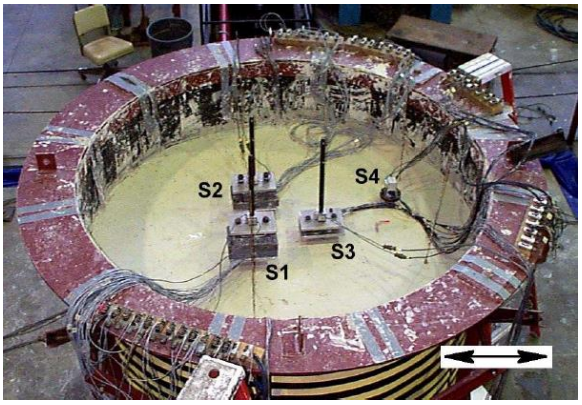

Figure 2.6 Test setup for 4 single piles, loaded by different loads (Meymand et al., 2000).

Horikoshi et al. (2003a) studied on the behavior of 2 × 2 piled raft foundation and its components in sand under static horizontal loading. The effect of pile-raft rigidity, such as rigid or hinged was also investigated in this study. The schematic figure for the experiments is given in Figure 2.7. The piles were made of aluminum pipe with a total length of 250 mm, where the outer diameter was 10 mm with a wall thickness of 2 mm. The spacing of the piles was 40 mm and the embedment length of the piles was 170 mm for the piled raft. The centrifuge acceleration was 50*g*, which means the model to prototype ratio was 1/50. The vertical load was applied by the help of adding mass on top of the raft before applying the horizontal load. The model ground was dry sand, having relative density of 60 %. The vertical loading of piled raft showed that although the applied load is carried by the pile at the beginning of the test due to the poor

contact of the raft and soil, about 65 % of the total load is carried by the raft at the end of the test. The horizontal loading test results showed that the ultimate horizontal resistance of the rigid pile head connection model is larger than that of the raft alone and the hinged pile head connection models. Therefore, the bending moments and the initial horizontal stiffness of hinged model were smaller than that of rigid piled raft connection. Moreover, the proportion of the horizontal load carried by the raft was larger than the piles at small displacements. However, the piles carried more load than the raft at large displacements. In addition, the change at the proportion of vertical load carried by the piles is negligible during horizontal loading.

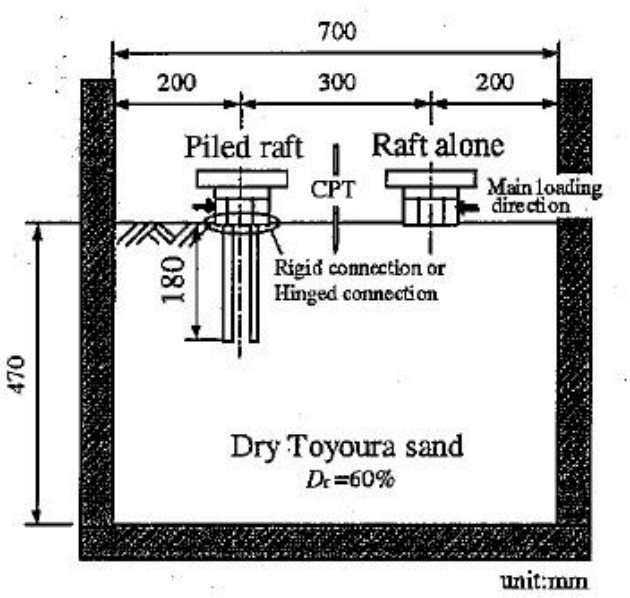

Figure 2.7 Experiment setup of the piled raft and raft alone (Horikoshi et al., 2003a).

Horikoshi et al. (2003b) has performed a series of centrifuge test to investigate the effect of rigidity at pile head connection, the contribution of the raft base to load transfer, the comparison of dynamic and static loading and the proportion of load

sharing between the piles and the raft base. In tests, the same models with the study of Horikoshi et al. (2003a) were used. The soil model was dry Toyoura sand. Input motion was a sinusoidal wave with amplitude of 50 m/s^2 and frequency of 50 Hz. It was observed that the raft-soil contact reduces the acceleration and bending moments of the piles. Horizontal load vs. horizontal displacement graphs of static and dynamic tests are in good agreement (Figure 2.8). In the figure, dynamic and static responses are very similar which means that inertia effects were much more dominant than kinematic effects since the mass of the raft was relatively large. Moreover, it was stated that front piles carried more load than rear piles in positive loading.

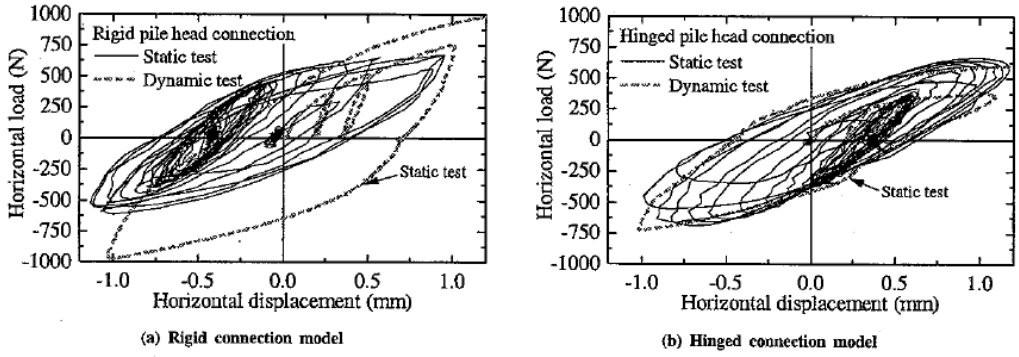

Figure 2.8 Comparison of horizontal load-displacement relationship of piled raft (Horikoshi et al., 2003b).

Matsumoto et al. (2004a) has studied a series of 1-g static horizontal load tests on pile rafts in dry Toyoura sand by changing the height of the acting force and the type of the connection between the pile head and the raft. In this study, the model pile diameter, D was 10 mm with a length, L of 170 mm. The connection between the raft and 2 × 2 group piles with 4D spacing was rigid. Test setup is given in Figure 2.9. The base of the raft was roughened to satisfy a friction between the raft and the soil, where friction angle, ϕ was calculated as 30.5^0 after the

horizontal loading tests of only raft. Parameters of the soil used in the analyses were determined using consolidated-drained (CD) triaxial tests for different relative densities and confining pressures. The proportion of vertical load carried by piles before horizontal load application was around 80 %. Pile head connection had minor influence on the pile axial forces. From the tests results, it could be concluded that as the moment load acting on the raft increases, horizontal displacement also increases. Moreover, hinged connection reduces the values of bending moments of the piles. The front pile carries more load than rear pile for all cases. The deformation and load distribution of a piled raft subjected to horizontal and moment loads depend on both the configuration of the piled raft and the pile-soil stiffness ratio.

In addition, test results were compared with analyses performed by the computer software, PRAB, which was developed by Kitiyodom and Matsumoto (2002, 2003). Analyses were limited to the elastic behavior of the piled raft model. Based on this comparison, it could be concluded that the behavior of the piled raft is similar both in model test and analyses, although the results are overestimated in calculations.

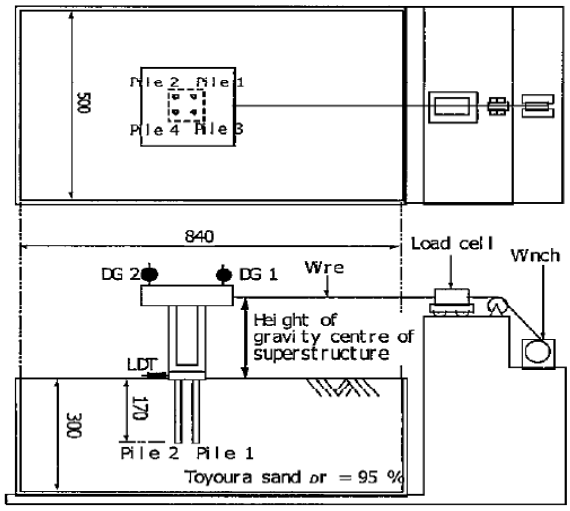

Figure 2.9 Test setup for static horizontal load test (Matsumoto et al., 2004a).

Matsumoto et al. (2004b) investigated the effect of the height of the superstructure and frequency of input acceleration on the response of piled raft. The piled raft model, used at the study of Matsumoto et al. (2004a) was also conducted for this study. The connection between the 2 × 2 piles and the raft was rigid. A laminar box, having dimensions of 210 mm × 560 mm with a depth of 310 mm was assigned as the soil box. Dry silica sand was used as model soil, having relative density of 95 %. Sinusoidal accelerations were applied as input motion, having frequencies of 5 Hz, 10 Hz and 15 Hz. Three different test setups were conducted, which were low, middle and high gravity center models. The results showed that, although the percentage of horizontal load carried by the piles decreases, the proportion of axial load carried by the piles does not change with increasing the height of the center of gravity (Figure 2.10). In the figure, DRL, DRM and DRH correspond to low, medium and high gravity center model with rigid connection between the pile and the raft, respectively. It was reported that front piles carry more load than the rear piles during shaking, which may be due to the increasing contact pressure between the raft and the ground surface around the front piles. Moreover, the behavior of the piled raft at lower input frequency was close to the static horizontal loading results. However, the behavior of the piled raft near resonant input frequency was significantly different than the static loading test results.

In the study of Kagawa et al. (2004), the simulation of large scale shaking table test was performed by centrifuge test for three cases. The model soil, having 65 % relative density sand was used for all tests. The laminar box had dimensions of 11 m × 3.5 m with a height of 6.0 m and 80 cm × 23 cm with a height of 41 cm for shaking table tests and centrifuge tests, respectively. First, free field responses of the sand were tested at shaking table with sinusoidal waves with two different frequencies (3 and 5 Hz) and variable intensities (0 to 200 cm/s^2). Second, four end-bearing steel piles (the pile tips were pinned to the base of the box and also their head were fixed against rotation) carrying 15.6 ton structural model in dry sand was tested with sinusoidal waves (Figure 2.11). The spacing between the

piles was more than 6 times of the pile diameter to minimize the group interaction effect. The test results showed that the largest pile strain occurs around the pile heads due to the fixity at the head and the tip. In the third case, four concrete piles carrying 22.2 tons structural model in liquefiable sand layer was tested. The head and tip conditions of the piles and the spacing between the piles were the same with the previous case. For this case, the input motion was Nanbu Earthquake records. The results of all cases of shaking table tests were compared with centrifuge test results. For the first case, the fundamental vibration frequencies were in good agreement for both systems. For the second case, although the responses of centrifuge tests were smaller than shaking table tests, the overall agreement was good. In the third case, the agreement was weak.

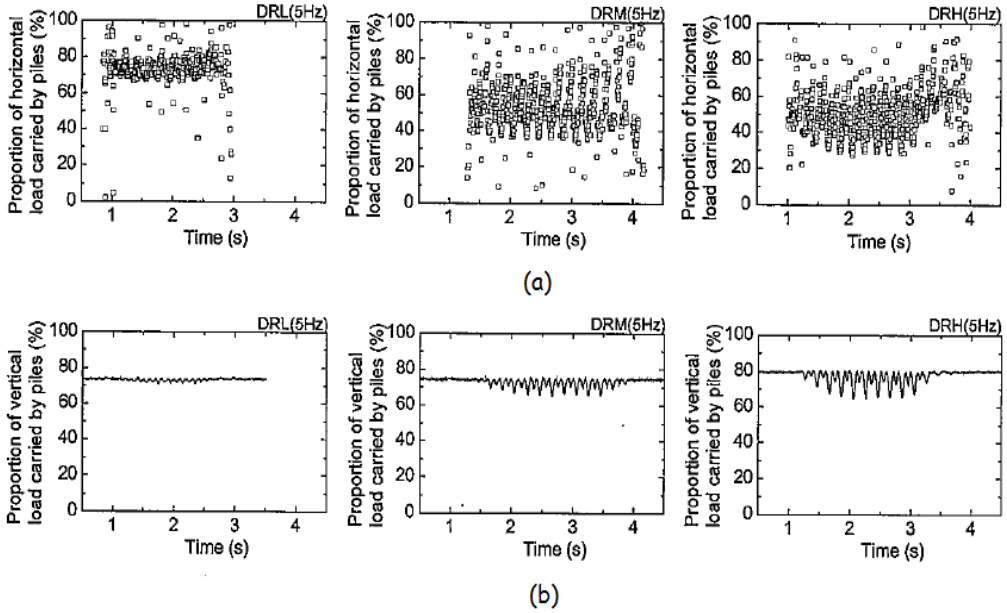

Figure 2.10 Proportions of (a) horizontal (b) vertical carried by piles (Matsumoto et al., 2004b).

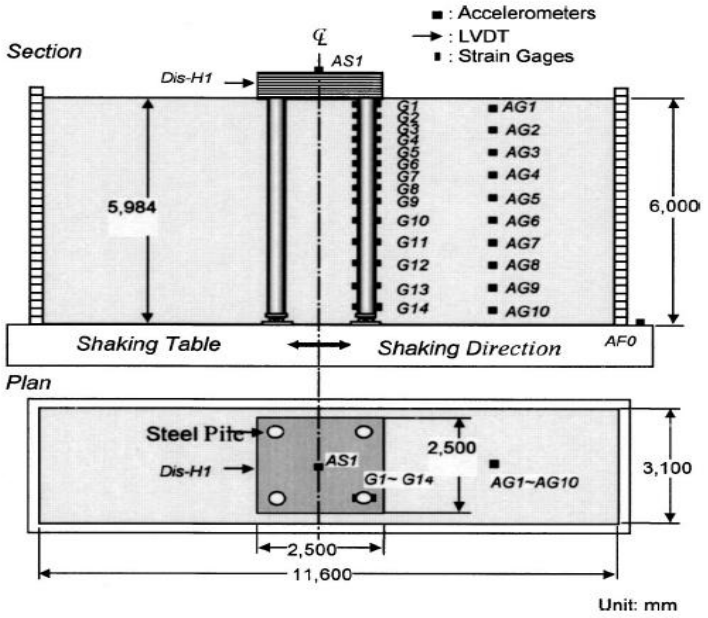

Figure 2.11 Large scale shaking table model for case 2 (Kagawa et al., 2004).

Another centrifuge model test has been performed by Roy et al. (2004) to study the response of laterally loaded single pile and pile groups in loose sand. They focused on lateral load-displacement characteristics of single pile and the pile in a pile group and the interaction factors. The model piles were made of aluminum and their lengths and diameters are 150 mm and 10 mm in model scale, respectively. Model tests were performed for 2 × 4 and 2 × 5 pile groups with same pile spacing. The scale factor of the model was 100, which means 100g centrifuge was applied to the model. The soil model was sand with a relative density of 35 % and the related friction angle was 31^0 (obtained from direct shear box test). The vertical load was applied with the self-weight of the cap. It was concluded that, although the pile group response to lateral load is stiffer than the single pile, the calculated *p* - *y* curves for front and back piles in the pile group are less stiff than that of the single pile (Figure 2.12).

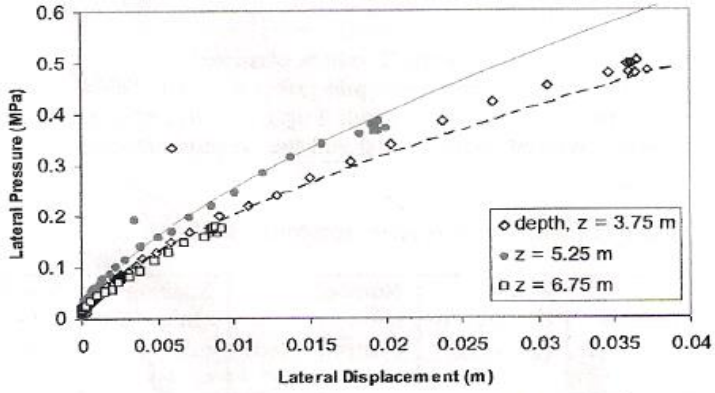

(a)

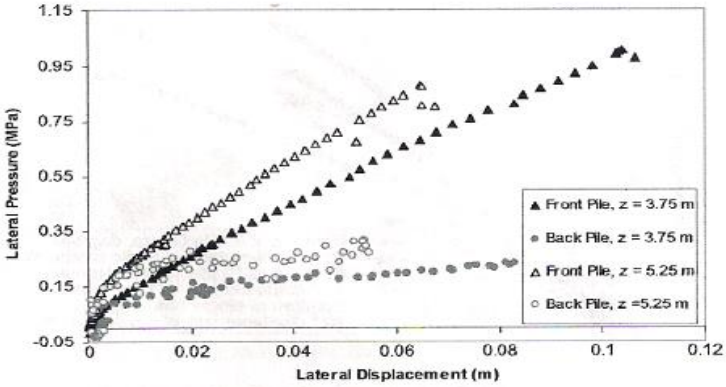

(b)

Figure 2.12 *p* - *y* curves for (a) single pile (b) 2 × 4 group pile (Roy et al., 2004).

Su and Li (2006) investigated the effect of shaking intensity on single piles' responses which were located in liquefiable soils. For this purpose, two single pile models with same initial conditions and different shaking levels were tested by using bi-axial shaking table. A laminar box was used for the experiments and saturated Toyoura sand was selected as model soil. The pile model was aluminum square tube having 1.9 cm width and 3.2 mm thickness (Figure 2.13). A rigid mass of 0.42 kg/pile was used as a raft to isolate dynamic effect of superstructure on the system. The tip of the pile was located 5 pile diameters above the base to eliminate base effect of the container. The input motion was sinusoidal wave with peak accelerations, 0.08*g* and 0.47*g*. The results of the two cases showed that, as the input acceleration increases the excess pore pressure and soil deformation also

increase, whereas motion amplification decreases due to the liquefaction of the soil.

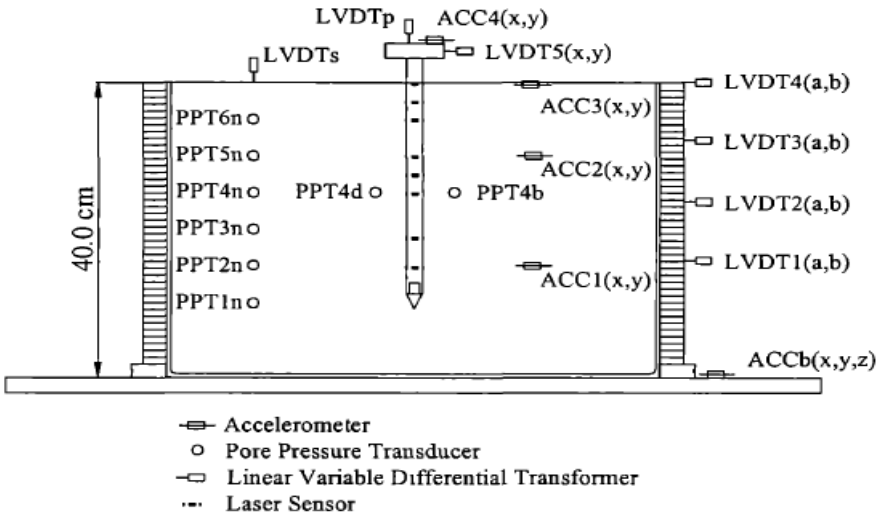

Figure 2.13 Single pile model and the instrumentation (Su and Li, 2006).

Feng and Wang (2006) studied on a scale factor for degradation of $p - y$ curve in saturated sand. They carried out shaking table test on an end-bearing single pile in a laminar box, filled with saturated sand having relative density of 50 %. The model pile was an aluminum pipe pile and the input motion was sinusoidal wave. It was found that static $p - y$ curves should be scaled to determine lateral bearing capacity of the pile depending on the pore water pressure ratio. This scaling factor was applied to the p values and they were estimated by pseudo-static calculation method.

A group of pile foundations including vertical and inclined piles in loose and dense Toyoura sand were studied with centrifuge test by Zhang et al. (2008). The model consisted of 8 aluminum pipe piles (8 vertical piles for the first case and 4 vertical and 4 inclined piles with an inclination of 10° for the second case) having

20 mm diameter and 1.0 mm wall thickness. The spacing between the piles was 2.5*D* for both cases. The details of the model and the instrumentations are shown in Figure 2.14. Input motion was Hyogo-Ken Nanbu Earthquake, 1995. It was stated from the two different densities of the sand that the maximum acceleration of the ground is larger in loose sand. It was also concluded that, although there is a correlation between the bending moment and the inertial forces in vertical piles, it is not valid for the inclined piles. In addition to centrifuge tests, 3D dynamic finite element analyses with nonlinear constitutive models were performed with the software, DGPILE-3D to compare the results with the experiments' results. It was seen that the agreement is good.

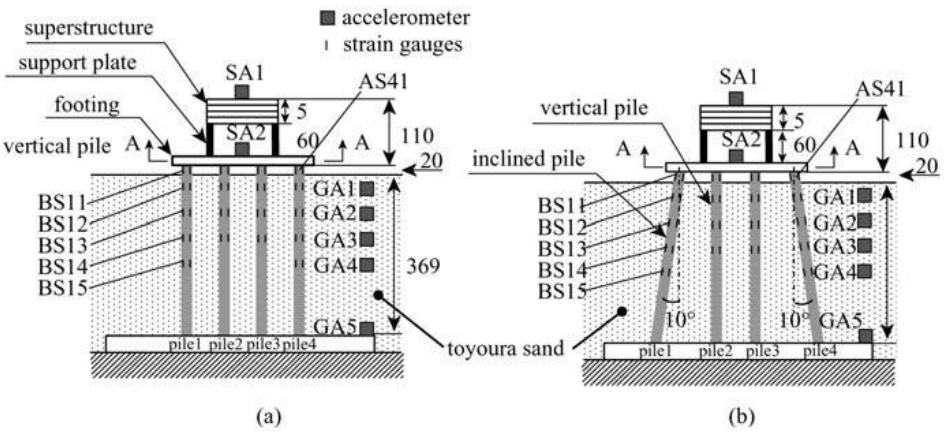

Figure 2.14 Layout for model tests (a) Vertical pile (b) Inclined pile (Zhang et al., 2008).

Another small scale physical model test was carried out on vertical loading of 4 pile-piled raft in medium sand in order to examine the contribution of the raft. The results of the test were compared with Flac-3D and the Poulos-Davis and Randolph method, named PDR. Piled raft model had a circular raft with 220 mm diameter and 400 mm thickness. Piles were modeled by steel rods with 25 mm diameter and 550 mm length (Figure 2.15). Model ground, sand had a relative

density of 45 %. In analyses, Mohr-coulomb constitutive model was used to model medium dense sand and interface elements were used between the soil and structure sub-grids. Load vs. settlement graph shows good agreement between computed and measured values. The results also show that 41 % and 35 % of applied vertical load carried by piles under the design load according to measurements and calculations, respectively (Baziar et al., 2009).

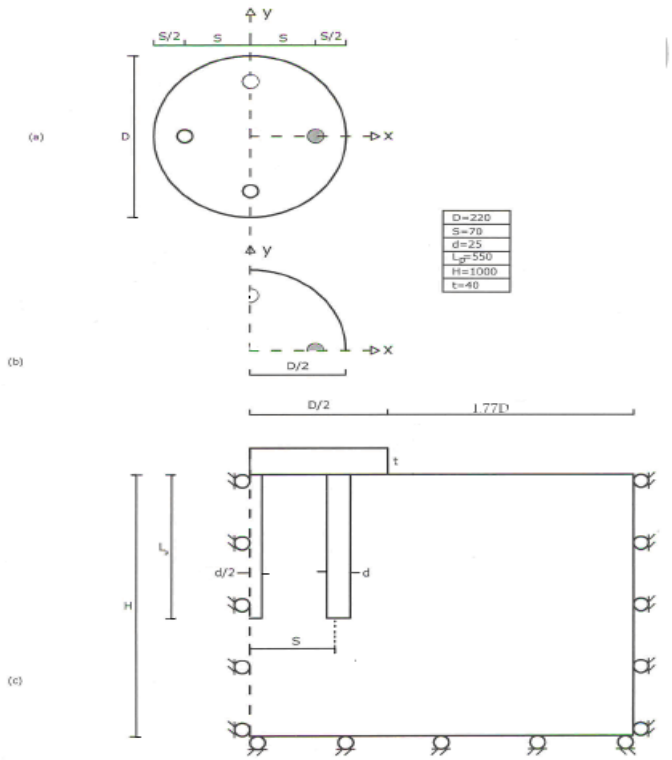

Figure 2.15 a) 1*g* Physical model geometry b) axi-symmetric numerical simulation with one quarter of the model c) boundary conditions of numerical simulation (Baziar et al., 2009).

In a recent study, Song and Wu (2009) were carried out experiments to investigate the seismic behavior of composite ground with rigid piles in silty clay model

ground by shaking table tests. As it can be seen in Figure 2.16, there was a sand gravel cushion layer between the foundation and the pile heads and stiffness of the piles was quite large for this type of pile foundations. Shaking table tests were performed on a model having the similarity ratio of 1:10 (prototype: model) in a flexible container. The similarity ratio for the soil density and modulus was 1 and 4, respectively. Therefore, according to Buckingham-pi theorem the similarity ratio for the acceleration was 2.5:1 which results in smaller weight and smaller stresses of the model compared to the prototype. This problem was solved by applying vertical forces on the foundation model using two pulling cables. The input motion was applied to the model includes El Centro, Kobe and Beijing earthquake acceleration records. The test results showed that the major difference of this system from ordinary pile foundations is lower bending strains at the pile head since the pile heads are not directly connected to the foundation. Additionally, finite element modelling was performed by SHAKE. From the analyses, it was concluded that the magnitude of the bending moment increases significantly when the soil profile has large modulus difference between the adjacent soil layers. Moreover, it was reported that the inertia force of the superstructure, embedment depth, soil modulus, pile diameter have significant effect on the response of the piles.

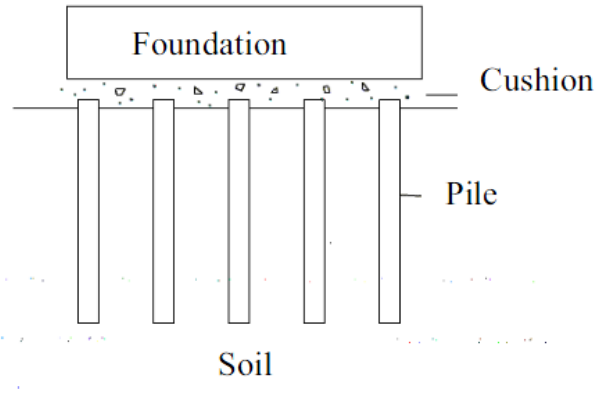

Figure 2.16 Composite ground with rigid piles (Song and Wu, 2009).

Matsumoto et al. (2010) carried out vertical loading and static cyclic horizontal loading tests on 2 × 2 piled raft to investigate the pile head connection and piled raft behavior. The model ground was dry Toyoura sand, having the height of 1000 mm. The raft of the model was made of stainless steel, whereas piles were made of aluminum, having the diameter of 40 mm, the wall thickness of 2 mm and the length of 600 mm (Figure 2.17). Four different piled raft connections were modeled which were labeled as rigid, semi-rigid, semi-hinged and hinged. The mechanical properties of Toyoura sand was obtained from CD triaxial tests, where friction angle was estimated as 40°. Two different types of foundations were considered; piled raft (which is composed of 4 piles and the raft, no space between the raft and the model ground) and pile group (which is also composed of 4 piles and the raft having 5 mm space between the raft and the model ground).

Results of the vertical loading showed that raft-pile connection has little effect on the settlement amount. Vertical load carried by the raft was measured about 30 % to 60 % for all cases which confirms the study of Kakurai (2003; cited in Matsumoto et al., 2010). In case of horizontal loading, horizontal stiffness of piled raft was larger than that of the pile group, where horizontal displacement was greater at hinged connection type. Moreover, pile-raft connection had a significant influence on the inclination such as, the inclination of the raft decreases as the pile head connection becomes less rigid. At the beginning of the loading, horizontal load mostly carried by the raft. However, after the slippage of the raft, piles started to carry loads effectively. Shear forces of the piles in piled raft was lower than that of the pile group due to the contribution of the raft base. In addition, pile head connection had no effect on the amount of horizontal load carried by model foundations.

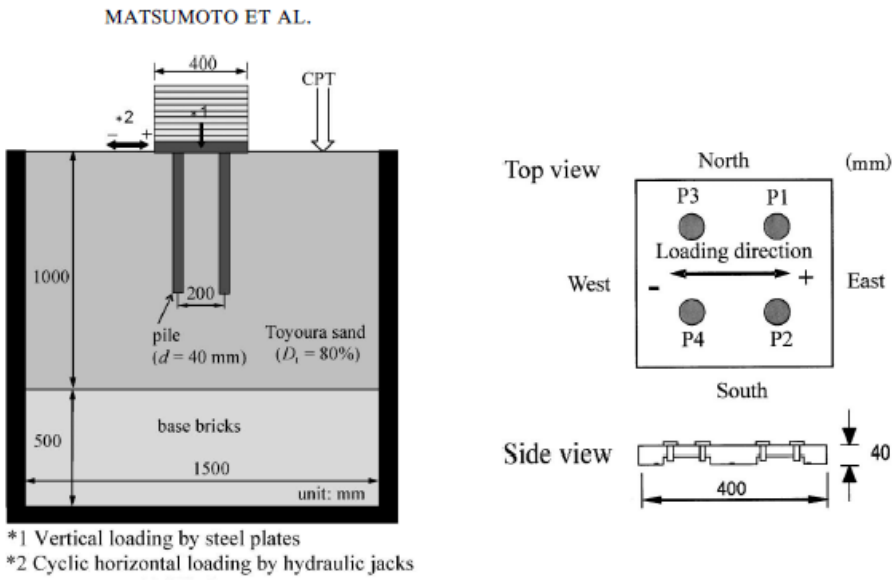

Figure 2.17 Test setup for static cyclic horizontal load test (Matsumoto et al., 2010).

2.2.3 Previous studies on pile foundations by finite element analysis

In order to prove the accuracy and applicability of finite element software, the test results are compared with the experiment results. Butterfield and Banerjee (1971) studied the behavior of pile group-pile cap system by using elastic analyses. It was found that, the proportion of the vertical load that carried by the cap is between 20 % to 60 % depending on the group size and pile spacing.

Franke et al. (1994) introduced a numerical model and a simplified method to analyze vertical loading of piled raft. In numerical model (BEM), the raft and the pile group were analyzed separately by the combination of finite element method and complete boundary element structure. In simplified method, piled raft was divided into a raft and a pile group and soil behavior was assumed as linear elastic. Both of these methods were used to analyze high rise buildings, founded in Frankfurt clay. The load-settlement curve of observed and calculated results

showed nearly linear behavior up to the actual applied load (Figure 2.18). It was concluded that, the behavior of single pile is totally different than the components of piled raft. Moreover, center pile carries little load than the corner and edge piles in piled raft model.

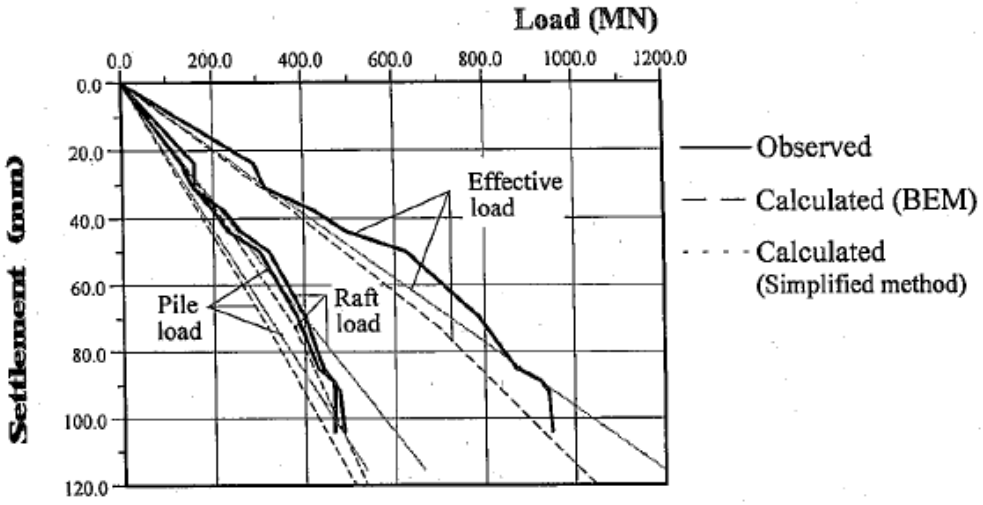

Figure 2.18 Load-settlement relationship of piled-raft elements (Franke et al., 1994).

El-Mossallamy (1999) analyzed load-settlement behavior of single pile and group pile in over consolidated clay by analytic method (BEM model) and finite element method (FEM). Note that, the analytic model considers nonlinearity of pile response and soil behavior. Finite element analyses were performed for two constitutive models; Mohr-Coulomb model (MCM) and Hardening soil model (HSM). The analysis result for single bored pile was compared with pile load test result, and it was seen that they are in good agreement (Figure 2.19). In addition, the single pile base shared 35 % of the total load when skin friction was fully mobilized, which pointed out that the single pile behaves as a friction pile. When pile group was analyzed, it was seen that the load settlement behavior of a pile in

a pile group is totally different than a single pile which depends on the geometry of foundation, the position of the pile and the applied load level.

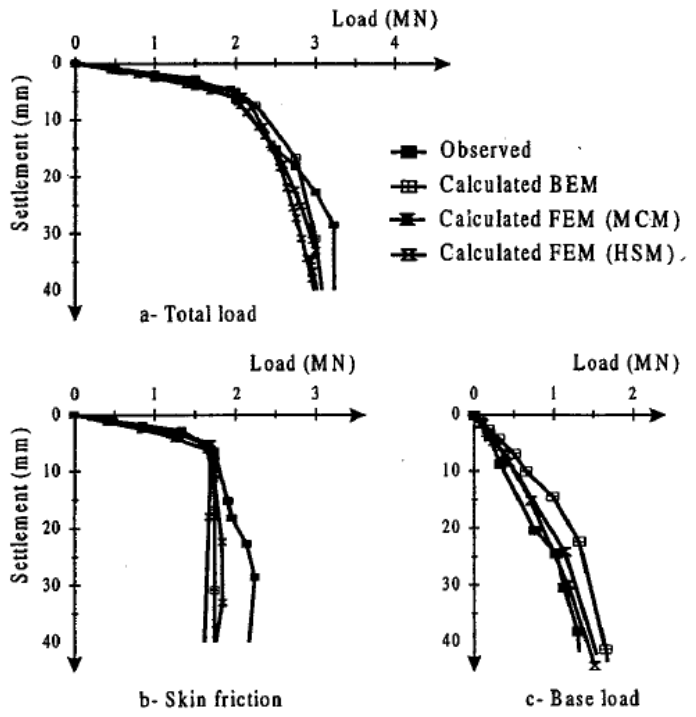

Figure 2.19 Comparison of pile load-settlement behavior of single pile (El-Mossallamy, 1999).

Finn and Fujita (2002) studied on the response of single piles in liquefiable soil. They stated that in elastic range, API (*p* - *y*) curves estimate the behavior reasonably, whereas it predicts the behavior poorly at strong shaking since their prediction is based on static or slow cyclic loading test data. For this reason, seismic response of a single pile in a centrifuge test was analyzed by PILE-3D and PILE-3DEFF (effective version of PILE-3D). The effect of inertial forces from the super structure was also investigated, and it was stated that including super structure load is important during strong shaking since it decreases the lateral

stiffness of the pile (Figure 2.20). Moreover, the rotation of the pile head is another important criterion that should be taken into account in any seismic analysis since most of the damages occurs at pile head and also at the boundary between liquefied and non-liquefied layers.

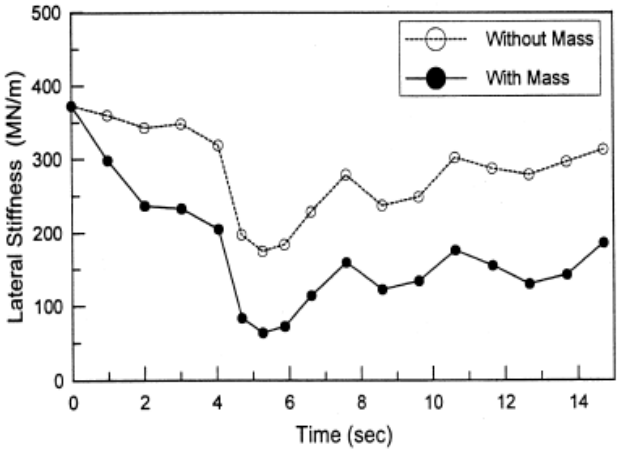

Figure 2.20 Lateral stiffness of the single pile with and without mass (Finn and Fujita, 2002).

Reul and Randolph (2003) compared in situ measurements and numerical analysis of three case histories in over consolidated clay, which were constructed in Frankfurt, Germany. The numerical analyses were carried out by three-dimensional elasto-plastic finite element analyses by using ABAQUS program. The results showed that overall agreement for settlements was good. However, the ratios of the sum of the pile load to the total load were overestimated about 30 % in the analyses.

Reul (2004) studied on the bearing behavior of piled rafts in over consolidated clays by analyzing different configurations with finite element software, ABAQUS. In the numerical study, number of piles, edge length, pile length, pile

diameter and pile spacing were varied. It was seen that, the skin friction in pile group remains same, whereas that of piled raft increases with the increment of the settlement or increment of load due to the load transfer from the raft to the soil.

Reul and Randolph (2004) were carried out finite element analyses on piled rafts with various configurations of piles and loads by using software ABAQUS to find the optimized piled length of the piled raft at Frankfurt clay, which is stiff and over consolidated clay. The clay was modelled by using elasto-plastic cap model, the raft and piles were modelled as linear elastic. It was found that, the average settlement becomes smaller with increasing pile lengths rather than increasing the number of piles. Moreover, differential settlements can be reduced by installing piles at the central area of the raft.

Extended pile shaft behavior, subjected to lateral cyclic loading in dry sand was investigated by full-scale tests (Hutchinson et al., 2005). The results of the test were compared by using finite element analyses. Two different kinds of piles were tested (heights of the piles were 2*D* and 6*D* above the ground level) in loose and dense sand conditions. Finite element model, used in this study was a beam-on-nonlinear-Winkler Foundation (BNWF) framework which was modeled by the help of finite element software, FEDEAS. Although dry sand was used, gap generation was observed during cyclic loading. After gap was closed stiffening effect can be observed on the reloading curve from measurements. Therefore, it was stated that the gap generation simulation is necessary during analysis. Moreover, important features of the soil-pile interaction such as initial elastic stiffness, post peak strength degradation, unloading and reloading response were reasonably captured by finite element model (Figure 2.21). Good correlation of bending moment and displacement between the test results and finite element analysis showed that the behavior of pile under lateral loading simulated well by using simple *p* - *y* springs and nonlinear beam-column elements as a pile model.

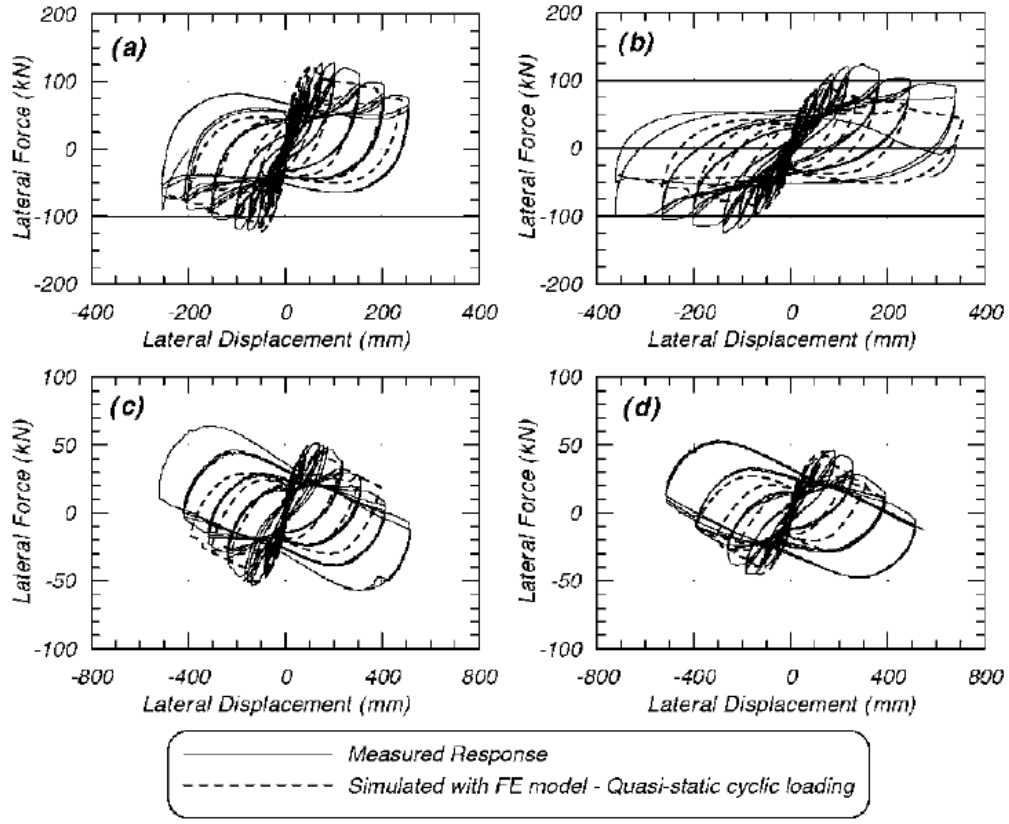

Figure 2.21 Measured and calculated hysteresis loops (a) 2*D* above ground in dense sand (b) 2D above ground in loose sand (c) 6D above ground in dense sand (d) 6*D* above ground in loose sand (Hutchinson et al., 2005).

In the study of Ramachandran (2005), the software, ABAQUS was used to model a group of nine steel piles and an isolated single pile under lateral loading. Half of the mesh was modelled due to symmetry. The model ground was over consolidated clay and Mohr-Coulomb model was used to reflect the soil nonlinearity in the analysis. Pile-soil interface was also taken into account by surface-based contact element to model contact behavior. In addition to contact pressure, frictional behavior might or might not be included to the model. Pile response was assumed as linear elastic. 3D finite element mesh for the single pile analysis is illustrated in Figure 2.22. The results of single pile analysis showed

that best match with experimental results are obtained when hard contact model with no friction is chosen as a contact behavior of the soil-pile interaction. In group analysis, the properties of the pile and soil-pile interface, which were obtained from single pile results, were used. It was seen that the most important factor that affects the interaction of the piles in a group is the pile spacing, which is followed by soil nonlinearity and pile-soil gapping.

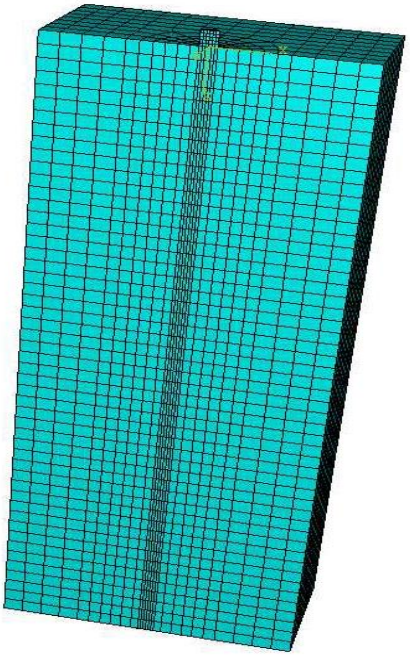

Figure 2.22 3D Finite element mesh of single pile (Ramachandran, 2005).

A series of shaking table tests on piles and sheet pile wall in saturated sand has been studied under lateral spreading for investigating various factors by an institute in Japan. Cubrinovski et al. (2005) has studied one specific case of these experiments for performing 3D effective stress analysis. The model consisted of 3 × 3 steel piles with 2.5*D* spacing. These piles were fixed at the base and rigidly connected to the pile cap (Figure 2.23). Input motion was 20 uniform cycles with a frequency of 5 Hz and peak amplitude of 470 cm/sec^2. Diana –J3 software was

used with Stress-Density model, which was an elastic-plastic constitutive model to represent sand behavior and the piles, pile cap and sheet pile were modelled as linear elastic material. The soil, the pile cap and the sheet pile were represented by eight node solid elements and piles were modelled by beam elements. Moreover, boundary conditions and soil-pile interfaces were also specified. The results showed that, the behavior of piles and the ground response are simulated reasonably good accuracy with the test results; however sheet pile displacement is underestimated by 3D analysis.

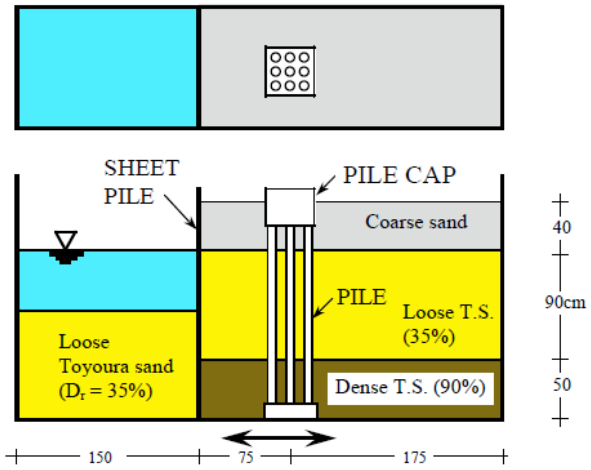

Figure 2.23 Soil-pile model of the experiment (Cubrinovski et al., 2005).

Finn (2005) used the results of a centrifuge test conducted by Finn and Gohl (1987; cited in Finn, 2005) at University of California, Davis to evaluate the nonlinear software, PILE-3D. The tested model was an end bearing single pile, the layout of the test and the finite element mesh are given in Figure 2.24. The soil profile was loose sand with a relative density of 38 %. The system was subjected to 60*g* centrifuge acceleration. Two input motions, having peak acceleration of

0.158*g* and 0.04*g* were applied to the model. It was seen that, the measured and computed bending moments with depth are in good agreement.

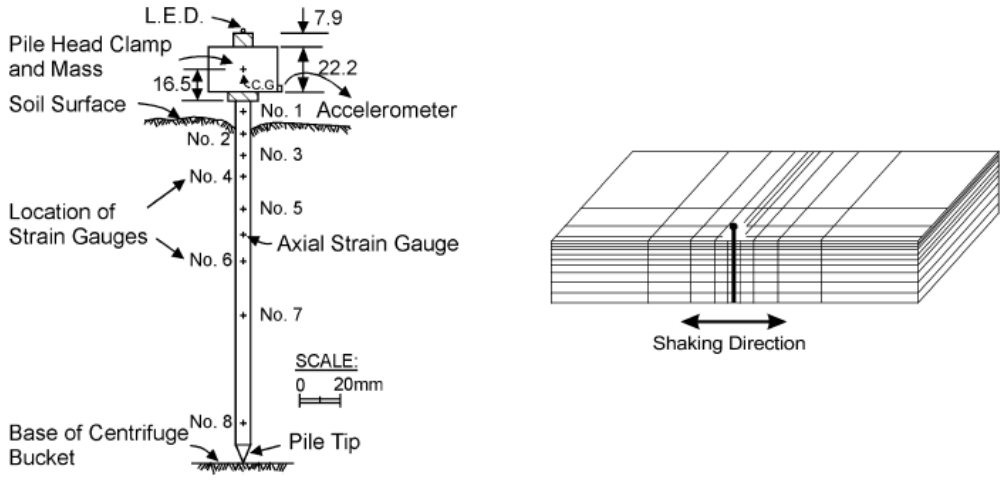

Figure 2.24 The instrumented model and the finite element mesh for the single pile (Finn, 2005).

Irshad and Akhtar (2006) studied on kinematic response of piles by analyzing end-bearing single pile, embedded in two layered soil, having highly contrasting stiffness with finite element software, SAP2000. The results show that kinematic seismic loading should be considered in dynamic analysis since it might damage the pile alone near the interface of soil layers due to the generated large moments. In addition, pile displacement was slightly different than the displacement of the ground therefore the superstructure experienced different input motion than the ground. Moreover, kinematic interaction introduces a rotational component into foundation input motion.

Kasali et al. (2006) compared dynamic pile test results with the results of finite element software, 2D Plaxis v. 8.2 in order to verify the capacity of the pile. An axisymmetric model with 6 nodes isoperimetric elements was used. Interface

elements were also introduced for the contact surface between the pile and the soil. Wave absorbing boundaries were used to prevent wave reflection during the analysis. Concrete pile and reinforcing steel was modelled as an elastic material and surrounding soil was modelled as elastic-perfectly plastic, Mohr-Coulomb model. Finite element mesh of the model is given in Figure 2.25. It was concluded that the agreement between the calculated and measured displacement and velocity can be improved by increasing the Young's modulus of the soil at the tip of the pile by five times. Therefore, developing a loading rate dependent soil model could give better results.

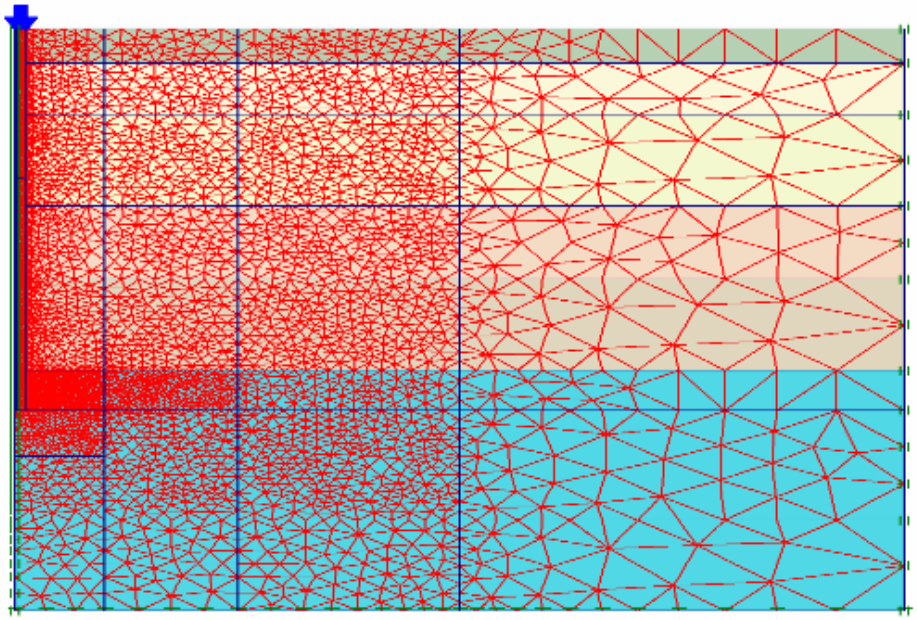

Figure 2.25 Finite element mesh of the model (Kasali et al., 2006).

Ordu and Özkan (2006) analyzed the seismic performance of pile foundations by 3D finite element analyses. They focused on nonlinear behaviors of soil layers, having different shear modulus. Drucker-Prager elasto-plastic soil model was used for all soil layers, and elastic model was used for structural elements. Interface

elements were not considered. The input motion was scaled San Fernando earthquake. It was concluded that calculated moments and shear forces on the piles strongly depends on soil layering and should be considered carefully.

In the study of Oh et al. (2008), numerical analyses of vertically loaded un-piled raft and piled raft foundation in mainly sandy soil conditions were considered. Plane strain analyses were performed by PLAXIS 2D. Mohr-Coulomb was used as a soil model, and raft was modeled as a plate element, while the piles were modeled as a series of beam elements. The effects of raft size, raft thickness, pile spacing on settlement and bending moment were investigated. It was concluded that, most effective way of decreasing maximum settlement is increasing the pile length, which does not affect differential settlement and bending moment significantly.

In the study of Poulos et al. (2011), 9-piled raft was tested at the field, then finite layer software, APRILS was used to analyze piled raft and piled group conditions and compared the results of the calculations with the test results. The steel piles had a diameter of 324 mm with a wall thickness of 9.5 mm, and the spacing was 3 × pile diameter. Hydraulic jacks were used to apply horizontal load. The soil was composed of clay, sand and sandy silt material. The results showed that best match is obtained with the assumption of contact between raft and both underlying and adjacent soil (Figure 2.26). Additional analyses were carried out to compare the response of pile group and piled raft conditions under vertical loading, which showed that piled raft continues to carry additional load, after pile capacities are fully mobilized on the contrary to pile group.

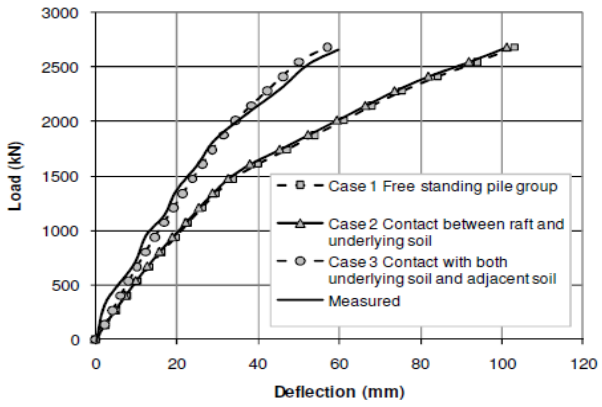

Figure 2.26 Load deflection behavior (Poulos et al., 2011).

Poulos et al. (2011) also analyzed a case study in Incheon, South Korea by finite element software, PLAXIS 3D foundation. The building was constructed on soft marine clay underlying by soft rock, where the foundation consisted of 172 piles. Two different cases were considered; piled raft in contact with the underlying soil and piled raft contact with both the underlying soil and adjacent soil. Mohr-Coulomb was used as a soil model. First, only vertical loading condition was considered, the results showed that adjacent soil contributes to the reduction of the settlement. Then, only lateral loading condition was considered, in addition to these two cases “no contact” between the raft and soil was also taken into account by placing a thin soft layer underneath the raft. It was seen that, the effect of the adjacent soil is less due to the large number of piles contribution (Figure 2.27). Therefore, for large number of pile groups, ignoring the embedment of the raft is adequate to calculate lateral response of foundation and bending moment of the piles.

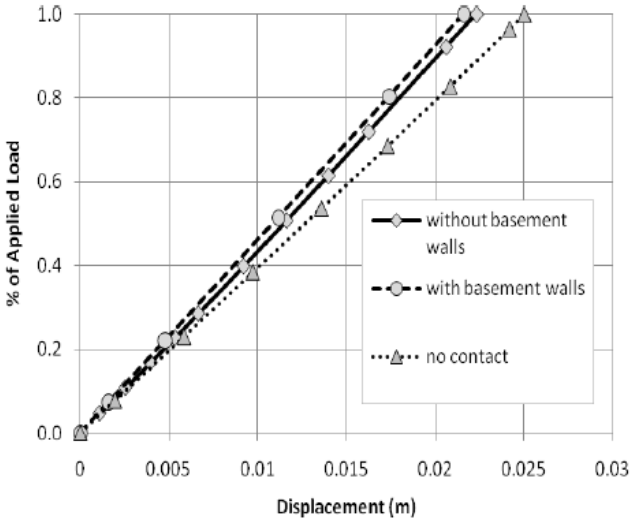

Figure 2.27 Lateral load deflection behavior of the midpoint of the raft (Poulos et al., 2011).

Kim and Jeong (2011) studied on the load distribution and deflection of piles by finite element analyses, PLAXIS 3D. Single pile under lateral loading was analyzed by using the typical mesh, shown in Figure 2.28. Both pile and the soil were modelled with finite elements to consider the soil-structure interaction. The ground was selected as clay, which was modelled with Mohr-Coulomb and the pile was considered as linear elastic. The interface element had the same material properties with the surrounding soil before slip occurs, and the decrement of the strength was explained with strength reduction factor, R_{inter} after slip occurs. The effect of pile installation was ignored at analyses. The results were validated with the field measurements from Korea. In addition, parametric study was performed by investigating the influence of the pile diameter, the pile length, the pile elastic modulus, the interface property and the bearing layer on lateral load transfer. It was seen that, pile elastic modulus, interface property and bearing layer do not have significant effect on *p - y* curves, whereas ultimate soil resistance increases with increasing pile diameter and this effect is more significant in flexible piles.

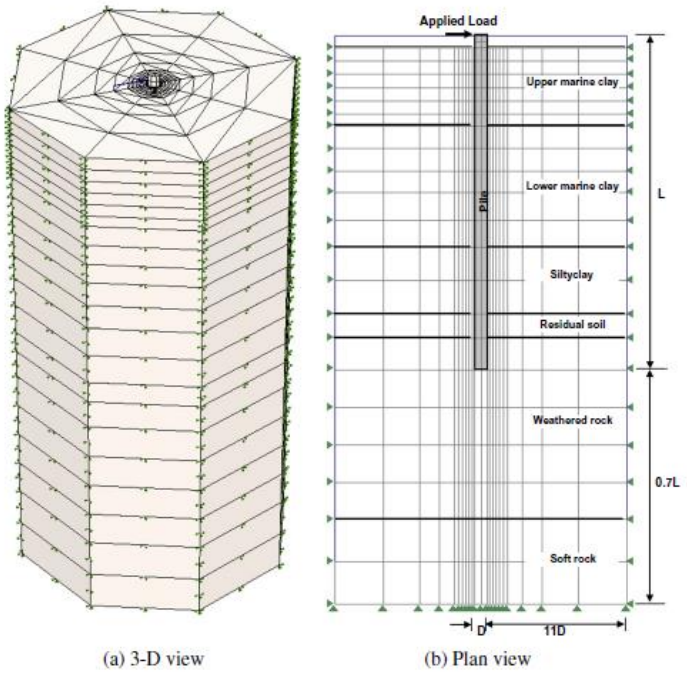

Figure 2.28 Finite element mesh for the analysis (a) 3D view (b) Plan view (Kim and Jeong, 2011).

CHAPTER 3

VERTICAL AND STATIC CYCLIC LOAD TESTS ON MODEL FOUNDATIONS

3.1 Introduction

In this chapter, the results of a series of load tests which include vertical and static cyclic horizontal loading of model foundations in dry sand are considered. Even when a piled raft or a pile group is subjected to horizontal loading alone, compression or tension loads are induced in piles depending upon locations of the piles and the nature of loading in the foundation. Hence, responses of the model foundations subjected to vertical loading were investigated first. The test results would be beneficial for understanding response of the foundations subjected to horizontal loading.

For this purpose, experiments on various model foundations such as single pile, capped pile, full raft, pile group and piled raft, were carried out to investigate the behavior of piled rafts and the main differences between the piled raft and the pile group due to the contribution of the raft. The same model foundation was used for the piled raft and the pile group, which consisted of 3 single piles and a raft. However, 20 mm space was provided for pile group model in order to eliminate the raft effect. The spacing between the piles was constant through the experiments since it was out of this study's scope.

3.2 Preparations of Experiments

3.2.1 Model piles

In order to investigate the behavior of piles and piled rafts under vertical and static cyclic horizontal loading, aluminum pipe pile was instrumented with vertical and shear strain gauges. The raft was made of steel, which was manufactured at a special laboratory. First, pile was cut at the desired length (280 mm for this case), and the decided locations for the gauges were marked on the pile by scratching. Next, the pile was instrumented with axial and shear strain gauges using superglue. Then, strain gauges were labelled according to their locations. As it is seen from Figure 3.1, there were 12 vertical strain gauges at 6 levels and 4 shear gauges at one level on each pile.

The tip of the pile was closed with a cap, which had a thickness of 5 mm. After that, bending tests were performed by applying known weights on the pile as shown in Figure 3.2. In order to define Young's modulus, E of the aluminum pile, back calculations were carried out by using simple beam theorem to fit the measured strains. Another reason for conducting bending tests was to pre-test the strain gauges before covering and verify that if they work properly or not (Figure 3.2). Then, pile was covered with special glue named "hard rock" and sand, which was used as model ground (properties of which are given in Section 3.2.3) to protect the wires and strain gauges and also to satisfy a frictional surface between the pile and the model ground (Figure 3.3). After covering, at least 24 hours were waited for hardening of the cover. Then, bending test was carried out again to check that if the pile had same properties with that of the pile before covering. It was seen that, covering didn't change the properties of the pile. Young's modulus of the pile was calculated as 64000 MPa, and the Poison's ratio was predicted as 0.31 from the previous test setups. The properties of the pile are summarized at Table 3.1. The same steps were also followed for the preparation of 3 piles of the

piled raft (or pile group). The photos of three piles before and after covering are given in Figure 3.4.

Table 3.1 Properties of the pipe pile.

Item	Value
Diameter, D (mm)	20.00
Wall thickness, t (mm)	1.1
Cross sectional area, A (mm^2)	65.31
2nd moment of area, I (mm^4)	2926.22
Young's modulus, E (N/mm^2)	64000
Poisson's ratio, υ	0.31

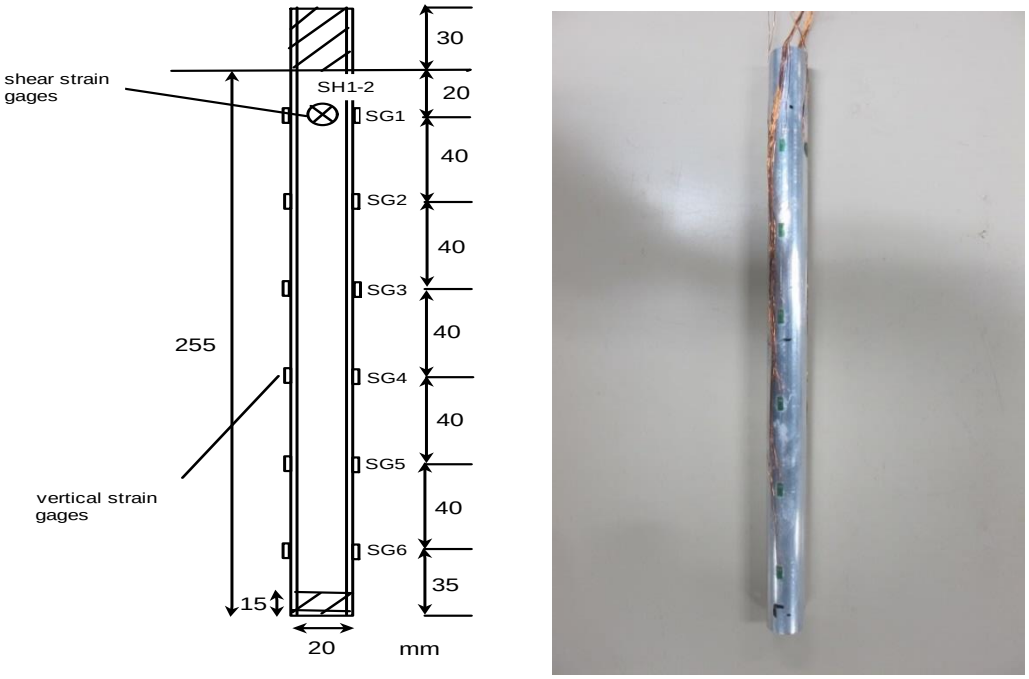

Figure 3.1 Arrangement of vertical and shear strain gauges.

Figure 3.2 Test setup for bending test of pile before covering.

(a)

(b)

Figure 3.3 (a) Covering the pile with special glue; “hard rock” and sand (b) hard rock material and the apparatus.

(a)

(b)

Figure 3.4 Preparation of the 3 piles (a) before covering (b) after covering.

3.2.2 Calibration of instruments

In order to measure the horizontal and vertical displacements and applied loads during the experiments, dial gauges and load cells were used. Before using them, calibrations were performed. Examples of calibration procedures are presented below:

Load cells (LC): Calibration of the load cells were performed by applying known weights on top of the instrument. Two load cells were labelled according to the

location during the experiments as right and left; LC-1 and LC-2, respectively (Figure 3.5).

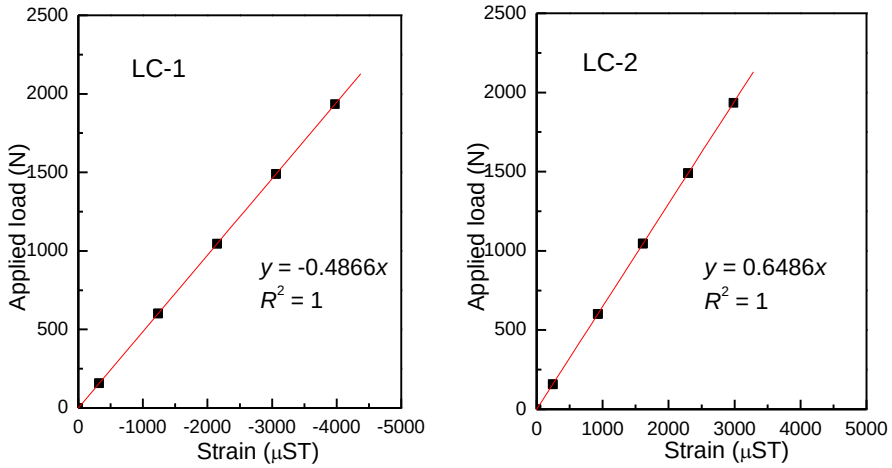

Figure 3.5 Calibration of right and left load cells.

Vertical dial gauges (VDG): During static cyclic load tests and vertical load tests, in order to measure the vertical deflection of the raft or the pile, two vertical dial gauges were located at right and left sides. Therefore, from these two measurements, average displacement and the inclination of the raft can be obtained. Calibration of the vertical dial gauges were performed by measuring the known thickness of objects. Two vertical dial gauges were labelled according to the location during the experiments as right and left; VDG-1 and VDG-2, respectively (Figure 3.6).

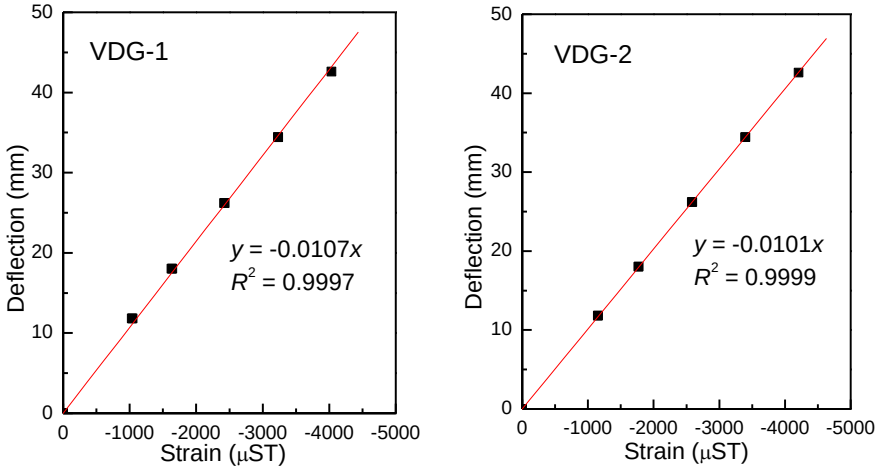

Figure 3.6 Calibration of right and left vertical dial gauges.

Cone penetration test rode: In order to check the homogeneity of the soil in the box and also to confirm that the soil model was prepared at almost same density for each experiment, it was decided to perform cone penetration test. Before the experiments, calibration of the miniature cone penetrometer, having a diameter of 20 mm with an apex angle of 60^0 was performed. Figure 3.7 shows the calibration setup of the apparatus. Horizontal and vertical strain vs. applied vertical stress curves were drawn at Figure 3.8. From these graphs, Poisson's ratio, υ, was calculated as 0.173 and Young's modulus, E of the rod was calculated as 2.58×10^5 MPa by considering temperature change during the experiment.

Table 3.2 shows the summary of the calibration factors of the instrumentations used during vertical tests and static cyclic horizontal tests with their maximum ranges.

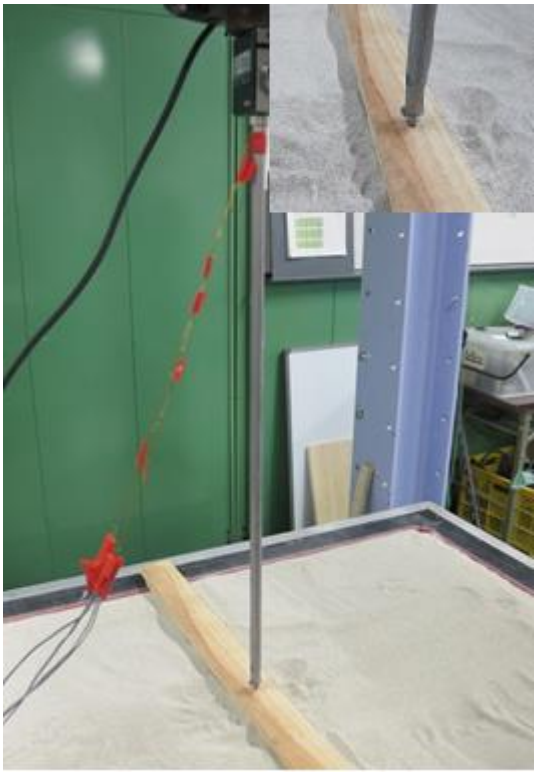

Figure 3.7 Cone penetration apparatus calibration test.

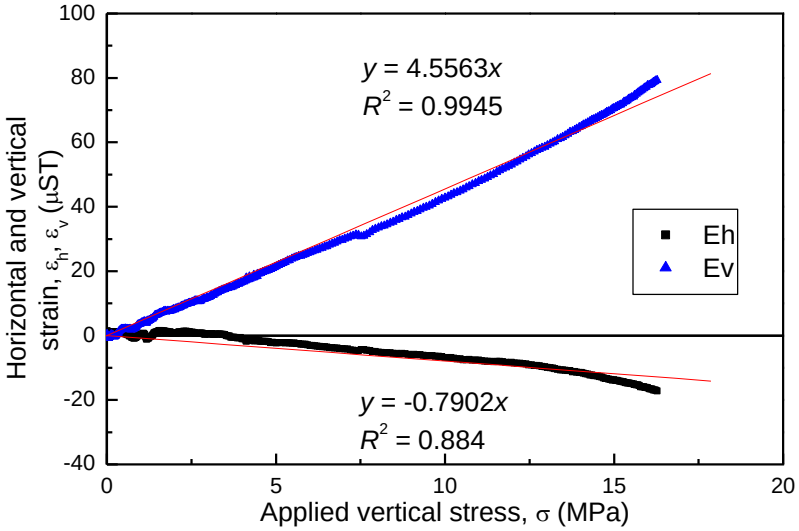

Figure 3.8 Horizontal and vertical strain graph of the rode.

Table 3.2 Summary of the calibration factors.

Instrumentation	**Coefficient**		**Max Range**
Horizontal Load Cell, Right (HLC-R)	0.0838	N/μST	500 N
Horizontal Load Cell, Left (HLC-L)	0.1628	N/μST	1000 N
Vertical Load Cell (VLC)	0.8196	N/μST	5000 N
Load Cell, 1 (LC-1)	-0.4866	N/μST	2000 N
Load Cell, 2 (LC-2)	0.6486	N/μST	2000 N
Horizontal Dial Gauge (HDG)	0.00996	mm/μST	50 mm
Vert. Dial Gauge, Right (VDG-R)	0.0068	mm/μST	20 mm
Vert. Dial Gauge, Left (VDG-L)	-0.0049	mm/μST	20 mm
Vert. Dial Gauge, 1 (VDG-1)	-0.0107	mm/μST	20 mm
Vert. Dial Gauge, 2 (VDG-2)	-0.0101	mm/μST	20 mm

3.2.3 Model ground and the soil box

Model ground: As a model ground, silica sand #6 was used. The grain size distribution of the sieve test is given in Figure 3.9, which was classified as poorly graded sand according to Unified Soil Classification System.

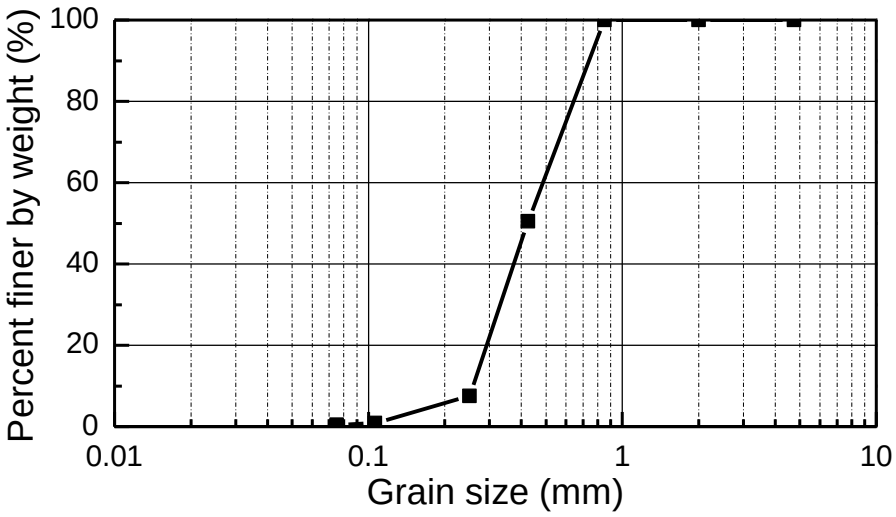

Figure 3.9 Sieve test results of sand.

In addition, one dimensional compression tests were carried out at the relative density, D_r = 70 % to find the relationship between constraint elastic modulus, E_c, and effective overburden pressure, σ_v' by using Eq. 3.1.

$$E_c = E_{cref}\left(\frac{\sigma_v'}{\sigma_{ref}'}\right)^n \tag{3.1}$$

E_{cref}: constraint elastic modulus at $\sigma' = \sigma'_{ref}$

σ_v': effective overburden vertical stress

σ'_{ref}: reference stress (taken as 100 kPa)

n: exponent

Test data and boundaries calculated by the help of Eq. 3.1 were drawn in Figure 3.10. From the figure, it is seen that the average boundary is estimated as E_{cref} = 55 MPa and n = 0.5.

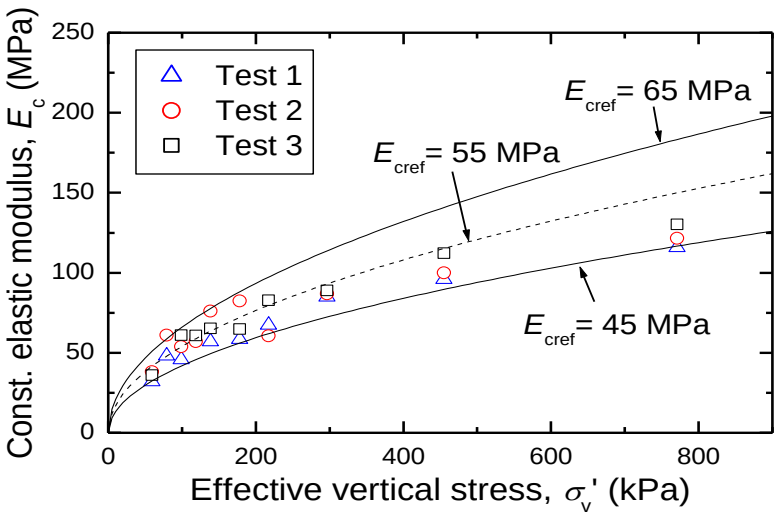

Figure 3.10. Relationship between the elastic constraint modulus, E_c, with effective vertical stress, σ_v'.

To estimate shear modulus, G, of the model ground by using the constraint elastic modulus, the following equation was used (Lambe and Whitman, 1969; cited in Duncan and Bursey, 2013):

$$G = \frac{1}{2(1+\nu)} E = \frac{1-2\nu}{2(1-\nu)} E_c \tag{3.2}$$

If Poisson's ratio, ν, was assumed as 0.3, the above equation becomes,

$$G = 0.2857 E_c \tag{3.3}$$

For the model ground, the distribution of shear modulus that obtained from 1D consolidation test is summarized in Table 3.3 with minimum (min.), maximum (max.) and average (aver.) values of shear modulus for each layer.

Table 3.3 Strength parameters .of the Silica sand #6.

#	Upper & lower bound. (mm)	Thickness, h (mm)	Dry unit weight, γ_d (kN/m^3)	Overbur Stress σ_v' (kPa)	Shear mod. G_{min} (kPa)	Shear mod. G_{max} (kPa)	Shear mod. G_{aver} (kPa)
1	0-100	100	14.239	0.712	1012.47	1591.03	1301.75
2	100-200	100	14.239	2.136	1753.65	2755.74	2254.70
3	200-280	80	14.239	3.417	2218.22	3485.77	2851.99
4	280-380	100	14.239	4.699	2601.09	4087.43	3344.26
5	380-480	100	14.239	6.123	2969.16	4665.82	3817.49
6	480-530	50	14.239	7.191	3217.69	5056.37	4137.04

After that, a series of triaxial CD tests of the sand having D_r = 70 % were carried out under different confining pressures, p_0 (p_0 = 11, 50, 100 and 150 kPa). In addition, a cyclic CD test was conducted under p_0 = 100 kPa. The details of the test will be explained in Chapter 5.

The peak friction angle, ϕ' of the model sand ground was estimated as 43.2^0 from the failure line, drawn according to CD triaxial test results under various confining pressures (Figure 3.11). The physical properties of the sand are summarized in Table 3.4.

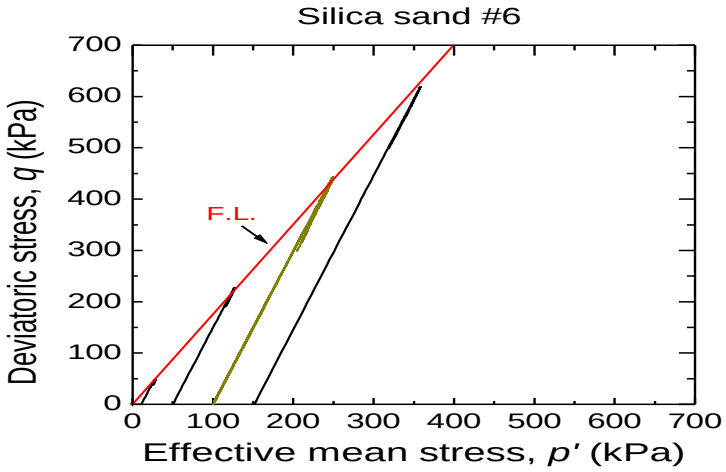

Figure 3.11 Effective mean stress, *p'* versus deviatoric stress, *q*.

Table 3.4 Physical properties of Silica sand # 6.

Item	**Value**
Density of soil particles, ρ_s (t/m^3)	2.66
Max. dry density, ρ_{dmax} (t/m^3)	1.542
Min. dry density, ρ_{dmin} (t/m^3)	1.280
Max. void ratio, e_{max}	1.079
Min. void ratio, e_{min}	0.725
Median grain size, D_{50}	0.423
Coefficient of uniformity, U_c	1.880
Internal friction angle, ϕ' (^{0})	43.2

Laminar box: Model ground was prepared in a laminar box that had dimensions of 800 mm (in x-direction) × 500 mm (in y-direction) with a depth of 530 mm (Figure 3.12). The box consists 10 frames having a height of 50 mm. Inside of the box was covered with rubber membrane to allow the movements of the ground in the box in x and y directions.

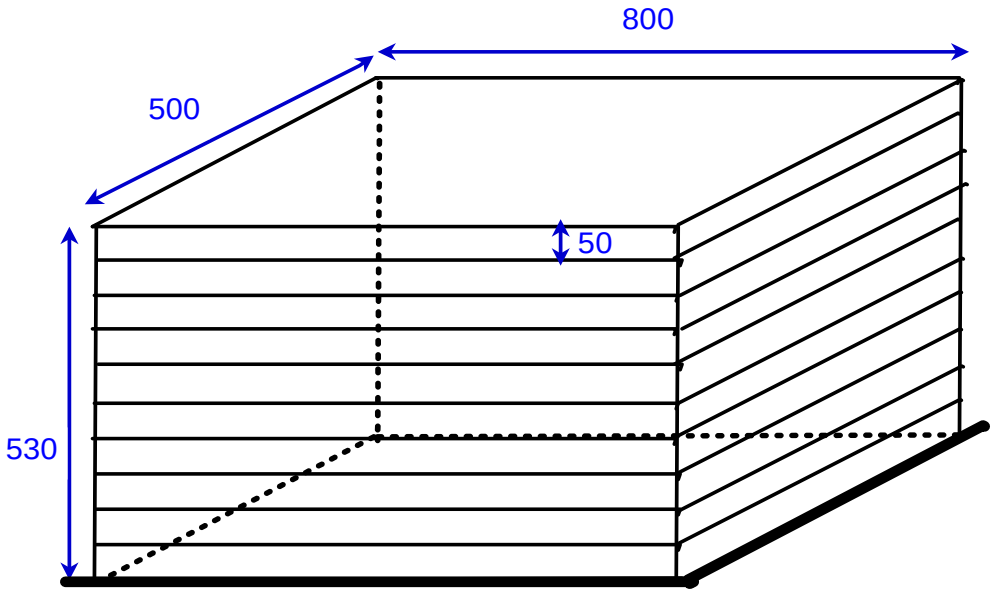

(a)

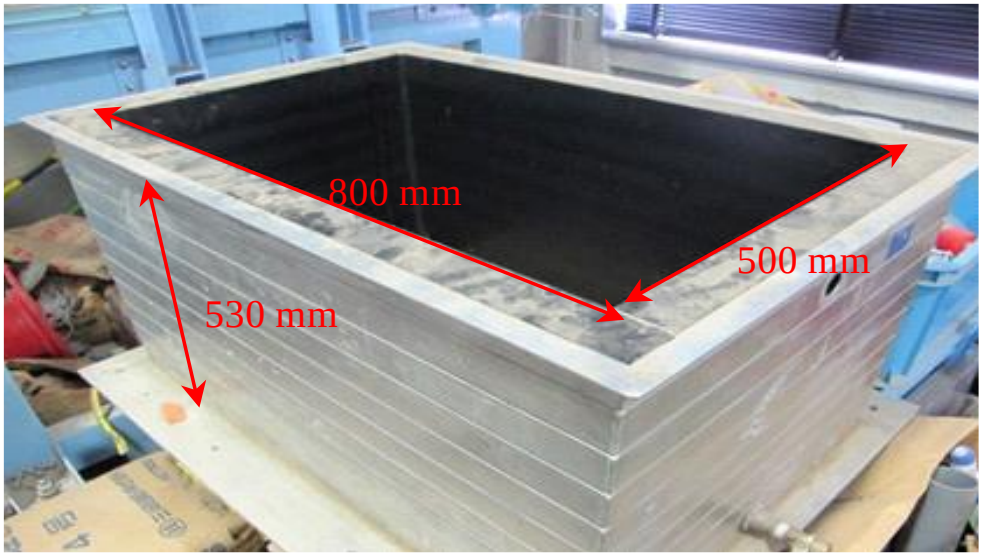

(b)

Figure 3.12 The Laminar box (a) drawing (b) photo.

In order to check the uniformity of the distribution of the soil strength of the model ground and to confirm the repeatability of the tests, Cone Penetration Test (CPT) with a miniature cone penetrometer, having a diameter of 20 mm with an

apex angle of 60^0 was carried out at six locations in the soil box. The measured tip resistance, q_c vs. ground depth, z graph is drawn by considering temperature change during experiments. Figure 3.13 and Figure 3.14 show the CPT results of piled raft and pile group's model grounds, respectively. As it is seen from these figures, model ground was compatible for both cases.

If CPT results of all experiments (for four different model grounds) are drawn in one graph to compare the model ground conditions of the experiments, it is seen that the results are in a reasonable range (± 350 kPa at the mid-depth) (Figure 3.15). Therefore, it confirms that, model ground conditions are almost uniform for all tests, and model grounds prepared by the described procedure were consistent throughout the tests. Moreover, q_c increases almost linearly with depth and it is not influenced by the side walls if the location is far from the side walls by 10 cm - 15 cm.

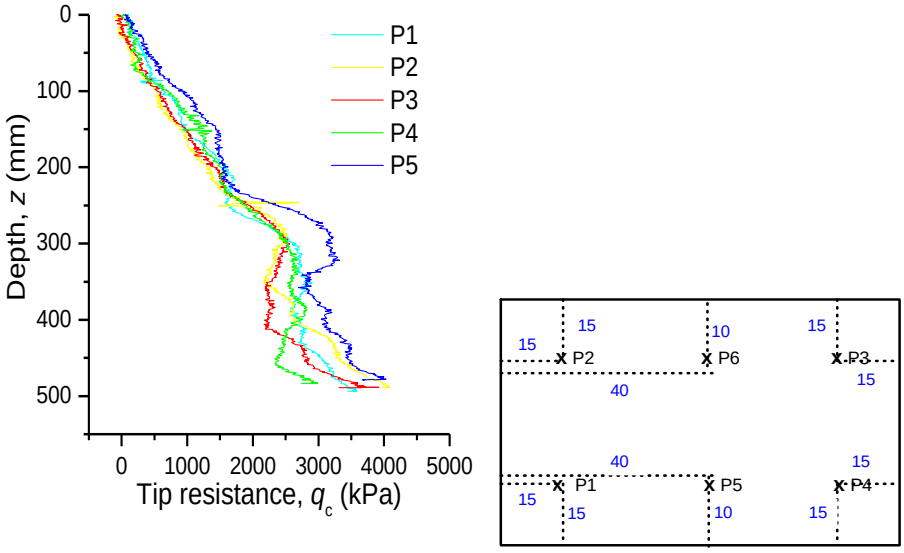

Figure 3.13 CPT results of PR test with locations.

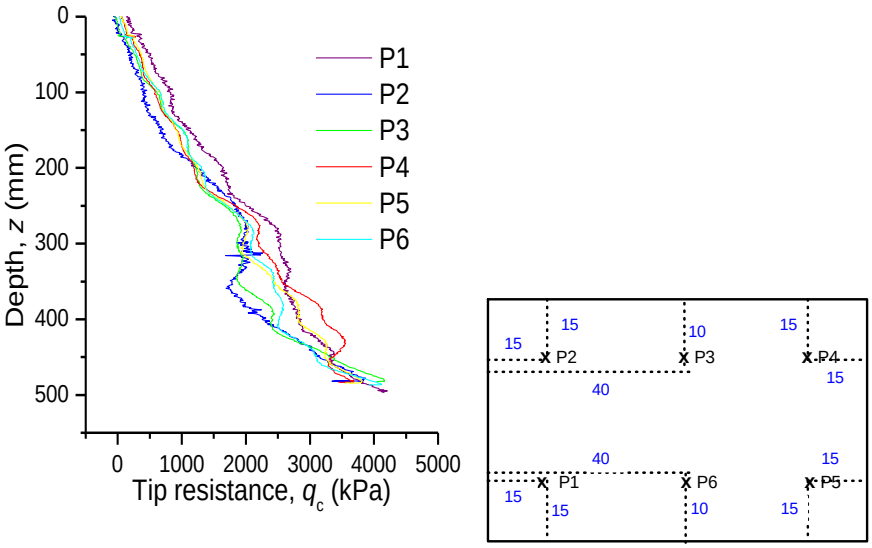

Figure 3.14 CPT results of PG test with locations.

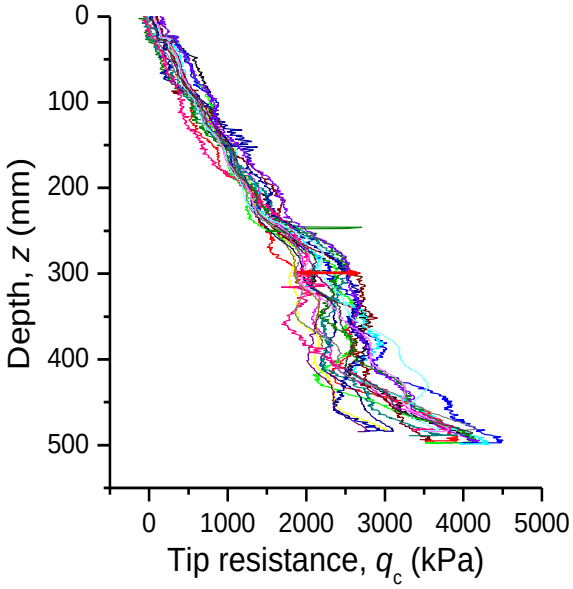

Figure 3.15 CPT results of all four tests.

3.3 Similitude of the model pile

Physical modelling is a critical point to be considered. The behavior of the prototype is investigated by using a smaller model which has more rapid response and closer control. In the model, the effects of the parameters can be investigated by changing one parameter and taking others constant.

In physical modelling, an important issue is how the results of the model can be translated to the prototype behavior. Since the material behavior is commonly nonlinear and the interaction between the several materials should also be taken into account, dimensional analysis can be performed by using Buckingham's pi theorem. This theorem helps to satisfy the same safety margin between the prototype and the model by keeping dimensionless parameters constant. In fact, this can be possible if gravitational acceleration, g which is a fundamental parameter for most of the geotechnical problems can be increased artificially by the help of geotechnical centrifuge equipment as mentioned before. However, in shaking table test, it cannot be possible to keep all the dimensionless parameters constant, in other words to scale gravitational acceleration.

In the experiment setup, aluminum pipe pile was used as a model pile, and silica sand #6 was used as a model ground. The similitude law which was proposed by Iai, 1989 is applicable to the present study that carried out at 1-g field (Table 3.5). In case of scale ratio of $\lambda = 30$, the bending rigidity, EI, and longitudinal rigidity, EA, of a prototype pile are 4.35 and 2.43 times those of a concrete pile ($E = 30 \times 10^6$ kPa) having a diameter of 0.6 m and a length of 7.65 m, which means a "short pile" condition. Note that the test results are presented in model scale throughout the study.

Table 3.5 Summary of similitude law for scale ratio, λ=30 (Iai, 1989)

λ (prototype/model)	**30**			
Item	**1-g**		**Centrifuge**	
Length	λ	30	λ	30
Density	1	1	1	1
Stress	λ	30	1	1
Strain	$\lambda^{1/2}$	5.477	1	1
Shear modulus	$\lambda^{1/2}$	5.477	1	1
Time	$\lambda^{3/4}$	12.819	λ	30
Frequency	$1/\lambda^{3/4}$	0.078	$1/\lambda$	0.033
Displacement	$\lambda^{3/2}$	164.317	λ	30
Velocity	$\lambda^{3/4}$	12.819	1	1
Acceleration	1	1	$1/\lambda$	0.033
Bending rigidity of pile (E.I)	$\lambda^{9/2}$	44.366×10^{5}	λ^{4}	81.00×10^{4}
Longitudinal rigidity of pile (EA)	$\lambda^{5/2}$	49.295×10^{2}	λ^{2}	900

3.4 Model Foundations

3.4.1 Single pile (SP)

Single pile was an aluminum pipe pile which had an outer diameter of 20 mm with a wall thickness of 1.1 mm. The total length of each pile was 280 mm, where the upper 30 mm was embedded into the raft. The tip of the pile was closed with pile cap which had a thickness of 5 mm, was also included to the pile length, resulting in the length beneath the raft base of 255 mm (Figure 3.1). In order to

measure the strains that occurred during the horizontal test, each pile was instrumented with 12 vertical strain gauges and 4 shear strain gauges as mentioned before.

3.4.2 Full raft (FR)

The design of the full raft is given in Figure 3.16. The raft had dimensions of 240 mm × 80 mm with a thickness of 30 mm. The hollows that designed for piles were filled with special cylinders, made of steel to obtain full raft model. Weights (lead plates) were prepared to apply vertical load on top of the model foundation by placing them on the loading plate. The loading plate was designed and fastened on top of the raft. There was a space between the plate and the raft top since the strain gauges cables were taken out through that space.

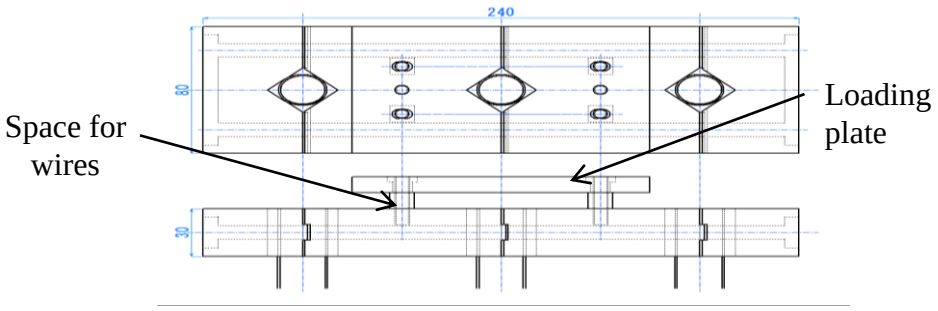

Figure 3.16 Design of the full raft.

3.4.3 Piled raft (PR)

Piled raft (or Pile group) was composed of a raft and 3 single piles, each of them had an outer diameter of 20 mm, with a thickness of 1.1 mm. The model foundation is shown in Figure 3.17. The bottom of the raft was covered with the silica sand particles to obtain frictional surface between the raft and the ground during horizontal loading. Center-to-center pile spacing, *s*, was 80 mm, 4 times

the pile diameter, D = 20 mm (s/D = 4). Pile spacing ratio s/D of 2.5 to 3 is usually adopted in conventional design of pile group. In contrast to the conventional design concept of piled raft, it is intended that the raft carries a portion of the applied vertical load by reducing the number of piles or the pile length. Hence, a pile spacing ratio s/D = 4 was selected in this particular study.

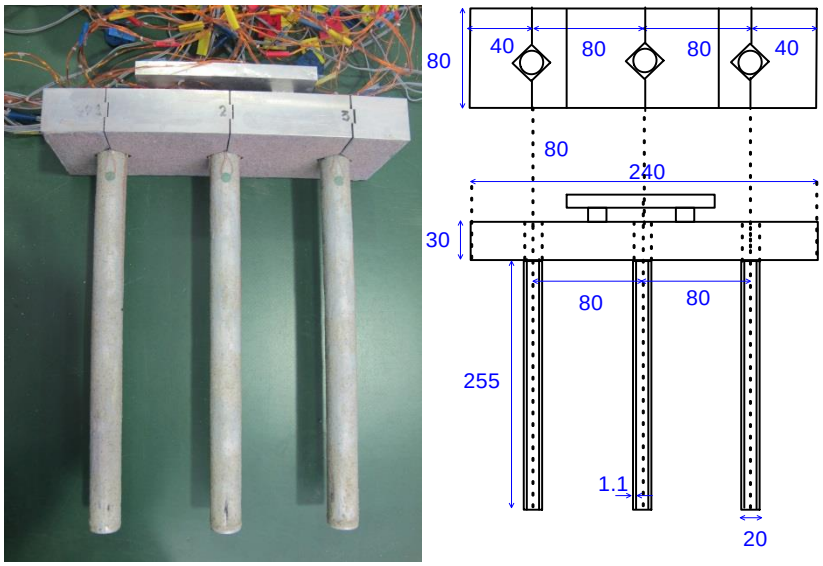

Figure 3.17 Design of 3-pile piled raft or 3-pile pile group.

3.4.4 Pile group (PG)

Although, the same model foundation of Piled Raft (PR) was used for Pile Group (PG) test, 20 mm space between the raft and the model ground was provided at PG test in order to eliminate the raft resistance. For PG case, the pile length was shortened 20 mm due to the space between the raft and the ground, therefore the effective pile length became 235 mm. Note that, the total soil layer was also 20 mm lower than PR test.

3.4.5 Small raft (SR)

The small raft model was consisted of 2 outer parts of full raft, each of them having 40 mm width. They were fixed with special screws to each other, where pile spaces were filled with special cylinders. The bottom surface of the raft was covered with Silica sand #6, to obtain a frictional surface between the raft and the ground during horizontal loading as mentioned earlier. The design of the raft is given in Figure 3.18. As it is seen, the small raft had dimensions of 80 mm × 80 mm with a thickness of 30 mm, which was 1/3 of the full raft.

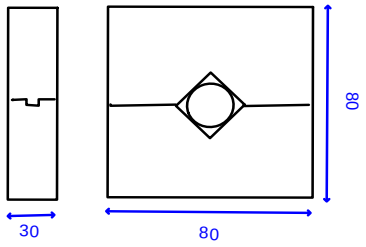

Figure 3.18 Design of the small raft.

3.4.6 Capped pile (CP)

Capped pile (CP) consisted of small raft and a single pile, as shown in Figure 3.19. The raft had dimensions of 80 mm × 80 mm with a thickness of 30 mm, which was identical with the small raft.

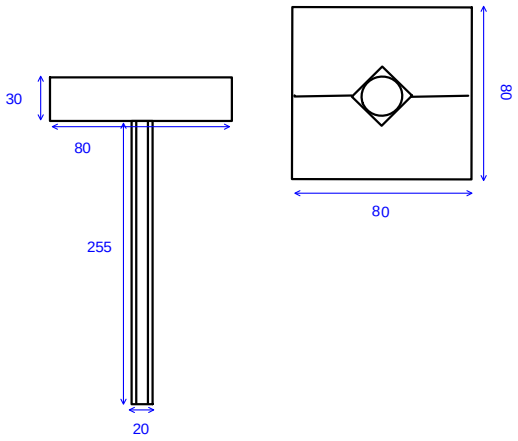

Figure 3.19 Design of the capped pile.

3.5 Vertical Loading Tests and Results

Set-up of the model ground and the model foundations:

In order to control the density of the model ground, the ground was prepared by layers (10 layers of 50 mm and one layer of 30 mm). First, 6 layers (which makes totally 280 mm height) was placed one by one and compacted until an intended relative density of 70 %. Then, the model foundation was fixed on the box by the help of clamps and rods. After that, 5 more layers of soil were placed with the same method until 530 mm height of the model ground was obtained. Finally, load cells and dial gauges were placed to measure applied loads and deformations.

The piles are considered to be cast-in-place piles by taking into account the preparation steps, because sand was poured around the piles then compacted lightly. In reality, variations of strains of the piles were very small during the preparation of the model ground. Therefore, strains of the piles were initialized (zeroed) at the end of preparation of the ground and the model foundation.

Procedure of the tests:

Vertical load was applied by the help of screw jack with constant displacement rate until the pile head displacement reached about 1 × *D* (pile diameter).

Instrumentations:

The following items were used to record the measurements during the test:

(i) 1 vertical load cell to measure applied forces

(ii) 2 vertical displacement gauges to measure vertical displacements

(iii) 12 axial strain gauges for each pile to measure bending moments and axial forces (if applicable, depending on the model foundation)

(iv) 4 shear strain gauges (one-gauge measurement method was used to measure strains) for each pile to measure shear forces (if applicable, depending on the model foundation)

3.5.1 Single pile (SP) and Capped pile (CP)

Vertical load test on Single Pile model (SP) and Capped Pile model (CP) were carried out to investigate the capacities of these two models under vertical loading. In this part, capped piled and single pile results are compared. CP model was composed of a small raft and a pile. At SP model test, the same pile was used without raft. The model ground was silica sand #6, with a relative density of D_r = 70 %. Figure 3.20 shows the vertical loading experiment setup for SP model. Note that, VDG-R and VDG-L indicate vertical dial gauges located at right and left sides of the model foundation, and VLC is the vertical load cell which measures the applied vertical load. The experiment setup of CP model test was identical with the SP model test.

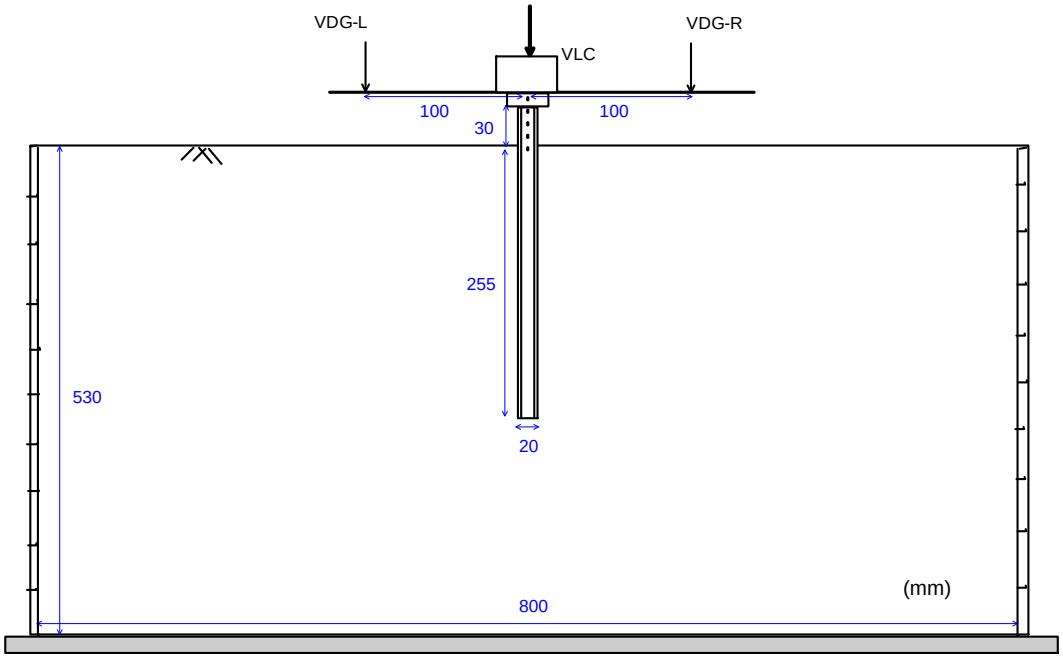

(a)

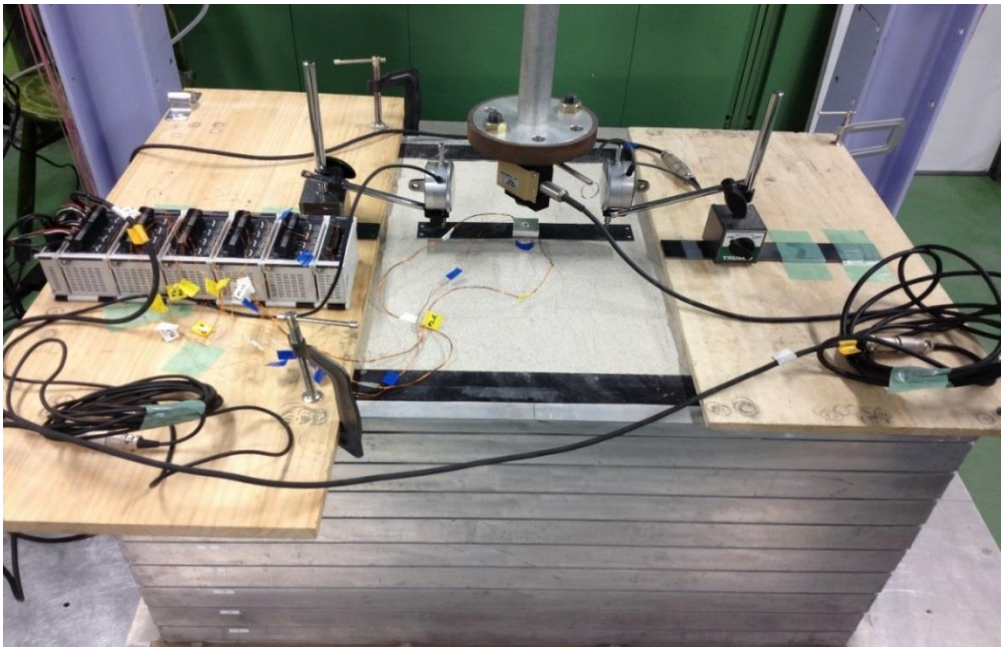

(b)

Figure 3.20 Test setup for SP model (a) drawing (b) photo of the experiment.

Test results:

In order to evaluate the performance of the raft, Capped pile and Single pile model tests were conducted, with the same effective pile length under same conditions. Figure 3.21 shows the vertical load-settlement relationship for vertical loading tests of SP and CP models. Although, the final settlement of both models is similar (about 17 mm), vertical load capacity of CP is two times larger than SP model. The comparison of single pile alone and the pile as a component of CP is given in Figure 3.22. It is seen that, the pile component of CP gives slightly larger values than SP, which may be due to the increment of confining stresses beneath the raft. Therefore, it can be said that, the increment of the vertical capacity of CP is due to the contribution of the raft.

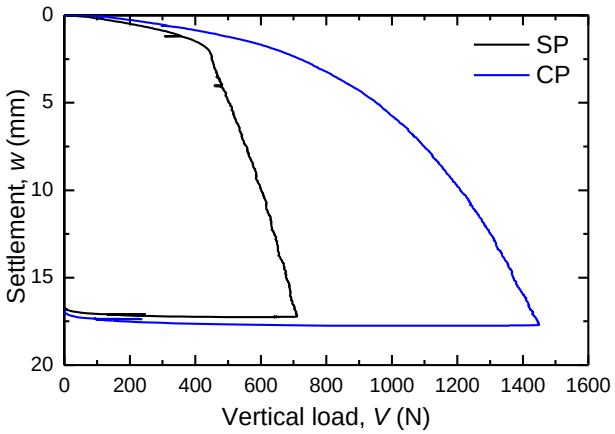

Figure 3.21 Vertical loading capacity of SP and CP.

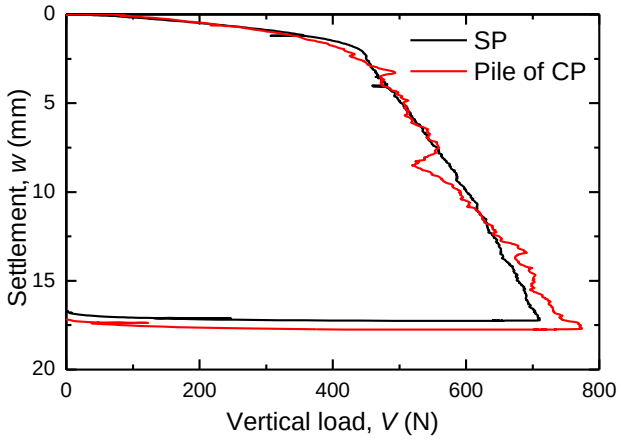

Figure 3.22 Comparison of SP and the pile component of CP.

Figure 3.23 indicates the vertical load carried by each components of CP model. In the figure, raft load was obtained by extracting pile loads from total applied load. From the figure, it is understood that, at the beginning of the test most of the load is carried by the pile due to the poor contact between the raft and the ground. The percentage of vertical load carried by the pile for CP model is given in Figure 3.24. As the settlement increases, the proportion of vertical load carried by pile decreases and, the proportion of vertical load carried by the raft increases, where each component carries 50 % of vertical load after w/D = 0.3 (6.0 mm settlement).

Figure 3.25 shows the distributions of axial forces along the pile shaft for SP and CP models at normalized settlements, w/D = 0.02, 0.05, 0.20, 0.40, 0.60 and 0.80. It is seen that, axial forces along the pile of CP model are slightly larger than SP model at each w/D. This may be caused by the load transfer from the raft bottom to the ground, resulting in increase in horizontal stresses on the pile shaft and stiffness of the ground surrounding the piles, as suggested by Horikoshi et al. (2003a). In addition, for both cases more than 50 % of pile head load is transferred to the pile toe.

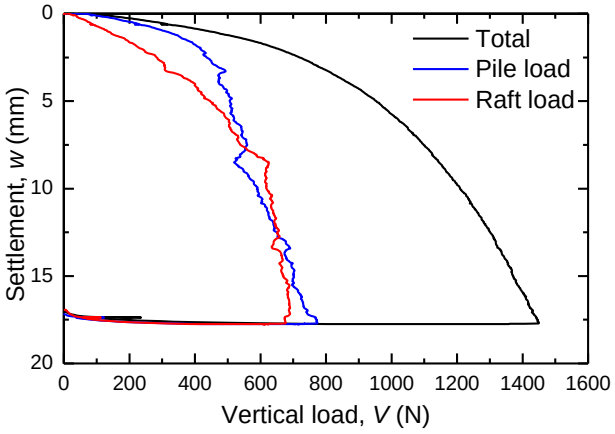

Figure 3.23 Load-settlement relationship obtained from vertical loading of CP.

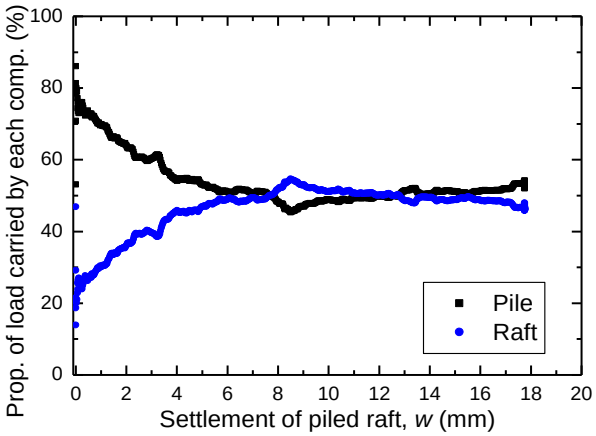

Figure 3.24 Proportion of vertical load carried by each component of CP.

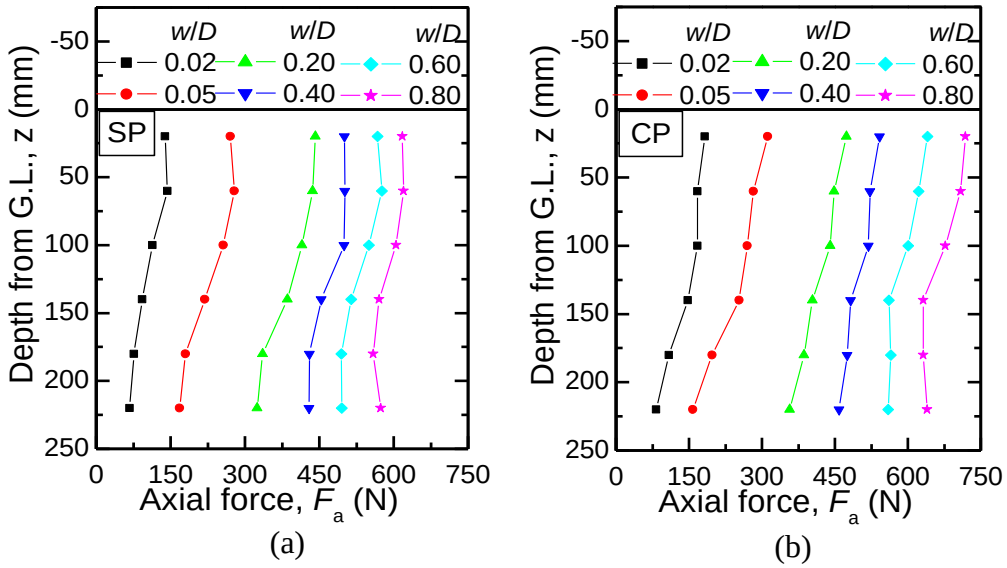

Figure 3.25 Axial force distributions along the pile (a) SP (b) CP, where *w*/*D* is normalized settlement of the pile.

3.5.2 Small raft (SR) and Full raft (FR)

Vertical load test on Small Raft model (SR) and Full Raft model (FR) (rafts without piles) were carried out to investigate the effect of raft size under vertical loading. The results of SR and FR tests, which were carried out under same conditions, are compared in this section. Both of the rafts were made of steel, with dimensions of 80 × 80 × 30 mm and 240 × 80 × 30 mm for SR and FR, respectively. The model ground was silica #6, with a relative density of D_r = 70 %. Figure 3.26 shows the experiment setup for FR model, where VDG-1, 2, 3 measure the average settlement of the raft. The experiment setup of SR model is not shown here, since it was same with the FR model test setup.

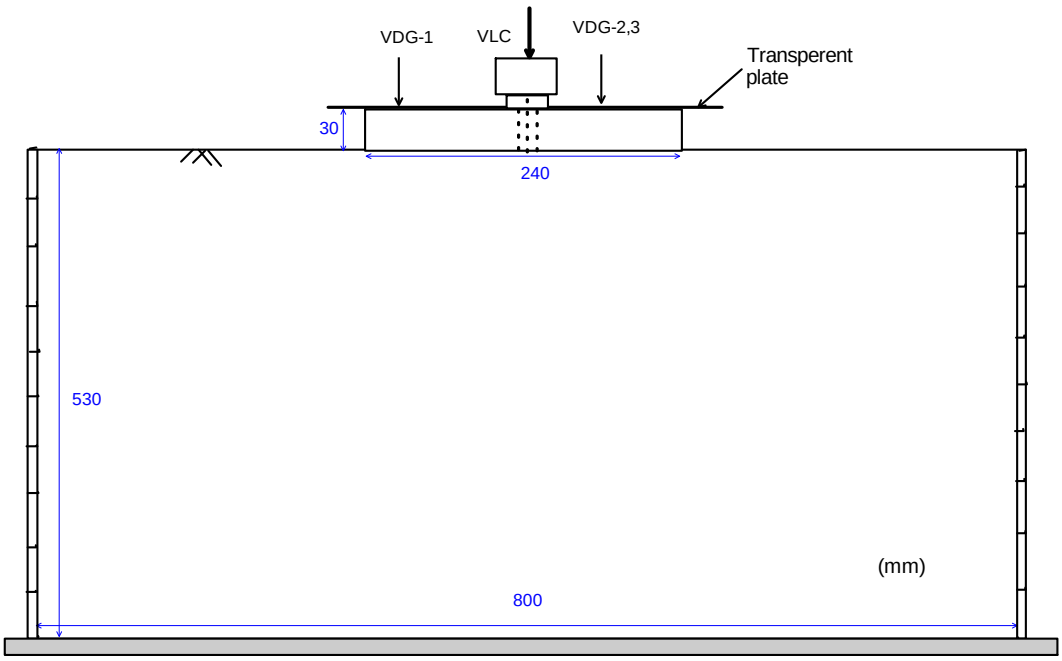

(a)

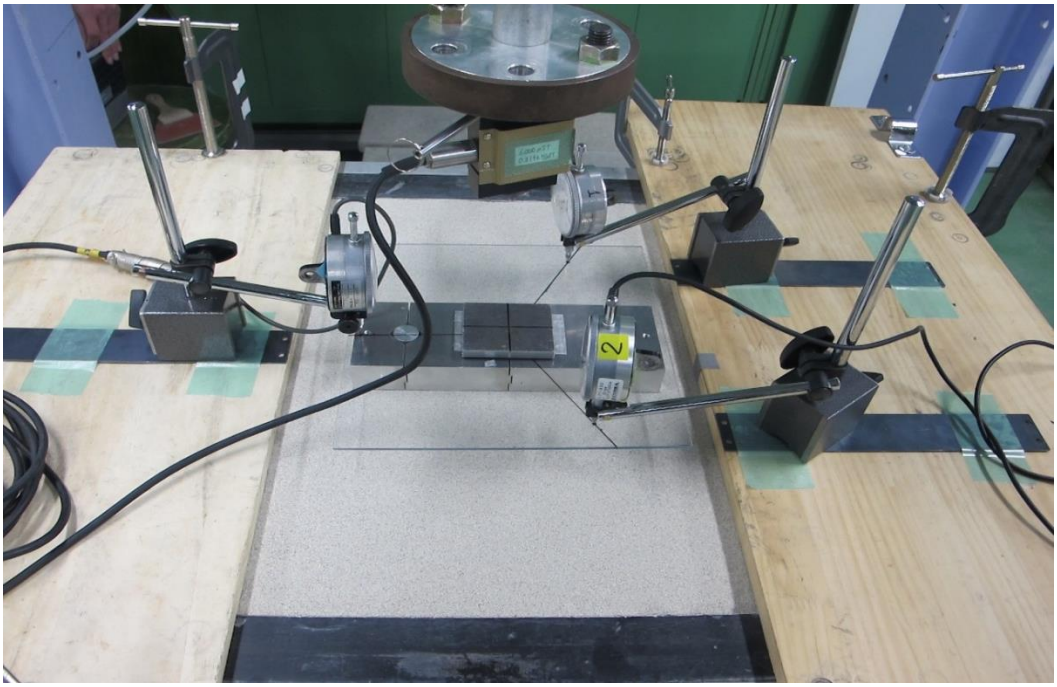

(b)

Figure 3.26 Test setup for FR model (a) drawing (b) photo of the experiment.

Test results:

Figure 3.27 shows the result of vertical loading tests of raft alone for cases; small raft (B= 80 × 80 mm) and full raft (B = 240 × 80 mm). Although, the final settlement of FR is about 25 % larger than SR, the total capacity of full raft is about 4 times larger than SR. The initial stiffness of the rafts (ratio of the vertical load to the settlement) was calculated as 0.31 kN/mm and 0.75 kN/mm for SR and FR, respectively.

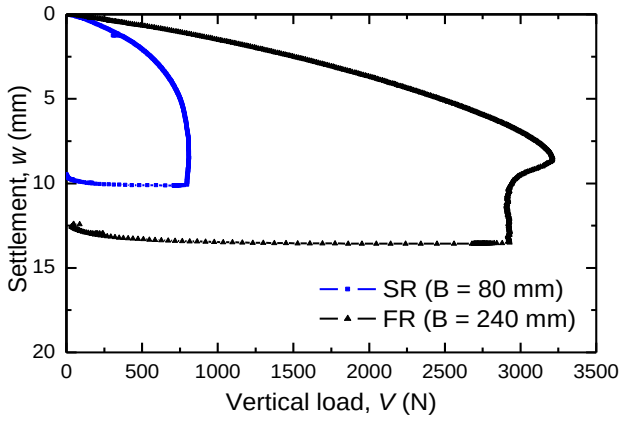

Figure 3.27 Vertical loading capacity of SR and FR.

Vertical load (*V*)-settlement (*w*) relationships obtained from Single pile (SP), Capped pile (CP) and Small raft (SR) experiments are shown in Figure 3.28. Load test of SR alone was terminated at a settlement, *w*, of 10 mm, because the ultimate capacity of 800 N was obtained at a settlement of 9 mm and the raft tended to tilt after the ultimate capacity. SP and CP were loaded until the settlements reached 17.5 mm that was 88 % of the pile diameter or 22 % of the square raft width. It can be seen from the figure that the sum of the resistances of SP and SR could be larger or smaller than that of CP depending on the settlement rate. This result clearly shows the interaction of the raft and the single pile in CP. That is, response of CP cannot be obtained from the mere summation of SP and SR.

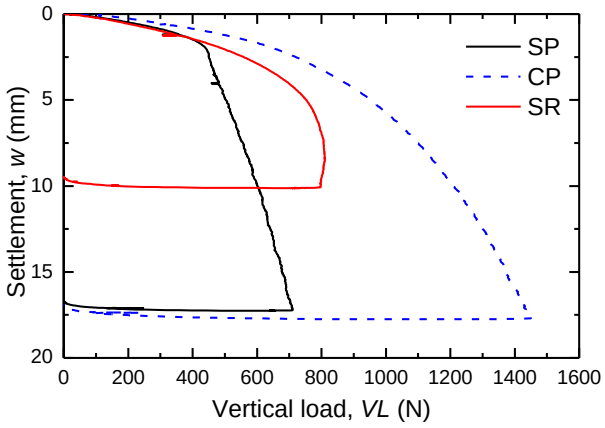

Figure 3.28 Load supported by components of CP with loads of SR and SP.

3.5.3 Piled raft (PR)

Vertical load test on Piled Raft model (PR) was carried out to investigate the capacity of the model under vertical loading. PR model was composed of a full raft and 3 piles, where each pile has an outer diameter of 20 mm, with a wall thickness of 1.1 mm. The model ground was silica #6, with a relative density of D_r = 70 %. Figure 3.29 shows the experiment setup.

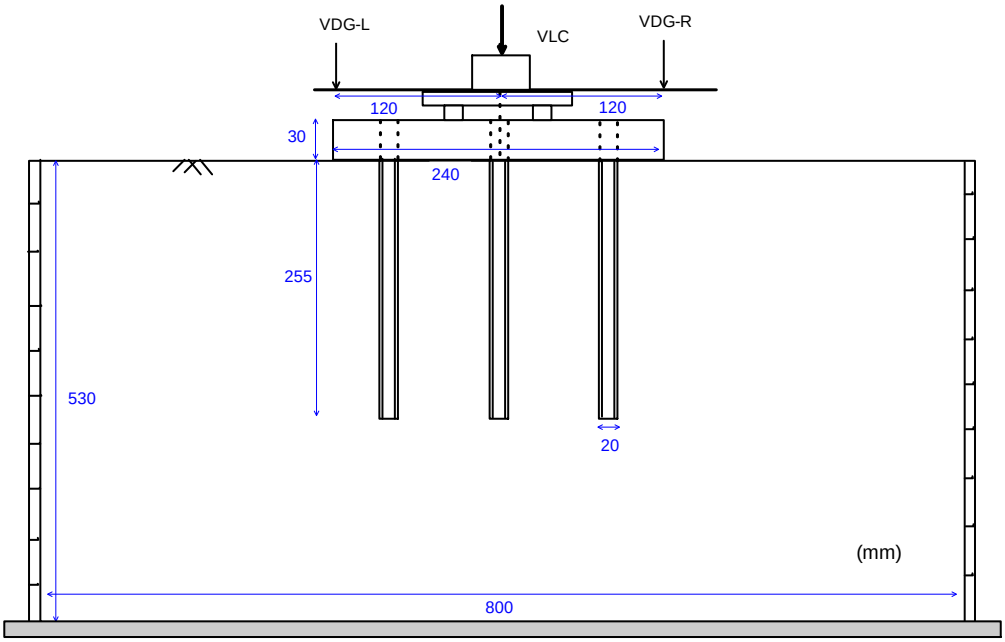

(a)

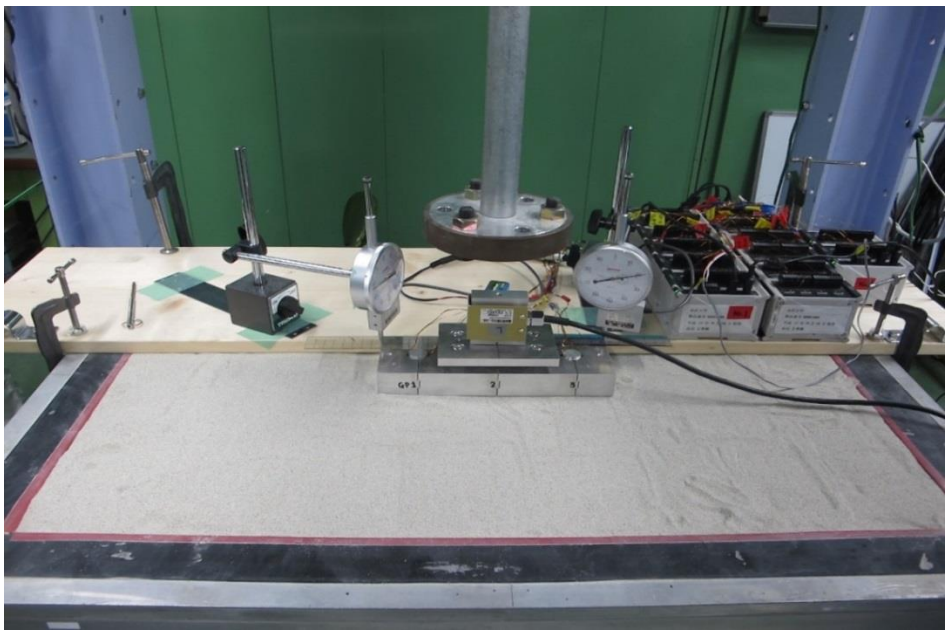

(b)

Figure 3.29 Test setup for PR model (a) drawing (b) photo of the experiment.

Test results:

In order to evaluate the performance of the vertical loading capacity of Piled Raft (PR), loading test was conducted, which had the same effective pile length under same conditions with single pile. Figure 3.30 indicates the vertical load carried by the components of PR model (3 Piles and raft) with total applied load. Note that, raft load was obtained by extracting pile loads from total applied load. From the figure, it is understood that, at the beginning of the test most of the load was carried by pile due to the poor contact between the raft and the ground, which was the case also for Capped Pile.

The percentage of vertical load carried by the 3 piles and the raft for PR model is given in Figure 3.31. Until a settlement of 0.8 mm (4 % of *D*), the piles support larger portion of the total vertical load. The 3 piles reach the yield state at this settlement (see Figure 3.30). Thereafter, the raft supports slightly larger load than the piles. The load supported by the piles again becomes larger than that of the raft after the settlement exceeds 5 mm, and finally the piles support 60 % of the total load.

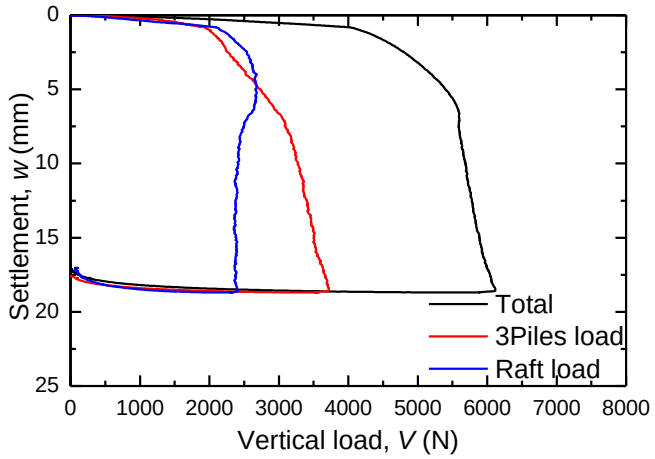

Figure 3.30 Load-settlement relationship obtained from vertical loading test of PR.

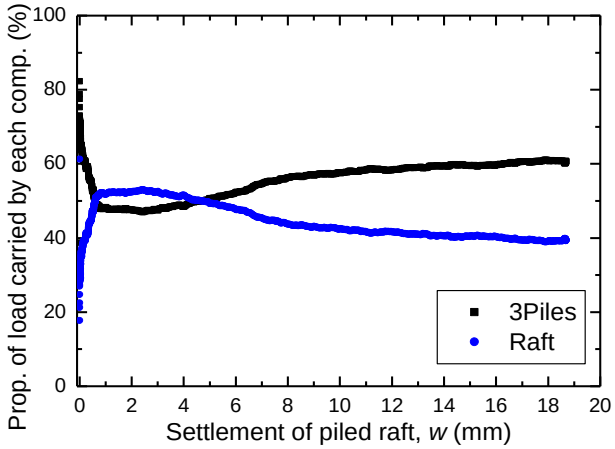

Figure 3.31 Proportion of vertical load carried by each component.

Figure 3.32 shows the result of vertical loading test for 3 piles of PR and 3 × SP (since there were 3 piles at PR model foundation). Although, the final settlement of both models are similar (about 17 - 18 mm), total vertical load capacity of piles of PR is almost two times larger than 3 × SP model, which indicates the influence of interaction of the piles and the raft in PR.

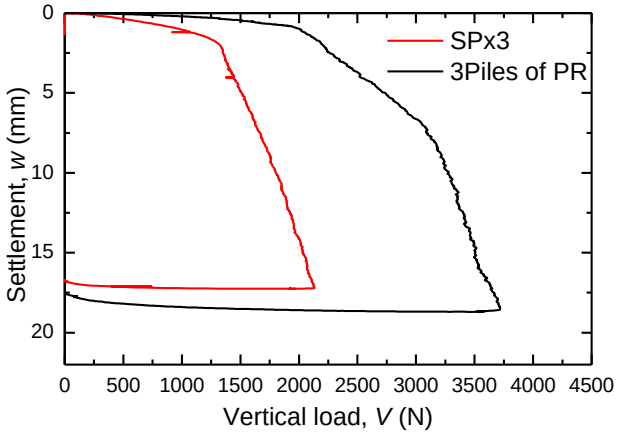

Figure 3.32 Vertical loading capacity of 3 × SP and 3 piles of PR.

The comparison of single pile, pile component of CP, and each pile (P1, P2 and P3) of PR is given in Figure 3.33. It is seen that, pile component of CP and SP results are very similar, which are both smaller than components of PR. Also, it can be said that, P1 and P3 gives similar results (each carries about 30 % of the total vertical load on 3 piles), where the mid-pile, P2 is considerably larger than these two (carries about 40 % of the total vertical load on 3 piles) (Figure 3.33). This figure also confirms the stress increment in the soil due to the load transfer through the raft, which causes larger capacity of the identical piles at higher stresses.

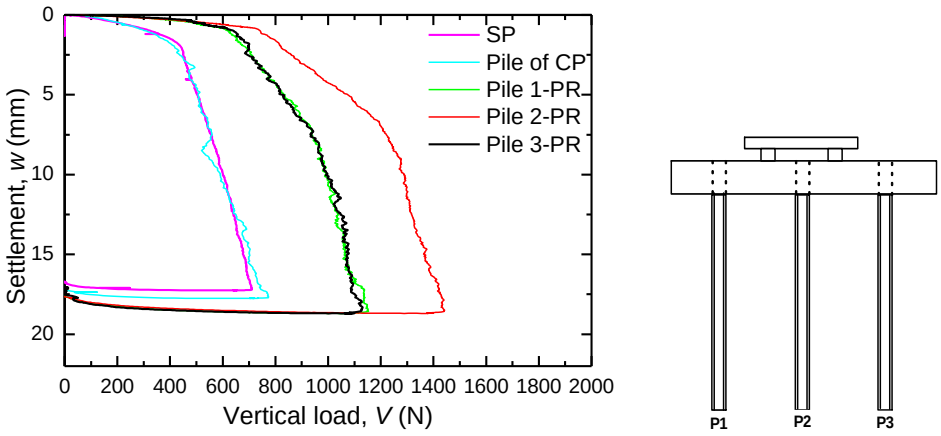

Figure 3.33 Comparison of SP, pile component of CP and each pile component of PR.

Figure 3.34 shows the distribution of axial forces along the pile shaft for each pile (P1, P2, P3) in PR model at different settlements. Note that, P2 is the center pile. It is seen that, axial forces along the pile P2 are larger than P1 and P3 piles. If the ground was uniform elastic material, the edge piles support larger vertical load compared with the center pile in case of a rigid raft because of interaction between the raft, the piles and the ground (Poulos and Davis, 1980). However, the measured results are in contrast to the above mentioned situation. This is again

explained by the influence of load transfer from the raft base to the ground. It is reasonable that the larger stresses are induced in the ground surrounding the center pile (P2) compared with the ground surrounding the edge piles (P1 and P3). As dry sand was used for the model ground in this study, rigidity and strength of the sand as well as horizontal stresses acting on the pile shaft would increase with increasing the stress level. As a result, the vertical resistance of P2 increased in this particular case of 3-pile piled raft. In case of piled rafts with a number of piles, similar phenomena might occur. However, distribution of vertical resistance of the piles would be influenced by the pile locations and the raft-soil stiffness ratio. In addition, for all piles 60 % of pile head load was transferred to the pile toe.

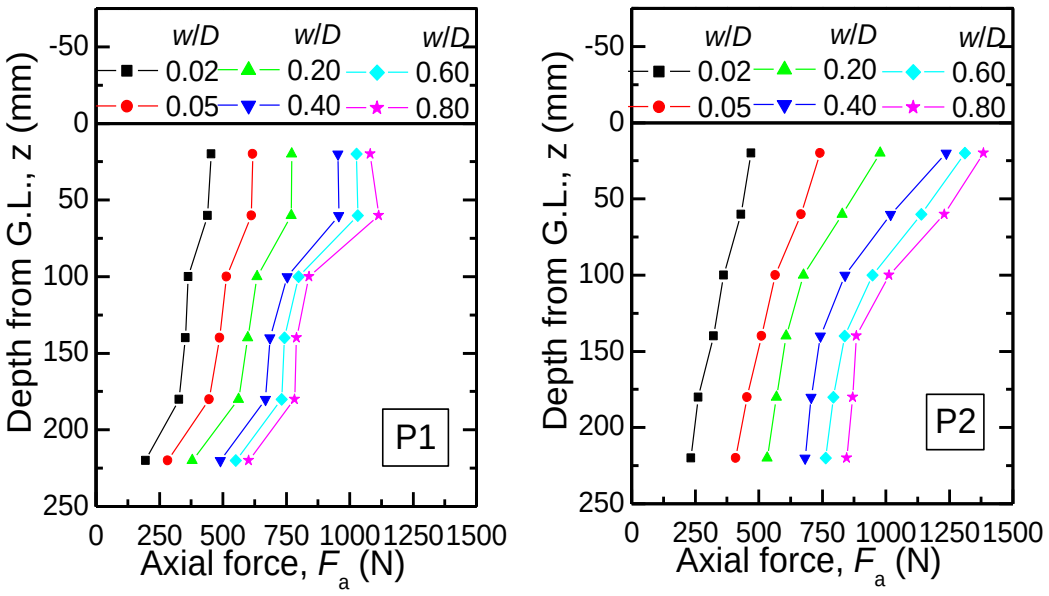

Figure 3.34 Axial force distribution along each pile (a) P1 (b) P2 (c) P3.

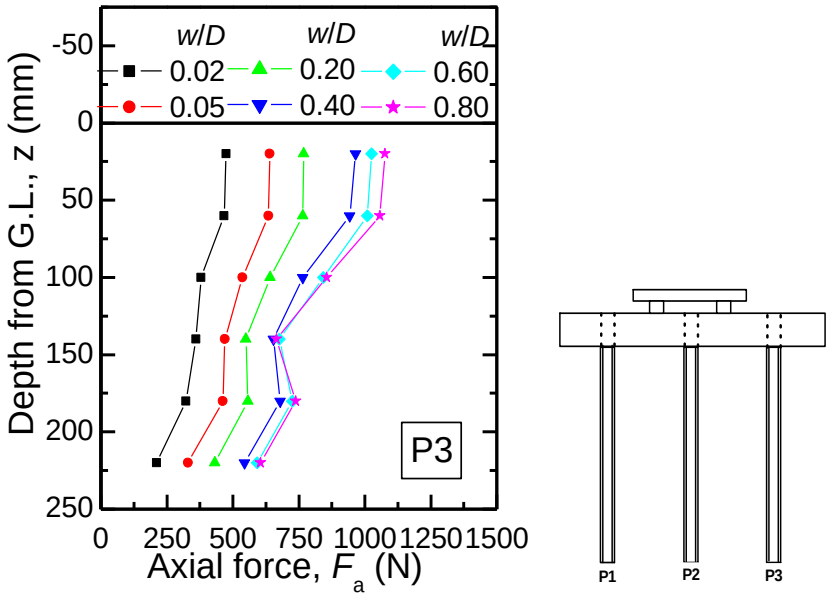

(c)

Figure 3.34 (continued).

3.6 Static Cyclic Horizontal Loading Tests and Results

Set-up of the model ground and the model foundation:

The model ground was prepared with the same method described in vertical load testing. Therefore, it will not be repeated here.

Stages of the test for SCHL:

Stage 1: Mass plates (weights) were placed one by one on top of the raft to apply vertical load, until the desired loading level was reached. For both Piled raft (PR) and Pile group (PG) tests, 5 plates, which correspond to a weight of 497 N in total (about 50 kg mass), were applied as a vertical load. Then, the plates were fixed to the raft and loading plate by the help of bolts.

Stage 2: Cyclic horizontal loading test was carried out by means of rotating wooden rods and pulling wires. In the first cycle, the displacement was applied to the raft until u/D reaches 0.2, where u is the horizontal displacement and D is the pile diameter, then it was reversed to the left (negative) direction. In total, 3

different horizontal displacements were applied at both right and left sides at each cycle, where normalized horizontal displacement, $u/D = \pm 0.2, \pm 0.4$ and ± 0.6.

Instrumentations:

The following items were used to take measurements during the test:

(i) 2 horizontal load cells to measure applied forces

(ii) 1 horizontal, 2 vertical displacement gauges to measure horizontal and vertical displacements

(iii) 12 axial strain gauges for each pile to measure bending moments, axial forces (if applicable, depending on the model foundation).

(iv) 4 shear strain gauges for each pile (one-gauge measurement method was used to measure strains.) to measure shear forces (if applicable, depending on the model foundation).

An approximate method:

In order to calculate shear forces, Q_i, and lateral soil resistance, R_{Hi}, generated on the pile section, *i,* approximately, the following approximation method and equations were used:

$$Q_i = (M_{i+1} - M_i) / dz \tag{3.4}$$

$$R_{Hi} = (Q_{i+1} - Q_i) \tag{3.5}$$

where M_i is the bending moment in the pile section, *i* and dz is the length of the pile section (Figure 3.35).

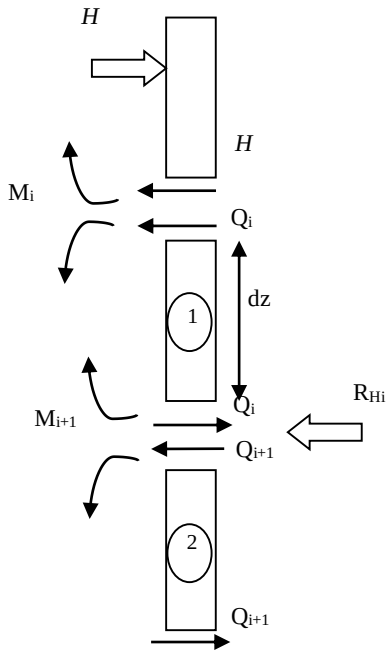

Figure 3.35 Approximate method to estimate shear forces and lateral soil resistance, generated on the pile.

3.6.1 Capped Pile (CP) Tests with/without Vertical Loading

Static cyclic horizontal load test on a Capped Pile (CP) model was carried out to investigate the behavior of CP model under horizontal loading with vertical loading (CP-V) and without vertical loading (CP-N). The model foundation was composed of a small raft and a pile. The model ground was silica sand #6, with a relative density of D_r = 70 %. The self-weight of the small raft was 7.79 N, and the total vertical load applied to the raft was 277.00 N excluding the weight of the raft. Figure 3.36 shows the experiment setup for the capped pile with vertical loading case (CP-V) where LC-R and LC-L represent the load cells placed at right and left side of the model foundation to measure applied horizontal loads. Moreover, horizontal displacements were measured by horizontal dial gauge labeled as HDG and average vertical displacement and inclination of the raft were measured by vertical dial gauges; VDG-R and VDG-L.

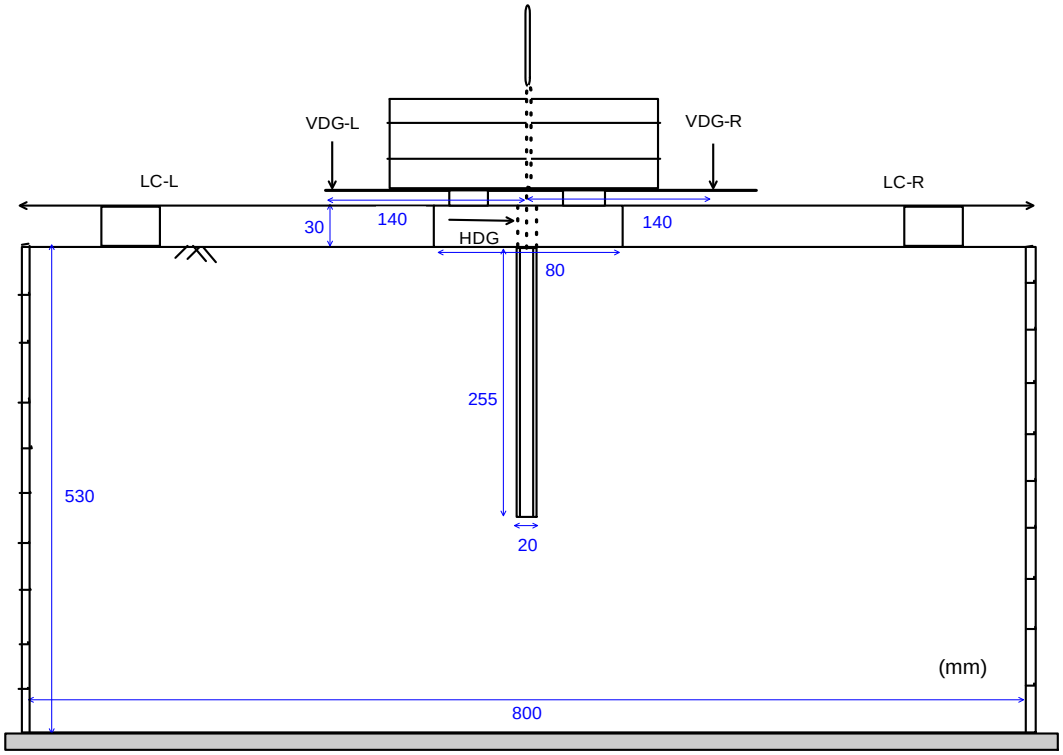

(a)

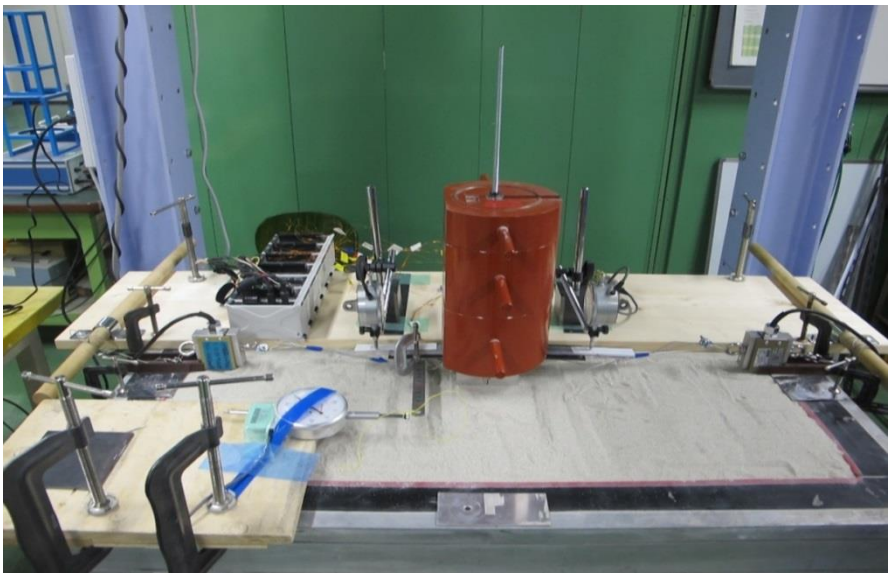

(b)

Figure 3.36 Test setup for horizontal loading of CP with vertical loading (a) drawing (b) photo of the experiment.

Test Results:

The horizontal load vs. normalized horizontal displacement of the static cyclic horizontal load test with and without vertical loading can be seen in Figure 3.37. Note that, for Capped Pile model with vertical loading, $u/D = \pm 0.6$ couldn't be recorded correctly. Therefore, CP-V results includes only $u/D = \pm 0.2$ and ± 0.4. The distribution of the applied horizontal load carried by the pile is also given in Figure 3.37 together with the total applied load. It is seen that, vertical loading increased the load carrying capacity of the model more than twice. Moreover, about 20% of the applied horizontal load was carried by the raft and the rest of the load was carried by the pile for both cases, which means that the existence of the vertical load does not change the sharing of loads between the pile and the raft.

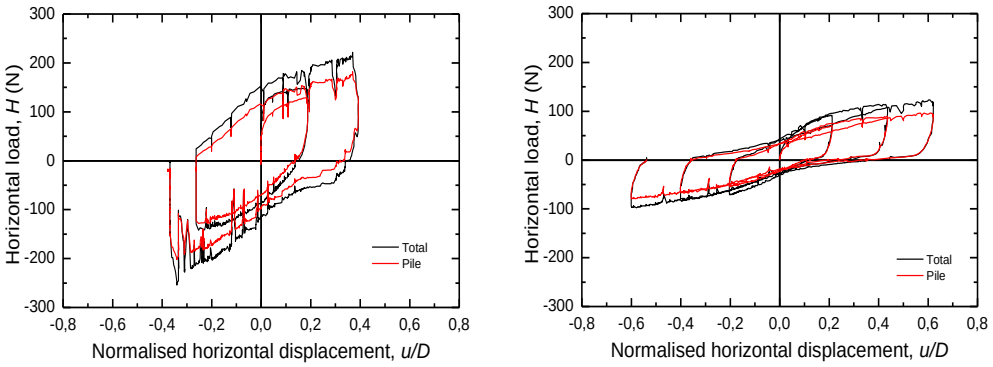

Figure 3.37 Horizontal load on the pile vs. normalized displacement (a) with vertical loading (b) without vertical loading.

Normalized vertical displacement and inclination of the raft during horizontal loading are shown in Figure 3.38 and Figure 3.39, respectively. Maximum settlement of the raft was about 60 % of the pile diameter for CP-V model, whereas it was -11 % of the pile diameter (which means heave) for CP-N. It indicates the importance of applying vertical load to the model foundation in order to model the existence of the superstructure. At normalized horizontal

displacement, u/D equals to ± 0.4, the inclination of the raft is between + 5.0 and - 3.0 degrees for CP-VL and + 3.0 and - 1.5 degrees for CP-NL cases, respectively (Figure 3.39). It is seen that the superstructure load does not have a significant effect on the inclination of the raft during horizontal loading. Note that, clock-wise inclination is taken as positive.

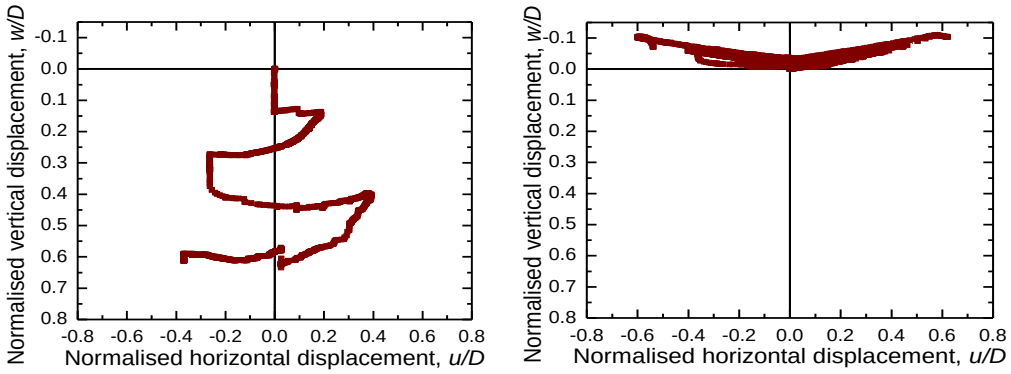

Figure 3.38 Vertical displacement of the small raft during cyclic horizontal loading displacement (a) with vertical loading (b) without vertical loading.

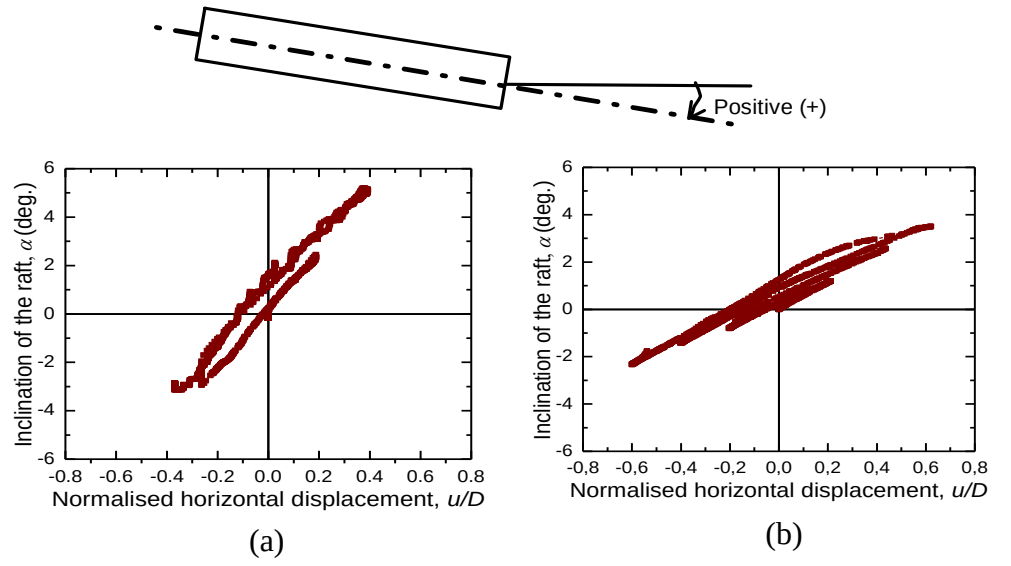

Figure 3.39 Inclination of the small raft during cyclic horizontal loading (a) with vertical loading (b) without vertical loading.

The percentage of horizontal load that was carried by the pile during cyclic horizontal loading is given in Figure 3.40 for both cases. It is seen that the pile component of CP-V model carried between 75 % - 90 % of the total applied horizontal load, and the pile in CP-N model carried 75 % - 85 % of the total horizontal load during horizontal loading.

The distributions of bending moment, shear force and lateral ground reaction of the pile during horizontal loading are given in Figure 3.41 and Figure 3.42 for CP-V and CP-N models, respectively. It is seen that, although the response of the CP with vertical loading is steeper and larger than CP-N, both cases show similar and symmetrical behavior. The bending moment, shear force and lateral ground reaction distributions of the pile of CP-V model are significantly greater than that of the pile of CP-N. It might be due to the stress increment of the soil ground due to the transmission of the vertical load through the raft, which again indicates the importance of existence of the vertical load in order to identify the actual capacity of the model foundations.

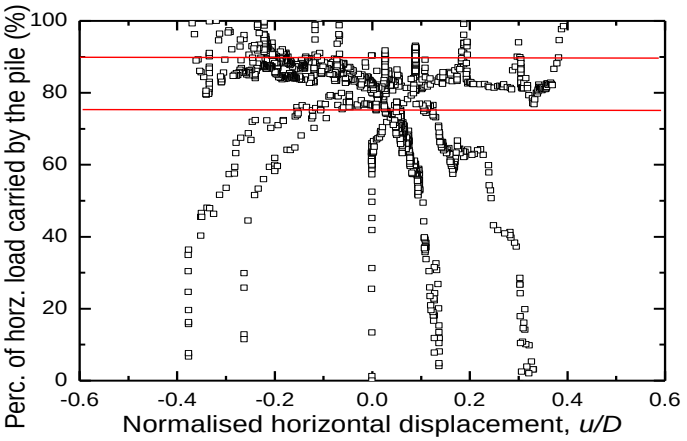

(a)

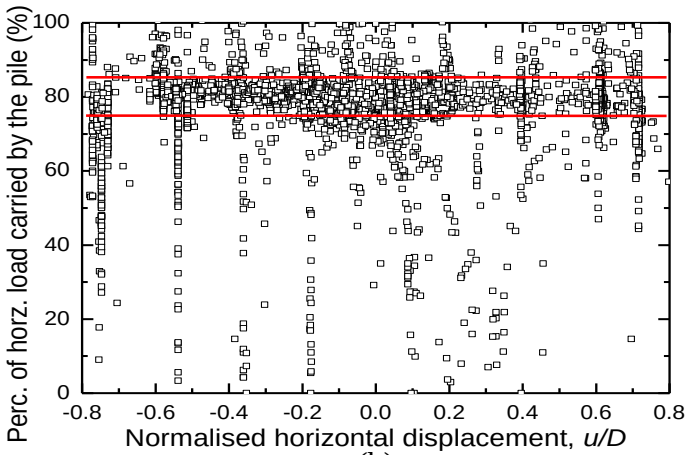

(b)

Figure 3.40 Percentage of horizontal load carried by single pile vs. normalized horizontal displacement (a) with vertical loading (CP-V) (b) without vertical loading (CP-N).

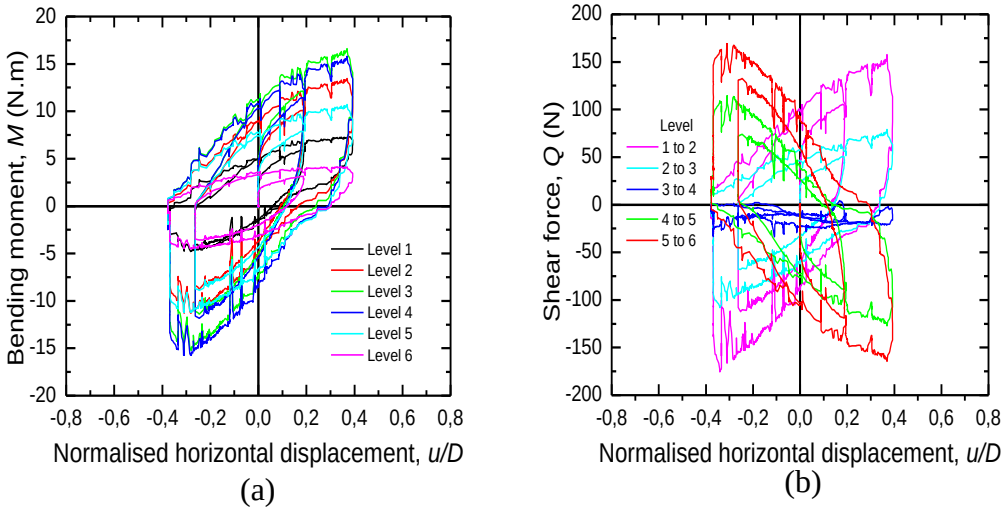

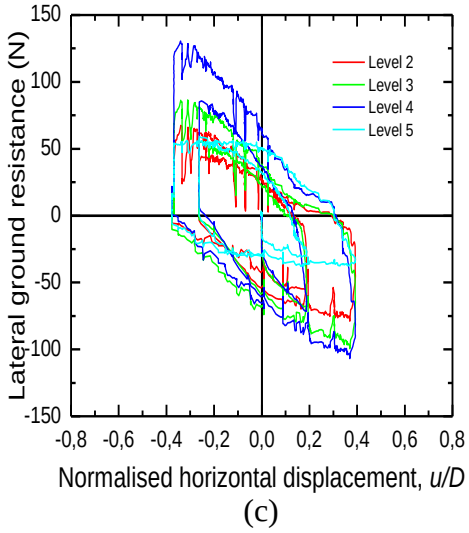

Figure 3.41 (a) Bending moment (b) shear force (c) lateral ground resistance on each pile node vs. normalized horizontal displacement with vertical loading (CP-V).

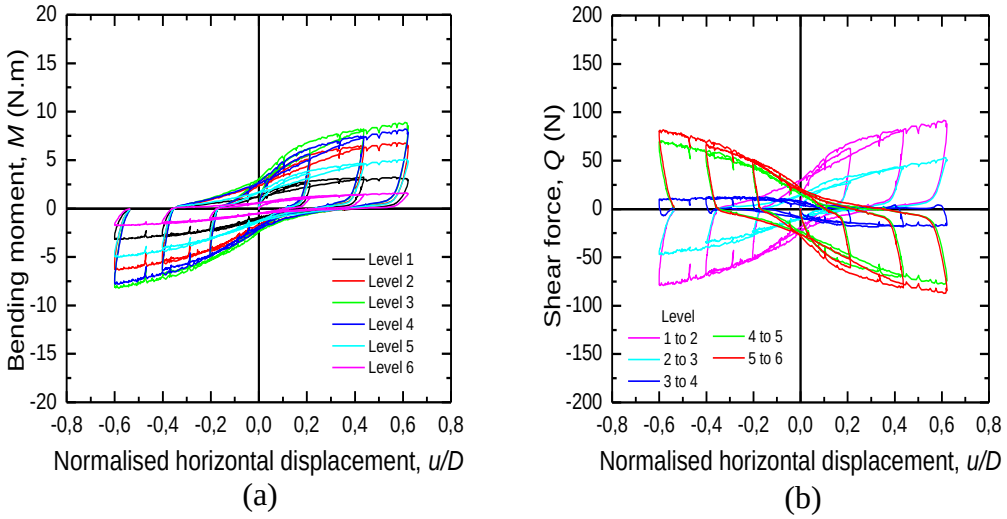

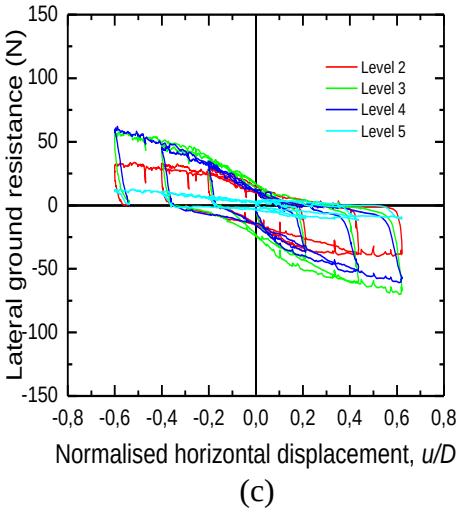

Figure 3.42 (a) Bending moment (b) shear force (c) lateral ground resistance on each pile node vs. normalized horizontal displacement without vertical loading (CP-N).

The distributions of bending moment, *M*, shear forces, *Q*, and lateral ground resistance along the pile at u/D = 0.2, 0.4 (and 0.6) for CP-V and CP-N are shown in Figure 3.43 and Figure 3.44, respectively. It is seen that bending moment graphs are almost symmetrical for both cases and it becomes maximum between 100 mm - 140 mm depth. On the other hand, shear forces are maximum at the top and at the bottom of the pile; and becomes zero at 110 mm and 120 mm depth, for CP-N and CP-V, respectively. In addition, at each displacement increment the response of the pile is smaller for CP-N, which emphasizes again the importance of modelling the superstructure.

Axial force distribution of CP-V along the pile depth is shown in Figure 3.45. At each cycle the response of the pile moves from right to left, which means the axial load carried by the pile is decreased with increasing displacement. It is also seen that, at larger displacements, the lower half of the pile shaft is in tension.

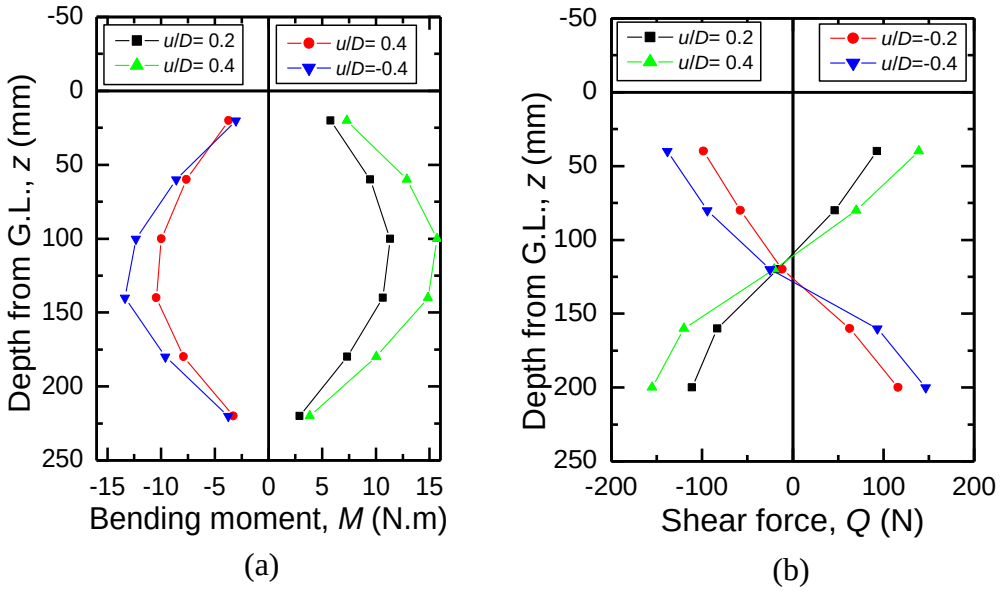

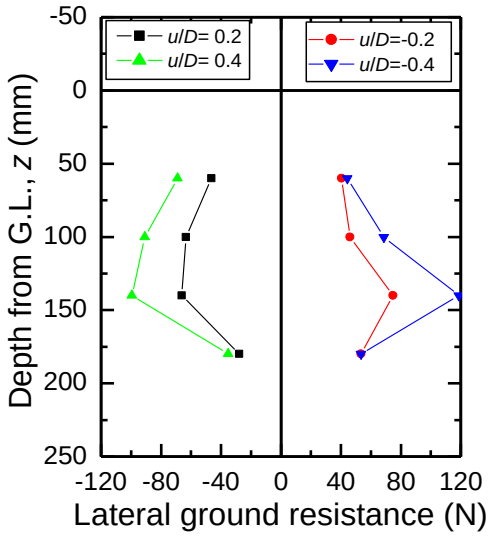

Figure 3.43 (a) Bending moment (b) shear force (c) lateral ground reaction distribution of the pile with vertical loading (CP-V).

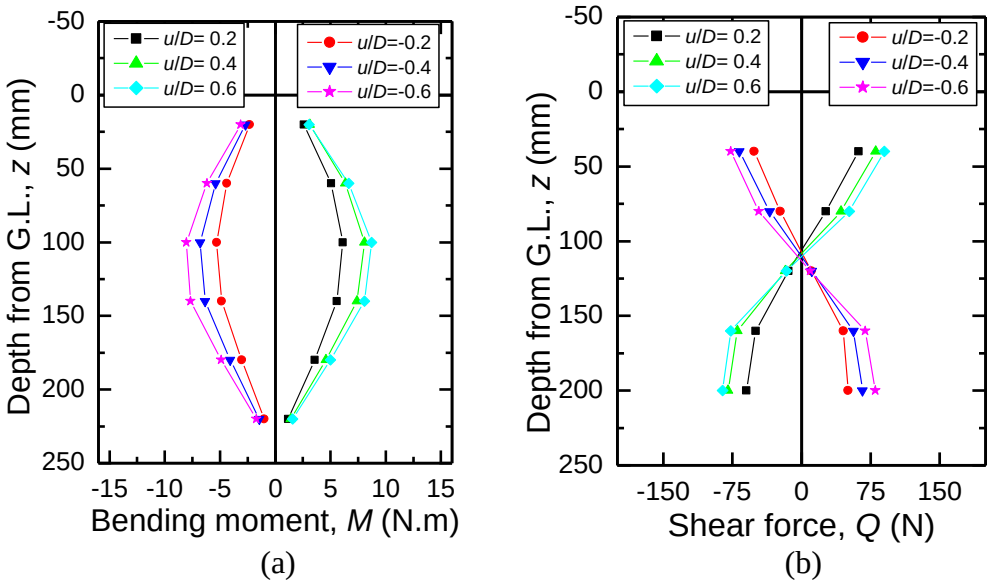

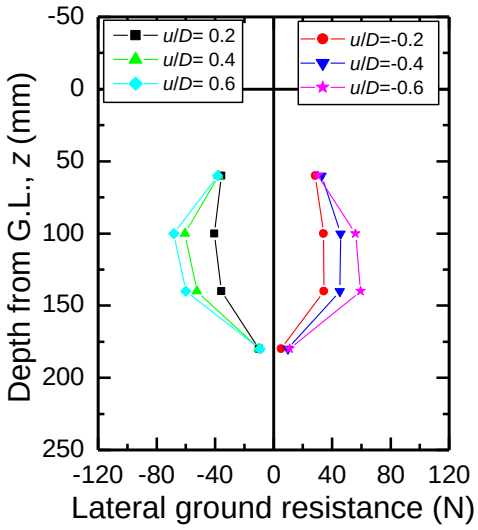

Figure 3.44 (a) Bending moment (b) shear force (c) lateral ground reaction distribution of the pile without vertical loading (CP-N).

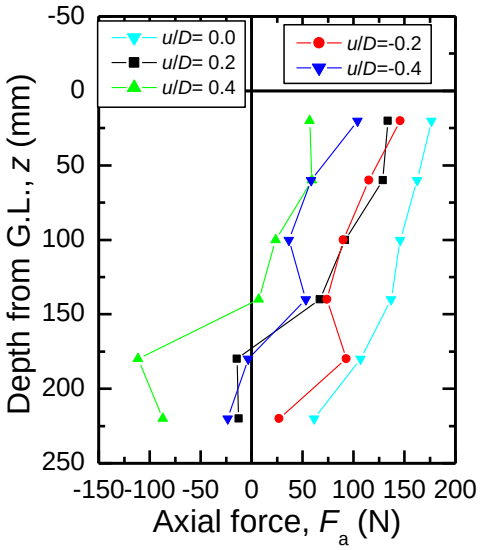

Figure 3.45 Axial force distribution of CP-V.

3.6.2 Full Raft (FR) and Small Raft (SR) Tests

For Full raft (FR) and Small raft (SR) models, 8 tests were performed in total for 4 different vertical loading levels for each model that summarized in Table 3.6. In the experiments, first horizontal load was applied from right side until slippage of the model raft, and then the horizontal load was applied from reverse direction. Test setup is depicted in Figure 3.46 for FR. The same setup was also used for SR model.

Table 3.6 Summary of vertical loads applied on FR and SR during static cyclic load test experiments.

	M1 (N)	**M2 (N)**	**M3 (N)**	**M4 (N)**
Full Raft (FR)	20.17	61.81	106.28	150.70
Small Raft (SR)	7.788	21.667	35.546	49.423

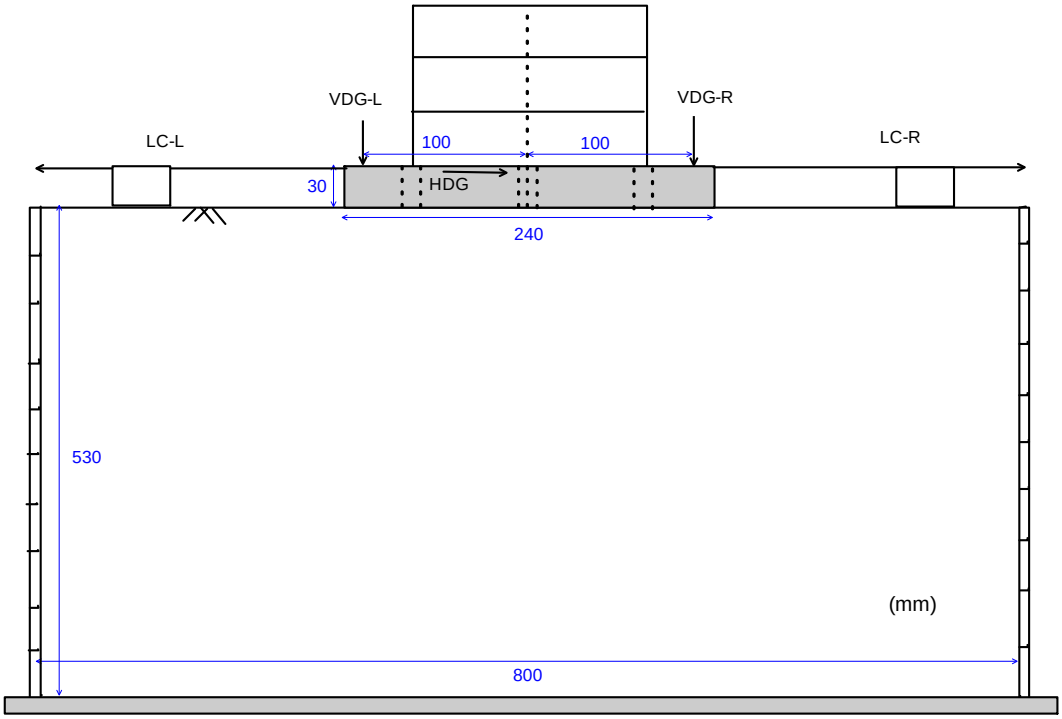

(a)

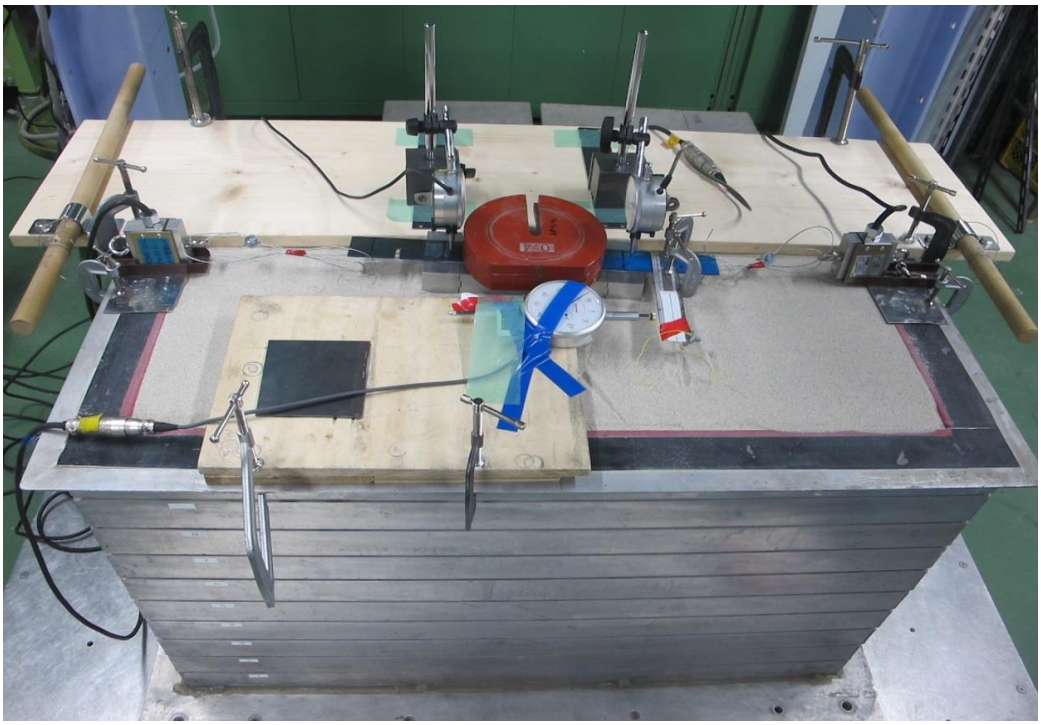

(b)

Figure 3.46 Test setup for FR model (a) drawing (b) photo of the experiment.

Test Results:

Horizontal load, *H* vs. normalized horizontal displacement, *u*/*D* of the horizontal cyclic tests for 4 different vertical loads of SR and FR can be seen in Figure 3.47 and Figure 3.48, respectively. Note that the raft models had no pile, but the horizontal axis represents the horizontal displacement, *u*, normalized by the diameter, *D*, of the model pile for a purpose of comparison with the test results of PR and PG presented later in this chapter. It is seen that, as the vertical load increases, the applied horizontal load also increases before slippage. In addition, the normalized horizontal displacements at which the slippage occurs are between 0.01 and 0.145 for all cases, indicating that the raft base shear resistance is very effective to reduce the horizontal displacement of the raft foundation until the occurrence of slippage. Therefore, in both experiments, the rafts are "horizontal displacement reducers" until the slippage occurs.

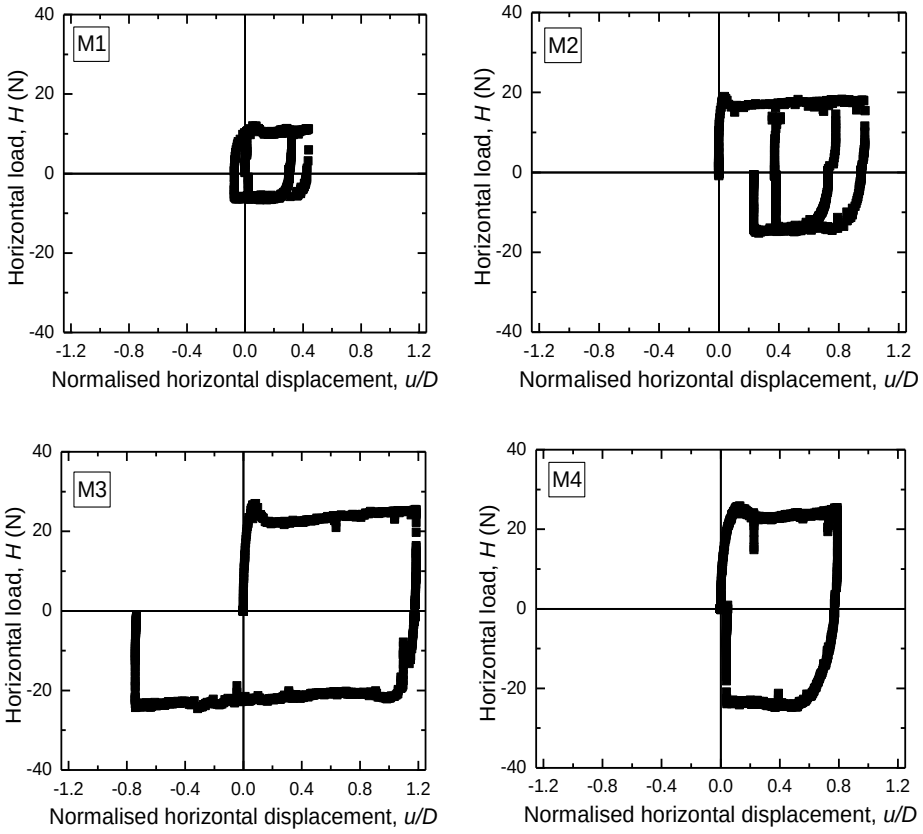

Figure 3.47 Horizontal load-displacement relationships of vertical loading for SR.

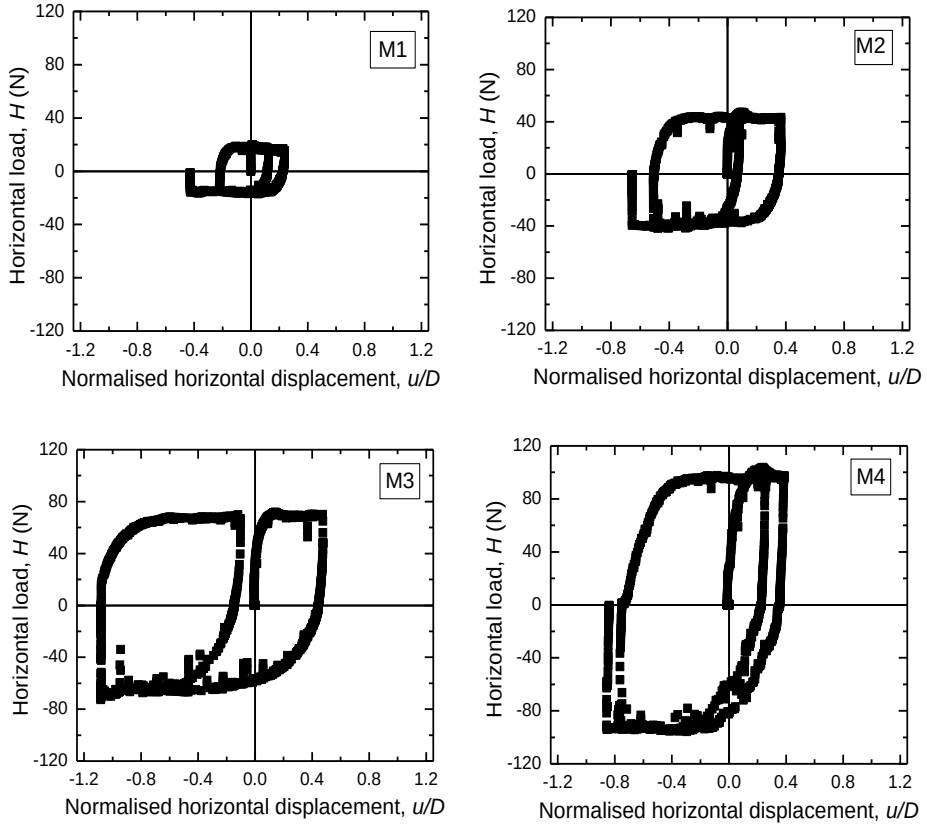

Figure 3.48 Horizontal load-displacement relationship of vertical loading for FR.

The relationship between the applied horizontal load and the vertical load for positive and negative horizontal loading were drawn for both residual and peak values (Figure 3.49 and Figure 3.50). From the figures, it was estimated that the average friction angle between the contact surface and the model ground is 29.3^0 and 31.1^0 for SR and FR, respectively. Note that M4 results didn't included at SR test, since it was inconsistent with the other three loading results.

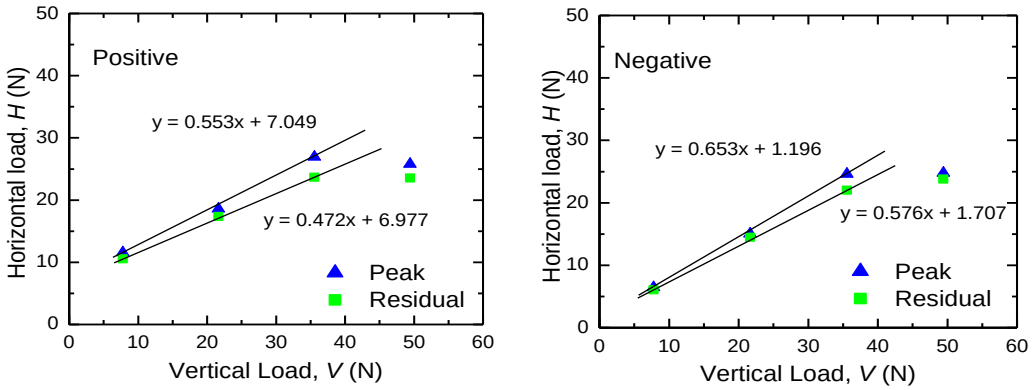

Figure 3.49 Horizontal load vs. vertical load relationships for SR.

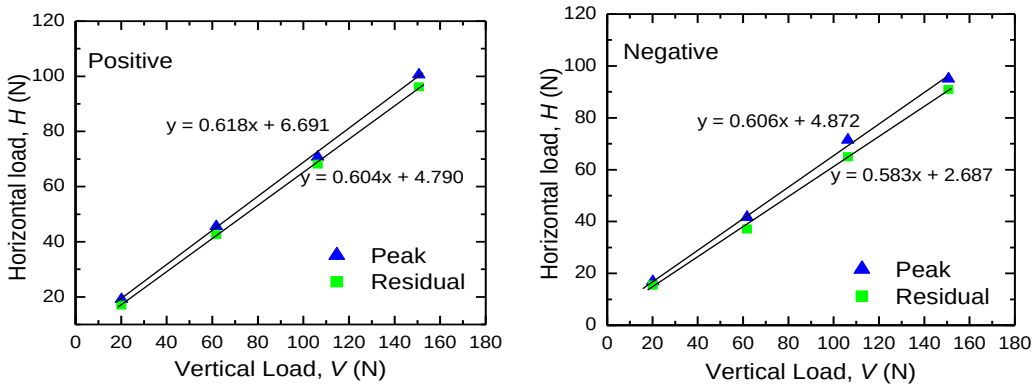

Figure 3.50 Horizontal load vs. vertical load relationships for FR.

Horizontal stiffness, $\Delta H/\Delta u$, of small raft and full raft are given in Figure 3.51, where ΔH is horizontal load increment and Δu is the horizontal displacement increment. As it is seen from the figure, $\Delta H/\Delta u$ tends to increase slightly with increasing average contact pressure, V/A. This tendency may be explained by the increase in the stress levels in the ground beneath the raft, resulting in increase of the soil stiffness.

If the stiffness, k_h, of full raft and small raft are compared, it is obvious that full raft has smaller stiffness (Figure 3.52). The ratio of k_h of the full raft to the small raft is about 1/3. This result shows the size effect on k_h recalling that the ratio of $A_{fullraft}/A_{smallraft}$ is 3.0. In other words, the ratios, $\Delta H/\Delta u$, are very close for SR and FR which may be attributed to size effect.

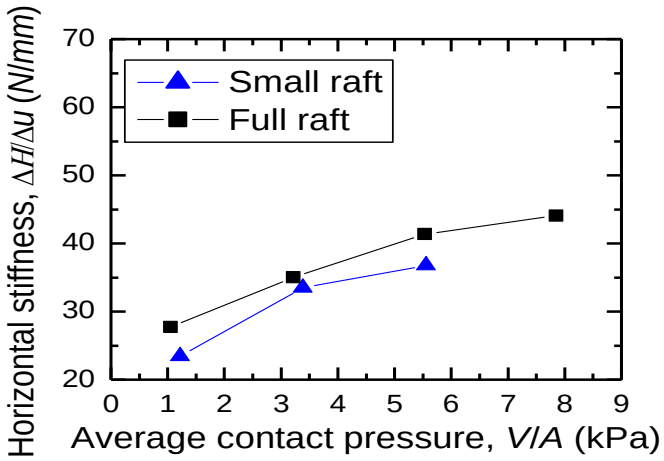

Figure 3.51 Horizontal stiffness vs. average contact pressure.

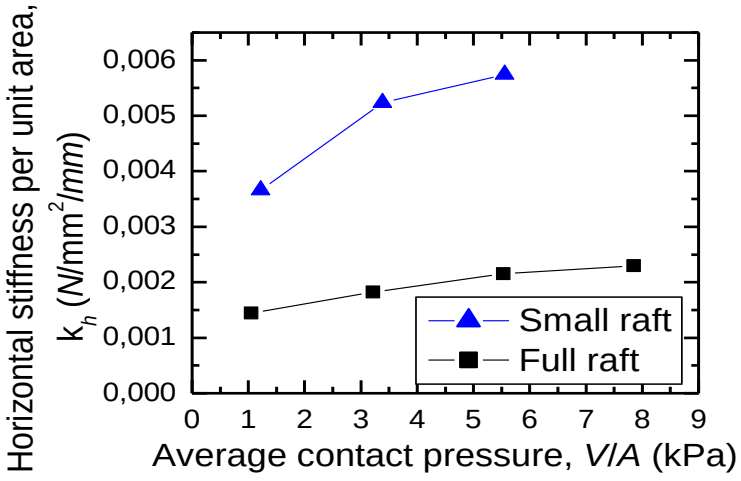

Figure 3.52 Horizontal stiffness per unit area vs. average contact pressure.

3.6.3 Piled Raft (PR) and Pile Group (PG) Tests

Static cyclic horizontal load tests on Piled Raft (PR) and Pile Group (PG) model were carried out to investigate the soil-pile interaction, load sharing and raft effect on the behavior of the model pile foundation under horizontal loading. Although, the same model foundation with Piled Raft (PR) test was used for PG test, there was 20 mm space between the raft and the model ground at PG test in order to eliminate the raft resistance. The model ground was silica #6, with a relative density of D_r = 70 %. Total weight applied to the models was 497 N, composed of 5 steel plates; each of them was about 100 N. Test setups illustrated at Figure 3.53 and Figure 3.54 for PR and PG, respectively. In figures, load cells; LC-R and LC-L were placed at right and left sides of the model foundation to measure applied horizontal loads. Horizontal displacement was measured by horizontal dial gauge, HDG and average vertical displacement and inclination of the raft were measured by vertical dial gauges, VDG-R and VDG-L through the test.

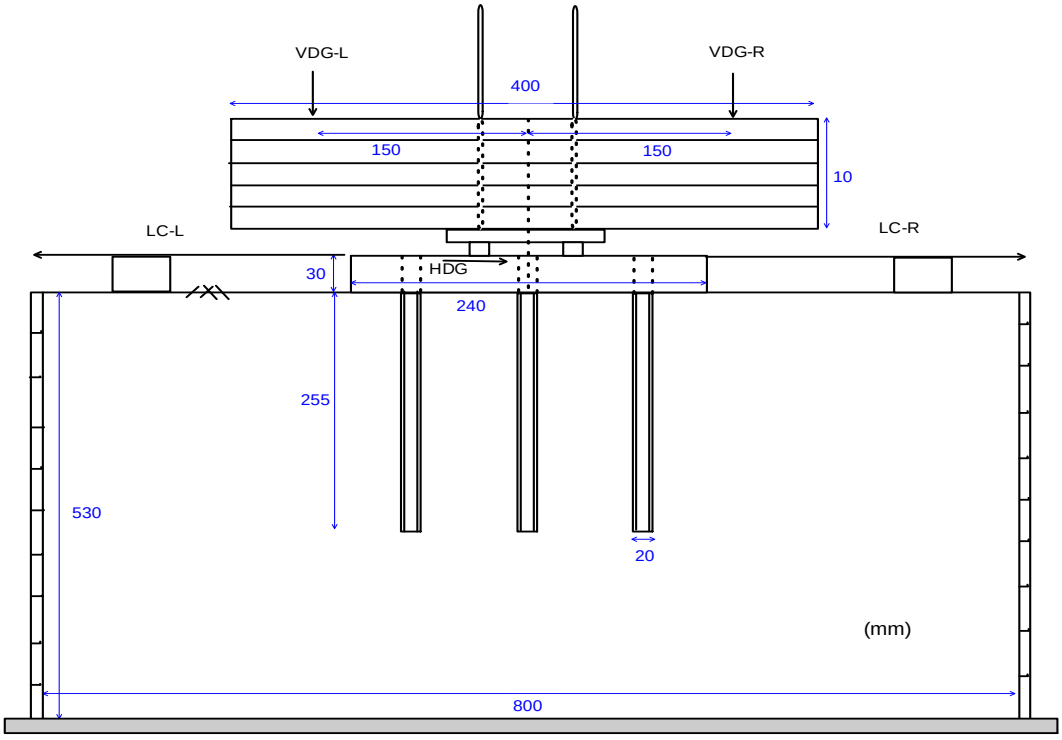

(a)

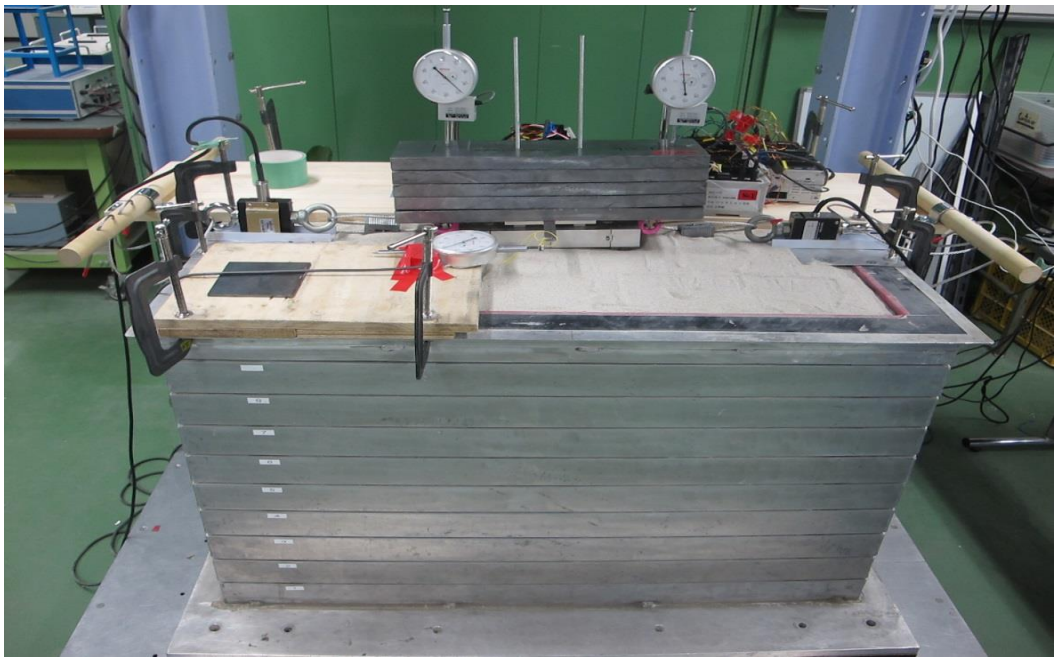

(b)

Figure 3.53 Test setup for PR model (a) drawing (b) photo of the experiment.

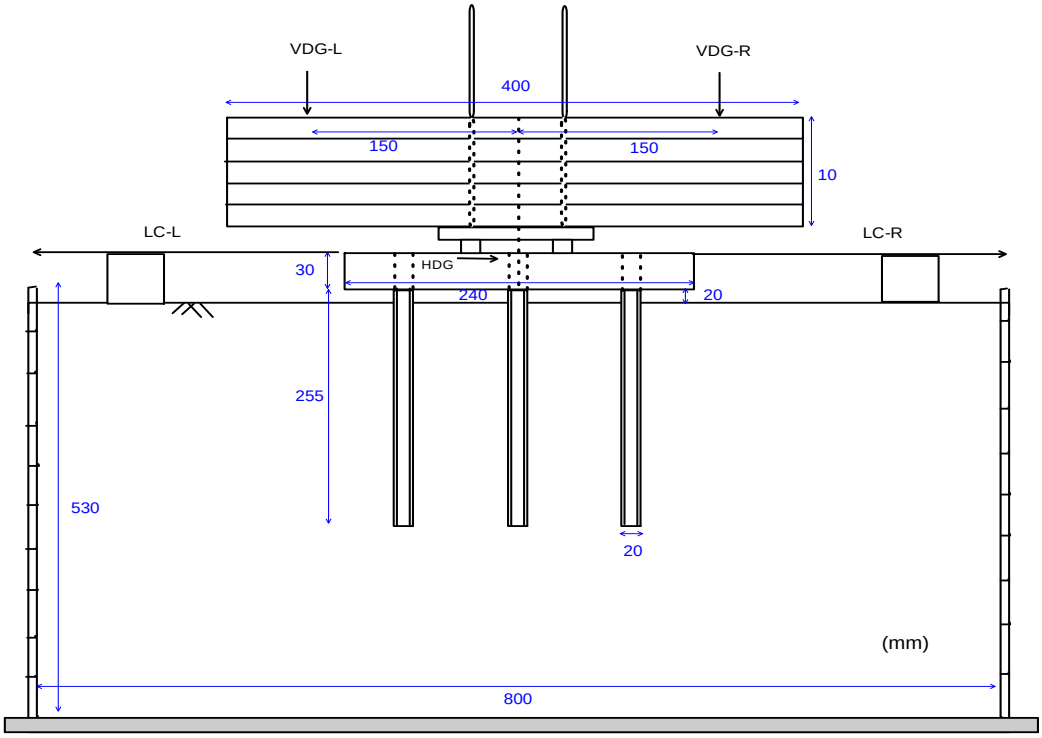

(a)

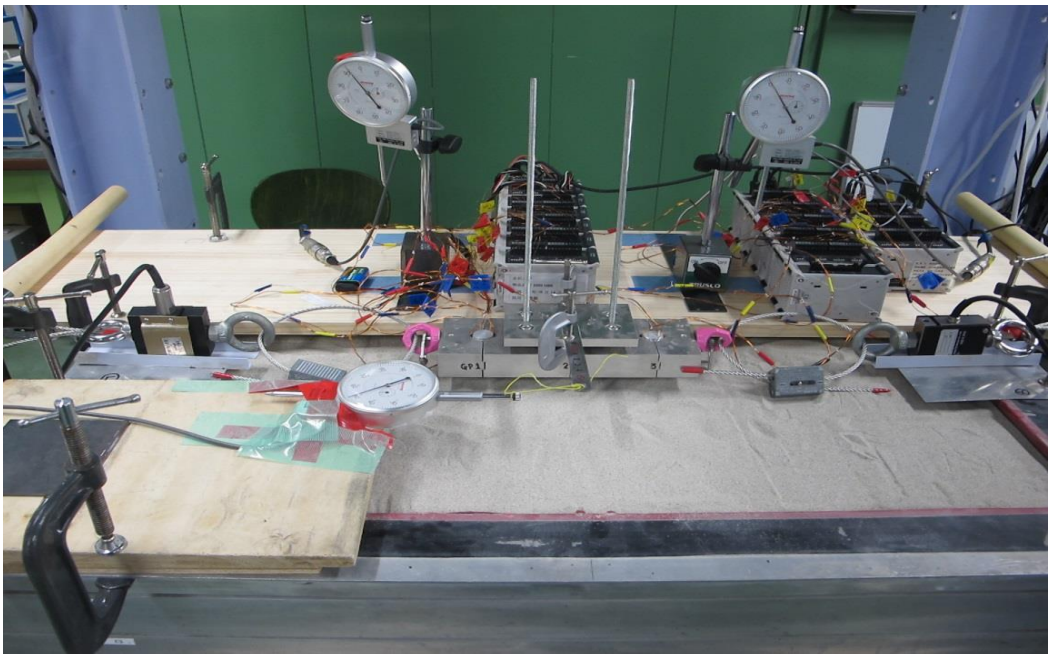

(b)

Figure 3.54 Test setup for PG model (a) drawing (b) photo of the experiment.

Test Results:

Horizontal load vs. normalized horizontal displacements of the horizontal cyclic test of PR and PG are illustrated in Figure 3.55. It is clearly seen that horizontal resistance of PR is larger than that of PG for all u/D. The horizontal resistance of PG levels off at $u/D = \pm 0.4$ having a value of about 310 N. In contrast, the horizontal resistance of PR continues to increase even after u/D exceeds ± 0.5 that reached the maximum horizontal load of 440 N. It can be said that, the raft increases the carrying capacity of the model about 40 %.

Zoom-up of the initial loading parts of two cases is shown in Figure 3.56. The horizontal stiffness of PR is larger than that of PG. That is, shear resistance at the raft base is effectively mobilized and suppresses the horizontal displacement in PR.

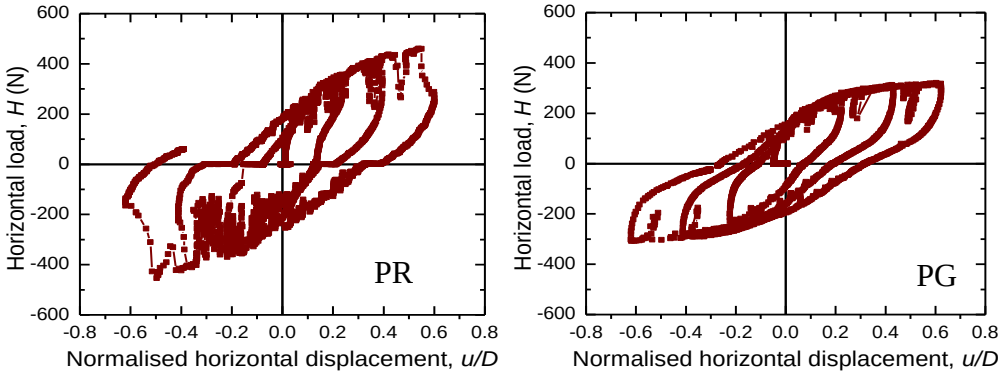

Figure 3.55 Horizontal load vs. normalized horizontal displacement relationship of PR and PG models.

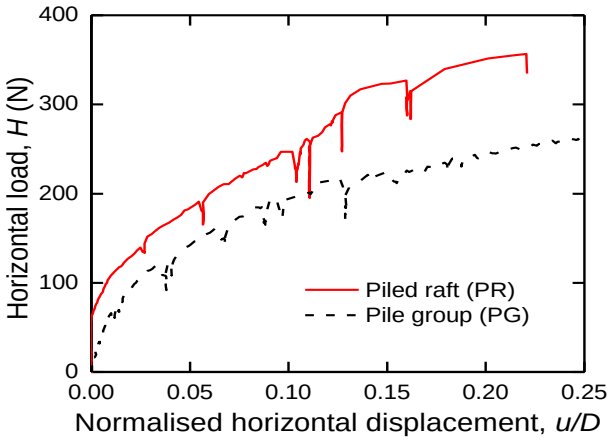

Figure 3.56 Zoom in initial loading stages of PR and PG models.

The horizontal load carried by each pile is given in Figure 3.57. P3 was the front pile and P1 was the rear pile for positive loading. Total load is the load applied to the raft, and load of each pile is the shear force measured near pile head (20 mm below the pile head). As it is seen from Figure 3.57, the front pile carries most of the horizontal load and the rear pile carries least of the load for both cases. The horizontal load, carried by center pile, P2 is almost equal in positive and negative loading directions. Also, the raft has an effect of increasing pile capacity of the front pile (Pile, P3 for positive loading and Pile, P1 for negative loading) during horizontal loading.

It is interesting to note that the front pile in PR supports higher load compared to that in PG. This result indicates an effect of load transfer from the raft base to the ground. As the raft moved in the positive direction, the raft inclined in clock-wise direction (as shown in Figure 3.59) and the settlement of the raft was larger at the position of P3. Hence, load transfer from the raft base to the ground is thought be larger in the ground around P3, resulting in higher strength and stiffness of the ground. As a result, the horizontal resistance of P3 (front pile) is enhanced.

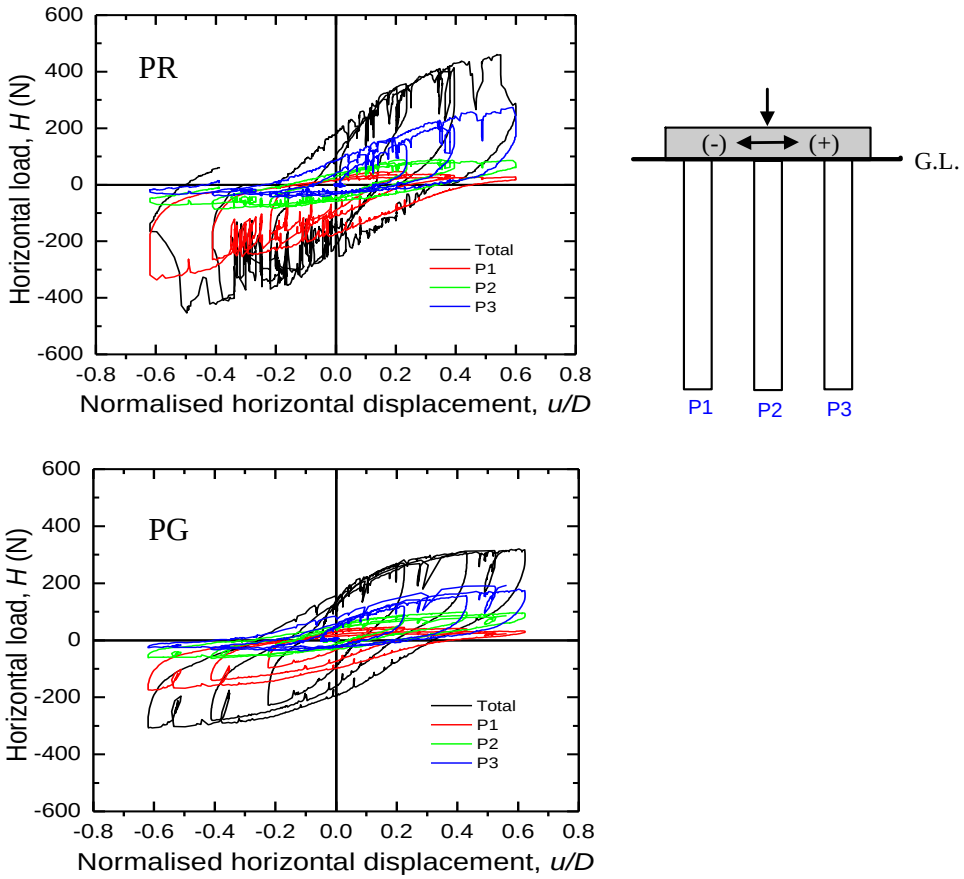

Figure 3.57 Horizontal load at each pile vs. normalized horizontal displacement of PR and PG.

Vertical displacement and inclination of the raft during cyclic horizontal loading for PR and PG are shown in Figure 3.58 and Figure 3.59, respectively. Vertical displacements were measured at two locations (see Figure 3.53 and Figure 3.54). Vertical displacement, shown in Figure 3.58 is the average of two measured vertical displacements. When the raft moved horizontally, locations of the measured points on the raft also moved as the locations of the dial gauges were fixed. Hence, the average vertical displacements at u/D = 0 alone are more representative values. It is clearly seen from Figure 3.58 that the settlement of PR was suppressed compared with that of PG, indicating a favorable effect of the

existence of the raft. Permanent settlement of the raft was about 10 % of the pile diameter in PR, which was the half of PG model.

The inclination, α, of the raft is between +2.0 and -3.0 degrees for PR, +2.5 and -1.0 degrees for PG, where positive inclination means clockwise rotation of the raft, and negative inclination corresponds to counter clockwise rotation (Figure 3.59). The inclination of the raft increases almost linearly with increasing horizontal displacement of the raft in both models. The same phenomenon was observed also at the study of Unsever et al., 2013.

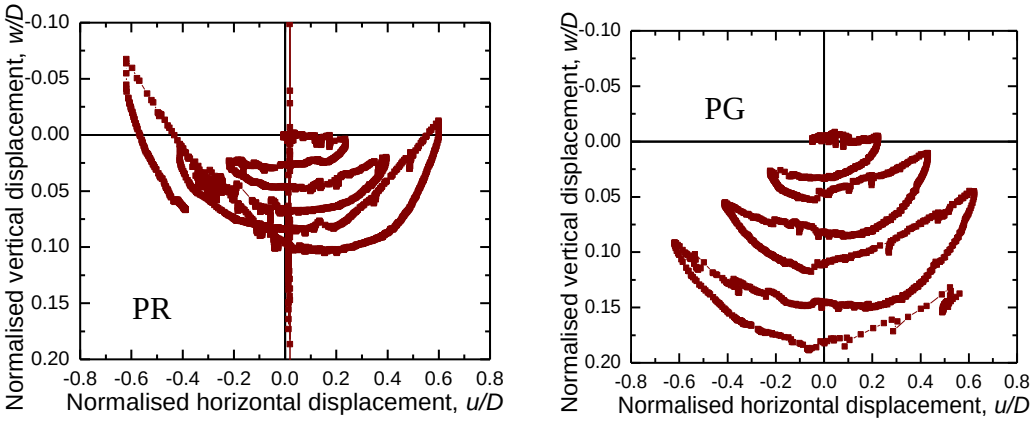

Figure 3.58 Vertical displacement of the raft during cyclic horizontal loading of PR and PG.

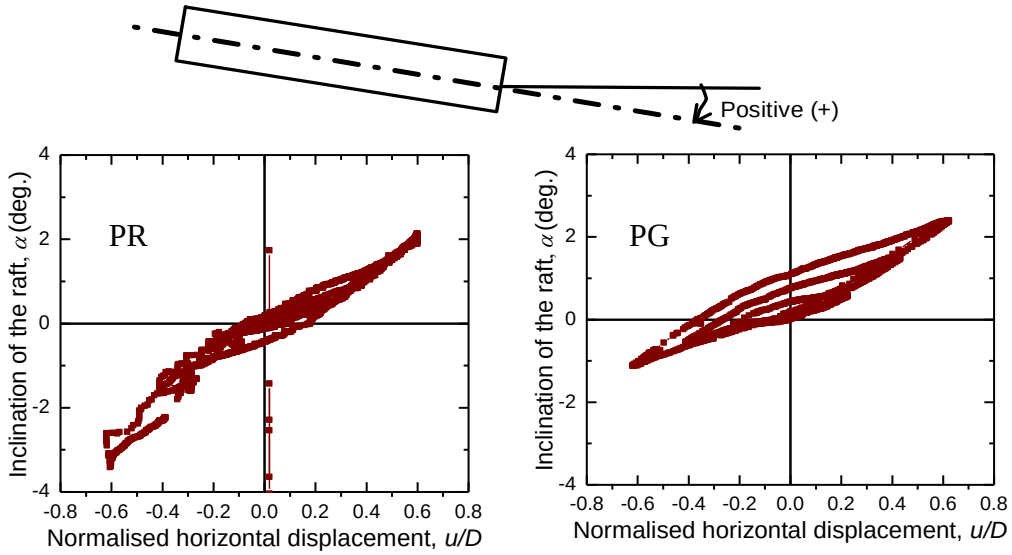

Figure 3.59 Inclination of the raft during cyclic horizontal loading of PR and PG.

For PR model, the sharing of the load between the raft and the piles with the total applied load is given in Figure 3.60. The load that is carried by the raft was almost constant through the test, and the trend of the total load and the 3 piles load is very similar. The proportion of horizontal load and vertical load that carried by 3 piles during cyclic horizontal loading of PR model is shown in Figure 3.61 and Figure 3.62, respectively. The proportions are relatively stable, being in the range of 60 % to 100 % for both horizontal and vertical load sharing during the cyclic loading.

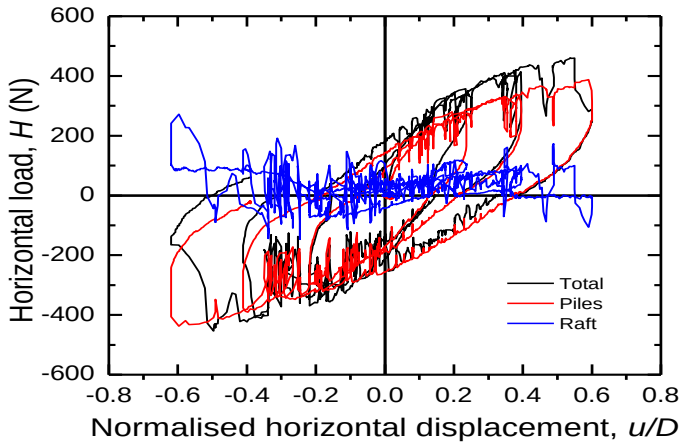

Figure 3.60 Load sharing between the 3 piles and the raft during cyclic horizontal loading of PR.

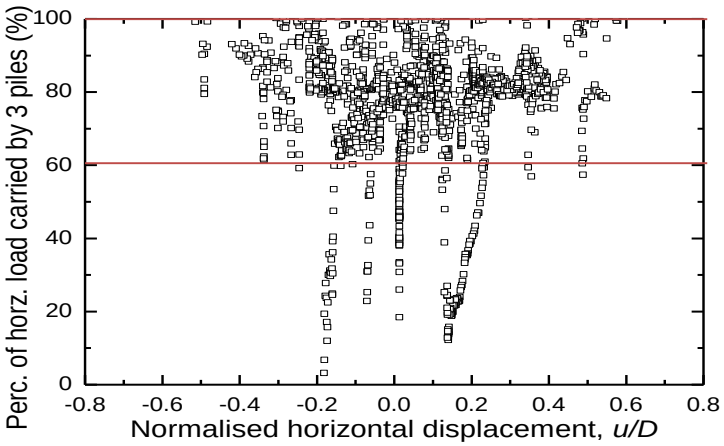

Figure 3.61 Percentage of horizontal load carried by 3 piles vs. normalized horizontal displacement of PR.

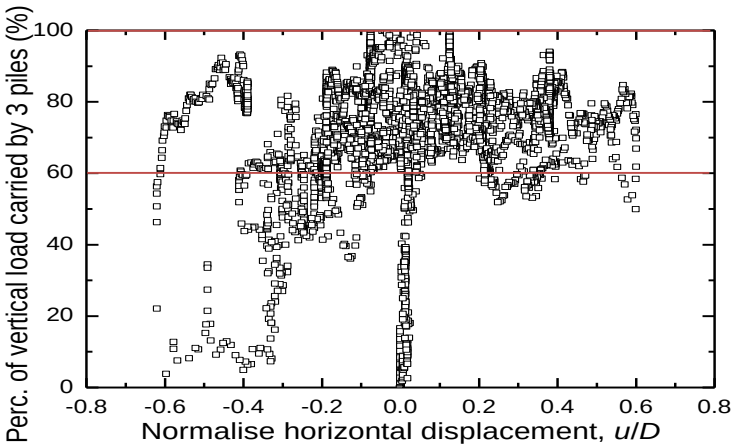

Figure 3.62 Percentage of vertical load carried by 3 piles vs. normalized horizontal displacement of PR.

The distributions of bending moment, shear force and lateral ground resistance of each pile component during horizontal loading are given between Figure 3.63 - Figure 3.68 for PR and PG models, respectively. Note that, P3 is the front pile for positive loading and P1 is the rear pile as mentioned before. From the figures, three cycles for positive and negative loading can be recognized clearly. It is also seen that, front pile carries most of the applied load, and the rear pile carries the least for both cases. Centre piles show almost a symmetric distribution for positive and negative loading.

When PR and PG graphs are compared by considering bending moment distribution, it is observed that although the values for PR are slightly larger than PG, their behaviors are similar (Figure 3.63 and Figure 3.64). This means that, the capacity of PR model increases comparing to PG without significant bending moment increase at pile components. However, the maximum shear forces on edge piles, P1 and P3 increase almost 50 % for PR case when the pile is front pile during horizontal loading (Figure 3.65 and Figure 3.66). Moreover, the middle pile, P2 shows same behavior for PR and PG models and is not affected from positive or negative loading. This result suggests that the piles in PR model are

likely to be damaged by shear forces, compared to PG model. The similar behavior with the shear force distribution is also observed for lateral ground resistance of pile components of pile raft and pile group models (Figure 3.67 and Figure 3.68).

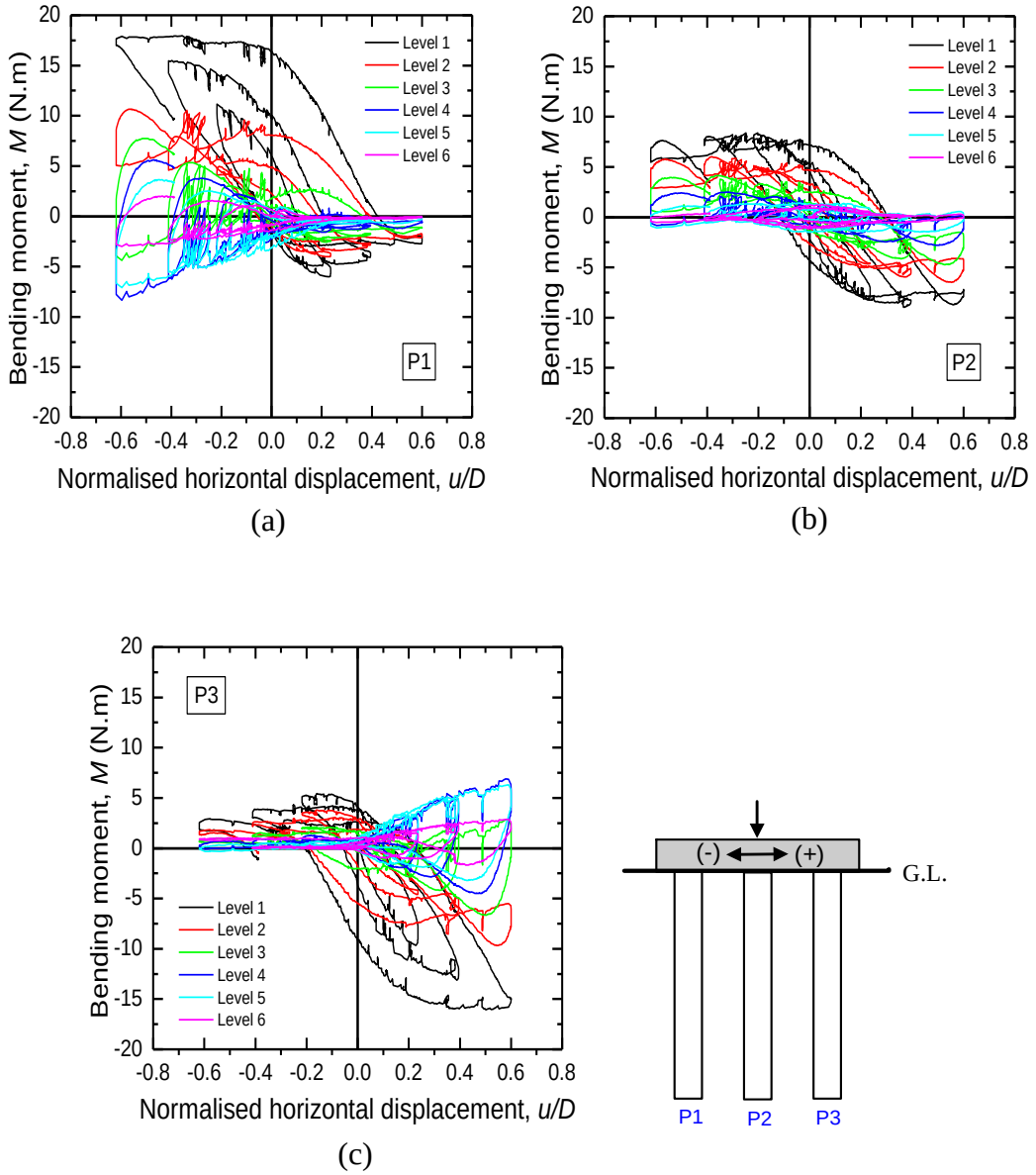

Figure 3.63 Bending moments on each pile node (a) P1 (b) P2 (c) P3 in PR model.

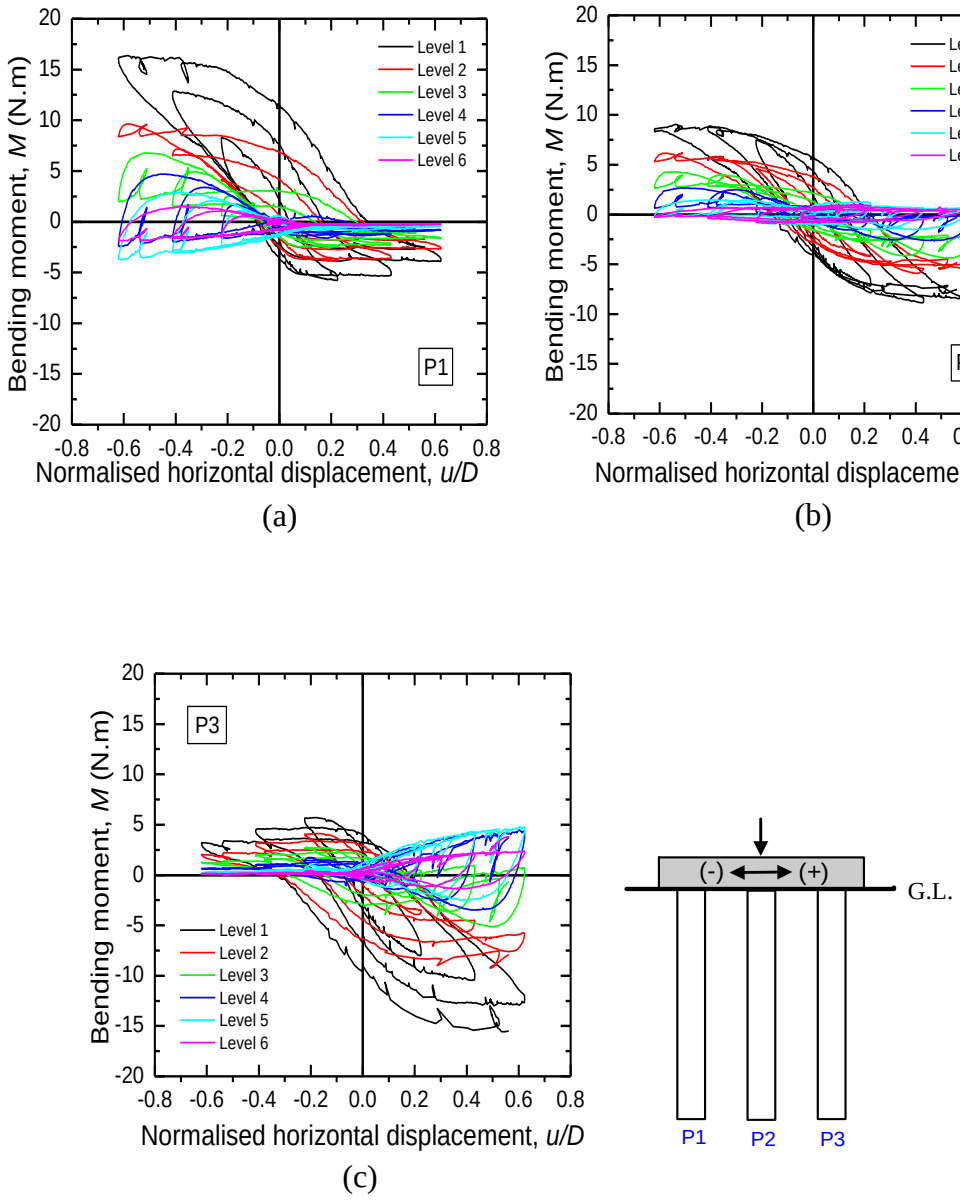

Figure 3.64 Bending moments on each pile node (a) P1 (b) P2 (c) P3 in PG model.

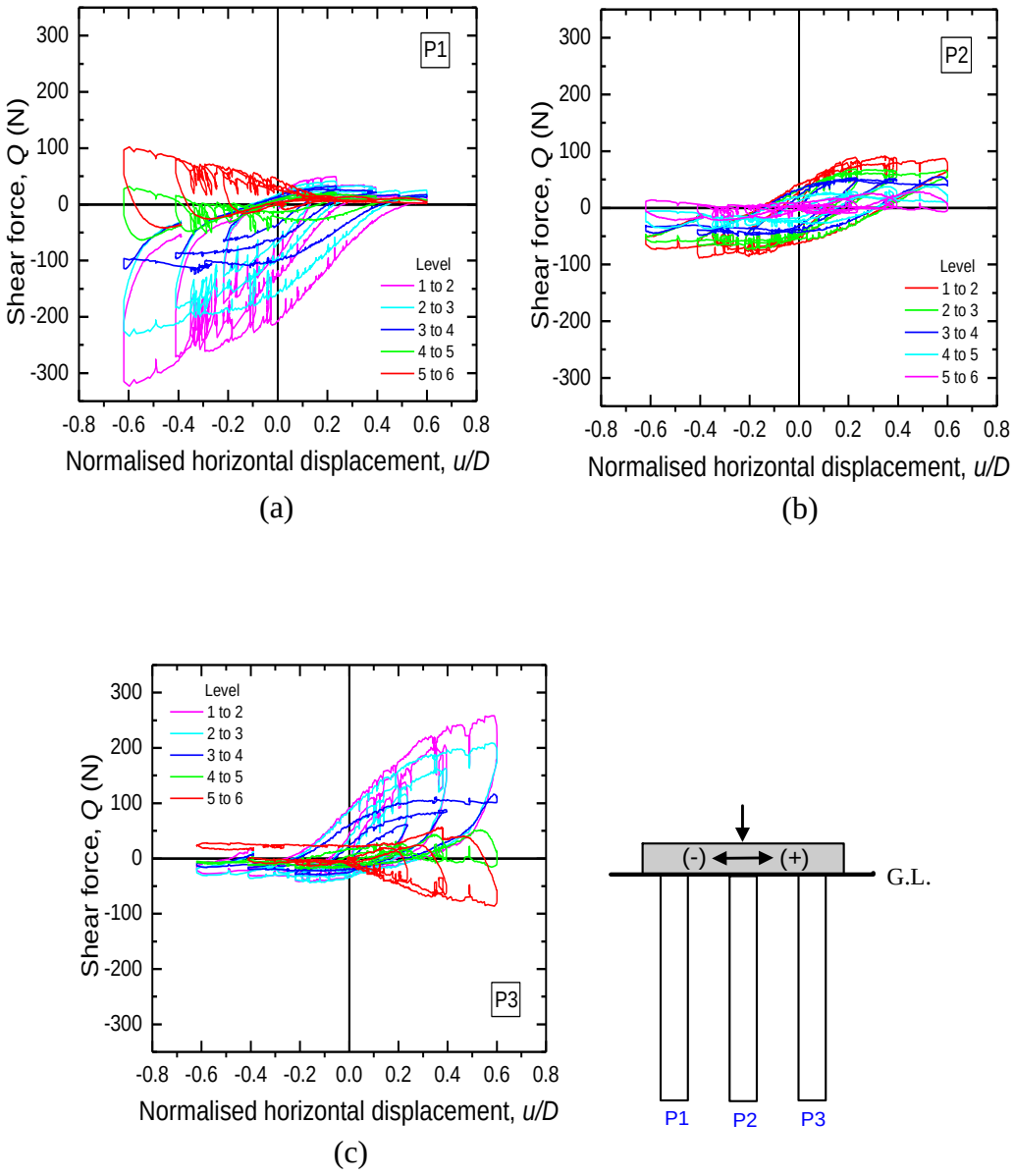

Figure 3.65 Shear force on each pile node (a) P1 (b) P2 (c) P3 in PR model.

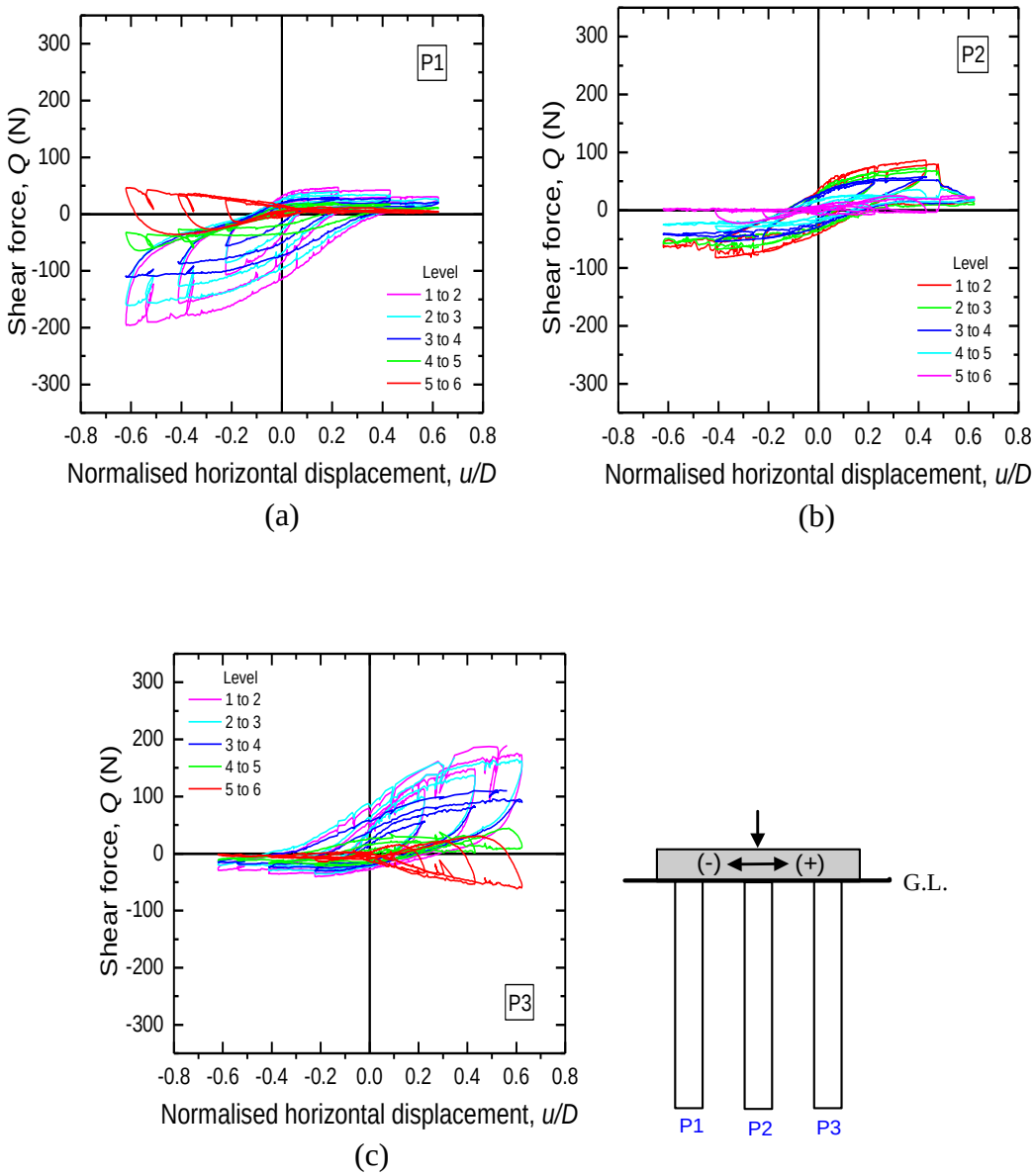

Figure 3.66 Shear force on each pile node (a) P1 (b) P2 (c) P3 in PG model.

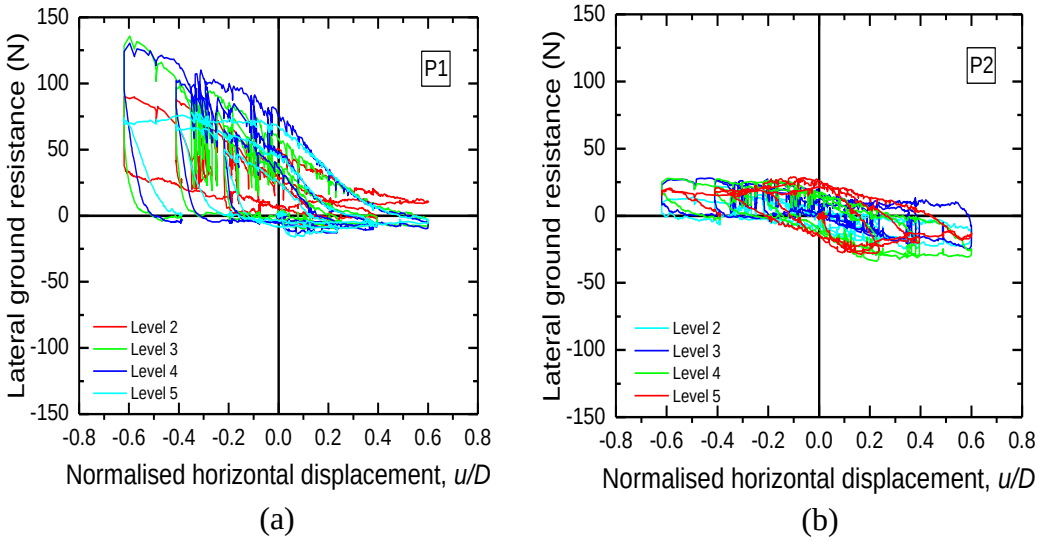

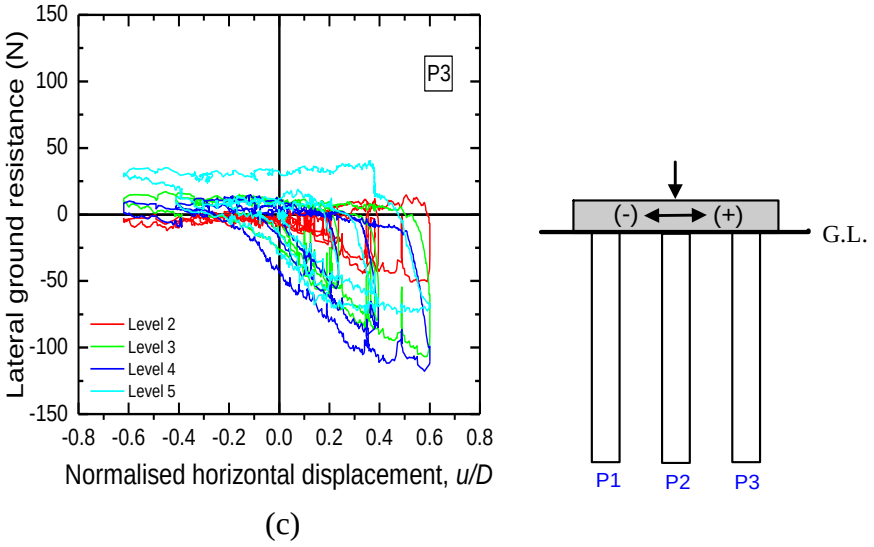

Figure 3.67 Lateral ground resistance on each pile node (a) P1 (b) P2 (c) P3 in PR model.

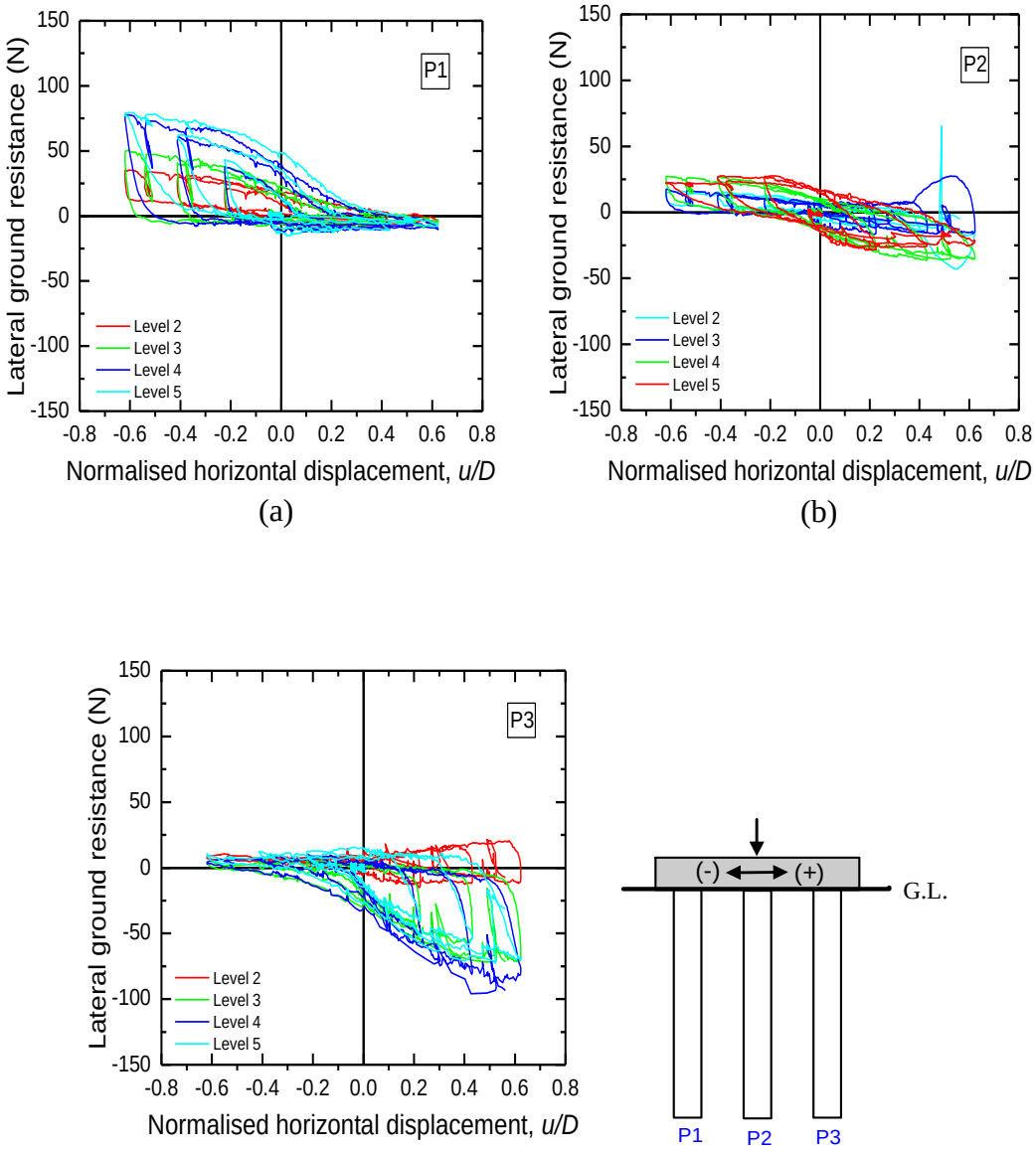

Figure 3.68 Lateral ground resistance on each pile node (a) P1 (b) P2 (c) P3 in PG model.

The distributions of bending moment, M, shear forces, Q, and lateral ground resistance along the pile at normalized horizontal displacement, $u/D = \pm 0.2, \pm 0.4$ and ± 0.6 are shown between Figure 3.69 - Figure 3.74 for PR and PG models. From Figure 3.69 and Figure 3.70, it is seen that maximum bending moments occur at the top of the piles and bending moments of the front piles are much larger than those of the rear piles in both PR and PG models. Bending moments of the center piles are almost equal in positive and negative loading as expected in both models. For PG case, bending moments are slightly smaller than PR. This means that the horizontal resistance of PR model increases compared to PG without significant bending moment increase at each pile. Although for PG case bending moments are slightly smaller, for both cases they become zero at similar depth of about 35 % - 45 % of the pile length for edge piles and 55 % of the pile length for mid-pile.

When Figure 3.71 and Figure 3.72 are investigated, it is seen that shear force responses are considerably larger at edge piles, P1 and P3 compared to mid-pile, P2 for both PR and PG cases. They have maximum value at the top of the piles and decrease gradually through the pile length and becomes zero around 65 % - 75 % of the pile length depending on the position and the type of the model. When, PR and PG models are compared, shear loads on edge piles of PR model are higher than that of PG models, whereas mid-pile carries almost the same load for both cases. Lateral ground resistance can be observed remarkably at front piles of the both models. The middle pile carries considerably small lateral ground resistance compared to front pile, whereas it carries slightly larger load than the rear pile, which is almost zero. Maximum lateral ground reaction occurs around the mid-depth of the each pile regardless of the amount of the load (Figure 3.73 and Figure 3.74).

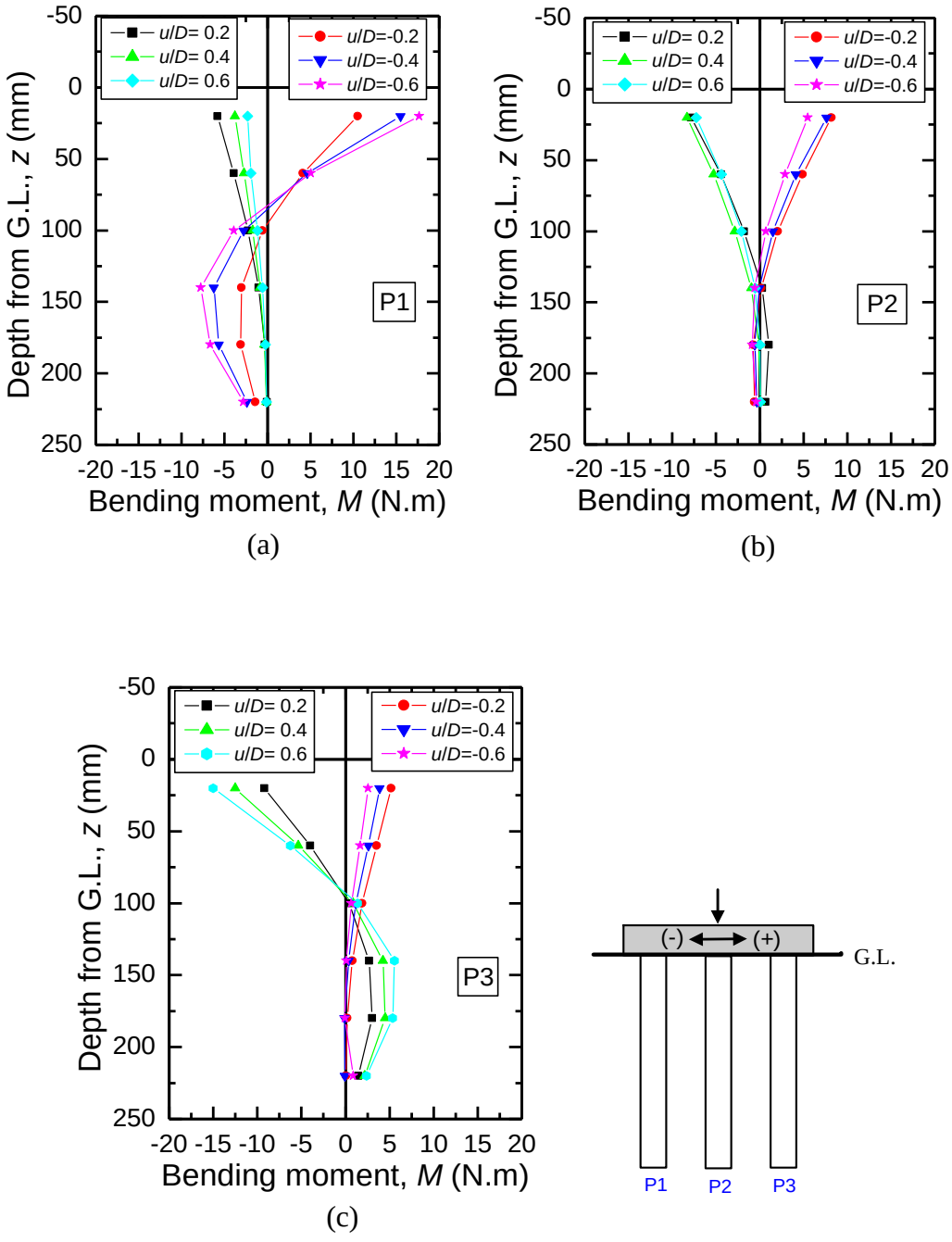

Figure 3.69 Bending moment distribution of each pile (a) P1 (b) P2 (c) P3 in PR.

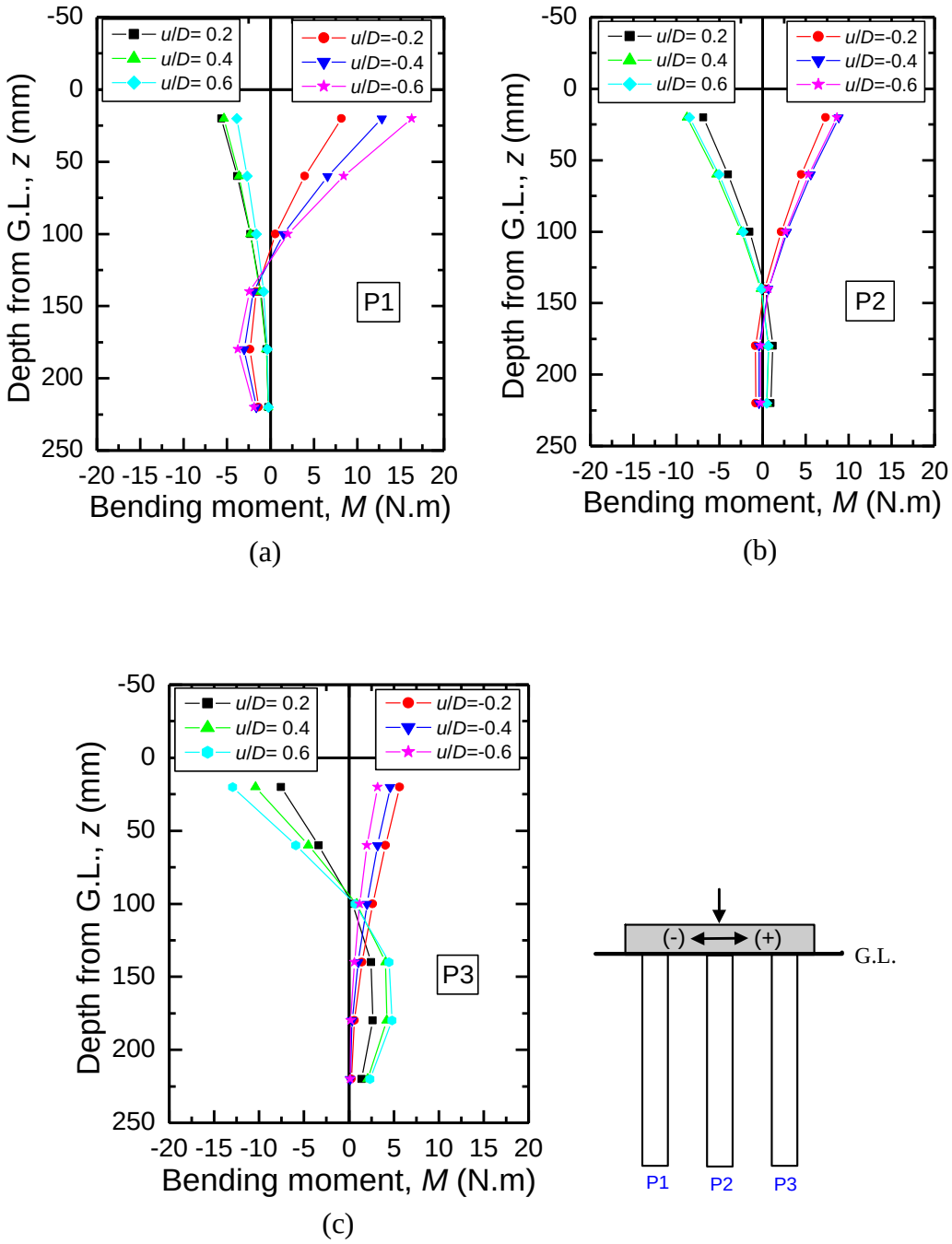

Figure 3.70 Bending moment distribution of each pile (a) P1 (b) P2 (c) P3 in PG.

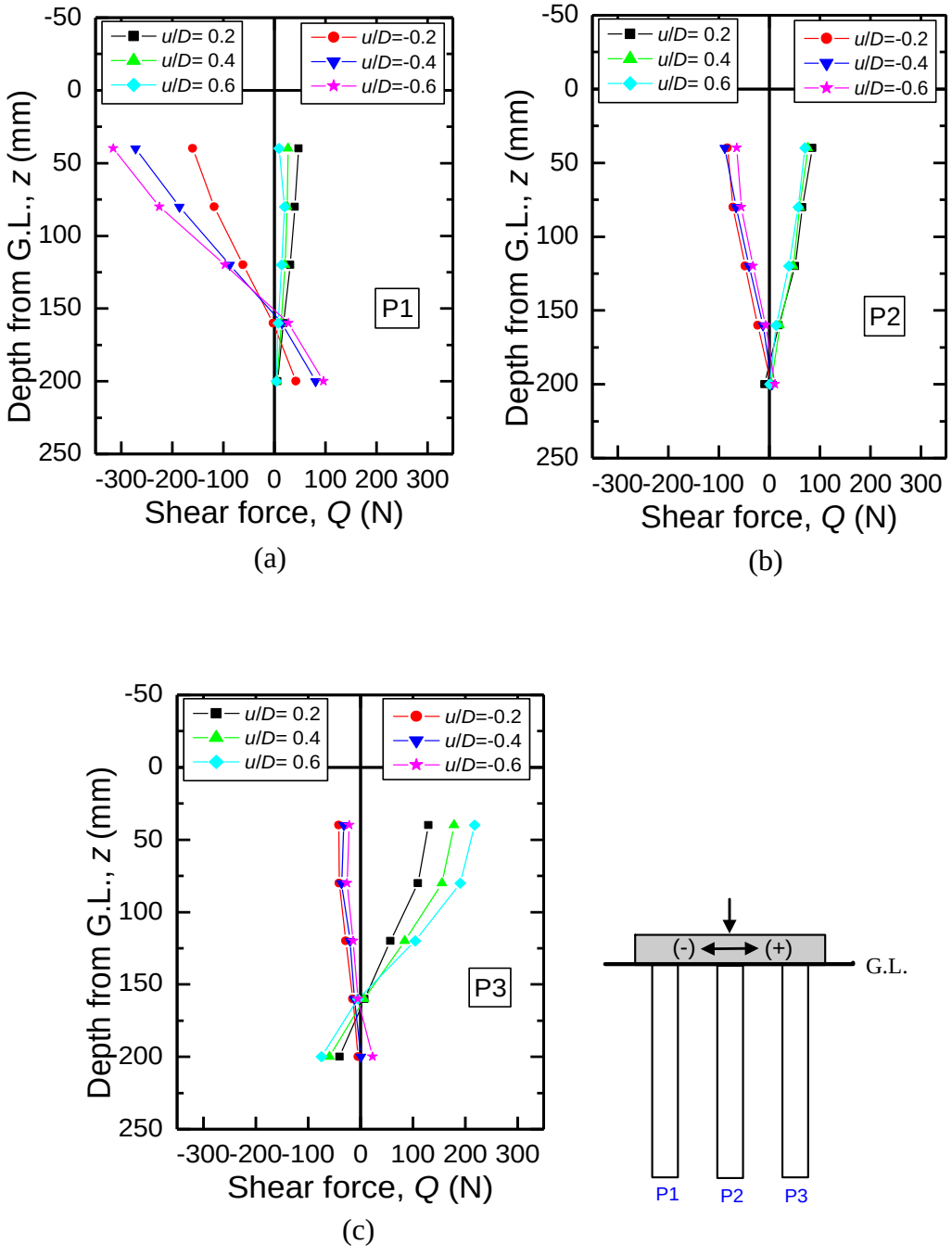

Figure 3.71 Shear force distribution of each pile (a) P1 (b) P2 (c) P3 in PR.

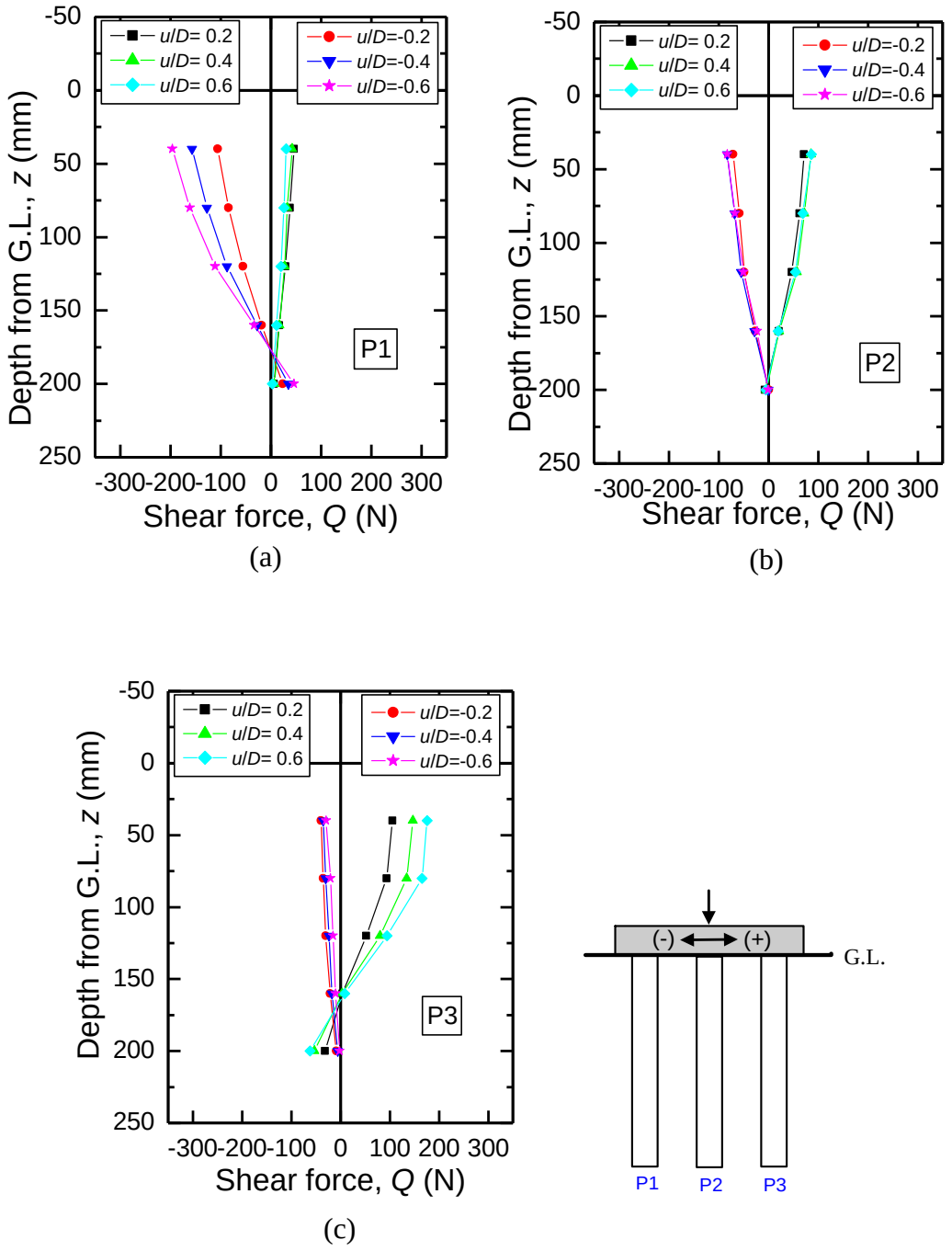

Figure 3.72 Shear force distribution of each pile (a) P1 (b) P2 (c) P3 in PG.

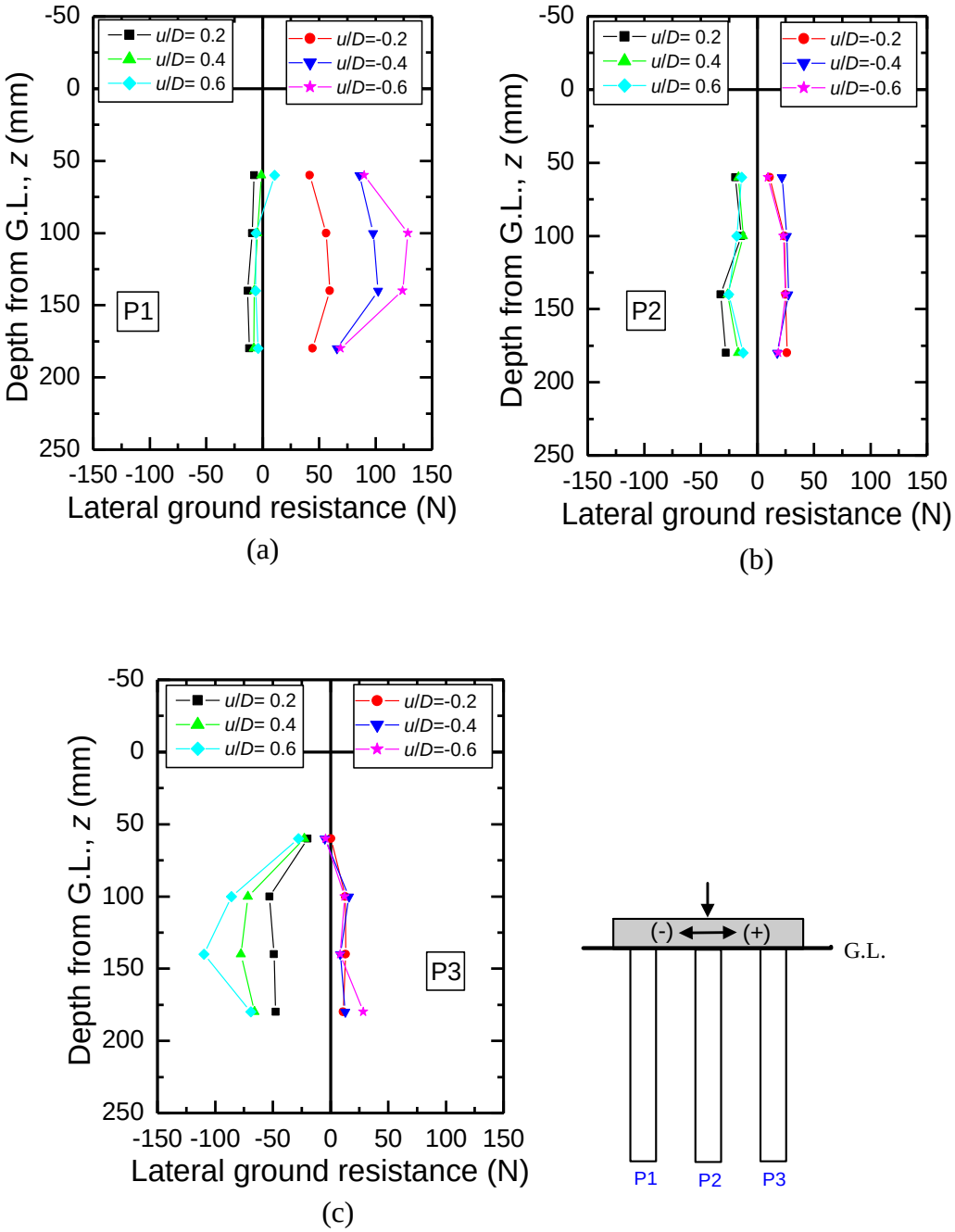

Figure 3.73 Lateral ground resistance at each pile (a) P1 (b) P2 (c) P3 in PR.

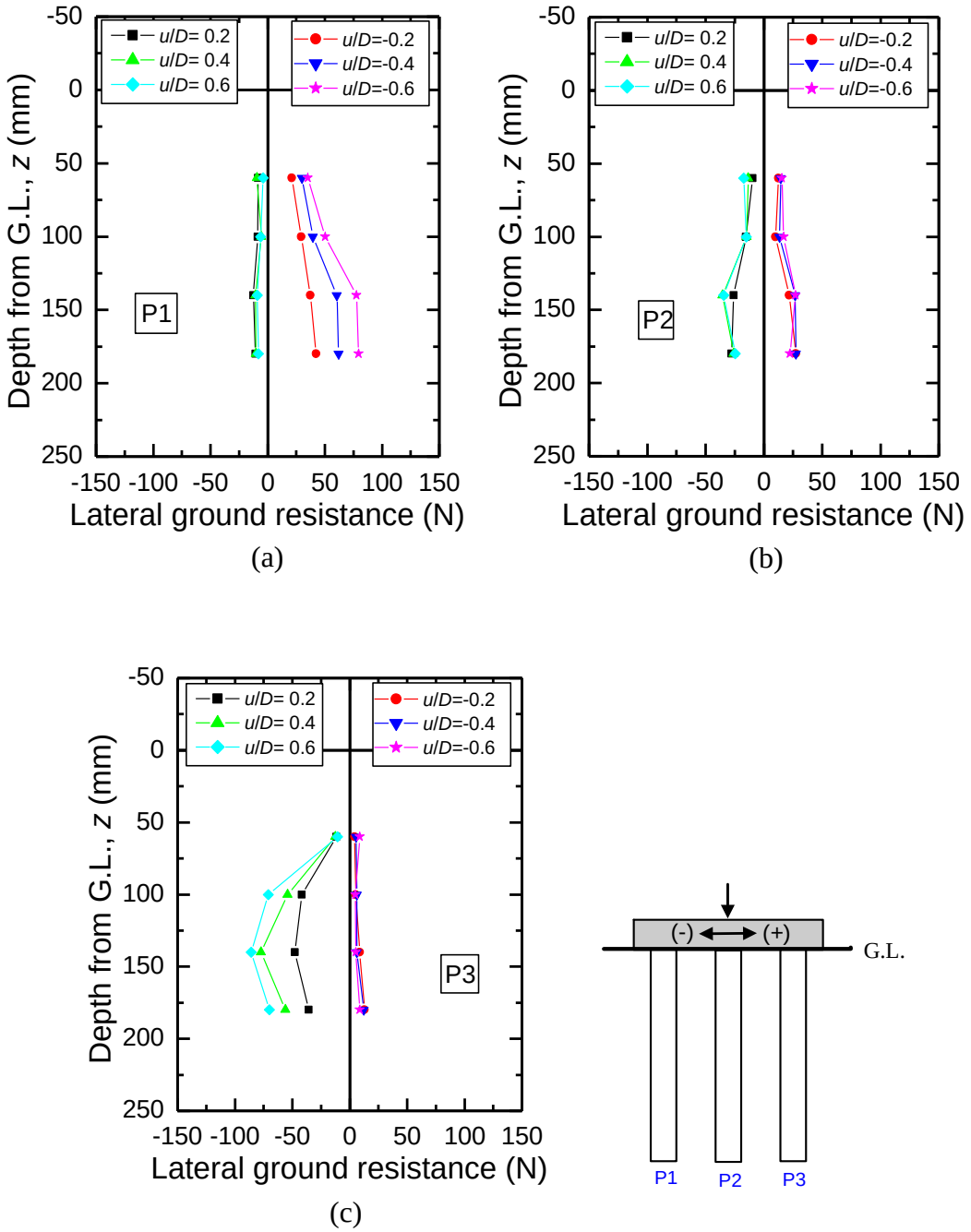

Figure 3.74 Lateral ground resistance at each pile (a) P1 (b) P2 (c) P3 in PG.

Axial force distributions at each pile component during horizontal loading for PR and PG cases are given in Figure 3.75. It can be seen that axial force, carried by center pile, P2 is constant throughout the test. In addition, front pile (P3 for positive loading and P1 for negative loading) carries most of the axial force and rear pile carries least of the axial force during the test, which is the case also for horizontal loads. Axial force distributions at each pile along the depth of the pile for PR and PG are shown in Figure 3.76 and Figure 3.77, respectively. Maximum axial force is generated at pile head and it decreases along the pile shaft for P1 and P3 when they are front piles. For center pile and rear pile, axial forces are remarkably small comparing to the front pile. It can be also said that axial forces at each pile tend to be smaller in PR compared to PG, which is due to the raft contribution.

.

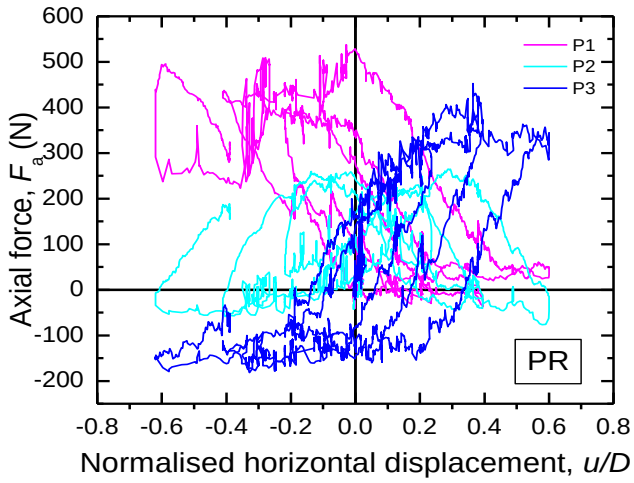

(a)

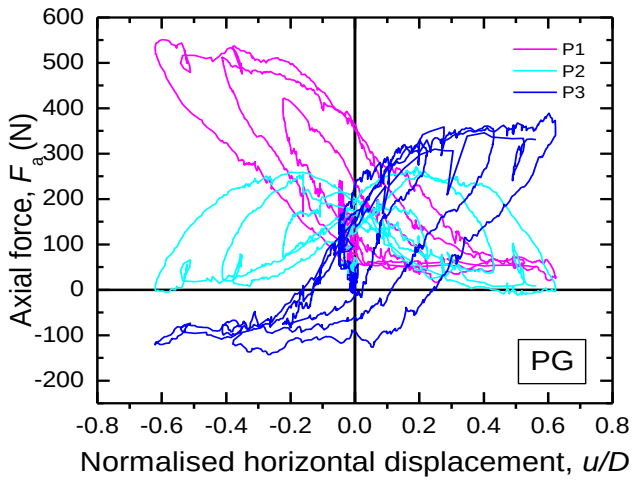

(b)

Figure 3.75 Axial force distribution during horizontal loading (a) PR and (b) PG.

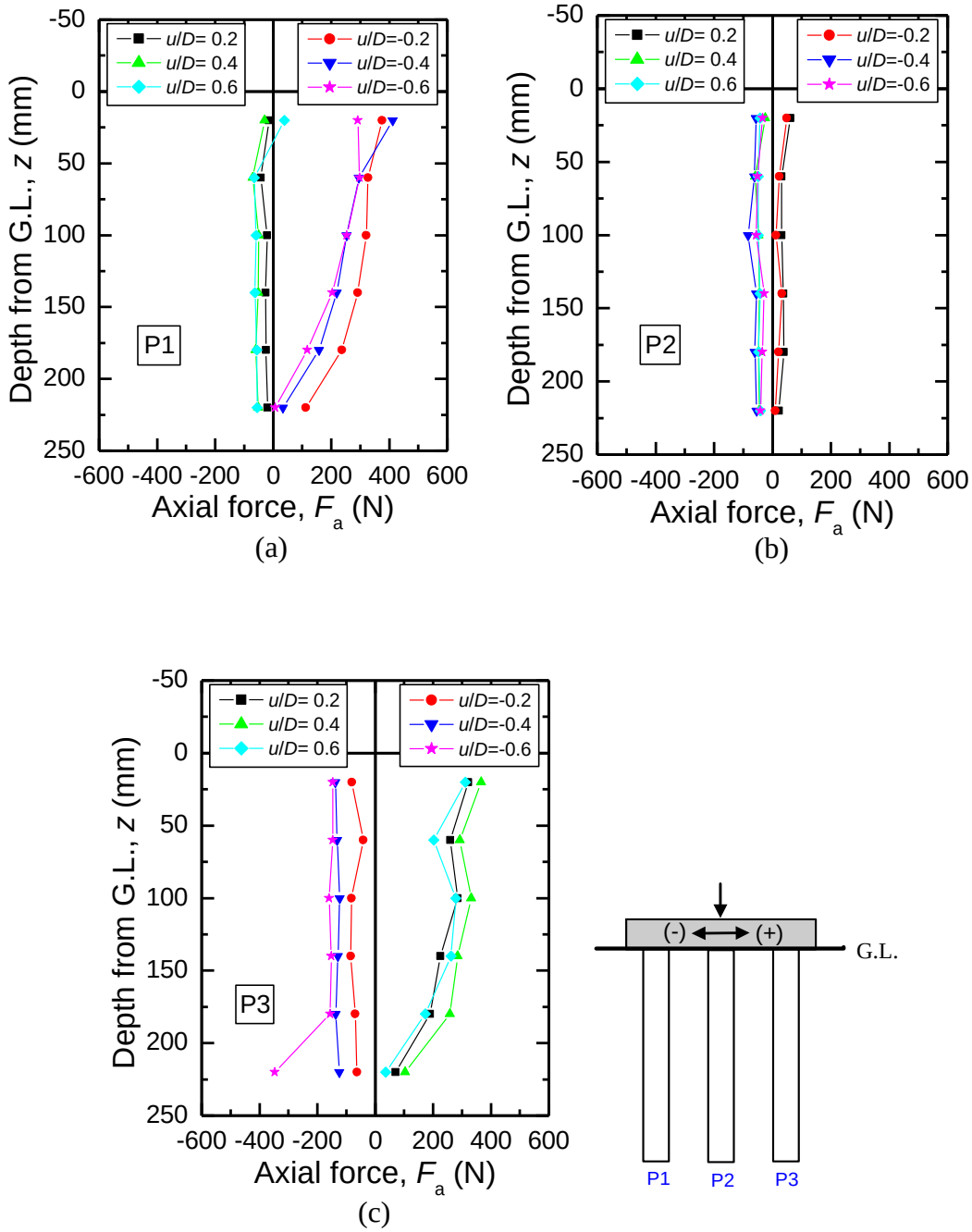

Figure 3.76 Axial force distribution at each pile along the pile length

(a) P1 (b) P2 (c) P3 in PR.

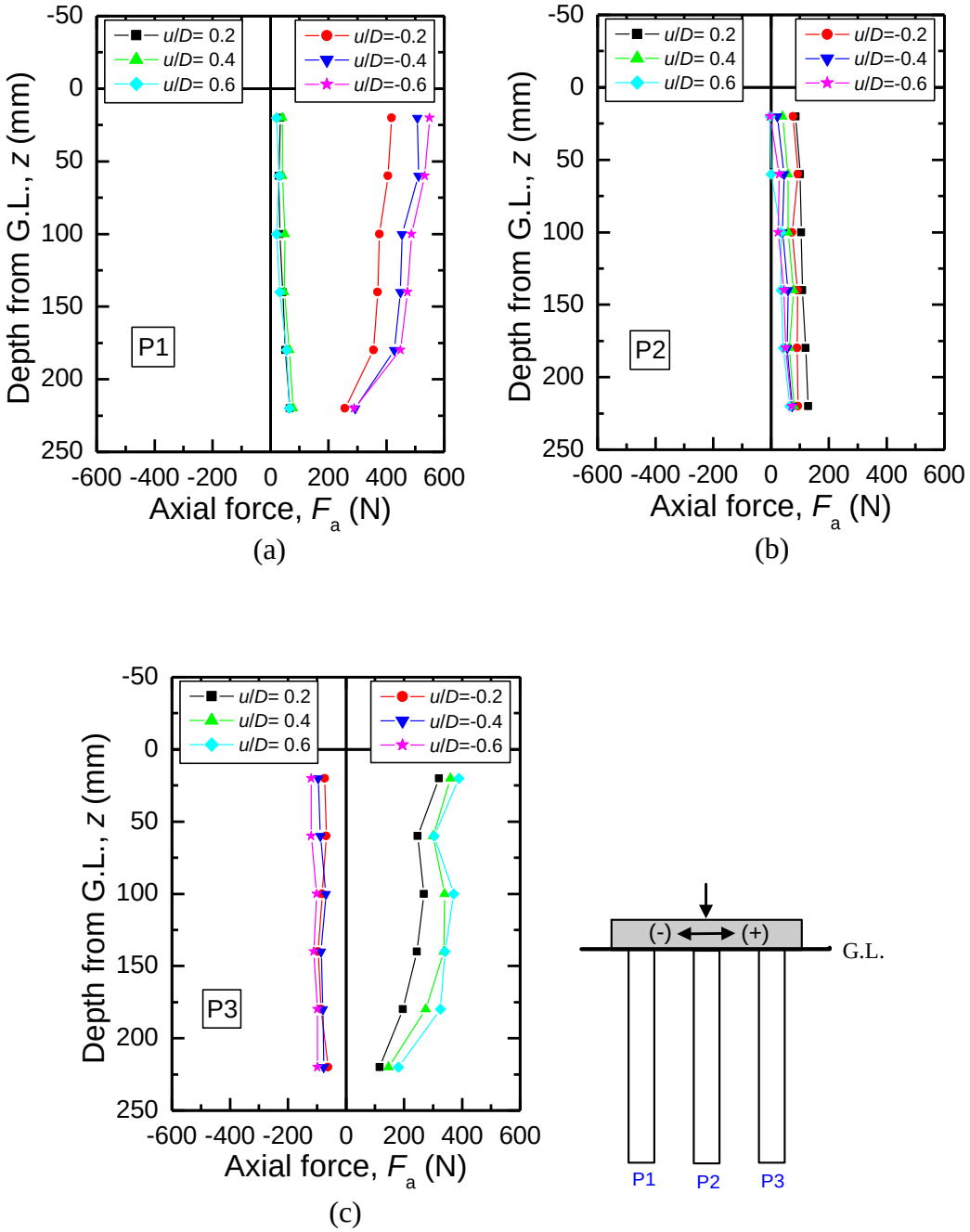

Figure 3.77 Axial force distribution at each pile along the pile length

(a) P1 (b) P2 (c) P3 in PG.

3.7 Conclusions

In this chapter, vertical load tests and static cyclic horizontal load tests on Single Pile, Capped Pile, Piled Raft, Pile Group, Small Raft and Full Raft are summarized. In order to represent superstructure load, steel plates were applied as a vertical load during horizontal loading. Applied horizontal load was controlled by horizontal displacement measurement, where normalized horizontal displacements, u/D, were ± 0.2, ± 0.4, ± 0.6. At vertical loading tests, vertical load was applied by screw jack by displacement controlled loading, where the maximum vertical displacement is equal to the diameter of the pile. In all experiments, the model ground was dry silica sand #6, with a relative density of 70 %.

When the vertical load capacities of capped pile and single pile are compared, it is seen that the capacity of capped pile is two times larger than single pile model, since the raft component of capped pile model increases the capacity of the model. Pile capacity of the single pile is slightly smaller than the pile component of capped pile, which may be due the confining stress increment beneath the raft. For capped pile model, at the beginning most of the load is carried by pile due to the loose contact between the raft and the ground. After settlement of the raft, the proportion of load carried by raft component increases considerably, and each component carries 50 % of the applied vertical load.

When considering the final settlement of small and full raft, it is seen that the full raft settlement is about 25 % larger than that of the small raft and vertical capacity of full raft is 4 times larger than small raft's capacity. Moreover, the initial stiffness of small raft and full raft is 0.31 kN/mm and 0.75 kN/mm, respectively.

If the vertical load capacities of 3 single pile and 3 piles of piled raft are compared, it is seen that the capacity of piled raft's piles is considerably larger than the capacity of 3 times of the single pile due to the increment of confining

stresses beneath the raft. Transferring the vertical load to the soil through the raft causes this stress increment. Moreover, the behavior and the capacity of mid-pile (P2) (40 % of the applied vertical load) is observed to have larger capacity than edge piles (P1 and P3) (30 % of the total piles load for each), which shows that the location of the pile affects the response and the capacity of piles. Axial force distribution of the piles along the pile depth also supports this phenomenon. In addition, at the beginning of the test most of the load is carried by the piles due to the loose contact between the raft and the ground which is also the case at capped pile model. After settlement of the raft and satisfying good contact between the raft and the soil, the proportion of raft component increases considerably, and at the end of the test the raft carries 40 % of the applied vertical load.

Static cyclic horizontal load tests on capped pile were carried out with and without vertical loading. The results show that, 80 % of the horizontal load is carried by single pile regardless of the amount of vertical load on the model foundation. However, vertical displacement of model foundation is more realistic for the model with vertical loading, which indicates the importance of modelling the superstructure during experiments. As far as bending moment, shear force and lateral ground reaction responses are of concern, although both cases show similar behavior, the capacity of the model with vertical loading is generally larger than that of capped pile without vertical loading.

Static cyclic horizontal load test on raft alone conditions (small raft and full raft) were carried out under 4 different vertical loadings for each model. It is found that the friction angle between the contact surface of the raft and the ground is 29.3^0 and 31.1^0 for small raft and full raft, respectively.

Static cyclic horizontal load test on piled raft and pile group were carried out with 497 N vertical load which was applied by the help of 5 steel plates. For pile group case, the only difference was the existence of 20 mm space between the raft and the model ground to eliminate the raft effect. The results show that, the raft

increases the carrying capacity of the model about 40 %. It is also seen that, 60 % and 58 % of the total horizontal load is carried by the front pile (P3 for positive loading and P1 for negative loading) for PR and PG, respectively. Moreover, 55 % and 65 % of the total axial load is also supported by front piles for PR and PG, respectively. Therefore, it can be said that front pile carries most of the horizontal and axial load for both cases.

The amount of inclination of the raft is similar for PR and PG cases. However, the settlement of model foundation of PG is almost two times larger than that of PR, which indicates one of the advantages of piled raft over pile group. For both tests, bending moments and shear forces are larger at the pile top and decrease along the depth of the pile since there is a rigid connection between the pile and the raft. Although, bending moments occurred along the pile during horizontal loading are similar for both cases, shear forces are 50 % larger at the piles of piled raft model, which means shear failure may probably be observed in piled raft model. Moreover, for piled raft case, 60 % - 100 % of horizontal and vertical loads are carried by three piles.

CHAPTER 4

SHAKING TABLE TESTS ON MODEL FOUNDATIONS

4.1 Introduction

In this chapter, pile group and piled raft behaviors under the combination of vertical and dynamic loading are compared. For this purpose, shaking table tests on 3-pile pile group and 3-pile piled raft with friction piles were carried out under sinusoidal waves, having frequency of 20 Hz and 5 Hz. Moreover, model ground without model foundation (green field) case was also tested to characterize the soil used in the dynamic loading experiments. Note that, the model ground and model foundations used in static cyclic horizontal load tests (which were described in detail in Chapter 3) were also used in dynamic tests for comparison purposes.

4.2 Preparation of the Experiments

4.2.1 Model foundation and model ground

In order to investigate the behaviors of piled raft and pile group under dynamic loading, the same model foundation as used in static cyclic horizontal load tests (see Chapter 3) was also used in dynamic experiments (Figure 4.1). Piled raft (or Pile group) was composed of a raft and 3 piles, each of them had an outer diameter, D of 20 mm, with a thickness of 1.1 mm, where the center-to-center spacing, s, of the piles was 80 mm, 4 times of the pile diameter (s/D = 4) as mentioned before. The details of the piled raft are given in Figure 4.1 and the properties of the pipe pile are summarized in Table 3.1.

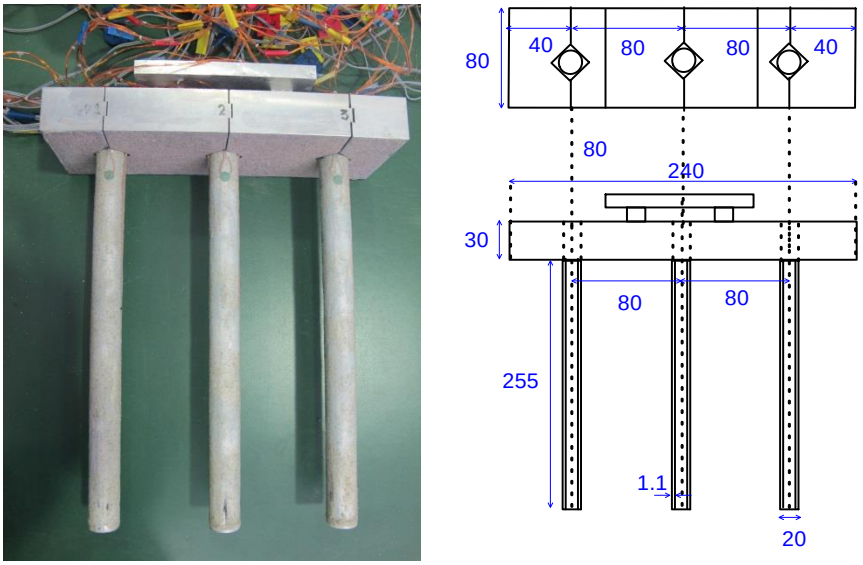

Figure 4.1 Model foundation (3-pile piled raft or 3-pile pile group).

As it was mentioned in Chapter 3, the same model foundation was used for Piled Raft (PR) test and Pile Group (PG) test. 20 mm space between the raft and the model ground was provided in PG test in order to eliminate the raft base resistance.

The model ground was dry silica sand #6 having a relative density of D_r = 70 % (the same model ground as the static experiments) was used through dynamic experiments to eliminate the effects of the variation of the model ground, since it is out of the scope of this study. The properties of the soil are summarized in Table 3.4.

Model ground was prepared in the laminar box that was used in the previous tests having dimensions of 800 mm (in x-direction) × 500 mm (in y-direction) with a depth of 530 mm (Figure 3.12). The box was consisted of 10 frames having a height of 50 mm and it was covered with rubber membrane to allow the movements of the ground in the box in horizontal (x and y) directions during

dynamic tests. As a result, the reflections of the waves from side walls of the box were minimized as much as possible so that infinite horizontal distance of the ground was simulated.

4.2.2 Calibrations of the instruments

In order to measure the horizontal and vertical displacements of the model foundation, laser displacement transducers were used. Generated accelerations in the model ground and on the model foundation during the dynamic experiments were measured by the help of accelerometers. Therefore, calibrations of these instrumentations were made before the experiments. Some of the calibrations are shown as examples:

Laser displacement transducers (LDT): In order to measure the average vertical deflection and the inclination of the model foundation during shaking table tests, two laser displacement transducers were located at right and left sides of the model foundation. In addition, two laser displacement transducers were used for horizontal deflections to measure the horizontal movements of the mass and the model foundation. Calibration of the laser displacement transducers were performed by measuring the known thickness of the objects. Two vertical laser displacement transducers were labelled as right and left; LDT-R and LDT-L, respectively, and their calibrations are shown in Figure 4.2. They can measure from a distance of 80 mm with a capacity of ± 15 mm. Figure 4.3 shows the calibration of the horizontal laser displacements, LDT-1 and LDT-2, which have a capacity of ± 100 mm and they can measure from a distance of 300 mm.

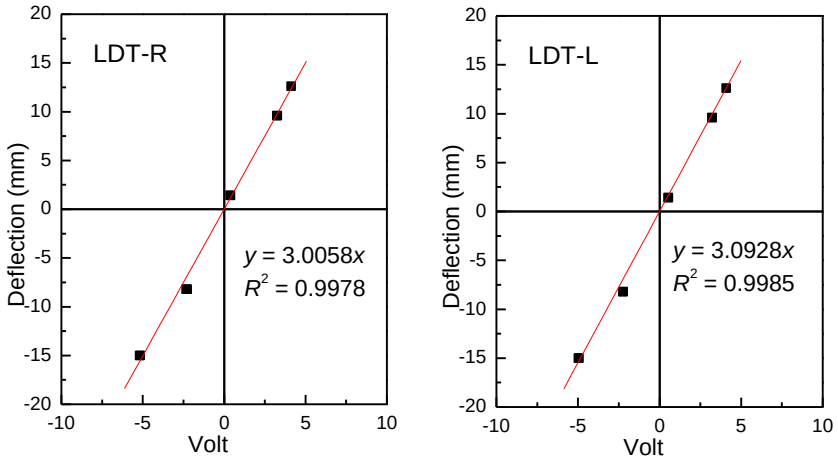

Figure 4.2 Calibration of vertical laser displacement transducers; LDT-R and LDT-L.

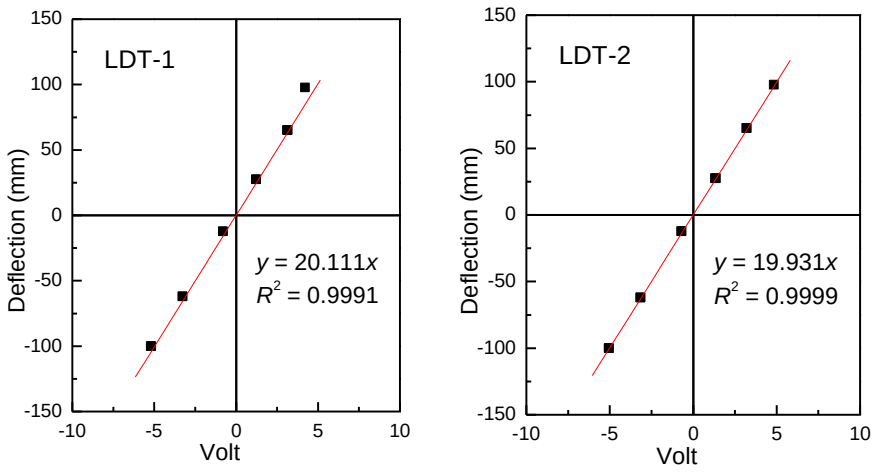

Figure 4.3 Calibration of horizontal laser displacement transducers; LDT-1 and LDT-2.

Accelerometers (ACC): Accelerometers were used to measure the accelerations of the input motion at the bottom of the box, and of the model ground at several depths during shaking table tests. Both horizontal and vertical accelerations of the model foundation were measured by accelerometers. In total, 12 accelerometers

were used to measure the accelerations on the model foundation and in the model ground. For the calibration of the accelerometers, 1g, 0g and -1g acceleration values were recorded as voltage differences and then linear calibration has been performed for each accelerometer. The calibration graphs of the first two accelerometers, ACC-1 and ACC-2 are given in Figure 4.4 as an example.

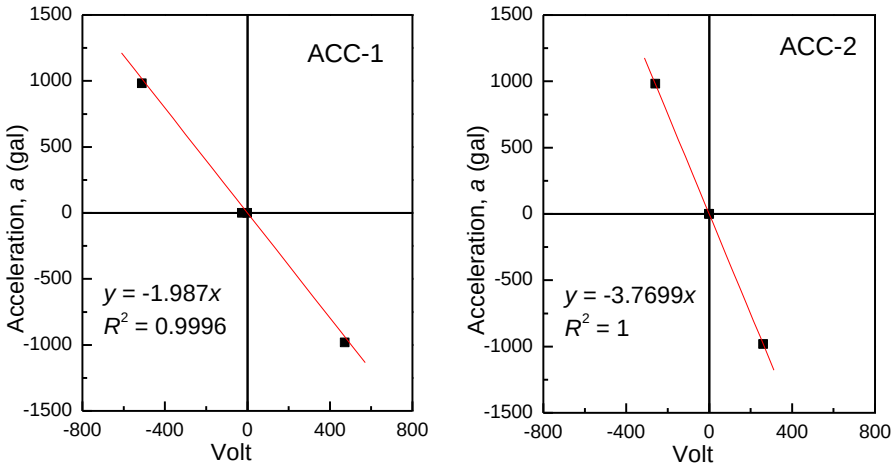

Figure 4.4 Calibration of accelerometers; ACC-1 and ACC-2.

Table 4.1 shows the summary of the calibration factors of the instrumentations that were used during dynamic load tests with their maximum ranges. In addition, each pile was instrumented with strain gauges at 6 levels to obtain axial forces, bending moments and shear forces induced in the pile during the tests as explained in Chapter 3.

Table 4.1 Summary of the calibration factors of the instrumentations.

Instrumentation	**Coefficient**		**Max Range**
Laser Disp. Cell - Right (LDT-R)	3.0058	mm/Volt	±15 mm
Laser Disp. Cell - Left (LDT-L)	3.0928	mm/Volt	±15 mm
Laser Disp. Cell - 1 (LDT-1)	20.111	mm/Volt	±100 mm
Laser Disp. Cell - 2 (LDT-2)	19.931	mm/Volt	±100 mm
Accelerometer - 1 (ACC-1)	-1.9870	gal/Volt	2000 N
Accelerometer - 2 (ACC-2)	-3.7699	gal/Volt	2G
Accelerometer - 3 (ACC-3)	-1.5896	gal/Volt	2G
Accelerometer - 4 (ACC-4)	-1.9968	gal/Volt	2G
Accelerometer - 5 (ACC-5)	-1.9802	gal/Volt	2G
Accelerometer - 6 (ACC-6)	-1.9399	gal/Volt	2G
Accelerometer - 7 (ACC-7)	-1.8997	gal/Volt	2G
Accelerometer - 8 (ACC-8)	-2.1169	gal/Volt	2G
Accelerometer - 9 (ACC-9)	-1.9205	gal/Volt	2G
Accelerometer - 10 (ACC-10)	-4.6468	gal/Volt	5G
Accelerometer - 11 (ACC-11)	-4.4703	gal/Volt	5G
Accelerometer - 12 (ACC-12)	-4.1911	gal/Volt	5G

4.3 Shaking Table Tests and Results

Shaking table used through the experiments has dimensions of 1.0 m × 1.5 m. The electric motor of the system provides one way sinusoidal harmonic motion up to the frequency, *f*, of 30 Hz and up to 20G acceleration. The mass limitation of the shaking table is 5 tons with a maximum stroke of 200 mm. Model ground for the dynamic tests was prepared with the same procedure as used in the static tests.

4.3.1 Shaking table test of the table alone

In order to investigate the properties of the shaking table and to predict the amplification factor (measured acceleration/nominal acceleration), first the table was tested without laminar box. For this purpose, different nominal amplitudes (A = 0.05G - 0.3G) and different frequencies (f = 5 - 30 Hz) were applied as an input motion.

Amplification factor vs. frequency is shown in Figure 4.5. It is seen from the figure that the amplification factor (measured acceleration/nominal acceleration) depends on nominal amplitude and frequency. However, this factor mostly depends on nominal amplitude rather than frequency. The average amplification factors depending on amplitudes of accelerations are summarized in Table 4.2.

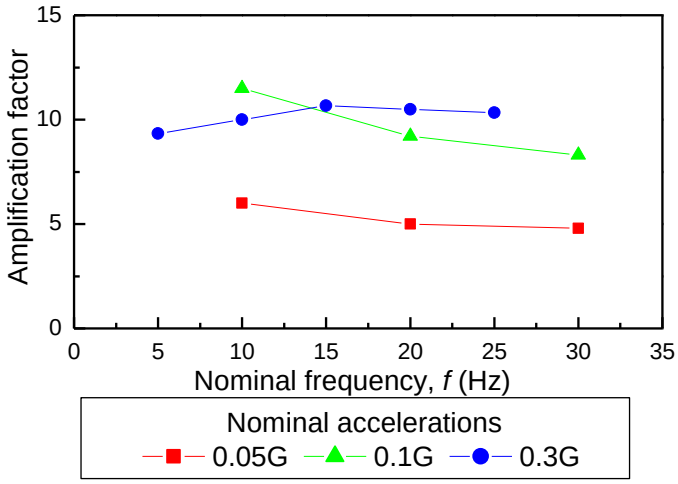

Figure 4.5 Amplification factor vs. frequency graph.

Table 4.2 Average amplification factors.

Nominal amplitude, *A* (G)	Avr. amplification factor
0.05	5.3
0.1	9.7
0.3	10.2

4.3.2 Shaking table test of the model ground alone

Shaking table tests of the model ground alone were carried out to investigate the response of the model ground under different input motions. Silica sand #6 was used as a model ground as mentioned before. The physical properties of the sand are summarized in Table 3.4. Figure 4.6 shows the experiment setup. 12 accelerometers were set to measure the horizontal and vertical accelerations at different depths, where ACC-1 was used to measure the input motion at the bottom of the box. The input motions applied to the model ground had different frequencies (f = 2, 4, 6, 8, 10, 12, 14, 16, 18, 20, 22, 24, 26, 28, 30, 50 Hz) with a constant nominal amplitude (A = 0.5 m/s^2) and having number of cycles of loading of 100.

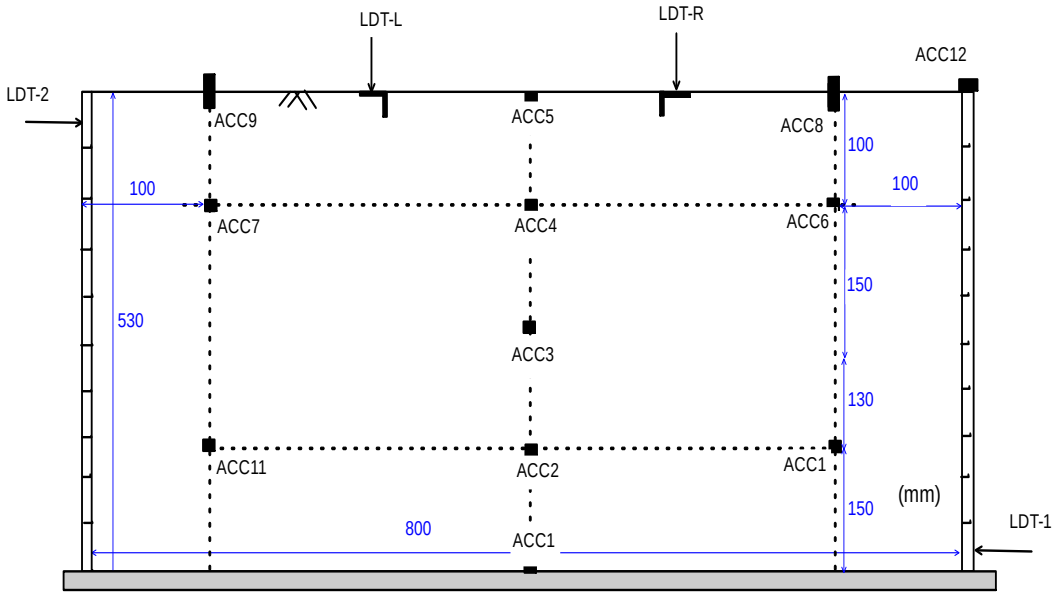

(a)

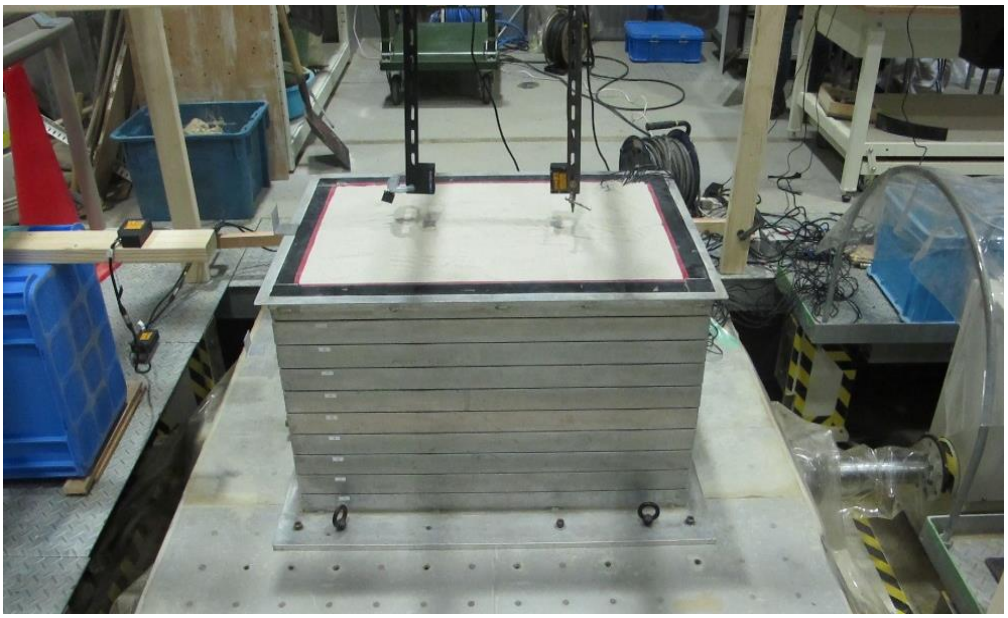

(b)

Figure 4.6 Test setup for model ground alone (a) drawing (b) photo.

Test results:

The ratio of the measured accelerations ACC5 (at the top of the model ground) to ACC1 (at the bottom of the box) gives amplification factor of the input motion through the ground. It is known that, at resonant frequency this amplification becomes maximum. From the 1st test series, the resonant frequency of the model ground was found to be between 16 - 28 Hz (Figure 4.7). In order to determine the resonant frequency, f_n, of the model ground more specifically, test series were conducted with small interval, 0.5 Hz. After the 2nd test series, the resonant frequency was estimated as 20 Hz for the model ground (Figure 4.7).

The purpose of using the laminar soil box is to minimize the influence of wave reflections at the side walls, so that the ground having infinite length in x-direction could be modelled. The measured accelerations of ACC4, ACC6 and ACC7, which were located at the same depth in laminar box (see Figure 4.6) are depicted in Figure 4.8 and Figure 4.9 for 6 Hz and 20 Hz input frequencies, respectively. The reasonable uniformity is confirmed by the measurements except that corner accelerometers are affected slightly by wave reflection from the laminar box walls at 20 Hz.

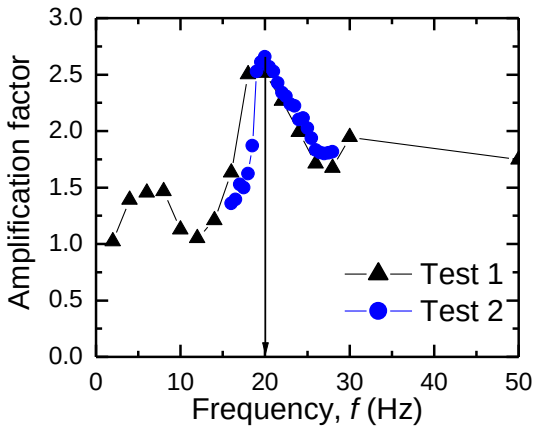

Figure 4.7 Model ground without foundation test result.

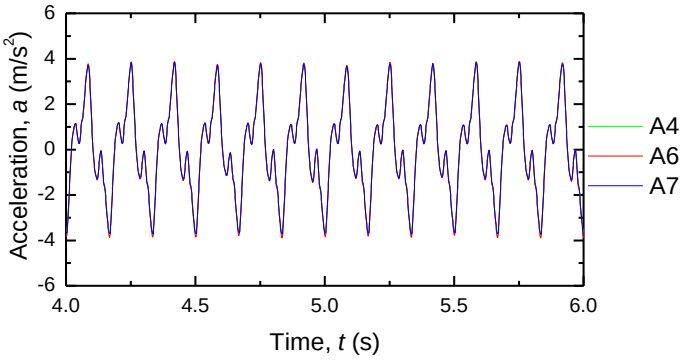

Figure 4.8 Acceleration vs. time graph at depth, z = 100 mm for input motion having f = 6 Hz.

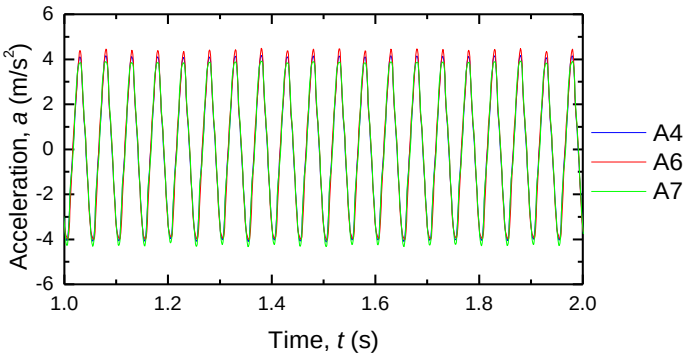

Figure 4.9 Acceleration vs. time graph at depth, z = 100 mm for input motion having f = 20 Hz.

4.3.3 Piled raft (PR) and Pile group (PG) models under the sinusoidal wave of 20 Hz frequency

Shaking table tests were carried out on a Piled Raft (PR) model and a Pile Group (PG) model to investigate the soil-pile interaction and the raft effect on the behaviors of the model pile foundations under dynamic horizontal loading. Dynamic loading was applied as a sinusoidal wave where the frequency of the wave was selected as 20 Hz since the resonant frequency of the model ground was

predicted as 20 Hz in previous experiments on model ground alone. 20 Hz in the model scale corresponds to 1.56 Hz (0.078×20 Hz) in prototype scale which was calculated by the help coefficients presented in Table 3.5. Note that, the dominant amplitude of the earthquake records are in the interval of 0.2 Hz – 2.0 Hz in literature. In addition, the input motion had nominal amplitude of 0.07G, with number of cycles of loading, N_w, of 100.

Setup of the model ground and model foundations:

First, the model ground was prepared by layers (10 layers of 50 mm and one layer of 30 mm) in order to control the density of the model ground by placing (pouring) soil (which makes totally 280 mm height) layer by layer and compacting until an intended relative density, D_r, of 70 %was reached. Then, the model foundation was fixed on the box by the help of clamps and rods. After that, 5 more layers of soil was placed (poured) until 530 mm or 510 mm height of the model ground is obtained for PR and PG cases, respectively. Note that, during the preparation of the model ground, accelerometers were placed at proper locations. Finally, the laser displacement transducers and accelerometers were placed on the model foundation.

Procedure of the tests:

Vertical load was applied on top of the raft by placing mass plates (weights) until the intended loading level was reached. Then, the plates were fixed to the raft by bolting (The total amount of vertical loading was 497 N for PR and PG tests). After that, the sinusoidal input wave was applied, which had a frequency of 20 Hz (or 5 Hz) and nominal amplitude of 0.07G.

Instrumentations:

The following items were used to record the measurements during the test:

(i) 4 laser displacement transducers to measure horizontal and vertical displacements.

(ii) 12 accelerometers to measure the input acceleration, accelerations in the model ground and on the model foundation.
(iii) 12 axial strain gauges at each pile to measure bending moments and axial forces.
(iv) 4 shear strain gauges (one-gauge measurement method was used to measure strains) at each pile to measure shear force close the pile head.

Test setups for PR and PG models under dynamic loading are illustrated in Figure 4.10 and Figure 4.11, respectively.

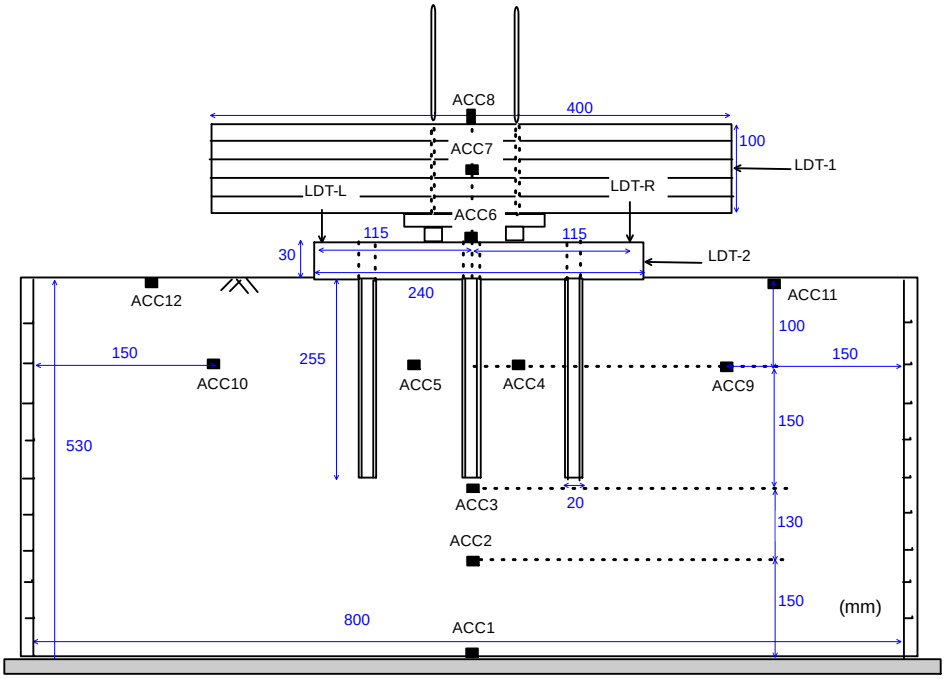

(a)

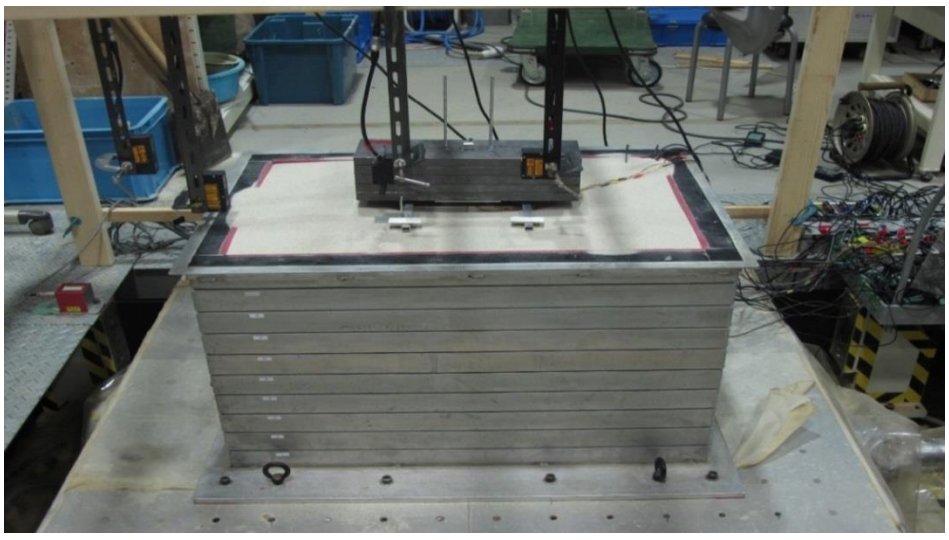

(b)

Figure 4.10 Test setup for PR model (a) drawing (b) photo of the experiment.

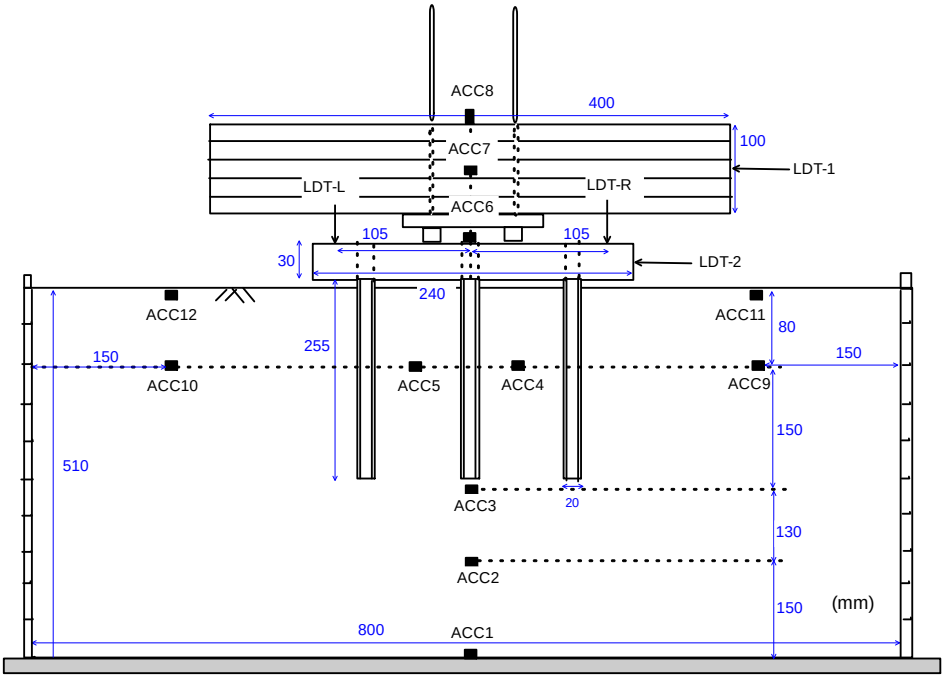

(a)

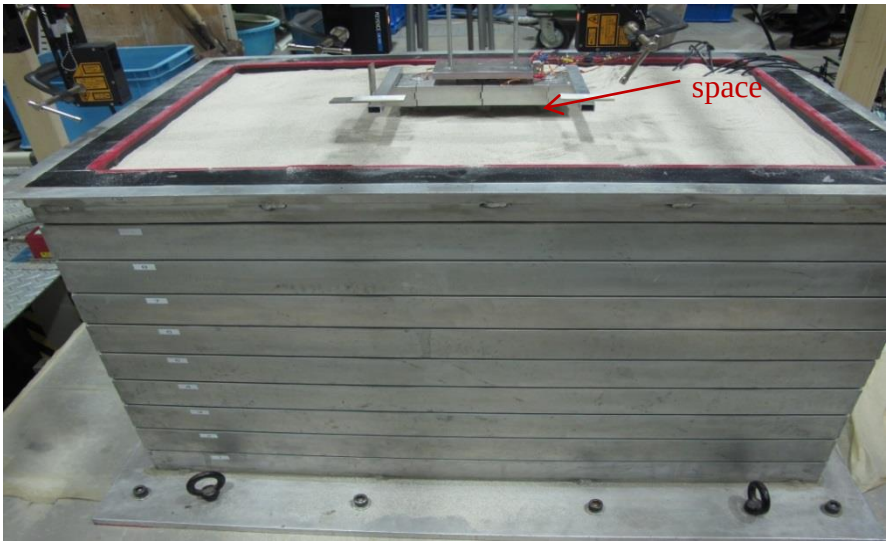

(b)

Figure 4.11 Test setup for PG model (a) drawing (b) photo of the experiment.

Test results:

Figure 4.12 (a) and (b) shows the input motions that were measured at the base of the laminar box for PR and PG models. A sinusoidal wave that had a frequency of 20 Hz and amplitude of 4 m/s^2 was measured as an input motion in both cases. It can be said that the input wave is similar in both tests. Therefore, it is reasonable to compare the results of the tests.

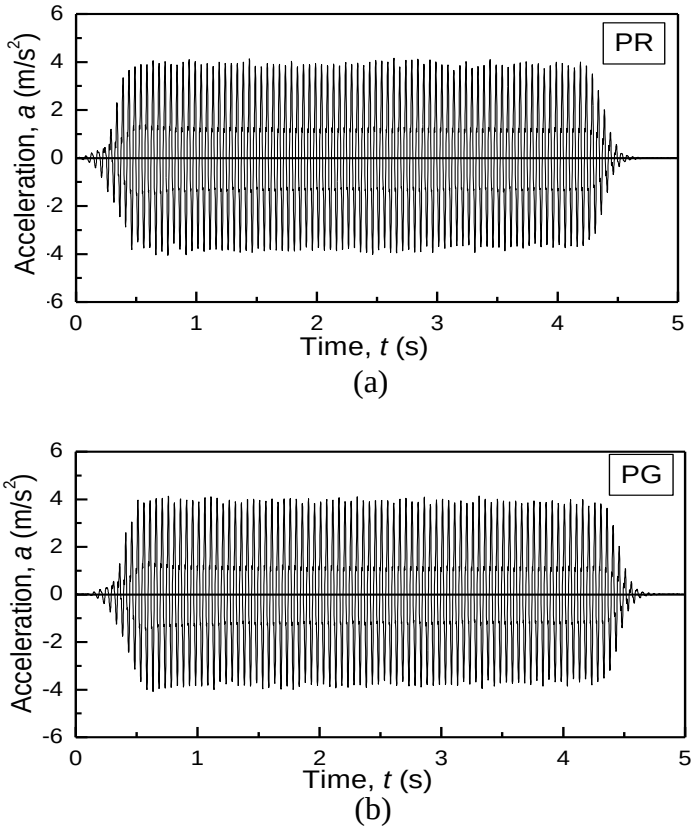

Figure 4.12 Input motion, measured at the bottom of the laminar box

(a) PR (b) PG.

Figure 4.13 (a) and (b) indicates the measured acceleration responses at the top of the raft and at the mid-height of the applied mass for PR and PG cases. The average responses of the raft and the mass have amplitude of 2 m/s^2 and they are

almost the same for PR test, which means that they behave as single mass. In contrast, the amplitude of the wave, measured at the mass is considerably smaller than that of the raft for PG test. It is interesting to note that the horizontal acceleration of the raft of PG attenuates with time after the peak acceleration is reached. Figure 4.14 shows the zoom in Figure 4.13 between 1.0 and 1.6 seconds. In this case, the responses of the mass and the raft can be seen in more detail. For PR model, the acceleration amplitudes of the raft and the mass are quite similar being about half of the input motion. For PG model, the acceleration response of the raft is about half of the input motion and twice of the mass amplitude.

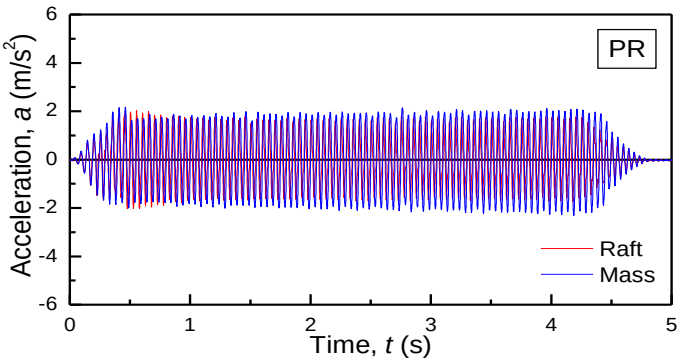

(a)

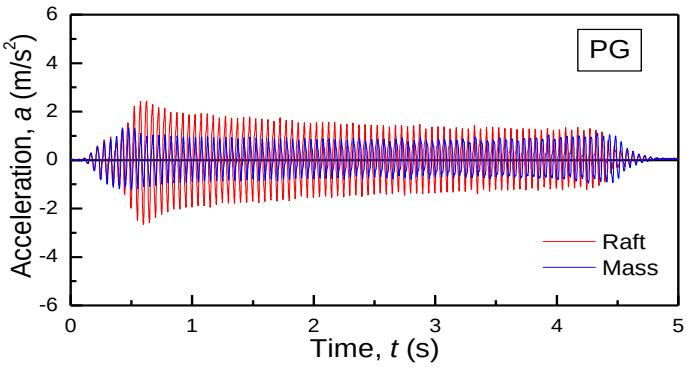

(b)

Figure 4.13 Acceleration responses measured at the raft and at the mid-height of the mass (a) PR (b) PG.

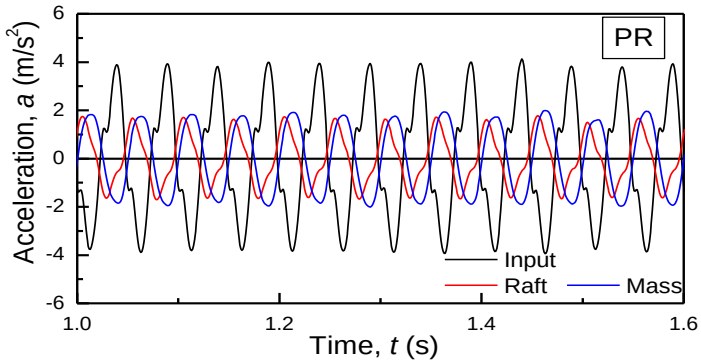

(a)

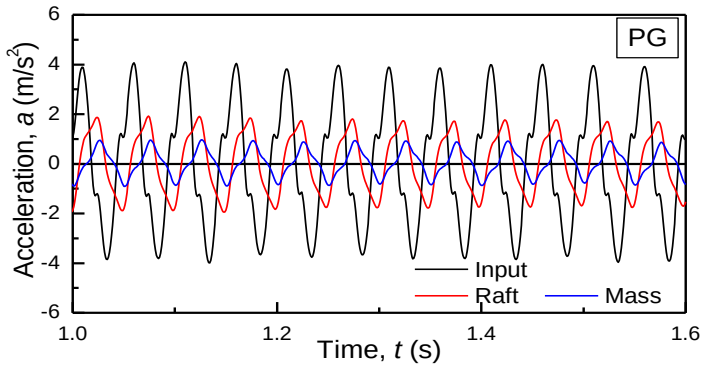

(b)

Figure 4.14 Zoom in acceleration response measured at the raft and at the mid-height of the mass with input motion (a) PR (b) PG.

Accelerometers, ACC4, ACC5, ACC9 and ACC10, were located at the same depth, z = 100 mm for PR and z = 80 mm for PG. However, ACC4 and ACC5 were located between the model piles and ACC9 and ACC10 were located at the outer sides of the piles (see Figure 4.10 and Figure 4.11). It can be said that, the magnitude of accelerations of the ground between the piles are smaller than those at the outside of the piles recalling that the soil sandwiched between the piles at the locations of ACC4 and ACC5 (Figure 4.15 and Figure 4.16).

The acceleration reaches to the highest value at the ground surface (at ACC 11 and ACC12), which is 50 % larger than the input motion accelerations as shown

in Figure 4.17 (a) and (b). Hence, it is seen that horizontal relative displacements between the ground and the raft in the case of PG is similar in the case of PR. This result suggests that the response acceleration of PR is not necessarily reduced compared to PG.

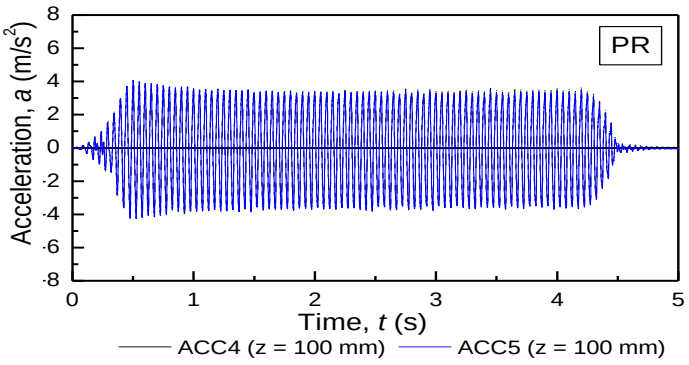

(a)

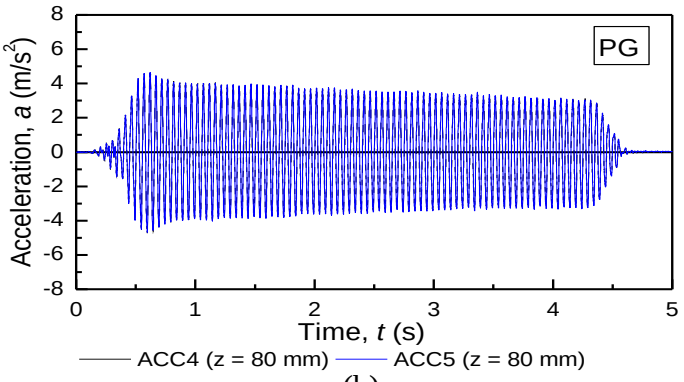

(b)

Figure 4.15 Measured accelerations at depth, z = 100 mm (or 80 mm), between the piles (a) PR (b) PG.

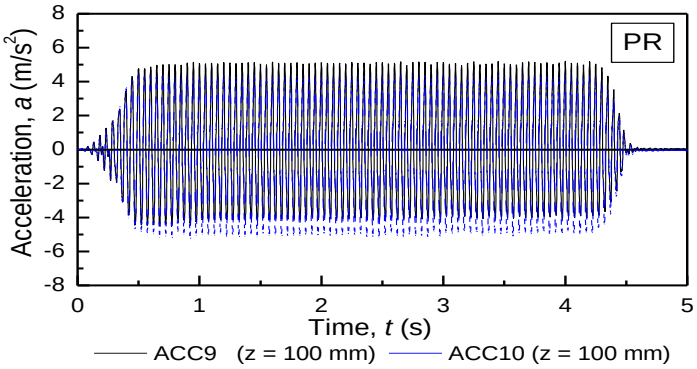

(a)

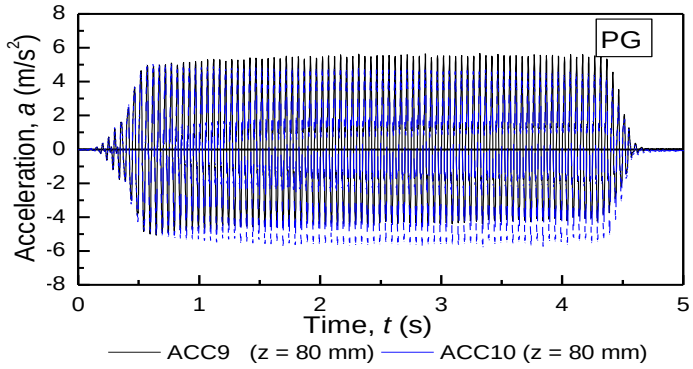

(b)

Figure 4.16 Measured accelerations at depth, z = 100 mm (or 80 mm), outside of the piles (a) PR (b) PG.

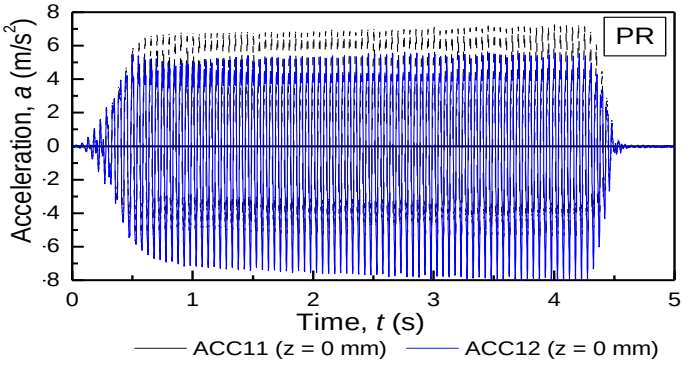

(a)

Figure 4.17 Measured accelerations at the ground surface (a) PR (b) PG.

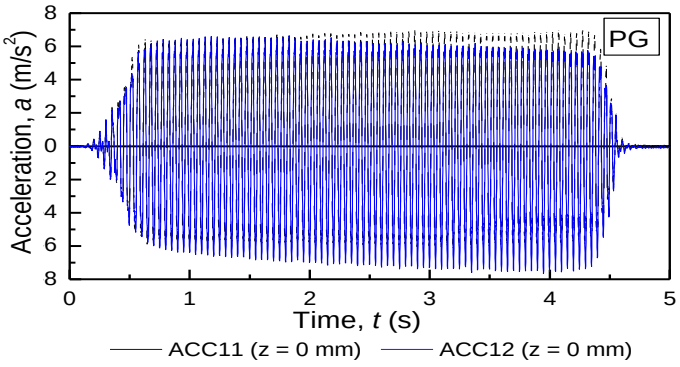

(b)

Figure 4.17 (continued).

The horizontal load-displacement behavior of the piled raft and pile group under the dynamic loading is given in Figure 4.18 (a) and (b), respectively. The horizontal load was calculated by multiplying the mass of the weight plates with the acceleration measured on the mass. Horizontal displacement was derived from measured acceleration on the raft. Maximum horizontal displacements of the raft for PR and PG are ± 0.1 mm and ± 0.15 mm, respectively, showing a superiority of PR for suppressing horizontal displacement over PG. It is seen from Figure 4.18 that the load-displacement relation is almost linear for the initial part of the response, where the amplitude of the acceleration increases to the steady value, thereafter the response becomes a steady loop for the steady sinusoidal input motion. Moreover, the maximum horizontal load on the PG model, i.e., without direct contact between raft and soil, is about 50 N, which is half of that of the PR model, i.e., where raft and soil are in contact, (110 N). Here again this behavior may be attributed to the fact that in PR model there is friction between raft and soil, whereas such force is missing in PG model.

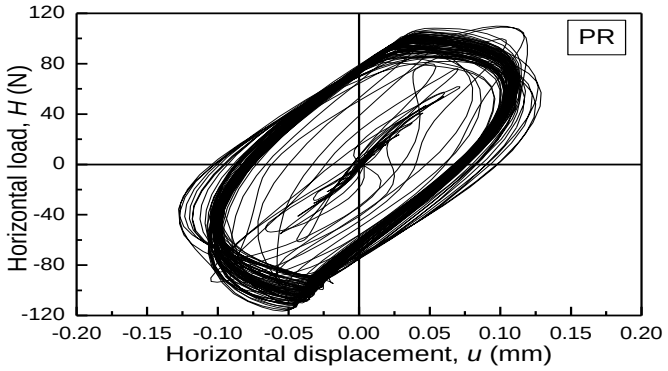

(a)

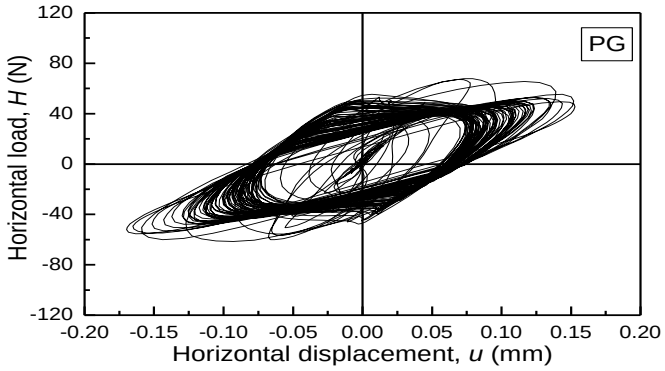

(b)

Figure 4.18 Horizontal load-displacement relationships (a) PR and (b) PG.

Figure 4.19 shows the horizontal load carried by each pile during dynamic loading. It is seen that the edge piles (P1 and P3) carry almost the same amount of horizontal load for both cases, while the center pile (P2) carries slightly larger load for PG case. Note that the total amount of load carried by PR is the double of the PG case, although the loads carried by piles are similar between PR and PG. This result shows that the raft base resistance is effectively mobilized in PR during dynamic loading.

Figure 4.20 indicates the vertical load sharing at each pile for PR and PG. It is seen that, in PR model, most of the axial load of 497 N is carried by 3 piles at negative displacements, and most of the load is carried by the raft in positive loading. This tendency is suggested to be due to the unplanned initial inclination of the raft at the initial phase of the test, following the vertical load application. Moreover, in PG case the axial load on each pile is larger than that of the piles of PR since the raft component does not have contribution on carried loads at PG case. Note that, the load carried by center pile, P2, is almost constant during shaking, regardless of magnitude of the horizontal displacement for both cases.

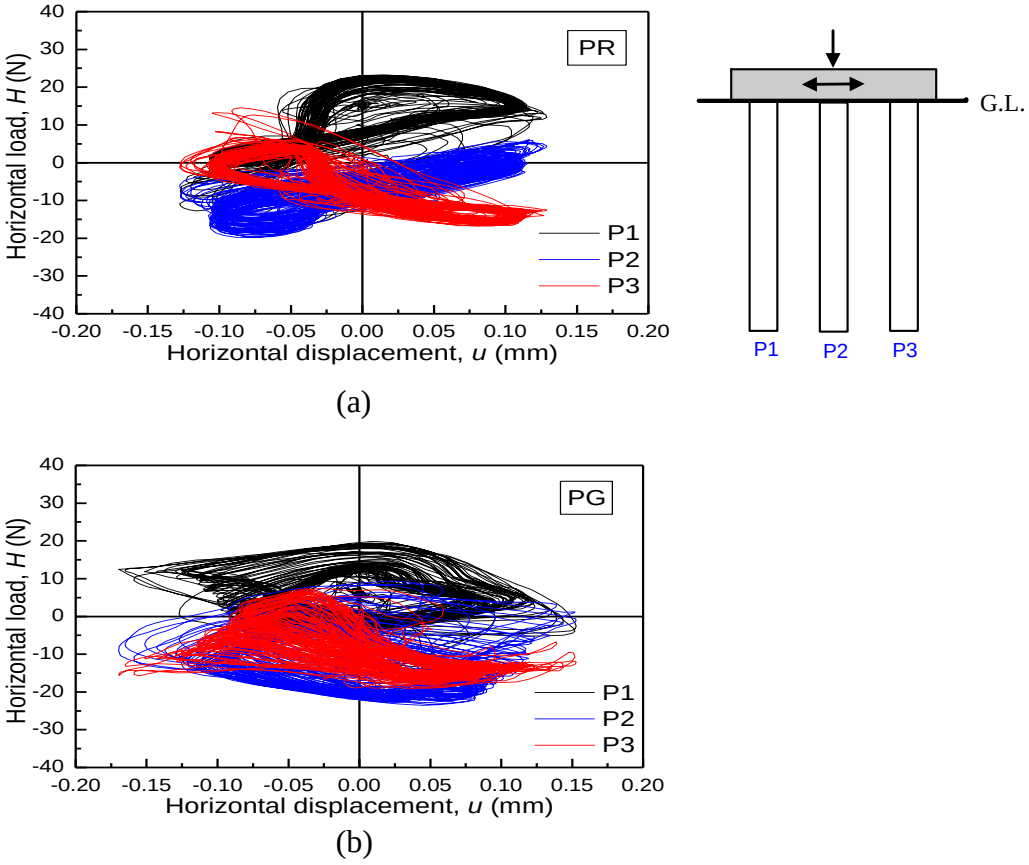

Figure 4.19 Horizontal load carried by each pile (a) PR and (b) PG.

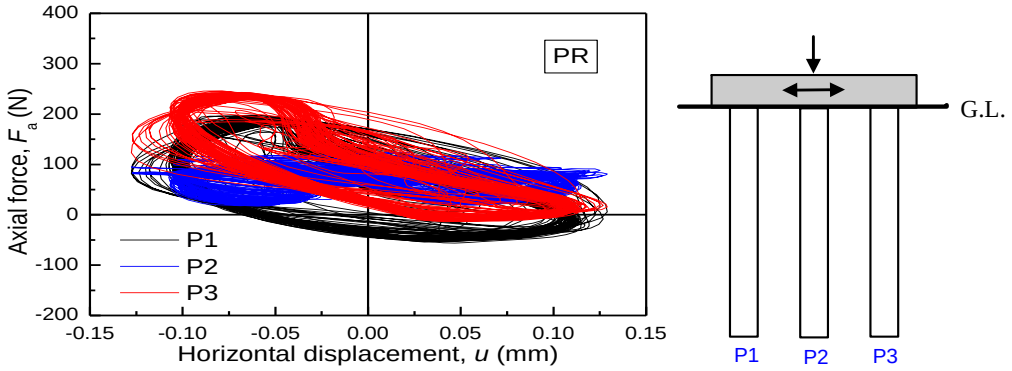

(a)

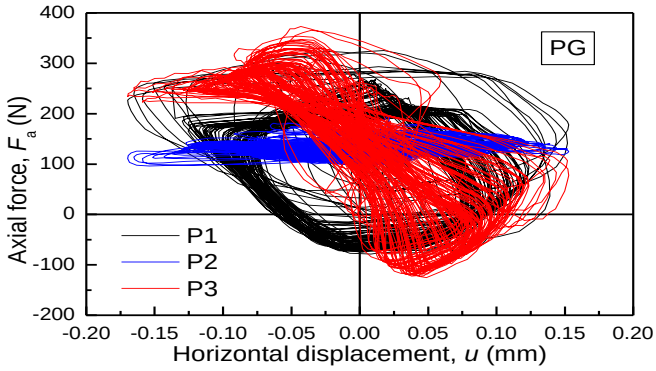

(b)

Figure 4.20 Vertical load carried by each pile (a) PR and (b) PG.

The settlements of the model foundations were measured at the top of raft by the help of two laser displacement transducers. Figure 4.21 shows the average of two measurements as the settlement of the raft during the shaking table tests for PR and PG. Before the input motion, there was a small settlement for both cases because of vertical loading. The initial settlement is slightly larger for PG test due to the space of 20 mm between the raft and the pile. After dynamic loading, the final settlement of the piled raft is about 9 mm, whereas it is measured as 17 mm for PG, which is almost double of PR. It can be said that, reducing the settlement amount is one of advantages of PR over PG which was also the case for static cyclic horizontal loading.

Figure 4.22 indicates the inclination of the raft during the shaking tests for PR and PG. As it is seen from the figure, the inclination of the rafts for both cases shows similar behavior and similar amount. However, the slope of the inclination for PG test is slightly steeper than PR. Note that, positive inclination means clockwise rotation (see Figure 4.22).

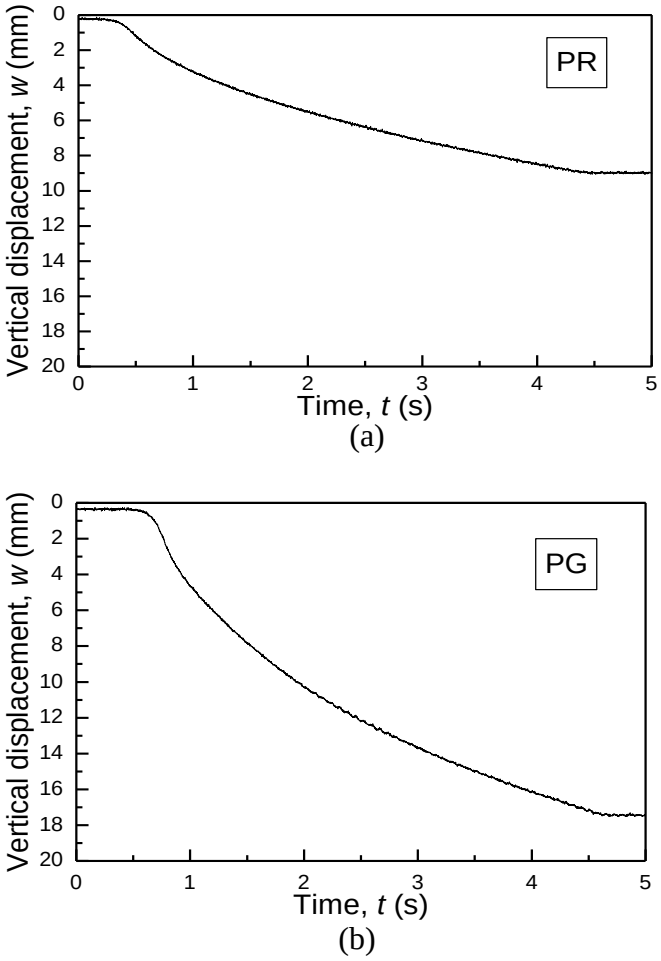

Figure 4.21 Vertical displacement of the raft for (a) PR and (b) PG.

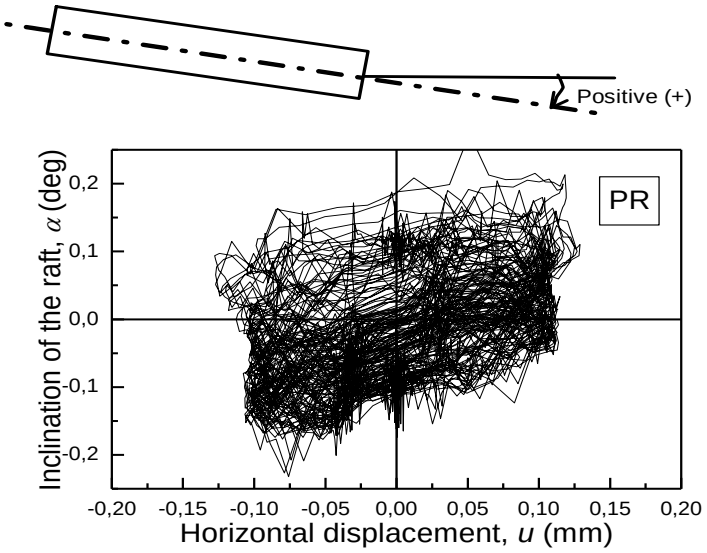

(a)

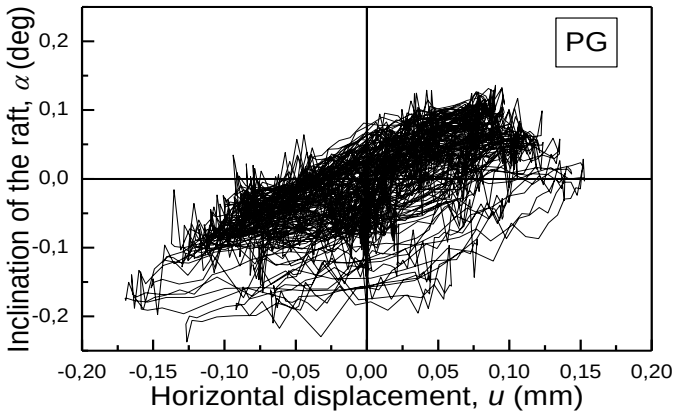

(b)

Figure 4.22 Inclination of the raft for (a) PR and (b) PG

Figure 4.23 shows the time history of the proportion of the horizontal load carried by 3 piles in PR model. Although it is not so stable, the trend is recognizable. It is seen that the percentage of horizontal load carried by 3 piles is between 20 % – 40 % of the total applied load. The proportion of vertical load carried by 3 piles is given in Figure 4.24. Before the input motion, 70 % of the total applied vertical load was carried by 3 piles, however after the shaking, vertical load sharing dropped to 50 % due to the contribution of the raft.

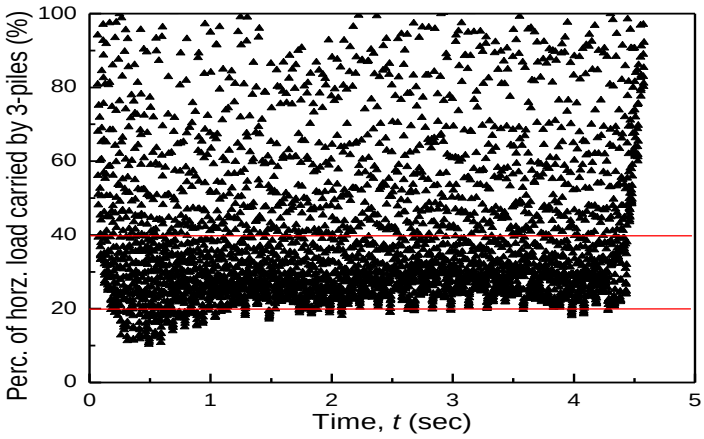

Figure 4.23 Percentage of horizontal load carried by 3 piles during shaking of PR.

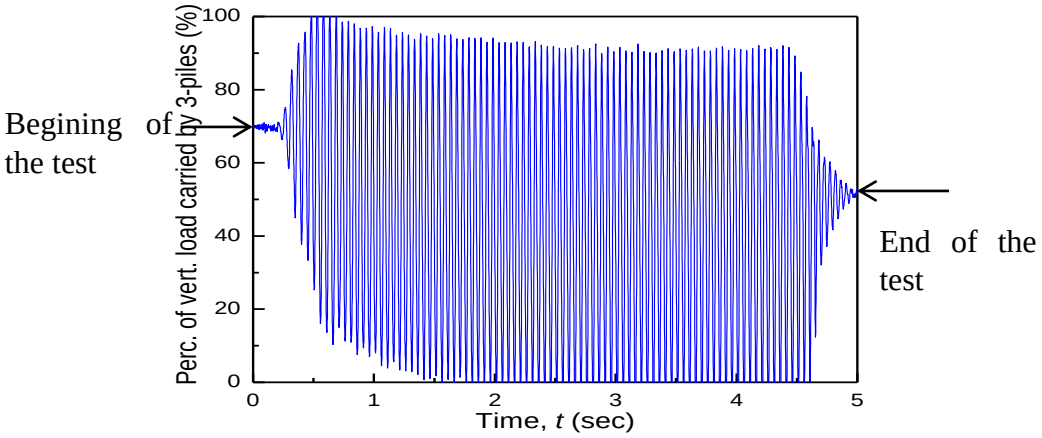

Figure 4.24 Percentage of vertical load carried by 3 piles during shaking of PR.

Figure 4.25 and Figure 4.26 show the bending moment, shear force and lateral ground resistance along the pile shaft on each pile when horizontal load is equal to ± 50 N for PR and PG models, respectively. Unfortunately, at PG model test results, distributions of P1 are not included in graphs due to the malfunction of the some strain gauges on that pile. It is seen that, for both models, positive and negative loading graphs are the reflection of each other as expected.

When bending moment graphs are investigated, it can be seen that the maximum bending moments occur at the top of the piles and they decrease with increasing depth for both PR and PG models. It can be inferred that the bending moments at the pile tips are nearly zero (Figure 4.25 (a) and Figure 4.26 (a)). It is seen from Figure 4.26 (a) that in case of PG, the bending moments decrease from the top to the tip monotonically without change of sign, whereas in PR, the bending moments of opposite sign are observed below specific depths (Figure 4.25 (a)).

From Figure 4.25 (b), it is seen that, shear forces are maximum at the top of the piles of PR due to the raft-soil contact. In contrast, the distributions of the shear forces are different for PG, where maximum shear force occurs at about mid depth of the pile (Figure 4.25 (b)). When Figure 4.25 (c) is investigated, it is seen that one of the strain gauge of P1 has abnormal behavior. If we ignore the response of P1, Figure 4.25 (c) shows that lateral ground resistance is larger at about mid-depth of the piles. On the other hand, for PG model, the lateral ground resistance has completely different response than that of PR (Figure 4.26 (c)).

Axial load distributions along the pile shaft are illustrated in Figure 4.27 for both cases. In PR model, most of the axial load of 497 N was carried by the raft at positive loading, and most of the axial load was carried by piles P1 and P3 at negative loading (Figure 4.27 (a)), which could be due to the slight inclination of the raft towards counter clockwise direction during vertical loading as an experimental error. As it is seen from Figure 4.27 (b), in PG model center pile carries almost same amount of load through the experiment, whereas the amount of load that carried by P3 increases at negative loading. Therefore, it can be said that P3 carries the largest portion of the vertical load at negative loading and P1 may carry the largest portion of the load at positive loading.

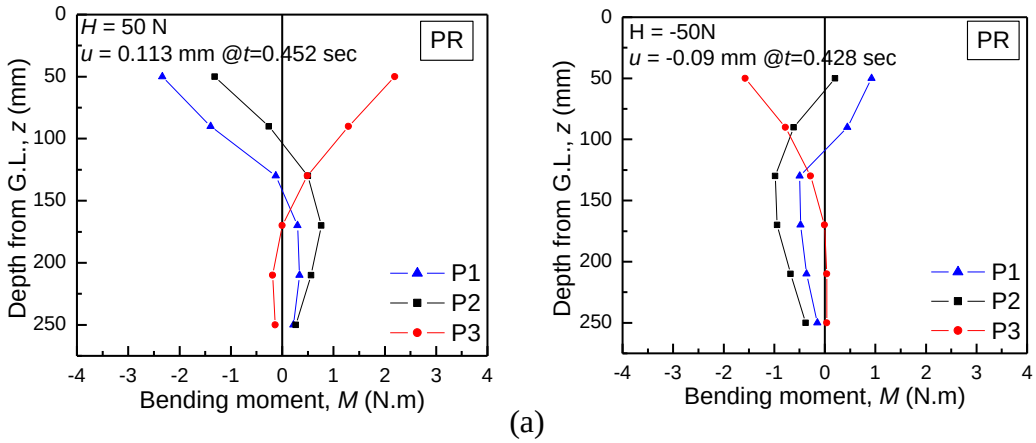

(a)

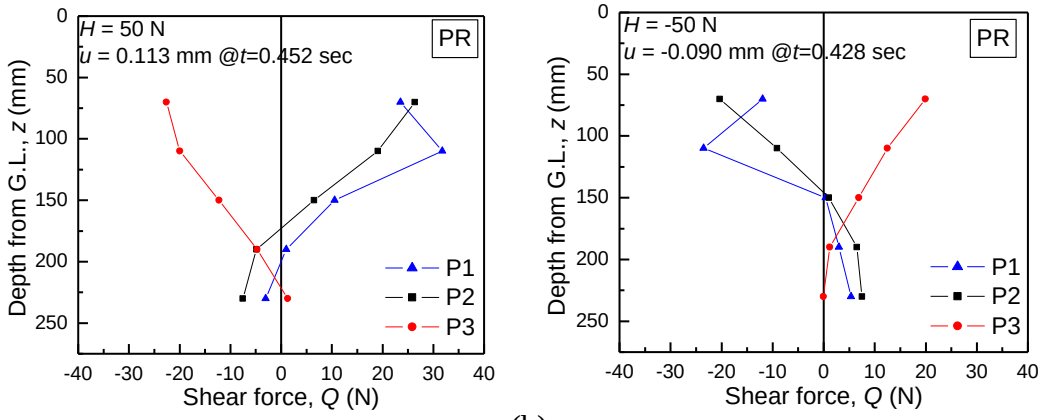

(b)

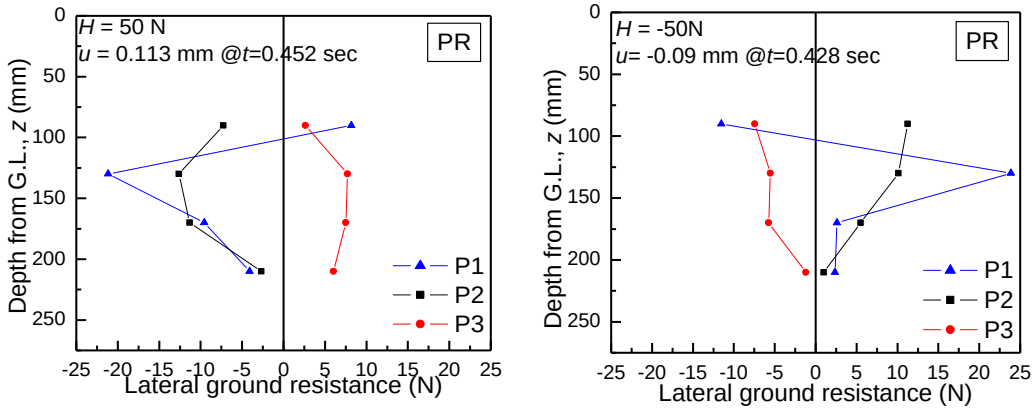

(c)

Figure 4.25 Distribution of (a) bending moment (b) shear force (c) lateral ground resistance along each pile shaft of PR, where $H = \pm$ 50 N.

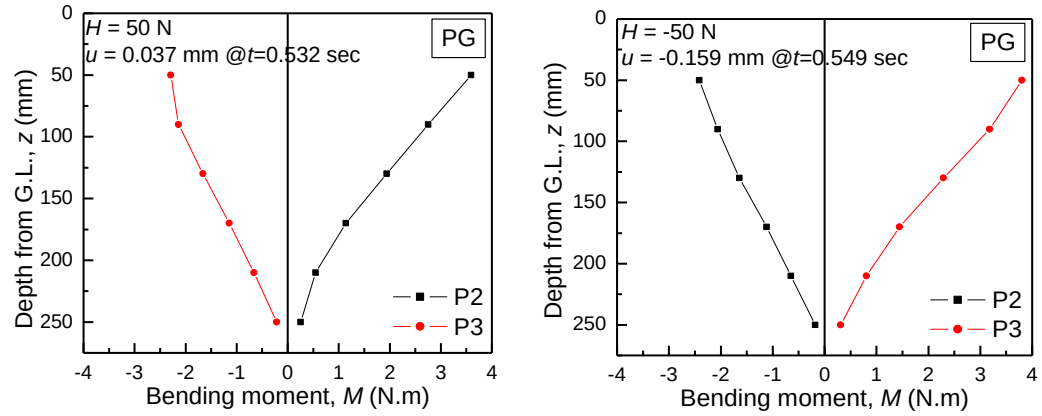

(a)

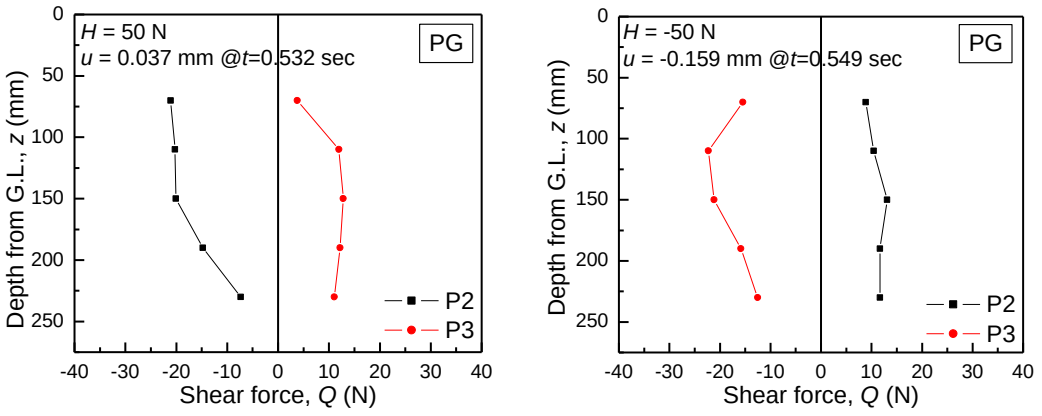

(b)

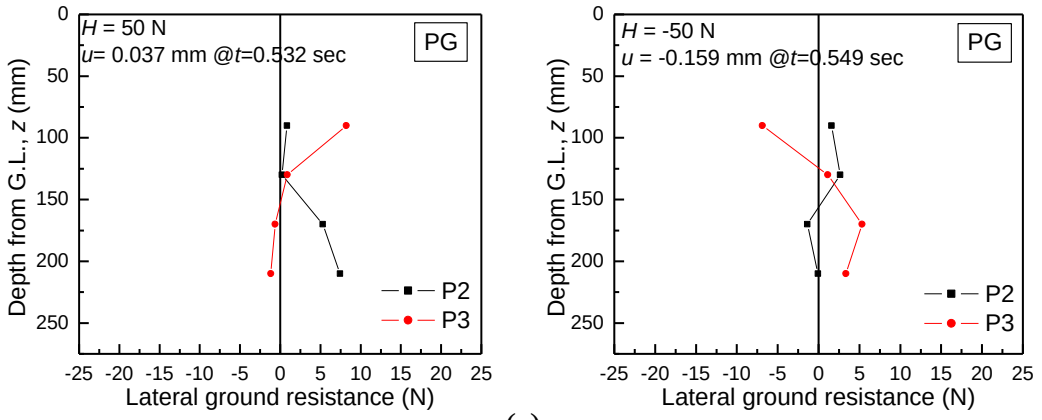

(c)

Figure 4.26 Distribution of (a) bending moment (b) shear force (c) lateral ground resistance along each pile shaft of PG, where $H = \pm 50$ N.

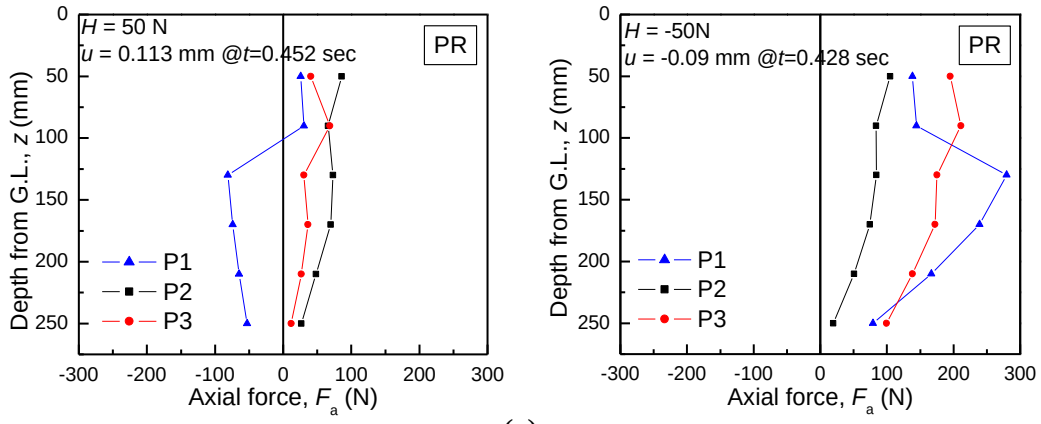

(a)

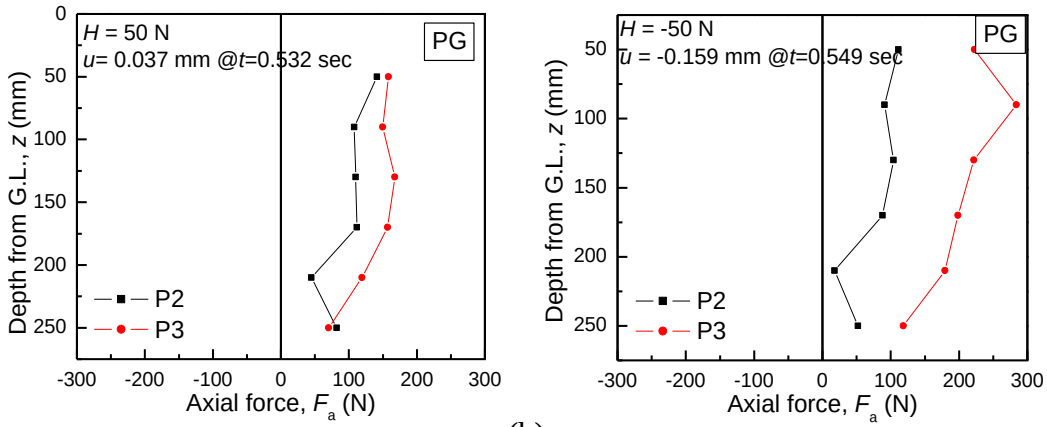

(b)

Figure 4.27 Distribution of axial force along each pile shaft of (a) PR and (b) PG, where $H = \pm 50$ N.

4.3.4 Full Raft (FR) model under a sinusoidal wave of 20 Hz frequency

Shaking table tests on a Full Raft (FR) model with two different vertical loadings were carried out to investigate the pile contribution and the vertical loading effect on the behavior of the raft model under dynamic horizontal loading. Test setup for FR model with 497 N vertical loading is illustrated in Figure 4.28. For FR with 198 N vertical loading test, the same test setup was used with two mass plates. Note that, vertical load was applied before applying dynamic load for both cases. The input motion was sinusoidal wave having a frequency of 20 Hz and nominal

amplitude of 0.07G, with number of cycles of loading, N_w, of 100, which was the same as those in piled raft and pile group dynamic experiments.

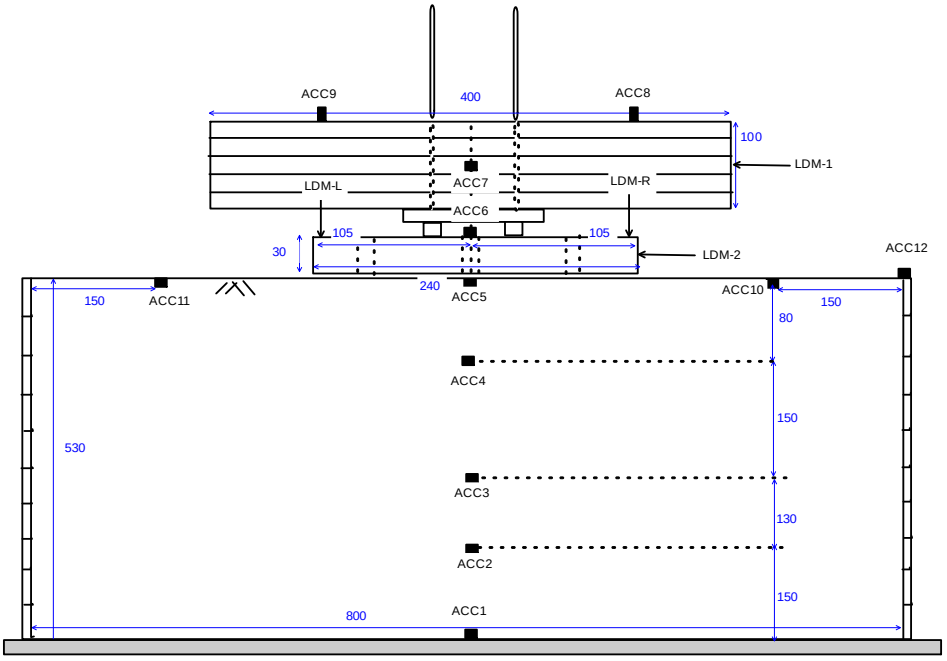

(a)

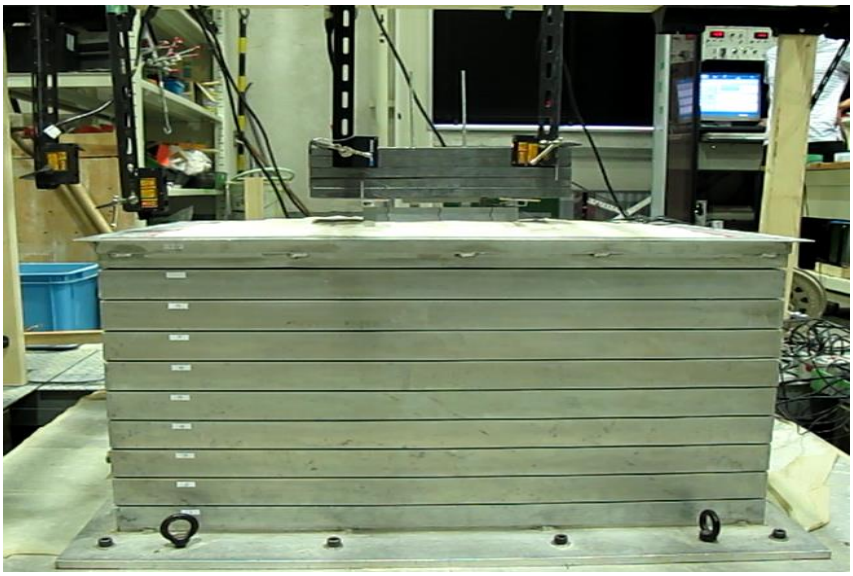

(b)

Figure 4.28 Test setup for FR model (a) drawing (b) photo of the experiment.

Test results:

Input motions of the full raft with two different vertical loadings are seen in Figure 4.29 (a) and (b). It is seen that the input motions are identical and the amplitude is 4 m/s^2. Note that, the input motion is also similar with that of the piled raft and pile group experiments (see Figure 4.12).

The response acceleration plots for the full raft with 497 N vertical loading (FR, V = 497 N) and the full raft with 198 N vertical loading (FR, V = 198 N) are given in Figure 4.30. FR, V = 497 N graph can be drawn until 2.8 sec since the raft overturned (failed) at that time of the experiment. Therefore, it could not possible to record all the response of FR, V = 497 N during the experiment. Zoom in version of Figure 4.30 is given in Figure 4.31 with input motion for more detail inspection of the raft and mass responses. When Figure 4.14 (a) and Figure 4.31 (a) are compared it is seen that, the behaviors of PR and FR are quite similar under same input excitation and same vertical load of 497 N. On the other hand, a comparison of Figure 4.31 (a) and Figure 4.31 (b) indicates that response of FR under a vertical load of 198 N is about twice larger than that of FR under 497 N vertical load, which emphasizes the effect of vertical loading during dynamic tests. In other words, the amount vertical load applied on the model may change the response of the model foundation under same dynamic loading.

Figure 4.32 illustrates the measured ground response of FR, V = 497 N and FR, V = 198 N cases. In Figure 4.32 (a), sharp change of the response at t = 2.8 s corresponds to the time of failure which caused malfunctioning of the accelerometers located at the surface of the soil. Overall, the ground responses of two cases are similar.

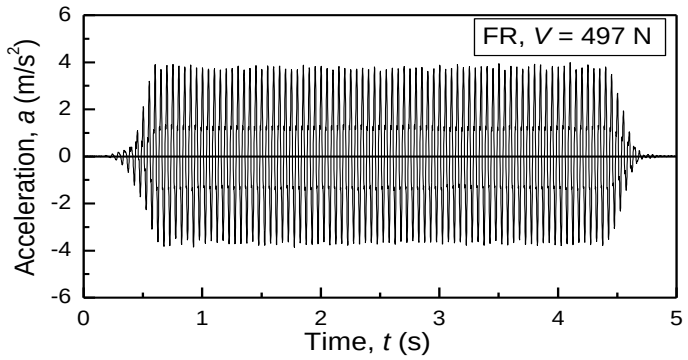

(a)

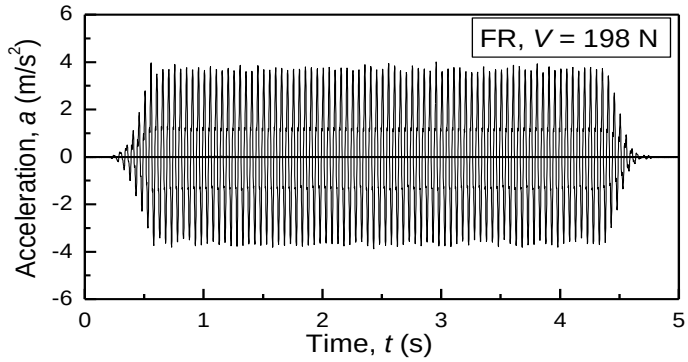

(b)

Figure 4.29 Input motion measured at the bottom of the laminar box (a) FR, V = 497 N (b) FR, V = 198 N.

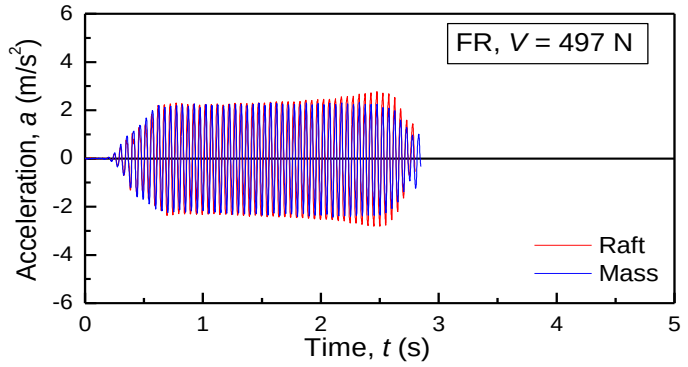

(a)

Figure 4.30 Acceleration responses measured at the raft and at the mid-height of the mass (a) FR, V = 497 N (b) FR, V = 198 N.

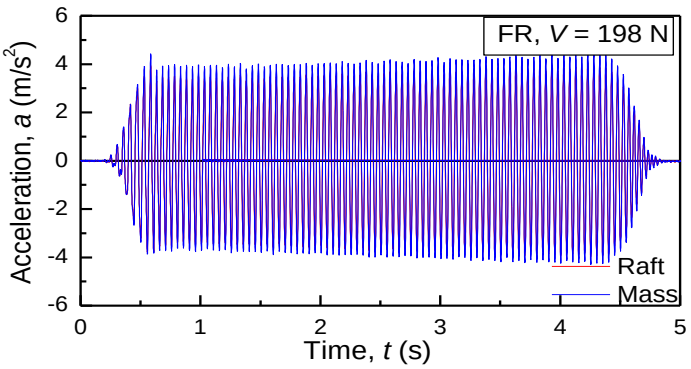

(b)

Figure 4.30 (continued).

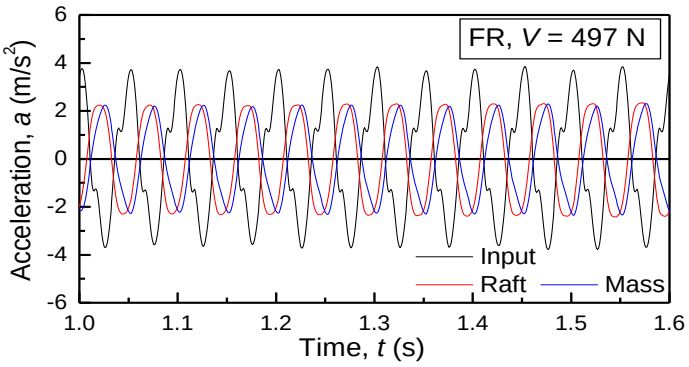

(a)

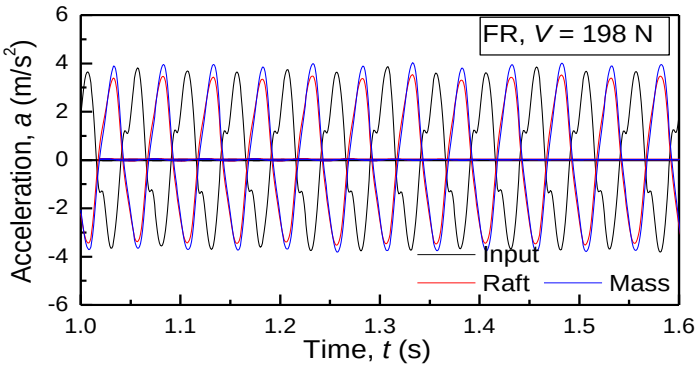

(b)

Figure 4.31 Zoom in acceleration response measured at the raft and at the mid-height of the mass with input motion (a) FR, V = 497 N (b) FR, V = 198 N.

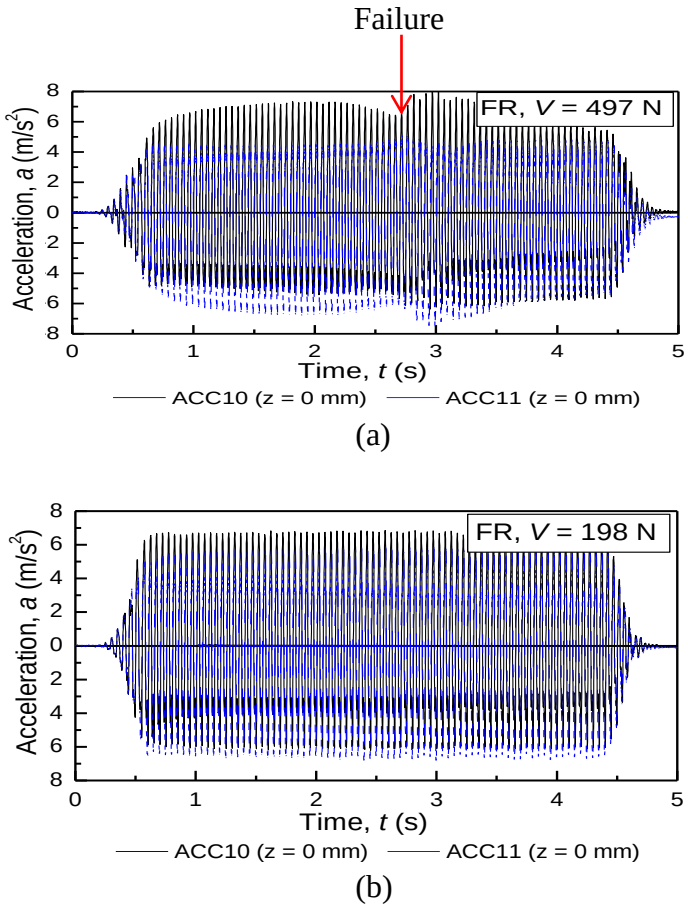

Figure 4.32 Measured accelerations at the ground surface

(a) FR, V = 497 N (b) FR, V = 198 N.

Horizontal load vs. displacement relationships of FR, V = 497 N and FR, V = 198 N are given in Figure 4.33 (a) and (b), respectively. It is seen that FR, V = 497 N model carries 1.5 times more load than the FR, V = 198 N model, although the mass on FR, V = 497 N is 2.5 times larger than that of FR, V = 198 N. Moreover, the energy absorption during the dynamic loading of FR, V = 198 N model is considerably less than that of the FR, V = 497 N model which is visible from the loop areas given in Figure 4.33 (a) and (b). This may be a factor causing larger acceleration response of the FR, V = 198 N model.

When the hysteresis loop of FR, V = 497 N is compared with that of PR, it is noted that the initial stiffness of the PR is larger than that of the full raft (see Figure 4.18 (a) and Figure 4.33 (a)). Moreover, the displacement of FR, V = 497 N (± 0.18 mm) is larger than the displacement of PR (± 0.13). In other words, PR model experiences smaller horizontal displacements than FR indicating the effect of piles under the raft.

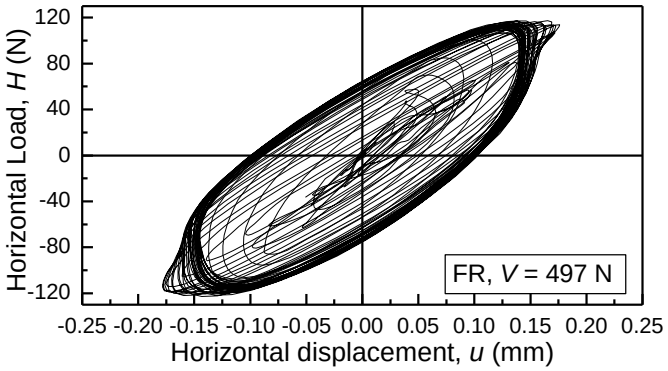

(a)

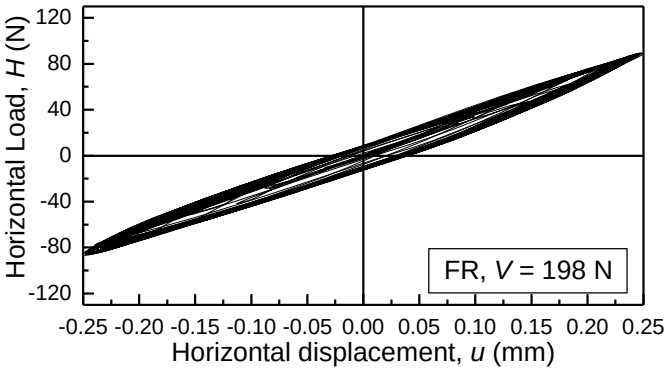

(b)

Figure 4.33 Horizontal load-displacement relationship of (a) FR, V = 497 N (b) FR, V = 198 N.

The vertical settlement and the inclination of the FR, V = 198 N model are given in Figure 4.34 and Figure 4.35, respectively. Unfortunately, the results for FR, V = 497 N model cannot be drawn because of the experimental errors of vertical laser

transducers. Before applying dynamic load, the raft settles about 3 mm due to the applied vertical load, which is larger than that of the PR, in spite of the fact that the applied load was rather small as compared to PR. The final settlement of the FR, V = 198 N is 6 mm and the inclination of the raft is between -0.10^0 to -0.45^0, which may be due to the unintended inclination of the raft in counter clockwise direction that might occur after applying the vertical load.

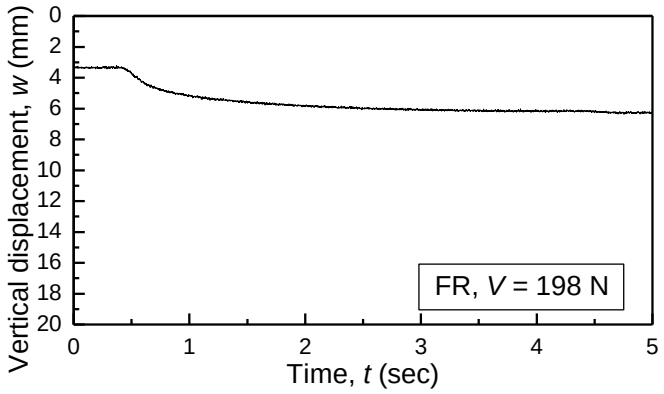

Figure 4.34 Settlement of full raft with 198 N vertical loading (FR, V = 198 N).

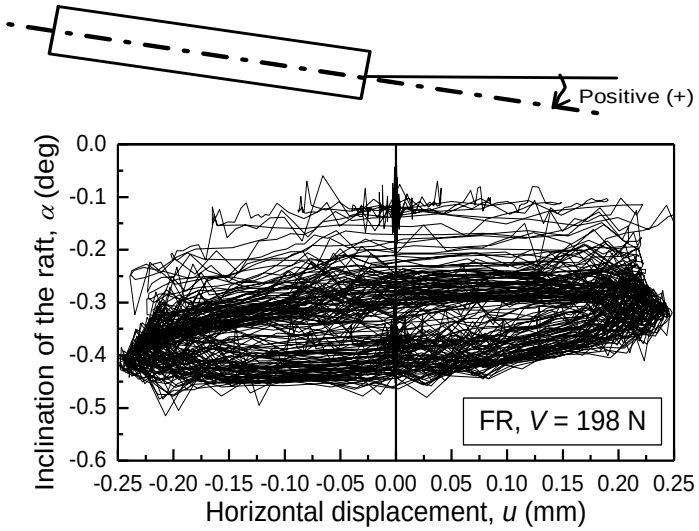

Figure 4.35 Inclination of full raft with 198 N vertical loading (FR, V = 198 N).

4.3.5 Piled raft (PR) model under a sinusoidal wave of 5 Hz frequency

In this part, the results of Piled Raft (PR) under 5 Hz harmonic horizontal loading with nominal amplitude of 0.07G are presented which are used to investigate the pile response under low frequencies. The results are also compared with the previous static cyclic horizontal load test results. Test set-up for this experiment was the same as the experiment on PR with 20 Hz frequency (see Figure 4.10). Note that, 497 N vertical load was also applied for this case before applying dynamic load (shaking) to compare the results without considering the change of vertical load. Test was terminated at number of cycles of loading, $N_w = 100$.

Test results:

Figure 4.36 shows the input motion of the experiment, measured at the bottom of the laminar box. As it is seen from the figure, the amplitude of the input acceleration is 5.5 m/s^2, which is more than that of 20 Hz frequency test (which was 4.0 m/s^2), although the same nominal amplitude, 0.07G, was entered (see Figure 4.12 (a)).

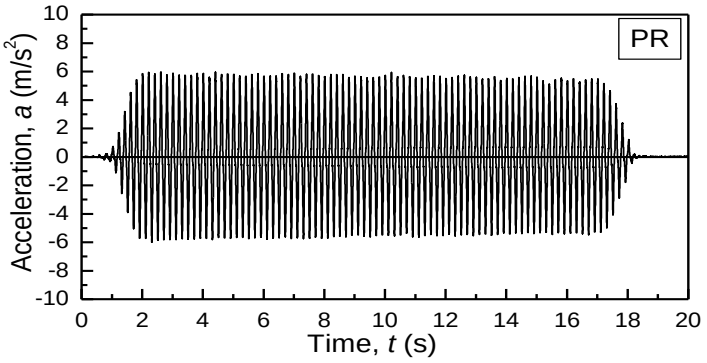

Figure 4.36 Input motion measured at the bottom of the laminar box for PR-5 Hz.

The response accelerations at the raft and at the mid- height of the mass are shown in Figure 4.37. It is observed that the response accelerations are not constant and increase slightly from the beginning to the end of the test. On the contrary to the 20 Hz test results of PR (PR-20 Hz), the amplitude of the input acceleration increases on the model foundation. This behavior can be observed in more detail in Figure 4.38 (a), which zooms in Figure 4.37 to consider only one second of the experiment in detail. It is seen that, the measured acceleration on the mass and the raft are almost same, which are 33 % larger than the amplitude of the input motion, while the response of the mass and the raft of PR-20Hz test is 50 % smaller than the amplitude of the input motion (see Figure 4.14a). Moreover, it can be said that the mass and the raft behave in unison in both PR tests.

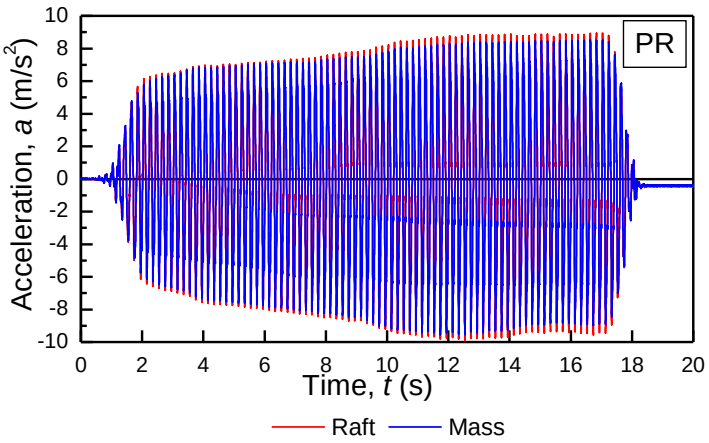

Figure 4.37 Acceleration responses measured at the raft and at the mid-height of the mass for PR-5 Hz.

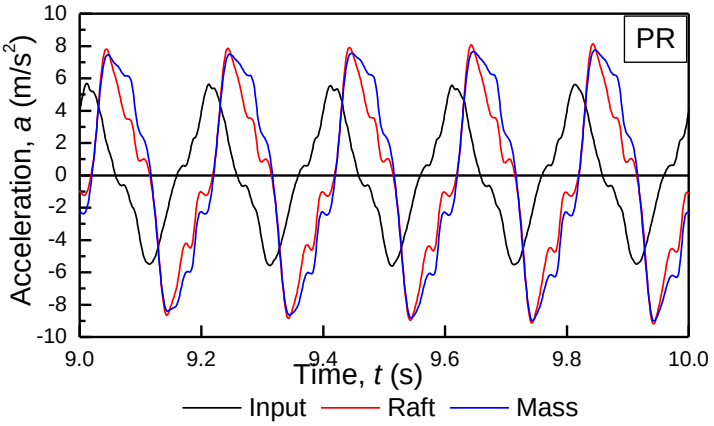

Figure 4.38 Zoom in acceleration response measured at the raft and at the mid-height of the mass with input motion for PR-5 Hz.

Accelerometers, ACC4 and ACC5, were located at a depth, z = 100 mm, between the model piles, and ACC9 and ACC10 were located at the same depth, outside of the (see Figure 4.10). It is seen that the acceleration responses measured by ACC4 and ACC5 are almost the same with the acceleration measured on the model foundation (see Figure 4.37 and Figure 4.39). On the contrary to ACC4 and ACC5, accelerations measured at ACC9 and ACC10 are more stable, which has average amplitude of 6.5 m/s^2, slightly larger than the amplitude of the input motion (see Figure 4.36 and Figure 4.40). It is reasonable since the inner accelerometers are affected more from the foundation behavior compared to the outer ones.

At the ground surface, the acceleration is almost constant and has average amplitude of 8.5 m/s^2 (Figure 4.41), which is larger than the amplitude of accelerations measured at ACC9 and ACC10, located at lower depth.

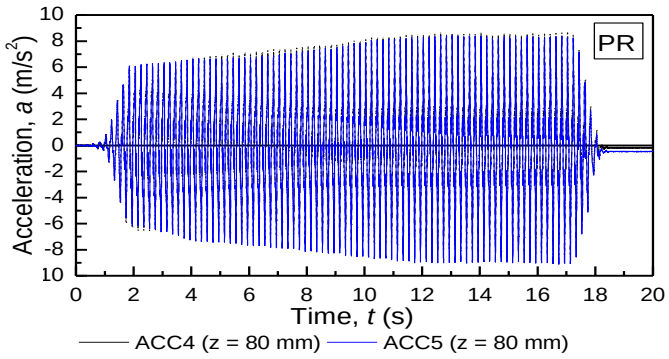

Figure 4.39 Measured acceleration at depth, z = 100 mm, between the piles for PR-5 Hz.

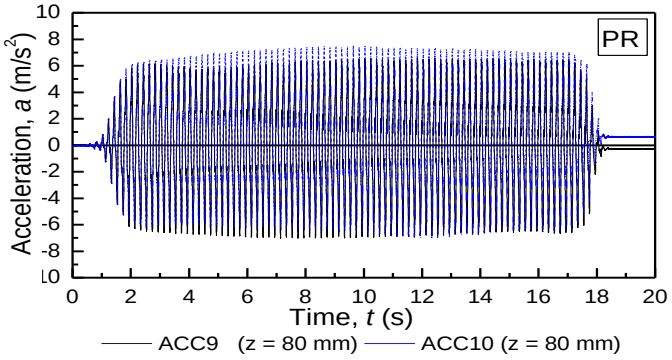

Figure 4.40 Measured acceleration at depth, z = 100 mm, outside of the piles for PR-5 Hz.

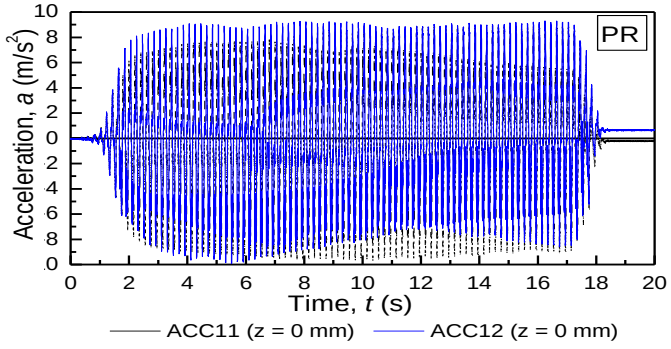

Figure 4.41 Measured acceleration at the ground surface for PR-5 Hz.

Figure 4.42 shows horizontal load vs. normalized horizontal displacement of the piled raft model under 5 Hz frequency. It is observed that, horizontal load carried by the PR model is about four times larger than that of the higher frequency test of PR (see Figure 4.18 (a)). This result clearly indicates that the natural (resonant) frequency of the ground-foundation-superstructure system dominates the response of the whole structure system. It is seen that, the natural frequency of the whole structure system was different than the resonant frequency of the green field, which was estimated as 20 Hz. Dynamic FEM analysis of the whole structure system would be beneficial for estimating its natural frequency in future. Also, horizontal displacement of the model is comparable with the static cyclic horizontal load test results rather than 20 Hz shaking table test results.

Horizontal load sharing of piles of the PR model is given in Figure 4.43, where front pile carries more load than other two piles (pile P3 in positive loading and pile P1 at negative loading). Note that, the horizontal load carried by the middle pile P2 is almost unchanged during the experiment. When axial load at each pile is examined (Figure 4.44), it is seen that 3 piles carry almost the same amount of load during dynamic loading.

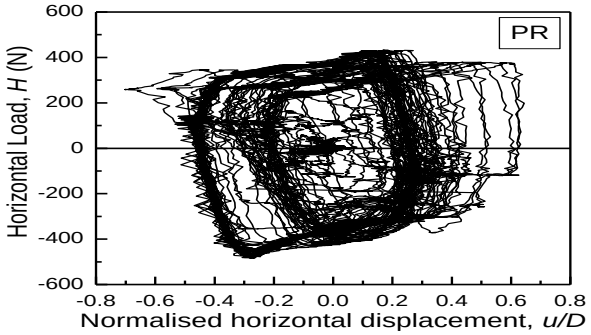

Figure 4.42 Horizontal load-normalized horizontal displacement relationship of PR -5 Hz.

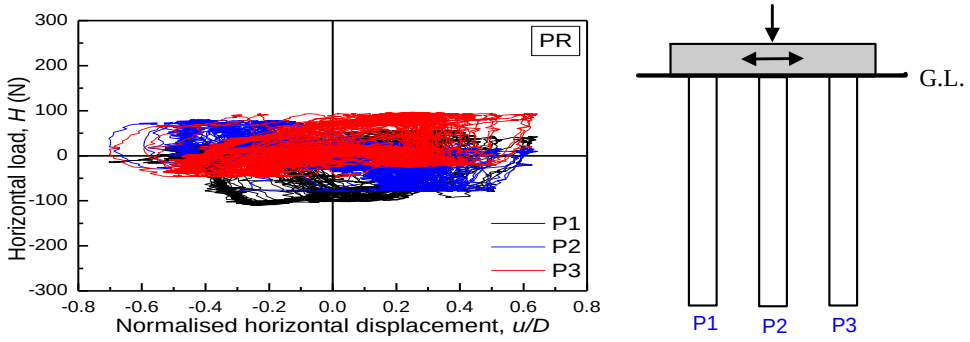

Figure 4.43 Horizontal load carried by each pile for PR-5 Hz.

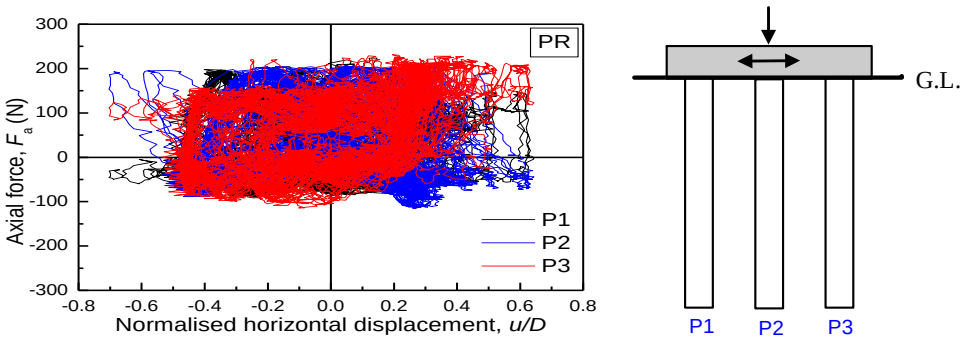

Figure 4.44 Axial force carried by each pile for PR-5 Hz.

Settlement of the piled raft during the test could be measured for first two seconds of the experiment due the limitations of laser displacement transducers (which are 30 mm) (Figure 4.45). It is seen that the foundation has a sudden settlement with the starting of the shaking test and reaches to 30 mm settlement. The inclination of the raft is between 2.5^0 to - 1.0^0 for the first two seconds, which is significantly larger than that of PR-20 Hz (Figure 4.46).

The percentage of horizontal load and vertical load carried by 3 piles are given in Figure 4.47 and Figure 4.48, respectively. From both graphs, it is seen that the load carried by 3 piles decreases drastically at the end of the test. The results of Figure 4.47 and Figure 4.48 clearly show the advantages of the piled raft

foundation. The reduction of the horizontal and vertical resistances of the piles at large deformations is compensated by the raft resistance, preventing the sudden collapse of the foundation.

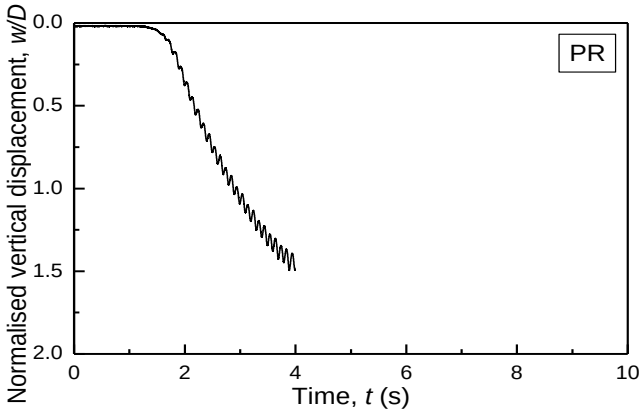

Figure 4.45 Settlement of the raft for PR-5 Hz.

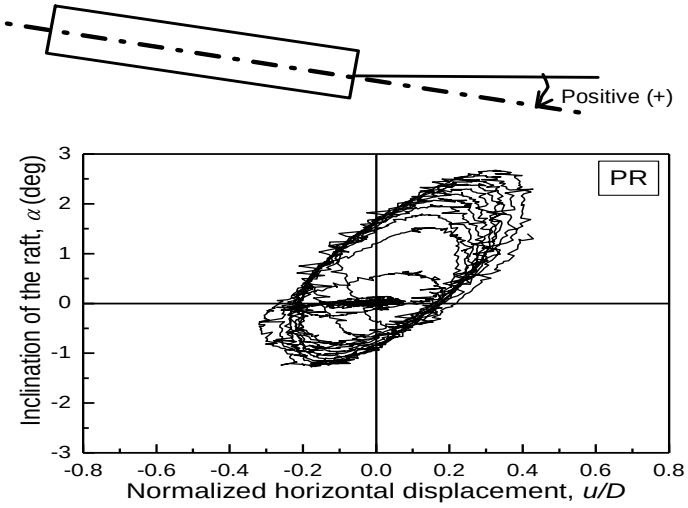

Figure 4.46 Inclination of the raft for PR-5 Hz.

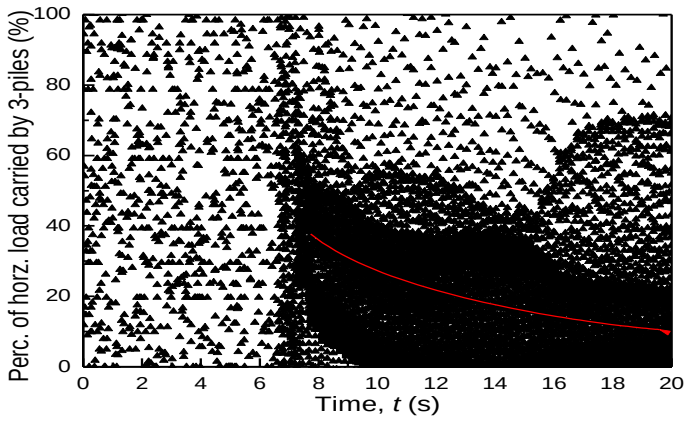

Figure 4.47 Percentage of horizontal load carried by 3 piles for PR-5 Hz.

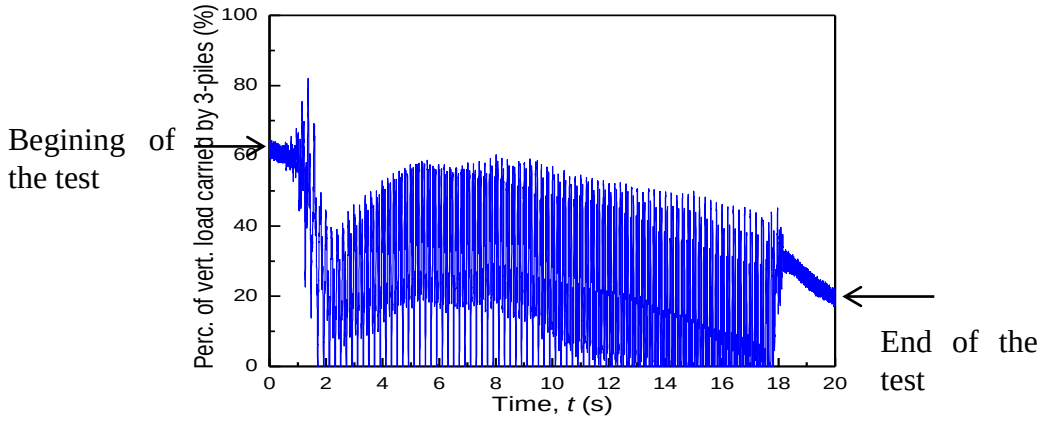

Figure 4.48 Percentage of vertical load carried by 3 piles for PR-5 Hz.

Bending moment and shear force distributions of each pile along the pile shaft for horizontal loads of ± 50 N are given in Figure 4.49. It is seen that, most of the horizontal load and shear force are carried by pile P3, independent of the loading direction. This may be due to the inclination of the raft towards the right direction prior to dynamic loading. It is also seen that bending moments on middle pile P2 is relatively smaller than the edge piles. Bending moments on the edge piles have the largest value at the top of the pile, and they decreases along the pile shaft until 40 % of the pile length. After that point, bending moment on P3 starts to increase

at reverse direction until it reaches its maximum value at 65 % depth of the pile. Figure 4.49 (b) shows that shear forces are larger in the edge piles, which become maximum at the pile top and become zero at about 60 % of the pile length.

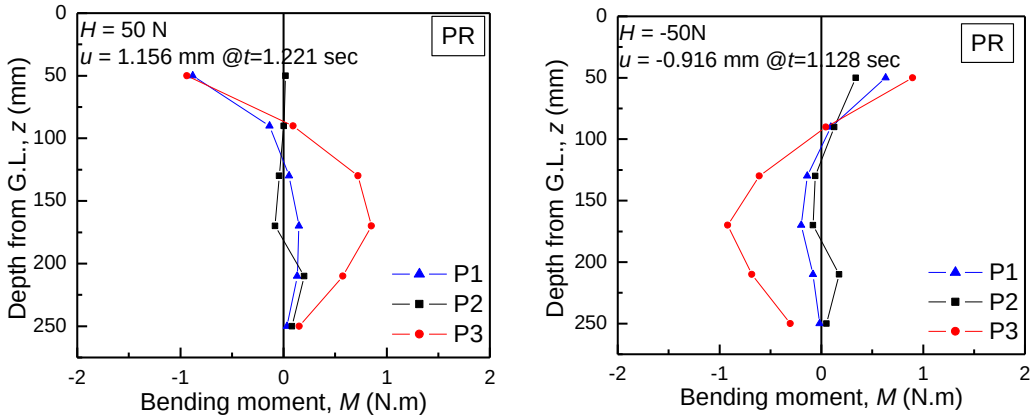

(a)

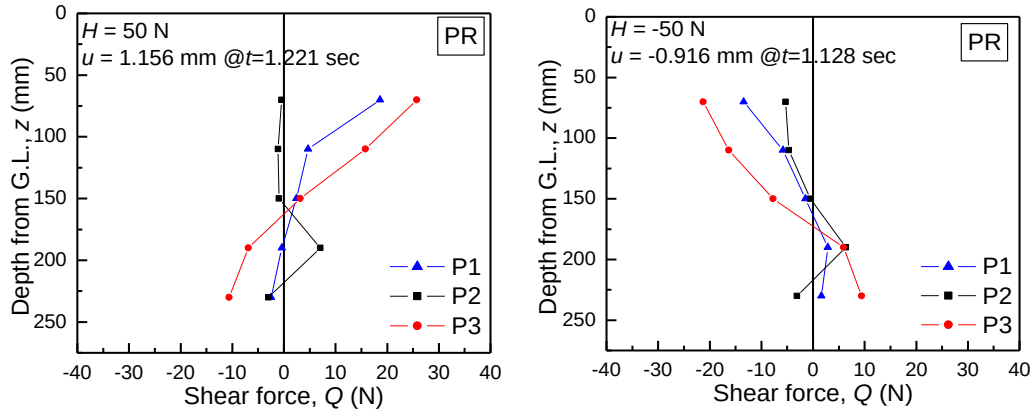

(b)

Figure 4.49 Distribution of (a) bending moment (b) shear force along each pile shaft of PR - 5 Hz frequency test, where $H = \pm 50$ N.

Axial force distributions of each pile along the pile length for ± 50 N horizontal loads are illustrated in Figure 4.50. It is seen that, most of the axial load is carried by the front piles (which is P3 in positive loading and P1 in negative loading). The center pile P2 carries almost the same load regardless of the load direction.

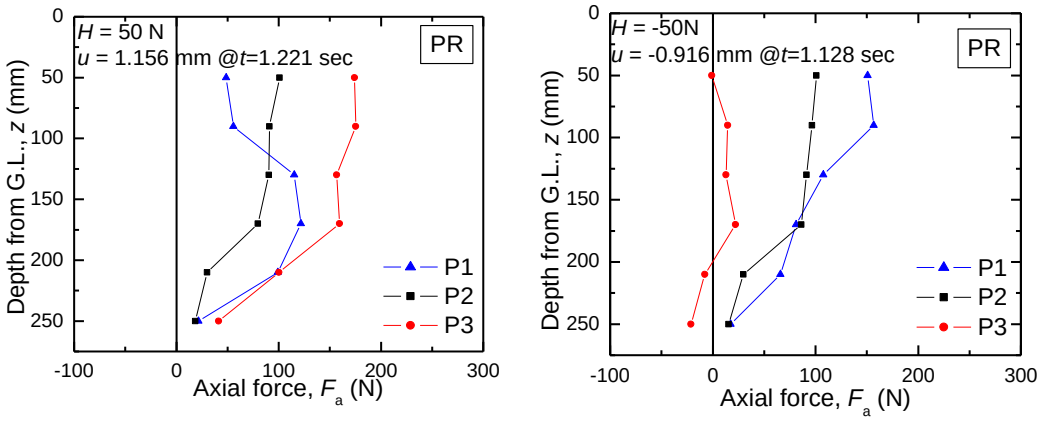

Figure 4.50 Distribution of axial force along each pile shaft of PR - 5 Hz frequency test, where $H = \pm 50$ N.

4.3.6 Comparison of PR model responses under static cyclic horizontal load test and dynamic test with a sinusoidal wave of 5 Hz frequency

In this part of the chapter, PR model responses under static cyclic horizontal load test and 5 Hz frequency dynamic load test are compared. Both dynamic and static test responses show hysteretic behavior (Figure 4.51). Although, normalized horizontal displacements are similar, initial stiffness of the dynamic test response is slightly smaller than that of static cyclic test response. When the horizontal load and the pile resistance obtained from shaking table test and static cyclic test are compared, the difference between the total horizontal load and pile resistance points out the contribution of the raft base for both cases (see Figure 4.52).

Vertical loads carried by 3 piles are shown in Figure 4.53. From the graph, it can be said that 3 piles carry 30 % more load in average in the static cyclic test compared to the dynamic test. The inclinations of the raft during static cyclic horizontal loading and dynamic loading are compared in Figure 4.54. It is seen that two cases show similar inclinations of the raft.

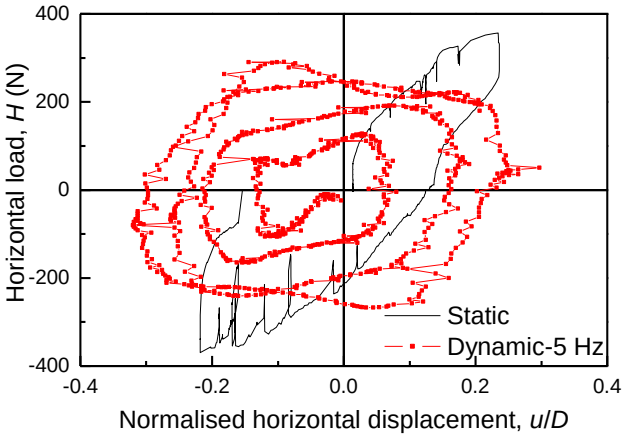

Figure 4.51 Comparison of total horizontal load on PR between 5 Hz frequency dynamic test and static cyclic test.

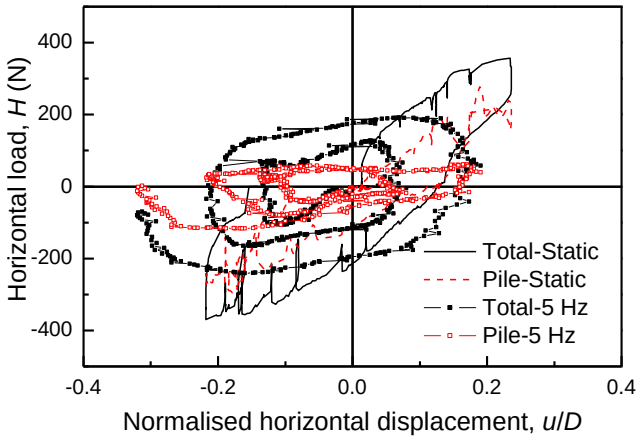

Figure 4.52 Comparison of horizontal load carried by 3 piles between 5 Hz frequency dynamic test and static cyclic test.

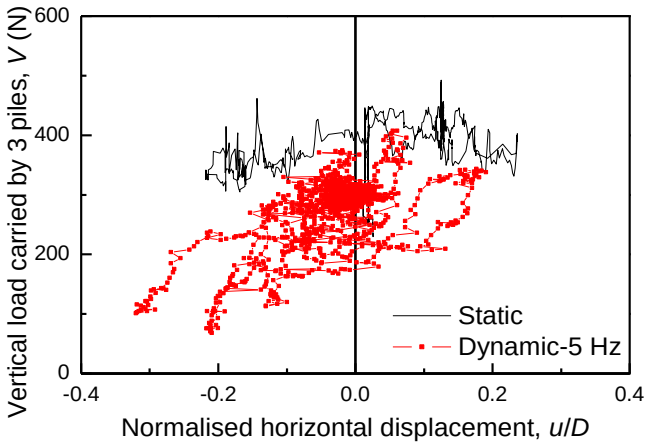

Figure 4.53 Comparison of vertical load carried by 3 piles between 5 Hz frequency dynamic test and static cyclic test.

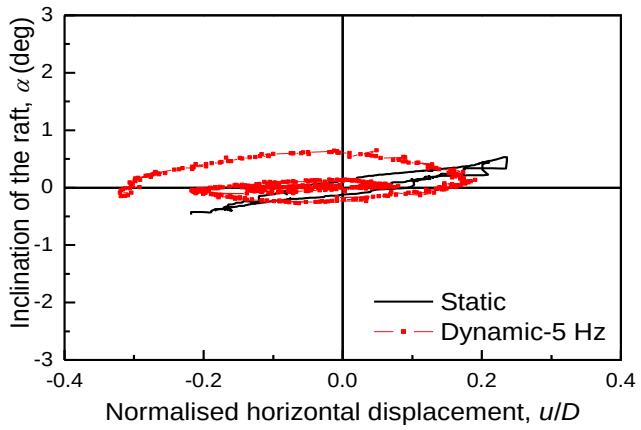

Figure 4.54 Comparison of inclination of the raft between 5 Hz frequency dynamic test and static cyclic test.

The distribution of bending moments, shear forces, lateral ground reactions and axial loads along the pile shaft obtained from static cyclic load test and shaking table test are compared in Figure 4.55. It is seen that the responses in the static cyclic and dynamic tests are comparable. The differences between the two tests are in reasonable range for all distributions.

In overall, static and dynamic responses are found to be similar which can be explained as the inertia force of the mass of the foundation is predominant and kinematic effect (soil displacement) on the foundation behavior would have been negligible in dynamic tests with 5 Hz.

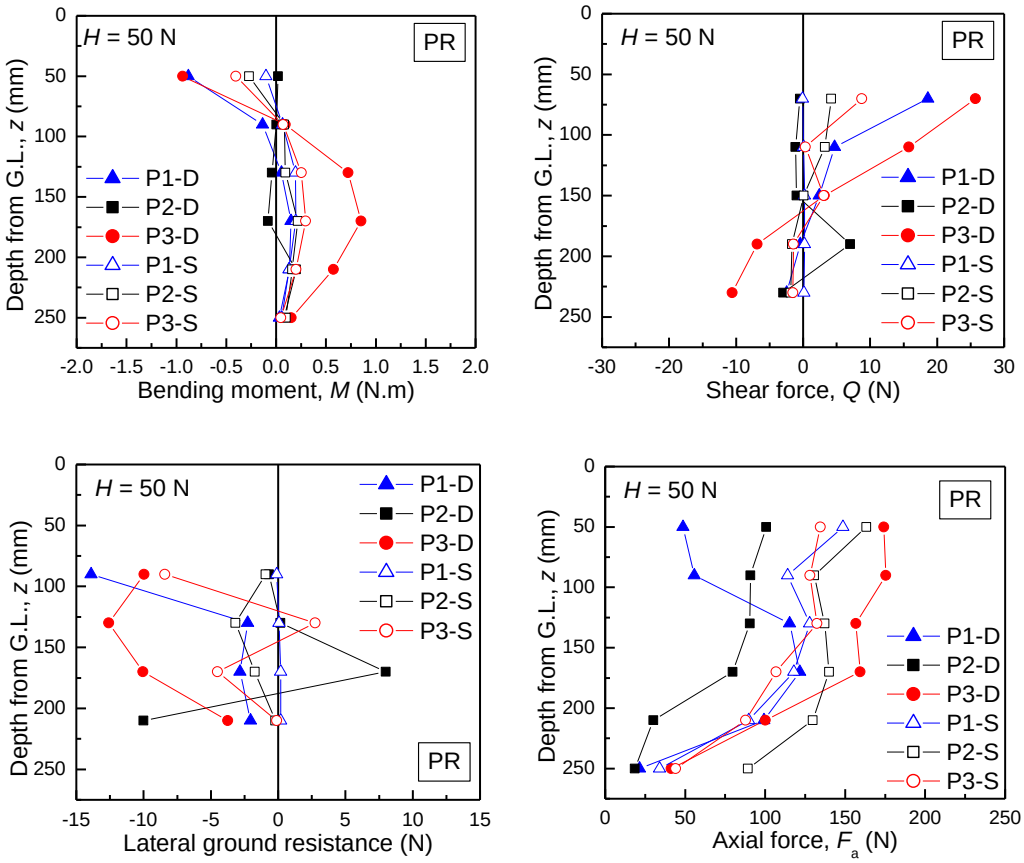

Figure 4.55 Comparison of bending moment, shear force, lateral ground resistance and axial force between 5 Hz dynamic test and static cyclic test.

4.4 Conclusions

A series of shaking table tests were performed on piled raft (PR), pile group (PG) and full raft (FR) model foundations in dry sand at 1-g field. The same model foundations conducted in static cyclic horizontal load tests were also used for this

setup. The vertical load applied prior to the horizontal loading was 497 N. In the experiments, the effect of raft base on piled raft model was examined by comparing piled raft and pile group test results under 20 Hz frequency since the natural frequency of the model ground is estimated as 20 Hz. Moreover, the piled raft model was tested by two different frequencies; 20 Hz and 5 Hz, in order to examine the responses of the piled raft under dynamic loads with "high" and "low" frequencies. Full raft model was also tested with two different vertical loads under 20 Hz dynamic load to grasp the contribution of the piles and to examine the effect of vertical load. For all the tests, sinusoidal wave with nominal amplitude of 0.07G and 100 cycles of loading was applied as the input motion.

When acceleration time histories of PR and PG are compared under 20 Hz frequency, it is seen that the acceleration recorded on the mass and the raft are similar in PR test, which is almost half of the input motion. Moreover, the mass and the raft response are in unison in PR test, whereas the accelerations of the raft in PG model attenuate the peak. Although the horizontal load on PR model is larger than the PG model, horizontal displacement of PR model is smaller than PG model, which points out the effectiveness of the raft base resistance to decrease horizontal displacement. Note that, 3 piles carry almost the same amount of load at both PR and PG tests, which indicates the horizontal load difference between two models is due to the contribution of raft resistance in PR model. Also, vertical settlement of the PR model is almost half of the PG model, which may show the advantage of PR over PG. Although the percentage of horizontal load carried by 3 piles vs. time plot is highly scattered, the trend shows that horizontal load sharing is about 30 %, which is rather smaller than the static cyclic horizontal load test results (80 %). In addition, in dynamic test the percentage of vertical load carried by 3 piles is 70 % of the total load at the initial phase of the test and it drops to 50 % at the end of the test. This decrement couldn't be observed at static cyclic load test. During dynamic loading, the most of the axial load is carried by the front pile in both PR and PG models. Note that, same behavior is observed in static tests.

When the responses of full raft model with 497 N vertical load (FR-V = 497 N) is considered, the acceleration response of FR-V = 497 N is similar with the PR test under 20 Hz frequency. Therefore, horizontal loads on PR and FR-V=497 N are almost the same, though the horizontal displacement of FR is larger than that of PR. It is also noticeable that the initial stiffness of PR is larger than that of FR-V = 497 N, which indicates the advantages of the PR compared to FR during dynamic loading. For full raft model for 197 N vertical loading (FR-V=197 N) accelerations on raft model are larger than that of FR-V=497 N resulting in larger horizontal displacements, but smaller horizontal loads. As a result, it can be said that the intensity of load on the model affects the response behavior of the foundation.

PR model under 5 Hz dynamic loading results show that, the input motion enhances on model raft and the mass during loading, contrary to the 20 Hz test results. This result indicates that the natural frequency of the ground-foundation-superstructure system is different than the natural frequency of the model ground (estimated as 20 Hz). In 5 Hz test, the percentage of horizontal load and vertical load carried by 3 piles decreases drastically, indicating the failure of the piles. Note that, these large deformations are compensated by the raft resistance.

The behavior of the PR under 5 Hz test is comparable to that of static cyclic load test, rather than the behavior under 20 Hz. When the initial stiffnesses of the PR model in dynamic test under 5 Hz and static cyclic test are compared, it is seen that the stiffnesses in two tests are comparable, though the stiffness in static cyclic test is slightly larger than that of dynamic test with 5 Hz frequency. Raft inclinations in two tests are almost same, whereas the settlement of the model at dynamic test is being slightly larger than the static test. This may be due to the settlement of the model ground by itself during dynamic loading. Moreover, the distribution of bending moments, shear forces and axial forces of static tests and dynamic tests are in good agreement. It may be due to the inertial effect on the foundation behavior which is predominant on the model foundation behavior.

As a conclusion, low frequency dynamic load tests yield reasonably close results with that of static cyclic tests. However, the behavior of the model foundations under higher frequencies is clearly different from that of the static cyclic load test behavior. This may lead to the suggestion to carry out dynamic analyses to understand the behavior more in depth under higher frequencies. Matsumoto et al., 2004b are suggested dynamic analysis for resonant frequencies after performing a series of static and dynamic tests to consider influence of superstructures.

CHAPTER 5

NUMERICAL ANALYSES OF MODEL FOUNDATIONS UNDER VERTICAL AND STATIC HORIZONTAL LOADING

5.1 Introduction

In order to throw further sight into the behavior of piled raft foundations under vertical and horizontal loading, a series of numerical modelling of vertical load tests and monotonic horizontal load tests on a 3-pile piled raft model were carried out for dry sand model. Load tests of the components of the piled raft model, such as full raft and single pile, were also analyzed to investigate their interactions with the piled raft. For this purpose, a FEM software, PLAXIS 3D, was used for numerical modelling. The hardening soil model (Schanz et al., 1999) was employed for modelling the sand behavior based on the triaxial consolidated drained (CD) compression test results on the sand, while elastic model was used to model piled raft, single pile or raft model to have a deeper understanding of the behavior of the piled raft subjected to vertical and horizontal loading.

5.2 Selection of Constitutive Model

In order to model numerically the behavior of the sand, the Hardening soil model (HS model) (Schanz et al., 1999) was employed since it is capable of modelling nonlinear and inelastic stress-strain behavior of the sand. Hardening soil model was developed from Duncan-Chang model (known also as the hyperbolic model) (Duncan and Chang, 1970).

Duncan and Chang model:

Duncan and Chang model assumes a hyperbolic stress-strain relationship between stress difference, (σ_1-σ_3), and axial strain, ε_a, by the following formula (Duncan et al., 1980):

$$\sigma_1 - \sigma_3 = \frac{\varepsilon_a}{\frac{1}{E_i} + \frac{\varepsilon_a}{(\sigma_1 - \sigma_3)_{ult}}} \quad (5.1)$$

where, E_i is the initial tangent modulus; σ_1 and σ_3 are the major and minor principal stresses; $(\sigma_1$-$\sigma_3)_{ult}$ is the asymptotic value of stresses difference, which is related to the soil strength by failure ratio, R_f:

$$(\sigma_1 - \sigma_3)_f = R_f . (\sigma_1 - \sigma_3)_{ult} \quad (5.2)$$

in the equation, deviatoric stress at failure, $(\sigma_1$-$\sigma_3)_f$ is governed by the Mohr-Coulomb criterion:

$$(\sigma_1 - \sigma_3)_f = \frac{2(c.\cos\phi + \sigma_3.\sin\phi)}{1 - \sin\phi} \quad (5.3)$$

where, c and ϕ are Mohr Coulomb strength parameters. The initial tangent modulus, E_i, is defined by Duncan and Chang model as:

$$E_i = K . P_a . (\frac{\sigma_3}{P_a})^n \quad (5.4)$$

where the modulus number, K, and modulus exponent, n, are dimensionless material parameters and P_a is the atmospheric pressure. Tangent modulus, E_t, is defined as:

$$E_t = (1 - R_f . S)^2 . E_i \quad (5.5)$$

where, $S = \frac{(\sigma_1 - \sigma_3)}{(\sigma_1 - \sigma_3)_f}$ (5.6)

if $(\sigma_1 - \sigma_3) <$ historical maximum; it is assumed that the soil is under unloading or reloading condition and unloading modulus, E_{ur} is equal to:

$$E_{ur} = K_{ur}.P_a.(\frac{\sigma_3}{P_a})^n \quad (5.7)$$

where, K_{ur} is the unloading/reloading modulus number, which is always greater than K, and the bulk modulus, B is expressed as:

$$B = K_b.P_a.(\frac{\sigma_3}{P_a})^m \quad (5.8)$$

where, K_b and m are the bulk modulus number and bulk modulus exponent, respectively.

Hardening soil model:

Although, Duncan and Chang model captures soil behavior well, it cannot model unloading/reloading behavior since it is a hypo-elastic model. The restrictions of Duncan-Chang model is overcome by hardening model since this model uses the theory of plasticity rather than the theory of elasticity. Moreover, it includes soil dilatancy and a yield cap. Hardening soil model is based on the hyperbolic relationship between the axial strain, ε_a and the deviatoric stress, q. The yield curves that are obtained from standard drained triaxial tests can be expressed as (Schanz et al., 1999):

$$\varepsilon_a = \frac{q_a}{2.E_{50}} \frac{(\sigma_1 - \sigma_3)}{q_a - (\sigma_1 - \sigma_3)} \text{ for } q < q_f \quad (5.9)$$

where E_{50} is primary loading stiffness, q_a is the asymptotic value of the shear strength and q_f is the ultimate deviatoric stress. q_a and q_f are defined by the following formulas:

$$q_f = (c.\cot\phi - \sigma_3)\frac{2.\sin\phi}{1-\sin\phi} \qquad q_a = \frac{q_f}{R_f} \tag{5.10}$$

In the equations, R_f is the failure ratio; c and ϕ are the Mohr-Coulomb strength parameters.

The hyperbolic relationship is given in Figure 5.1. In the model, instead of initial modulus, E_i, secant modulus, E_{50}, which is confining stress dependent stiffness modulus, is introduced, where unloading/reloading stiffness, E_{ur}, is used for unloading/reloading stress paths. It is seen from the figure that, when the ultimate deviatoric stress, q_f is reached, the soil behaves like a perfectly plastic material. Mohr-Coulomb failure criterion is adopted in Hardening soil model.

E_{50} and E_{ur} are defined by the following expressions:

$$E_{50} = E_{50}^{ref}\left(\frac{\sigma_3 + c.\cot\phi}{\sigma^{ref} + c.\cot\phi}\right)^m \tag{5.11}$$

$$E_{ur} = E_{ur}^{ref}\left(\frac{\sigma_3 + c.\cot\phi}{\sigma^{ref} + c.\cot\phi}\right)^m \tag{5.12}$$

where, E_{50}^{ref} is reference stiffness modulus and E_{ur}^{ref} is the reference Young's modulus for unloading/reloading at reference stress, σ^{ref}, and m is the amount of stress dependency.

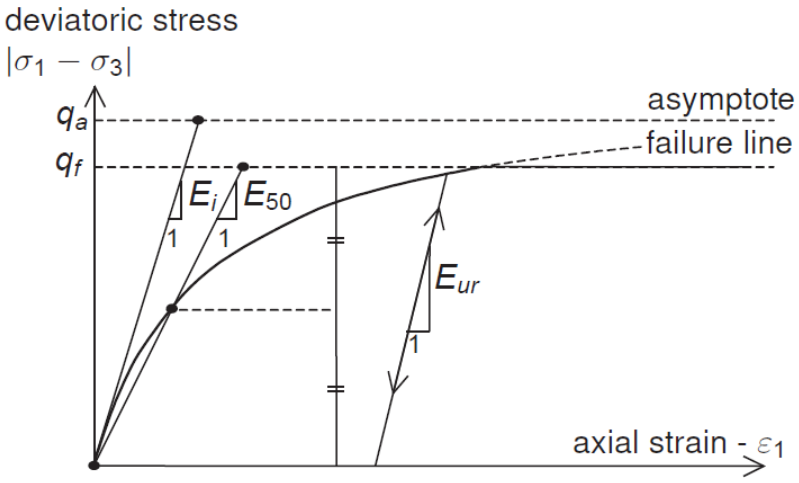

Figure 5.1 Hyperbolic stress-strain relationship for a standard drained triaxial test (Schanz et al., 1999).

5.3 Triaxial Tests and Results

A series of triaxial CD tests on the model sand with D_r = 70 % were carried out under various confining pressures, p_0 (p_0 = 11, 50, 100 and 150 kPa). In addition, a cyclic CD was conducted under p_0 = 100 kPa. The soil specimens had a height of 100 mm and a radius of 50 mm.

The test results, deviatoric stress, q, versus axial strain, ε_a, and volumetric strain, ε_{vol}, versus ε_a, under different confining pressure with hardening soil model are shown in Figure 5.2 and Figure 5.3, respectively. It is seen that the initial stiffness increases with increasing p_0 and stress-strain relations exhibit non-linearity (Figure 5.2), and that a relatively large dilatancy occurs (Figure 5.3).

In the cyclic CD test, two cycles of unloading/reloading process were conducted as shown in Figure 5.2. Therefore, the peak of the deviatoric stress, q, in the monotonic CD test with p_0 = 100 kPa was 430 kPa. The first unloading in the

cyclic CD test was conducted when q reached 215 kPa that was 50 % of the peak of q in the monotonic CD test, and the second unloading was conducted when q reached 300 kPa that was 70 % of the peak of q in the monotonic CD test. It is seen from Figure 5.2 that stiffness's (inclinations) of unloading/reloading curves in the two cycles of unloading/reloading were almost equal.

The results of the numerical simulations of the CD tests are also compared with the measured results in Figure 5.2 and Figure 5.3. The numerical modelling simulates the measured results fairly well, although the post-peak softening behaviors measured in the CD tests are not simulated using the numerical modelling.

Principle parameters of HS model are summarized in Table 5.1. The parameters except for oedometer stiffness, E_{oed}, power of stress dependency, m, and failure ratio, R_f, were estimated from the cyclic CD test with $p_0 = p_0^{ref} = 100\,\text{kPa}$. It was assumed that $E_{oed} = E_{50}/1.2$ (Plaxis, 2013). The values of m and R_f listed in Table 5.1 were determined so that the results of numerical simulations fit to the measured results.

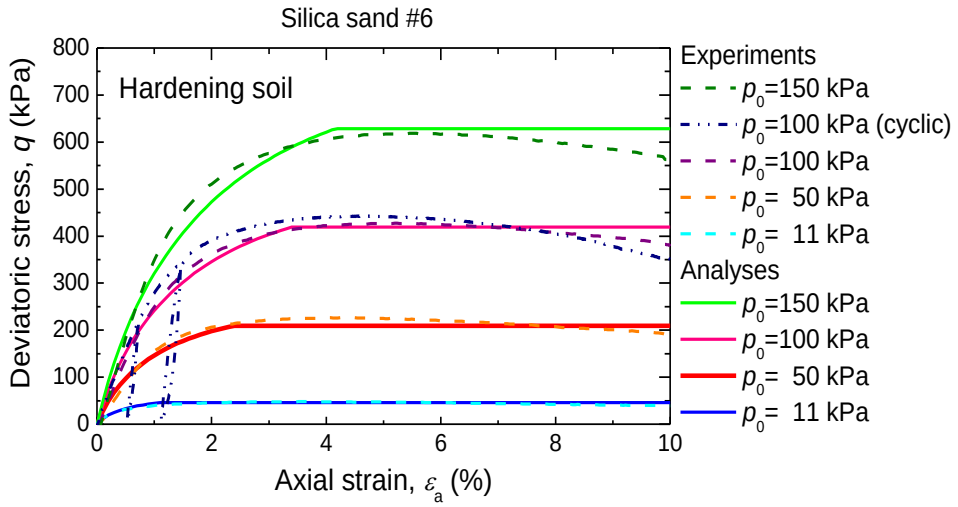

Figure 5.2 Deviatoric stress q vs. axial strain ε_a.

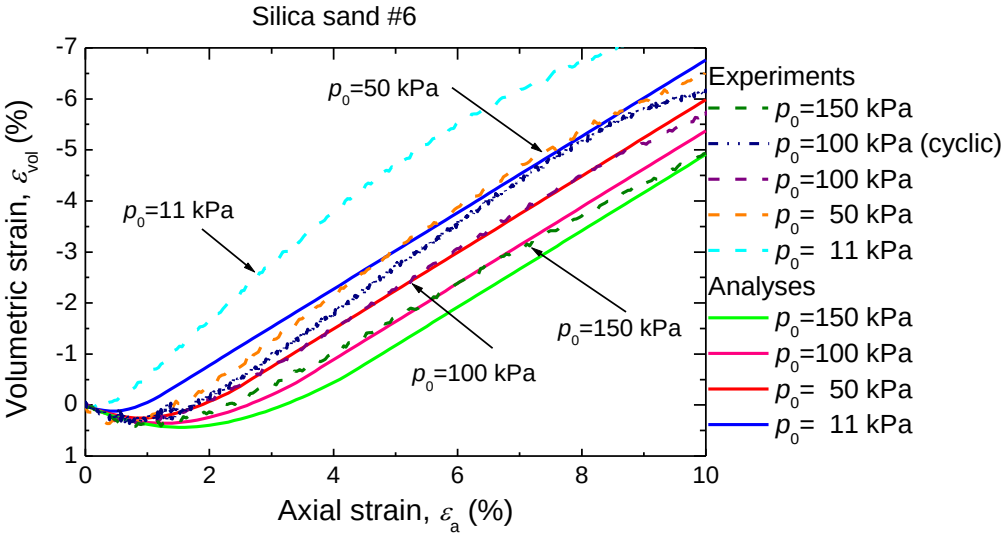

Figure 5.3 Volumetric strain ε_{vol} vs. axial strain ε_a.

Table 5.1 Material properties of the sand.

Item	Value
Secant stiffness, E_{50} (kPa)*	29.56×10^3
One-dimensional stiffness, E_{oed} (kPa)*	24.65×10^3
Unloading/reloading stiffness, E_{ur} (kPa)*	99.59×10^3
Stress dependency parameter for stiffness, m	0.5
Non-linear factor, R_f	0.75
Poisson's ratio, v	0.19
Internal friction angle, ϕ' (^{0})	43.2
Dilatancy angle, ψ (^{0})	15.8
(from the peak strength)	
Cohesion, c (kPa)	0.1

* values for a reference stress, p_0^{ref} = 100 kPa

5.4 Numerical Modelling of the Experiments

The numerical study was carried out using a three dimensional finite element software, PLAXIS 3D (2013). Figure 5.4 and Figure 5.5 show the finite element mesh of the vertical loading and monotonic horizontal loading of the piled raft model, respectively. Only half of the model foundation and the model ground were modelled due to symmetric conditions. Interface elements were arranged along the pile shafts and at the raft base. The finite element mesh consists of 10-noded 35471 and 35735 tetrahedral elements for the vertical and horizontal loading of piled raft model, respectively. Similar FEM modelling was adopted for the cases of single pile and full raft.

The sand ground was modelled throughout using the Hardening soil model having the parameters listed in Table 5.1. The interface friction angle for the raft base was estimated as 31.1^0 from the horizontal loading tests of the full raft model on the model ground. The study of Uesugi and Kishida (1986) reported that the frictional resistance between the steel and the soil is mostly affected by the steel roughness, R_{max}, median grain size and sand type. According to the direct shear tests between Toyoura sand (a kind of silica sand) and mild steel, interface friction angle is about 20^0 for $R_{max} < 10$ μm and about 31^0 for $R_{max} > 10$ μm. As mentioned earlier, the sand particles were adhered on the raft base intending to increase the interface angle. It was estimated, however, from the horizontal loading tests of the full raft model on the model ground that the interface friction angle is 31.1^0, showing minor effects of the sand particles on the raft base. Although poor contact (gluing) between the sand particles and the raft base seems to be a reason for lower raft-soil interface friction angle compared to the internal friction angle of 43.2^0, a definite reason is not obvious. Moreover, in the study of Matsumoto et al. (2004a, 2004b), they found similar interface friction angles between the raft and the soil, such as 30.5^0. Therefore, it was decided to use the raft-soil interface angle of 31.1^0 that was estimated from the horizontal loading tests of the full raft model on the model ground.

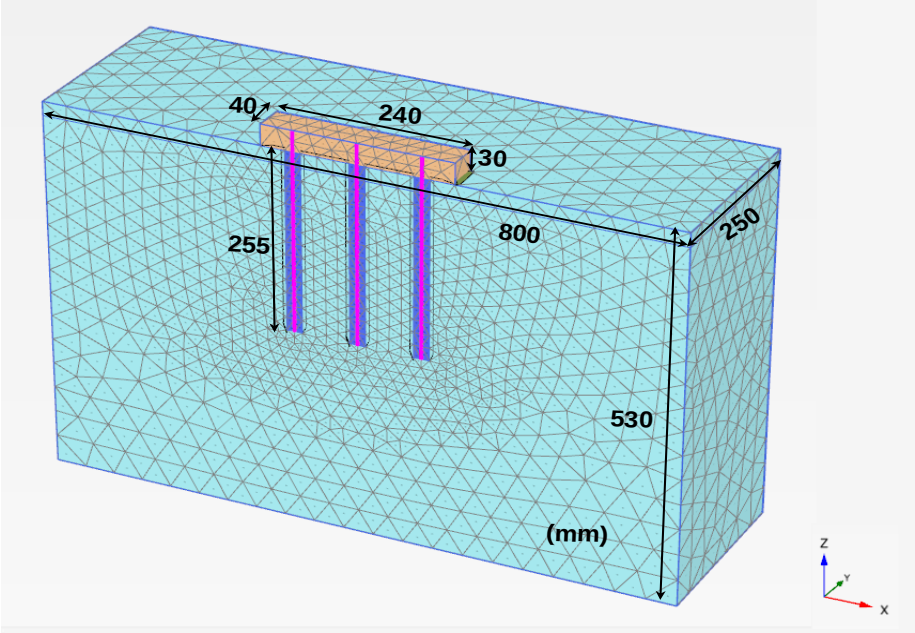

Figure 5.4 Finite element mesh of the piled raft model for vertical loading test.

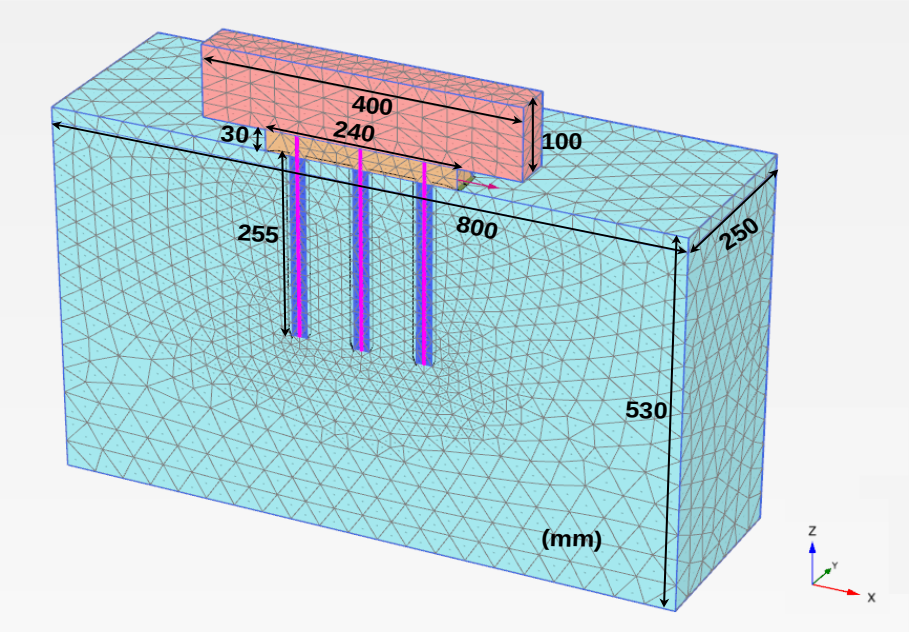

Figure 5.5 Finite element mesh of the piled raft model for horizontal loading test.

The raft and the piles were assumed to be linearly elastic. Although the model piles were hollow cylinders with an end plate, they were modelled by combination of beam elements surrounded by solid elements, following Kimura and Zhang (2000). In the hybrid modelling of pile, a large portion of the bending stiffness, *EI*, and axial stiffness, *EA*, of the pile are shared by the beam elements, still keeping large enough stiffness of solid pile elements compared to the stiffness of the surrounding ground (Figure 5.6). According to these criteria, the stiffness ratio sharing between the beam and the solid was selected as 9:1. The big advantage of the hybrid modelling of pile is that axial forces, bending moments and shear forces of the pile can be estimated easily from the factored values of those of the beam elements. The properties of the solid pile, the beam, the raft and the weight plates are summarized in Table 5.2.

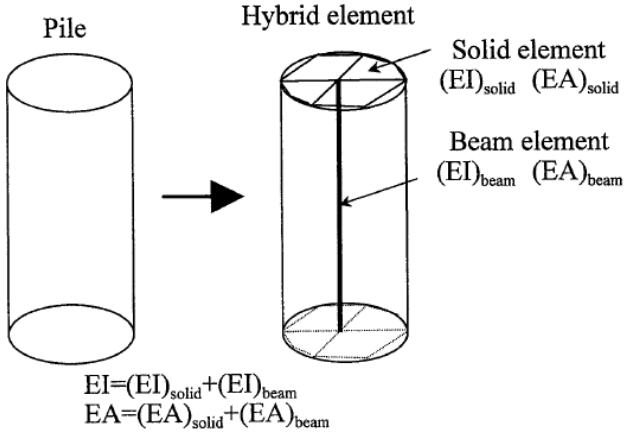

Figure 5.6 Mechanism of hybrid elements (Kimura and Zhang, 2000).

Table 5.2 Material properties of the pile and the raft.

	Solid Pile	Beam	Raft	Weight plates
Unit weight, γ (N/mm^3)	2.25×10^{-6}	2.02×10^{-5}	2.65×10^{-5}	0.113×10^{-3}
Young's modulus, E (N/mm^2)	54.40×10^{2}	48.96×10^{3}	64.00×10^{3}	16.10×10^{3}
Bending stiffness, EI (N.mm^2)	21.44×10^{6}	71.64×10^{6}	81.92×10^{9}	67.08×10^{9}
Axial stiffness, EA (N)	8.55×10^{5}	1.60×10^{6}	6.14×10^{8}	3.22×10^{8}
Poisson's ratio, υ	0.31	-	0.31	0.40

The following FEM analysis procedure was adopted:

Step 1: K_0 consolidation of the ground alone, where $K_0 = 1 - \sin\phi'$ was assumed. Note that the solid pile elements created in Step 1 have the properties of the soil.

Step 2: Setting the foundation in the model ground and gravity (self-weight) calculation. Note that the pile beam elements, the interface elements and the raft elements were created, and the properties of the pile solid elements that have been created in Step 1 were changed to the pile properties in Step 2. This procedure of pile installation in the FEM analysis intended to simulate the pile installation process adopted in the experiments.

Step 3: Calculation of loading process (placing of weight plates is included, if present).

In the analyses, loading of the model was performed by displacement-controlled manner. The displacement of the model foundation was increased by 0.2 mm increments until 2.00 mm displacement was reached then the interval was increased to 0.4 mm and analyses were continued until failure occurred.

5.5 Comparison of Experimental and Analytical Results

5.5.1 Vertical load tests

Single pile: Finite element mesh for the vertical loading of single pile is given in Figure 5.7. The upper 30 mm is kept on the ground surface since this part is embedded in the raft in piled raft experiments. Beam element, solid element and the interface element of the single pile can be seen in Figure 5.8 in detail.

As mentioned before, the interface friction angle between the raft and the soil was estimated from the experiments (as $\delta_{raft\text{-}soil} = 31.1^0$), whereas interface friction angle between the pile shaft and the soil could not be obtained from the experiments. Therefore, it was decided to estimate that parameter from the back calculation analysis of the vertical loading test of the single pile. After a series of analyses, the interface friction angle, $\delta_{pile\text{-}soil}$ was estimated as 40.2^0 that was slightly smaller than the internal friction angle of the sand of 43.2^0.

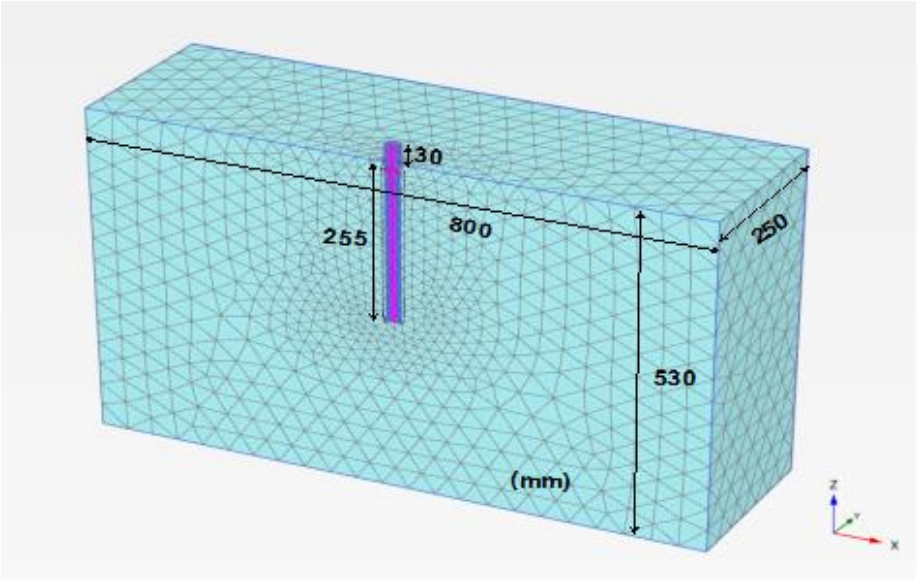

Figure 5.7 Finite element mesh of the single pile model for vertical loading test.

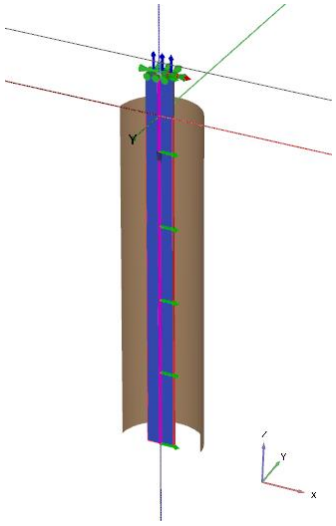

Figure 5.8 Single pile model in detail.

Figure 5.9 shows the measured and calculated relationships of the vertical load, *V*, and the pile head displacement, *w*, according to this estimation of $\delta_{\text{pile-soil}}$. Both measured and calculated results have similar initial stiffness which is an important criterion in design. Maximum vertical load capacity is found as 470 N in the analysis. Although the capacity of the single pile is underestimated by the analysis at large displacements, the calculated capacity is similar to the measured one at failure.

The calculated load-settlement curve exhibits a bi-linear response. El-Mossallamy (1999) analyzed the vertical loading of a single bored pile using a linear elastic Mohr-Coulomb soil model and the Hardening soil model (HS model). The calculated load-settlement relation showed a linear response until the shaft resistance reaches its ultimate value, followed by a non-linear behavior. The non-linear portion is caused by non-linear response of the tip resistance. A significant difference of the soil properties between the present analysis and the analysis in El-Mossallamy (1999) using HS model is the value of the dilatancy angle, Ψ. In the analysis in El-Mossallamy (1999), Ψ is assumed to be 0, while $\Psi = 15.8^0$ (as

obtained by CD tests) is used in the present analysis result shown in Figure 5.9. It is reasonable that the higher Ψ causes the higher stiffness of load-displacement relation at the pile tip. Mean stresses higher than the confining pressures used in the triaxial tests of the sand were caused in the soil beneath the pile tip in the analysis. Under such large stress level, Ψ would reduce. If reductions of Ψ under high mean stress were modelled in the present analysis, more non-linear response would have been obtained.

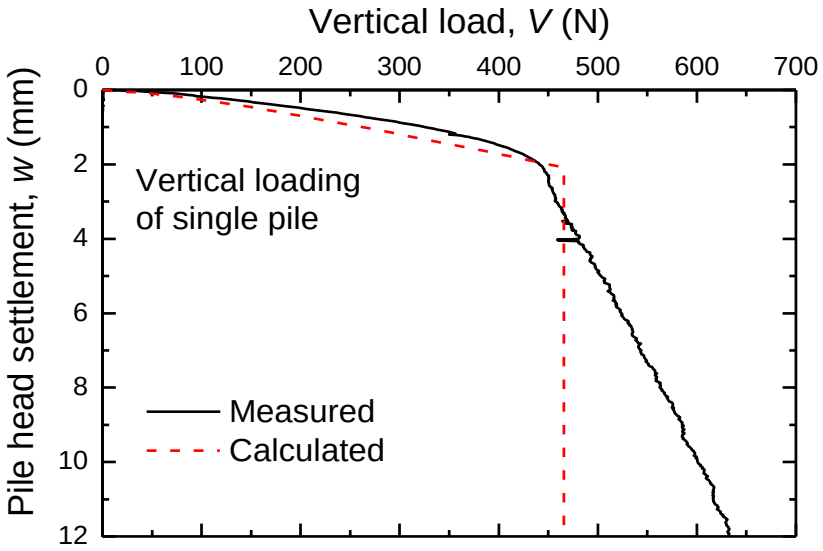

Figure 5.9 Vertical load-pile head settlement relationship of the single pile.

The measured and calculated distributions of the axial forces along the pile shaft at normalized displacements, w/D = 0.02, 0.04, 0.06, 0.08 and 0.10, are given in Figure 5.10. It was observed in the experiment that negative skin friction is generated along the pile section between strain gauges, SG1 and SG2. This measured results may be doubtful when they are compared with the calculated results in which no negative skin friction is generated. A possible reason for the negative skin friction between SG1 and SG2 is the influence of confinement of the

pile top section. Hence, axial strain at SG1 might become smaller due to the confinement of radial deformation. However, a definite explanation for the measured negative skin friction is difficult at present. There is reasonable agreement between the measurements and the calculations, both quantitatively and qualitatively, except for the axial force distributions near the pile head. Mean stress contour graph at w/D = 0.10 (at failure) is given in Figure 5.11. As it is seen, stresses are almost same along the pile shaft, and concentrated at the pile tip.

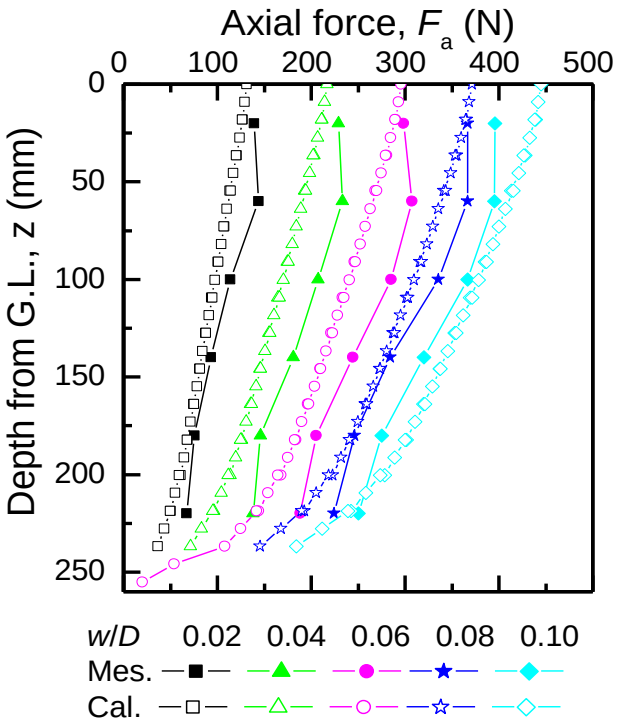

Figure 5.10 Distribution of axial forces along the single pile shaft.

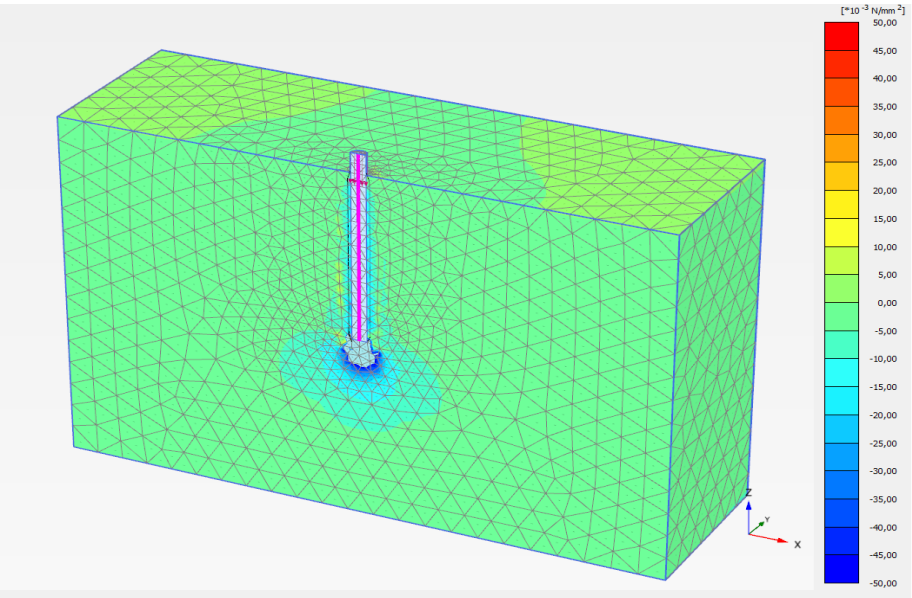

Figure 5.11 Mean stress contours for single pile vertical loading analysis.

Full raft: Figure 5.12 and Figure 5.13 show the finite element mesh and the model raft in detail for vertical loading analysis of full raft, respectively. There is an interface element between the raft and the ground, where interface friction angle is taken as $\delta_{\text{raft-soil}} = 31.1^{o}$.

Figure 5.14 compares the measured and calculated load-settlement relationship of the full raft model. In the experiment, the maximum load of 3200 N is attained at w = 8.5 mm. Post-peak softening behavior is observed and the residual ultimate load of 2915 N is obtained. It is seen from the figure that initial stiffness of the raft is simulated very well until w reaches 0.6 mm. After this settlement, the calculated stiffness of the raft is larger than the measurement. The calculated maximum load of 2650 N is about 10 % smaller than the measured residual load, although the analysis does not express the measured softening behavior.

It should be noted that the calculated load-settlement curve exhibits basically a bi-linear response, whereas the measured curve exhibits a non-linear response. The

discussion on the influence of Ψ made for pile head settlement of single pile may be valid for this case as well. In the calculation in Figure 5.14, failure zone extended from the edge of the raft to the center of the raft as load level increased, and the soil beneath the whole raft attained the failure state at the ultimate load of 2650 kN. At the same time, mean effective stress in the soil continued to increase as the load level is enlarged, resulting an in increase in the soil stiffness. As a result, the calculated load-settlement response exhibited bi-linear response.

Mean stress contour graph for vertical loading of the full raft model at w/D = 0.13 (which is the maximum settlement before failure) is given in Figure 5.15. In the figure, stress contours confirm the above discussion on soil stress increment with the increasing load level.

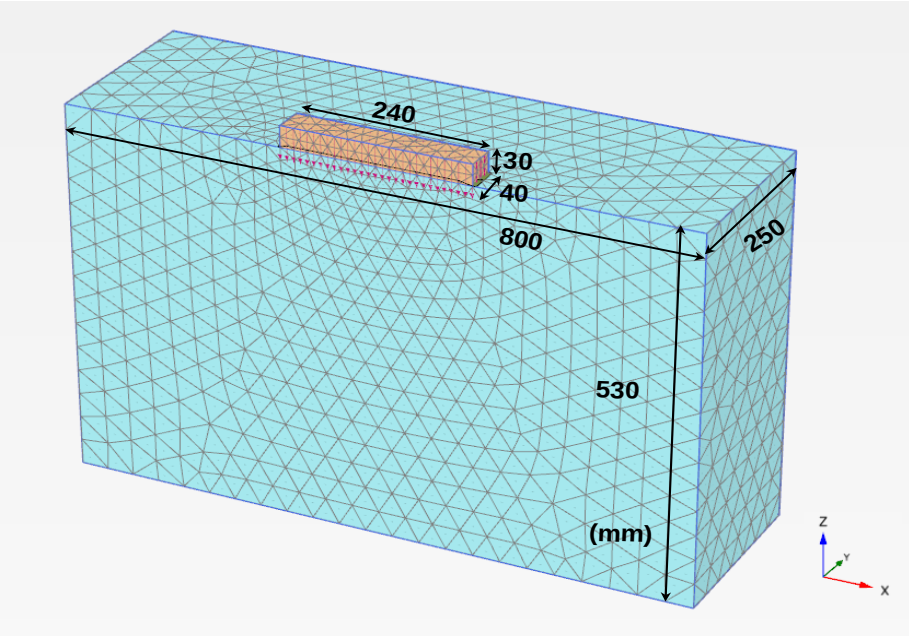

Figure 5.12 Finite element mesh of the full raft model for vertical loading test.

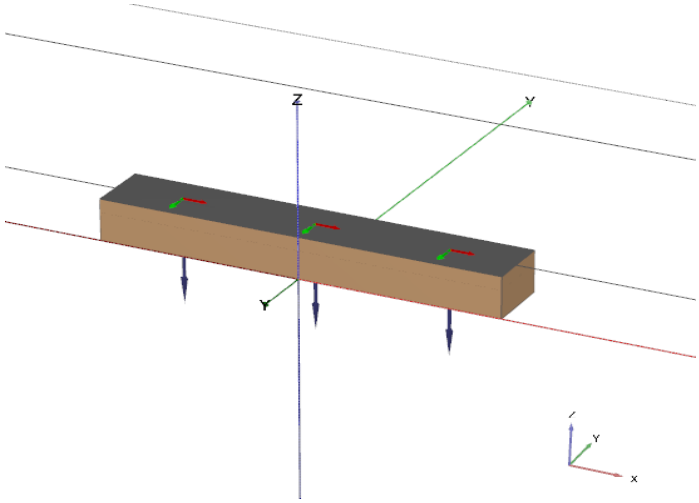

Figure 5.13 Raft model in detail.

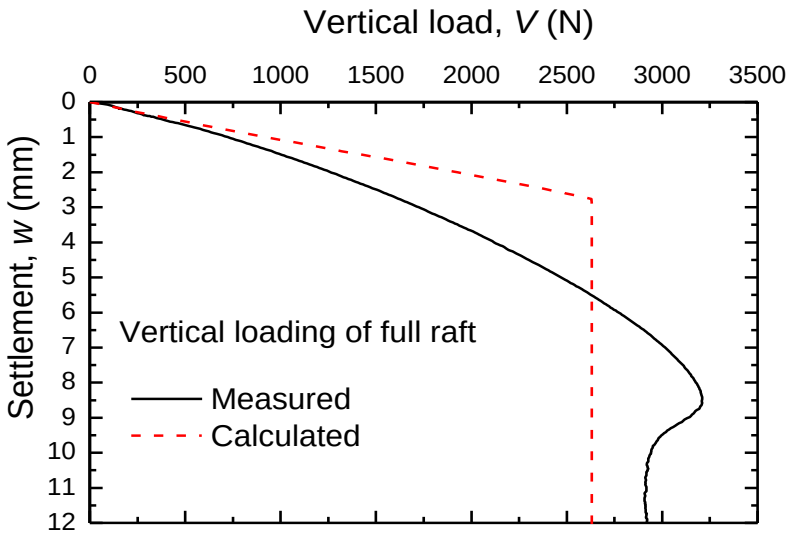

Figure 5.14 Load- settlement relationships of the full raft.

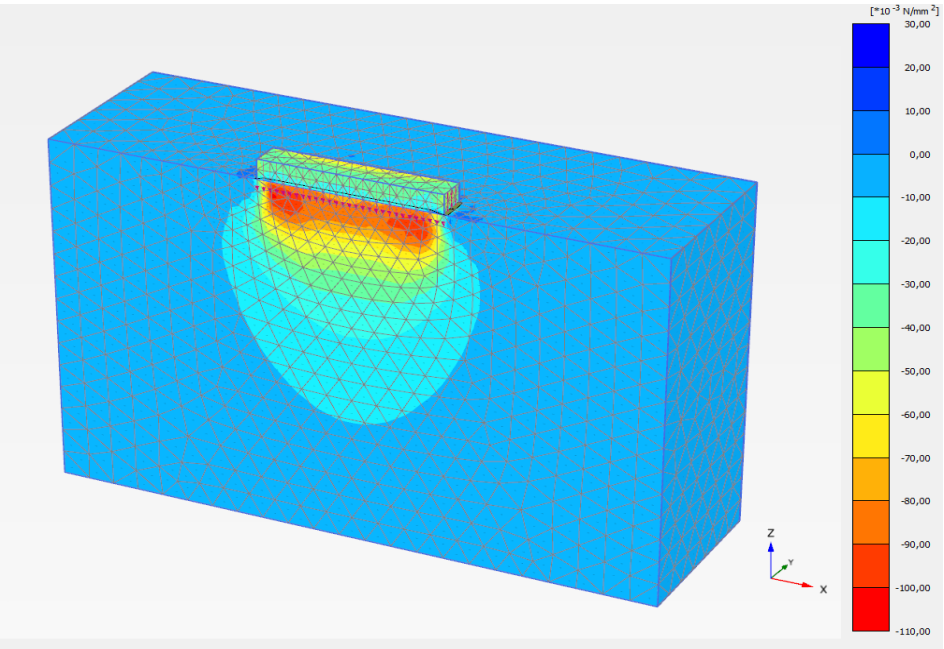

Figure 5.15 Mean stress contours for full raft vertical loading analysis.

Piled raft: Finite element mesh for vertical loading of piled raft is given in Figure 5.4. As it is seen from the figure, piled raft is the combination of the three single piles and the raft, which were analyzed separately in the previous sections. Note that, in the model, interface elements exist around the piles and below the raft.

The measured and calculated relationships of the vertical load and the settlement of the piled raft are shown in Figure 5.16. The measured and calculated loads supported by the components of the piled raft such as 3 piles and the raft are also shown in the figure. It was observed in the experiment that the raft load reaches the peak value of 2684 kN at w = 8.5 mm then slightly decreases with increasing w. The behavior of the raft in the piled raft is comparable with that of the measured in the vertical load test of the full raft as shown in Figure 5.14. In contrast, the behavior of the 3 piles in the piled raft is totally different from that of the single pile. The load of the 3 piles in the piled raft is 1692 N at w = 3 mm and 3184 N at w = 12 mm. The load of the single pile was 460 N at w = 3 mm (Figure

5.9) and 633 N at w = 12 mm. That is, the load of the 3 piles in the piled raft is higher than 3 times that of the load of the single pile. This tendency becomes significant for larger settlements. It is plausible to suggest that the load transfer from the raft base to the ground enhances the pile resistance in the piled raft due to the result of increase in the stiffness and the strength of the soil surrounding the piles in the piled raft. The calculation reasonably simulates the above-mentioned experimental results, although the calculated responses of the total load, the raft load and the 3 piles load exhibit bi-linear (elastic-perfectly plastic) response. Moreover, the initial stiffness of the piled raft is estimated well by the analysis and the calculated capacity of the piled raft model is almost the same as the measured one.

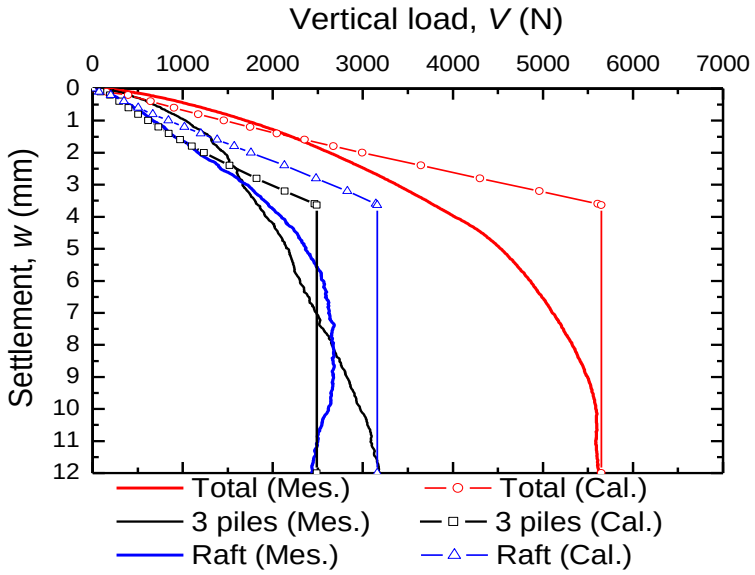

Figure 5.16 Vertical load- settlement relationship of the piled raft.

The measured and calculated percentage of vertical load carried by the 3 piles and the raft with the change in normalized settlement, w/D, are given in Figure 5.17. In the experiment, the 3 piles take about 70 % of the applied load at very early

stage of loading, then the load proportion taken by the 3 piles decreases with increasing *w*/*D* and levels off at a value of 48 % when *w*/*D* is 0.15. The load proportion taken by the raft, of course, has the counter trend. Although the calculated proportion of the load by the 3 piles is smaller than the measurement at small displacements, the difference between the measurement and the calculation becomes smaller after *w*/*D* = 0.15.

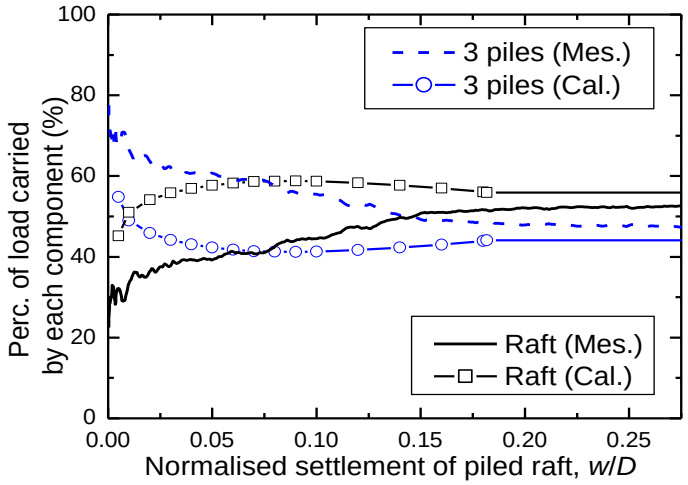

Figure 5.17 Load sharing of 3 piles and the raft under vertical loading.

Vertical loads on the edge piles (P1 and P3) and the center pile (P2) are plotted against *w*/*D* in Figure 5.18. Measurements show that the edge piles (P1 and P3) support slightly larger load than the center pile (P2) until *w*/*D* reaches 0.10, and thereafter P2 supports larger load than the edge piles. The above mentioned response of the piles at smaller *w*/*D* is similar to that of a piled raft having a rigid raft in a uniform elastic ground. This result is also in good agreement with research work published previously (e.g. Franke et al. (1994), Reul (2004)). The larger load of P2 at larger *w*/*D* is thought to be due to a larger stress level in the soil surrounding P2 caused by load transfer from the raft base to the soil which is the case as seen from the mean stress contours of piled raft analysis (see Figure

5.19). This aspect has been pointed out by Reul (2004) through a numerical study on bearing behavior of piled rafts.

In the calculation, the edges piles (P1 and P3) and the center pile (P2) carry the same load until *w*/*D* reaches 0.03, and thereafter the center pile carries somewhat larger load than the edges piles. Although higher initial stiffness of the piles measured in the experiment is not simulated well in the calculation, the calculation results in Figure 5.18 simulate reasonably well the measured trend qualitatively.

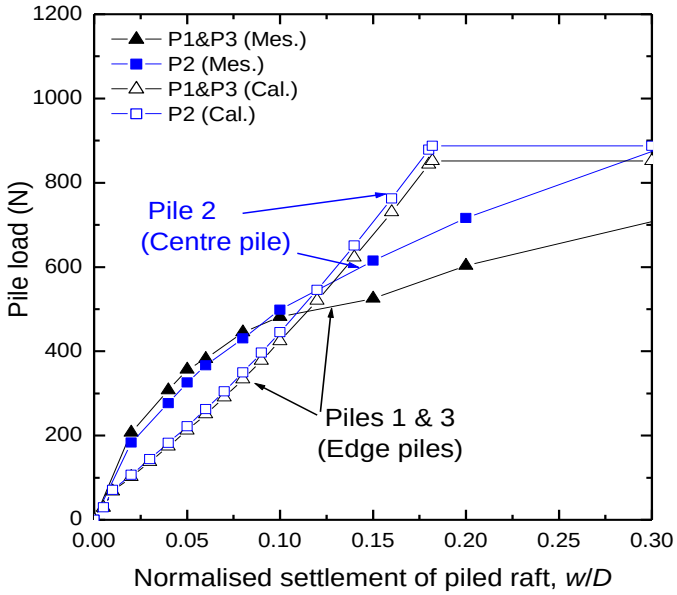

Figure 5.18 Vertical loads at edge and center piles.

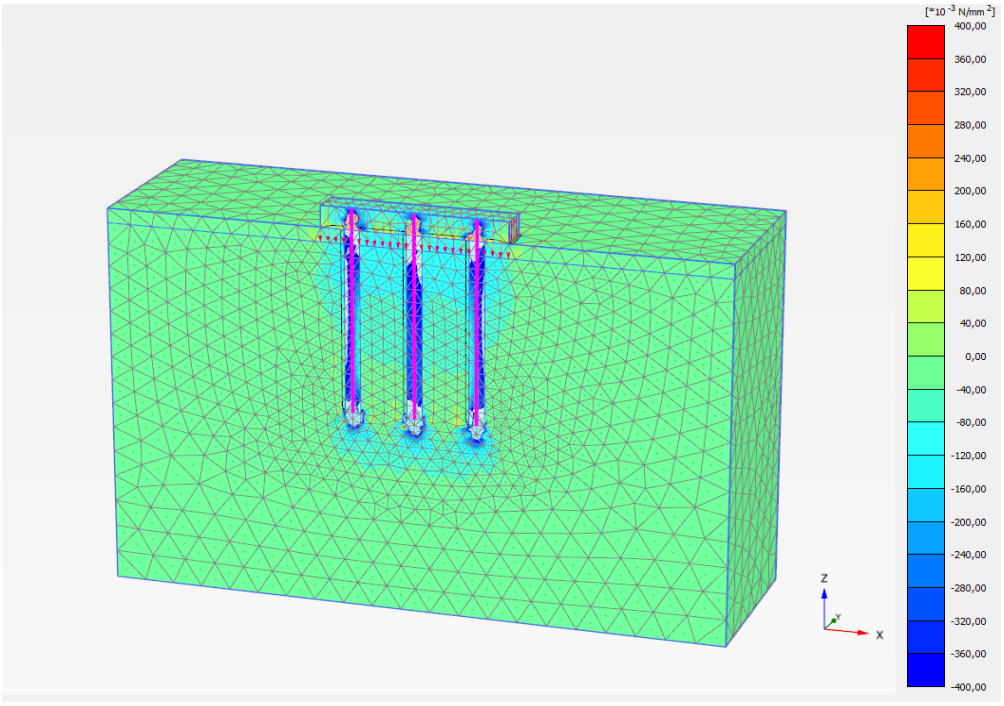

Figure 5.19 Mean stress contours for piled raft vertical loading analysis.

The measured and calculated axial force distributions of each pile (P1, P2 and P3) at various normalized settlements, w/D = 0.02, 0.04, 0.06, 0. 10 and 0.15 are given through Figure 5.20. It is seen that the measured shaft resistance of P1 and P3 reaches the ultimate value at w/D = 0.02, since rate of change of axial force with depth are not changed after w/D reaches 0.02 with the increase of the pile tip resistance. In contrast, the shaft resistance of the center pile P2 continues to increase even after w/D = 0.02. A possible reason for this is larger level of stress in the soil surrounding P2 compared to the edge piles.

The calculated developments of the axial forces with increasing w/D are moderate compared to the measured results. However, the calculated axial forces at w/D = 0.15 (at the ultimate state) converge to the measured results. It should be noted that in the calculation, the axial forces increase from the pile head to 20 mm below the pile head, indicating negative skin friction are caused along this pile

section. Unfortunately, as the top level of strain measurement was 20 mm below the pile head, detailed discussion on this aspect could not be made (Figure 5.20).

The measured and calculated distributions of mobilized shaft resistance are shown in Figure 5.21. The mobilized shaft resistance was estimated from the axial forces measured at strain gauge levels and plotted against the midpoint of each pile section. The same procedure was used for the calculation results for a purpose of comparison between the measurement and the calculation. The calculation results indicate that mobilized shaft friction along the mid-section (z = 60 to 160 mm) of P2 (center pile) are larger than those in P1 and P3 (edge pile). In contrast, the mobilized shaft resistance at the bottom section (z = 200 mm) of P1 are larger than those in P2. Although the measured distributions have large scatter with depth, they have a similar tendency as the calculations.

Figure 5.22 shows the total displacement contours of piled raft for vertical loading analysis at failure. It is seen that larger displacements concentrated under the raft and at the pile tips.

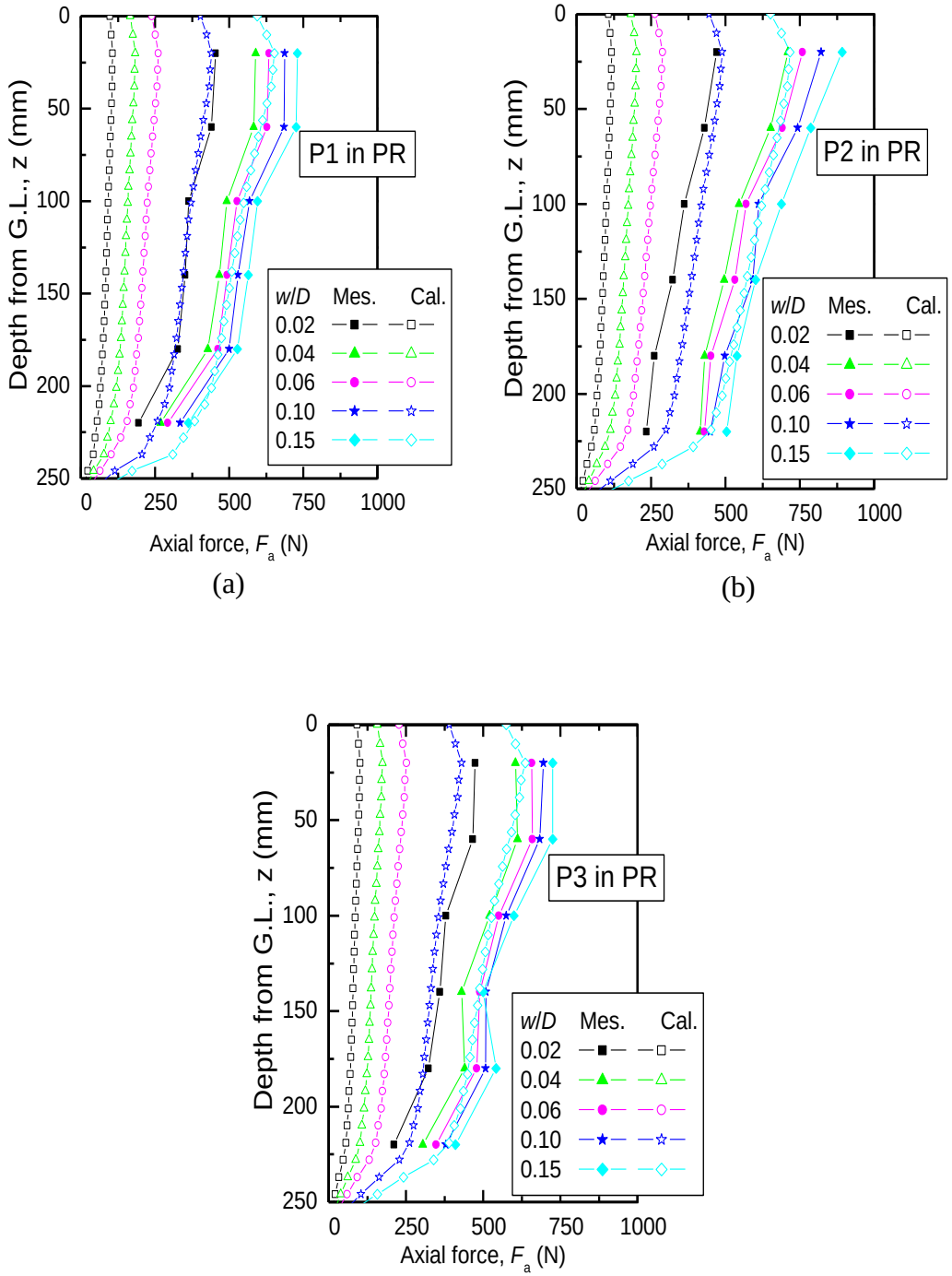

Figure 5.20 Distribution of axial forces along each pile shaft (P1, P2 and P3).

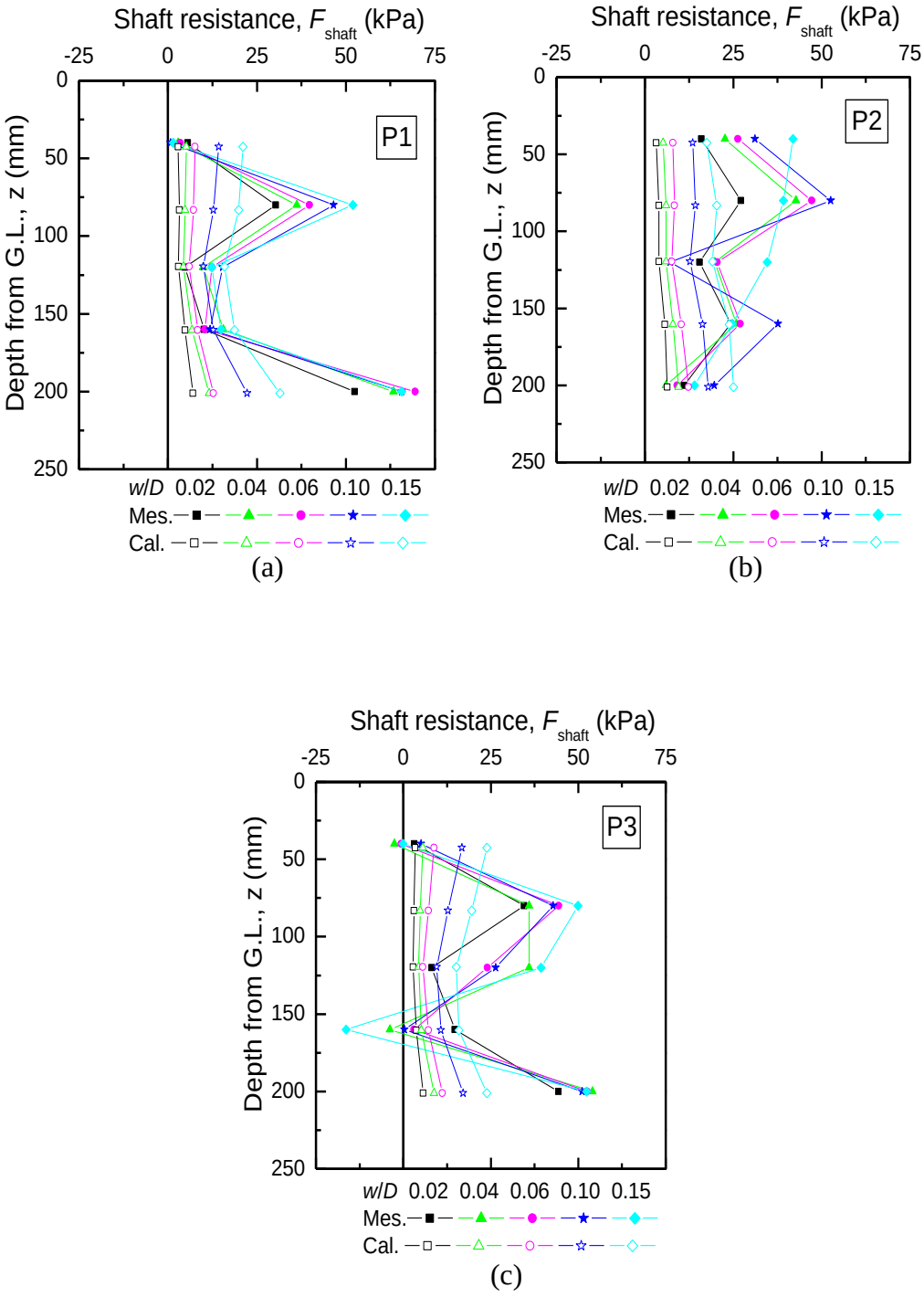

Figure 5.21 Distribution of shaft resistance along each pile (P1, P2 and P3).

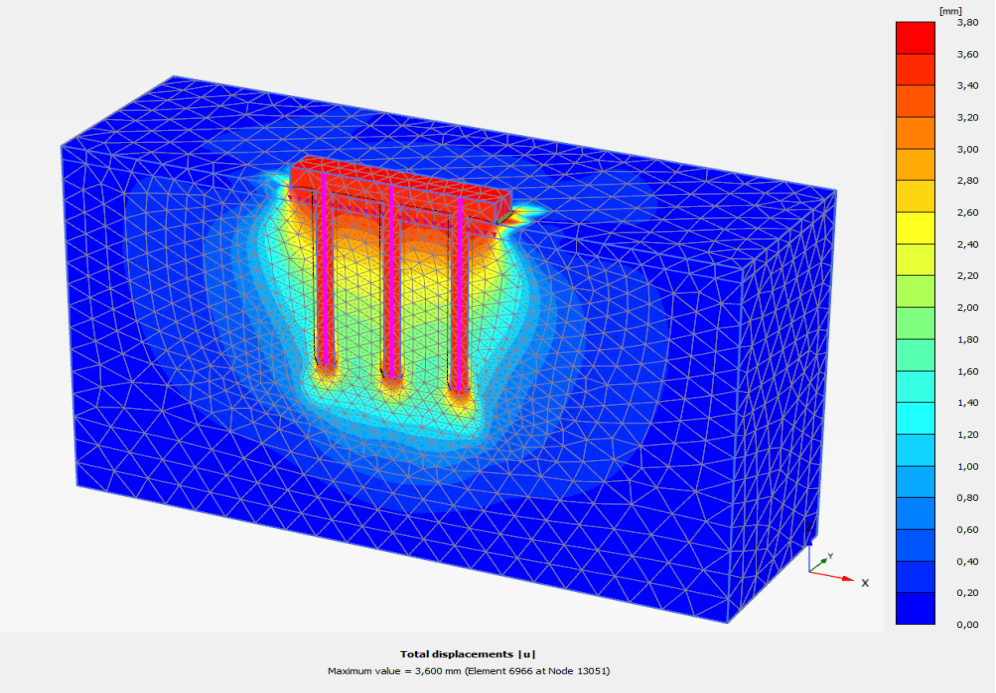

Figure 5.22 Total displacement contours of piled raft under vertical loading.

5.5.2 Horizontal load test of piled raft and pile group

In the cyclic horizontal load test of the piled raft and pile group models, a vertical load of 497 N in total was applied on the top of the raft prior to the start of horizontal loading. Although cyclic horizontal loading was applied to the models (Unsever et al., 2014), the behavior in the 1st loading in positive direction is focused in this part. It can be noted that, the horizontal displacement, u, of the piled raft model in the 1st loading in positive direction reached to 22 % of the pile diameter, D (u/D = 0.22). It is also interesting to note that the allowable horizontal displacement of pile foundations for highway bridges in Japan is limited to only 1 % of the pile diameter (u/D = 0.01) (Japan Road Association, 2012). Hence, the behavior in the 1st loading in positive direction (monotonic loading stage) is focused in this chapter.

Finite element mesh of piled raft and pile group models under horizontal loading are given in Figure 5.5 and Figure 5.23, respectively. The only difference between the two cases is the 20 mm space between the raft and the ground at pile group analysis (this phenomena is explained in Chapter 3 in detail).

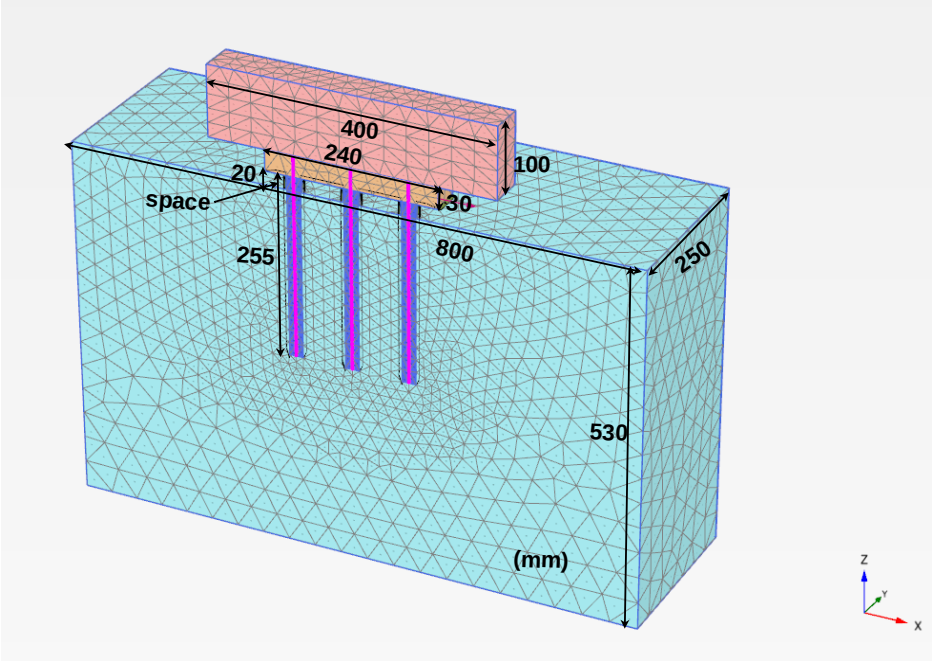

Figure 5.23 Finite element mesh of the pile group model for static horizontal loading test.

The measured and calculated relationships of horizontal load, *H*, and normalized horizontal displacement, *u*/*D*, for both models are shown in Figure 5.24 (a) and (b). The measured and calculated resistances of the 3 piles and the raft in the piled raft are also indicated in Figure 5.24 (a). In the experimental results of piled raft, relatively large oscillation of the horizontal forces of the total, the 3 piles and the raft are observed for *u*/*D* larger than 0.12. As mentioned earlier, horizontal displacement was applied to the raft manually using wires and rotating rods (see Figure 3.53). Hence, unexpected unloading/reloading may have occurred. If we

focus on the experimental results until u/D = 0.12, it is seen that the horizontal load carried by the 3 piles continues to increase with increasing u/D, whereas the raft resistance tends to level off after u/D exceeds about 0.05. Moreover, it is interesting to note that the calculated curves of the total load, the load of 3 piles and the raft load exhibit significant non-linearity before failure, which is in contrast with the calculated results of the vertical loading of the full raft (Figure 5.14) and the piled raft (Figure 5.16).

When measurements and calculations are compared, it is seen that calculation overestimates the experimental results. The calculated raft resistance reaches the maximum at u/D = 0.07 and the resistance of the 3 piles reaches the maximum at u/D = 0.12 resulting in the ultimate state of the horizontal resistance of the piled raft system at u/D = 0.12 (Figure 5.24 (a)).

In Figure 5.24 (b), calculated and measured horizontal load vs. normalized horizontal displacement graph is given for PG. It should be noted that, there is a minor difference between the 3 piles and the total load due to the approximations. The difference between the measurement and the calculation is larger at the beginning of the experiment; however it gets closer at the end, which means that the initial stiffness of the pile group is overestimated by the analysis. Also, the difference between the measurement and calculation is smaller in pile group results than the piled raft case which may be due to the existence of the space between the raft and the ground that prevents the increment of load capacity of the piles during calculation.

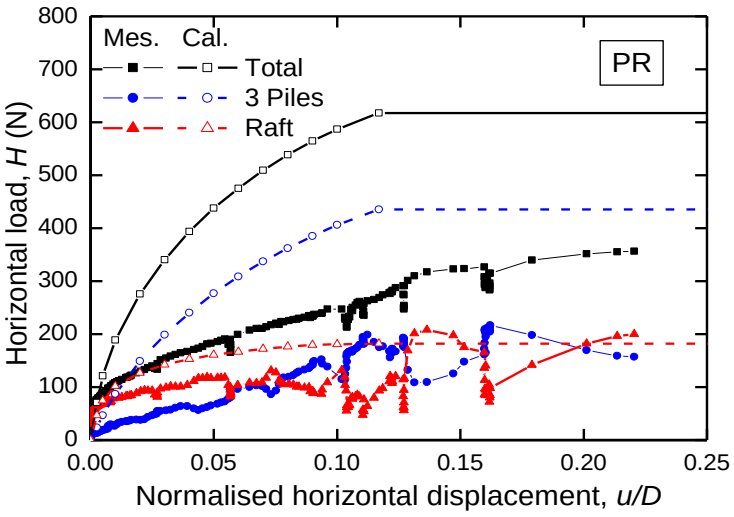

(a)

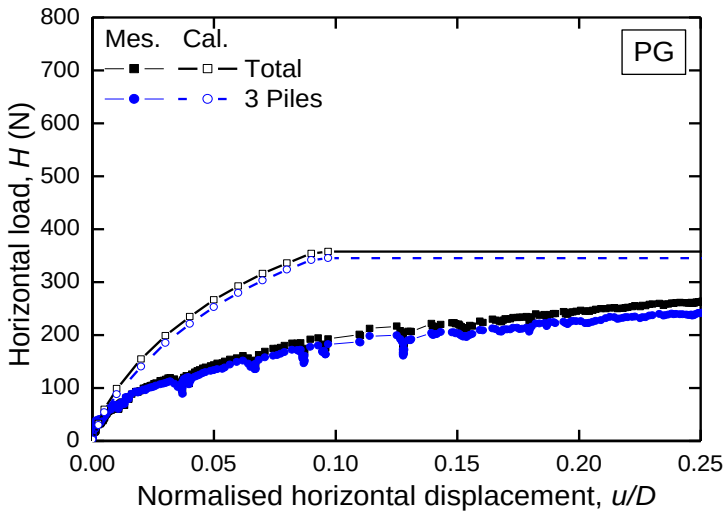

(b)

Figure 5.24 Horizontal load-normalized horizontal displacement relationship of (a) PR (b) PG.

The vertical load at the pile head of each pile in the piled raft is given in Figure 5.25 (a). Before applying the horizontal load on the piled raft, loads carried by all piles are equal in calculations, whereas measured load carried by edge piles, P1 and P3, are equal, which is smaller than that of the center pile (P2). After starting of the horizontal loading, the vertical load on the front pile (P3) starts to increase,

while the vertical load on the rear pile (P1) starts to decrease, which reveals that the contact pressure at the raft base increases around P3 and decreases around P1. Although the measured axial loads are larger than the calculated ones, the calculation simulates well the measured trend of the changes of pile loads. In the measurement, the rear pile P1 had no tensile load before u/D exceeded 0.1. On the contrary, in the calculation, pile P1 starts to be in tension after u/D exceeded 0.04 and the maximum tensile load reaches a relatively large value of 75 N at u/D 0.12. It is attributed to the fact that larger tension load in the rear pile P1 is one of reasons for the calculated larger horizontal resistance of the piles, compared to the measured value.

In Figure 5.25 (b), vertical load at the pile head of each pile in the pile group is shown. From the experiments results, it is seen that, pile components P2 and P3 carry almost the same load, whereas P1 carries more load than those two piles at the beginning of the test. This may be due to the slight tilting of the pile group model towards P1 during the placement of the weights on top of the model. Ignoring this shortcoming, the analysis predicts the measurements well. When horizontal loading started, the behavior of the pile components is similar with that of the piled raft. The measured behaviors of P2 and P3 are estimated well quantitatively and qualitatively.

The shear load carried by each pile in the piled raft and pile group is given in Figure 5.26 (a) and (b). In Figure 5.26 (a), before applying the horizontal load to the piled raft, the shear load carried by each pile is zero as expected. After starting of the horizontal loading, shear load on all piles start to increase, where the front pile, P3 carries the largest shear force, and the rear pile, P1 carries the smallest one. Although the calculated shear loads are larger than the measured ones, the calculation simulates well the measured trend of the changes of pile loads. In the pile group, the same trend with the piled raft is observed (Figure 5.26 (b)). However the shear load capacity of each pile is smaller than that of the piled raft, which is more obvious from the front pile, P3.

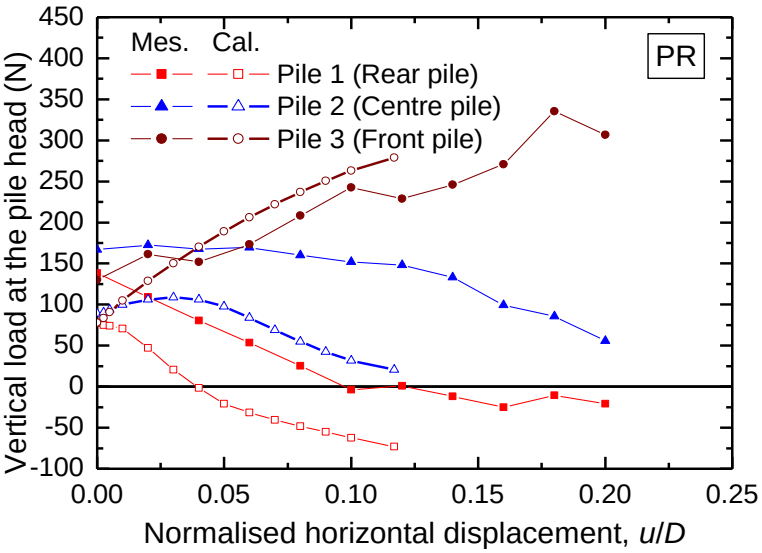

(a)

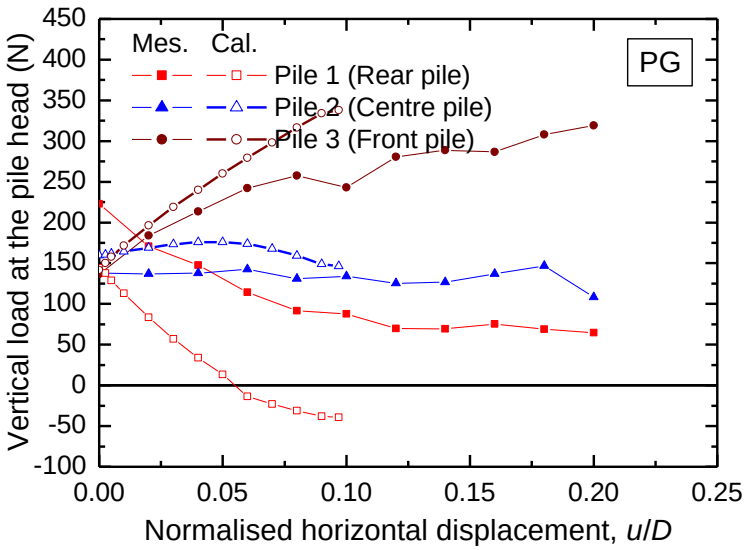

(b)

Figure 5.25 Vertical load-displacement relationships of (a) PR (b) PG.

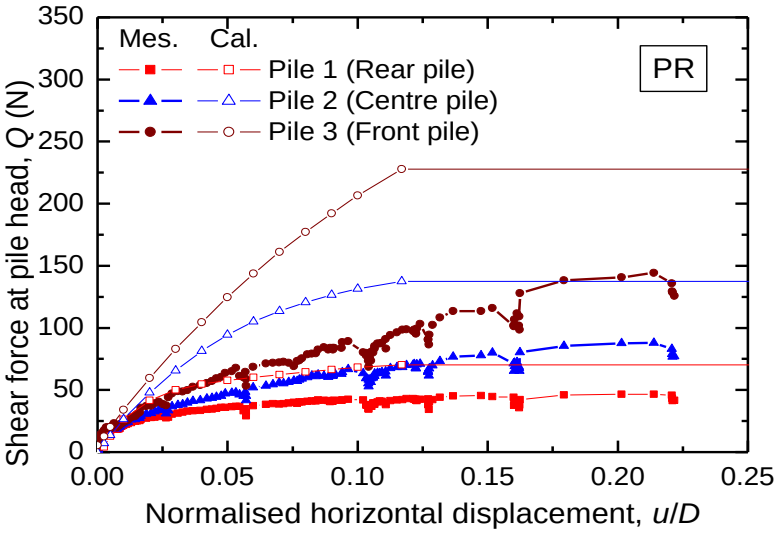

(a)

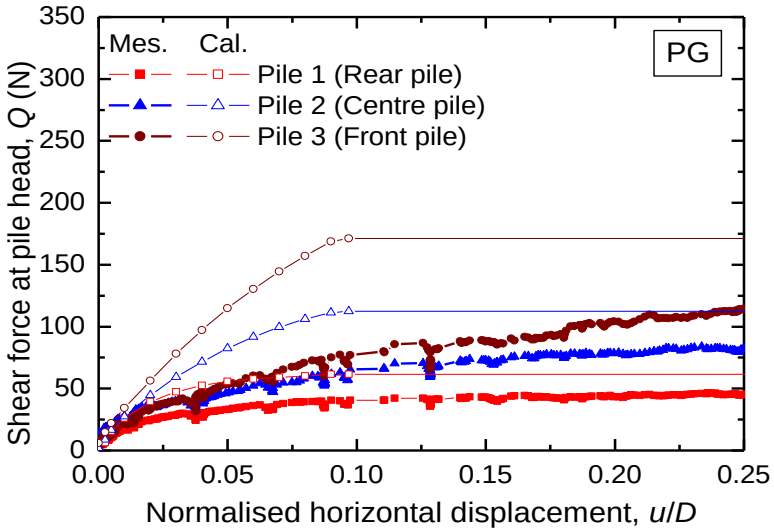

(b)

Figure 5.26 Shear load-displacement relationships of (a) PR (b) PG.

Mean stress contours in the soil for the horizontal loading of the piled raft at the failure are shown in Figure 5.27 (a). As it is seen from the figure, larger stress contours occur around pile P3 than around piles P1 and P2 due to higher raft contact pressures. Higher raft contact pressurei the soil around the front pile P3 increases the horizontal resistance of this pile, resulting in higher bending

moments in pile P3 compared to the center pile P2 and the rear pile P1. When mean stress contours of piled raft and pile group are compared, it is seen that the stress increment around the piles of pile group model (Figure 5.27 (a)) is smaller than that of the piles of piled raft (Figure 5.27 (b)) which causes smaller capacity of the piles in pile group.

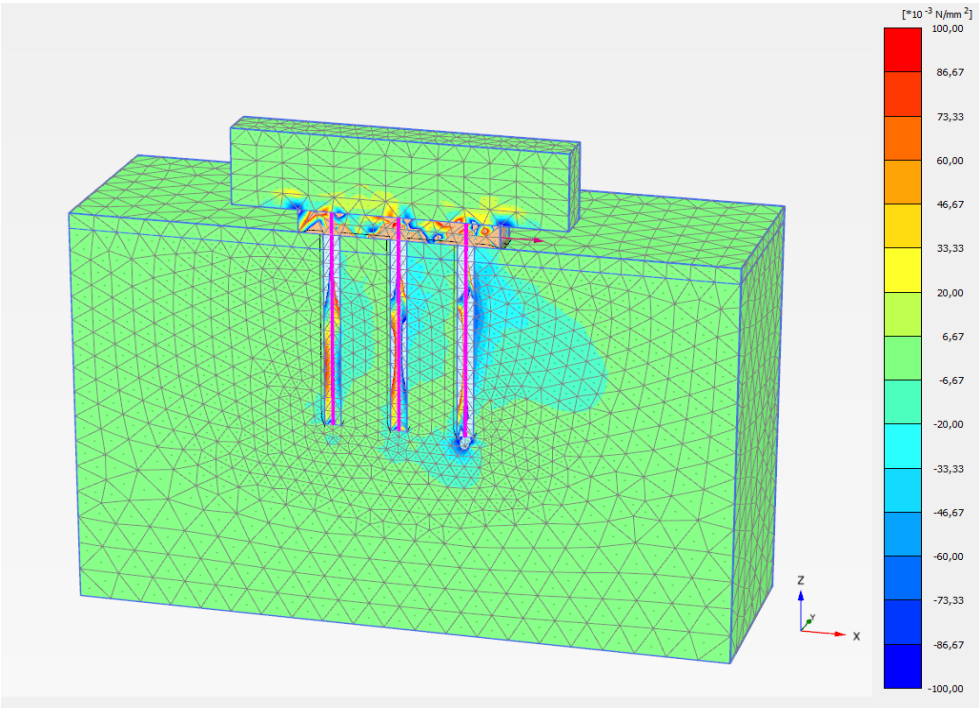

(a)

Figure 5.27 Mean stress contours for horizontal loading analysis (a) PR (b) PG.

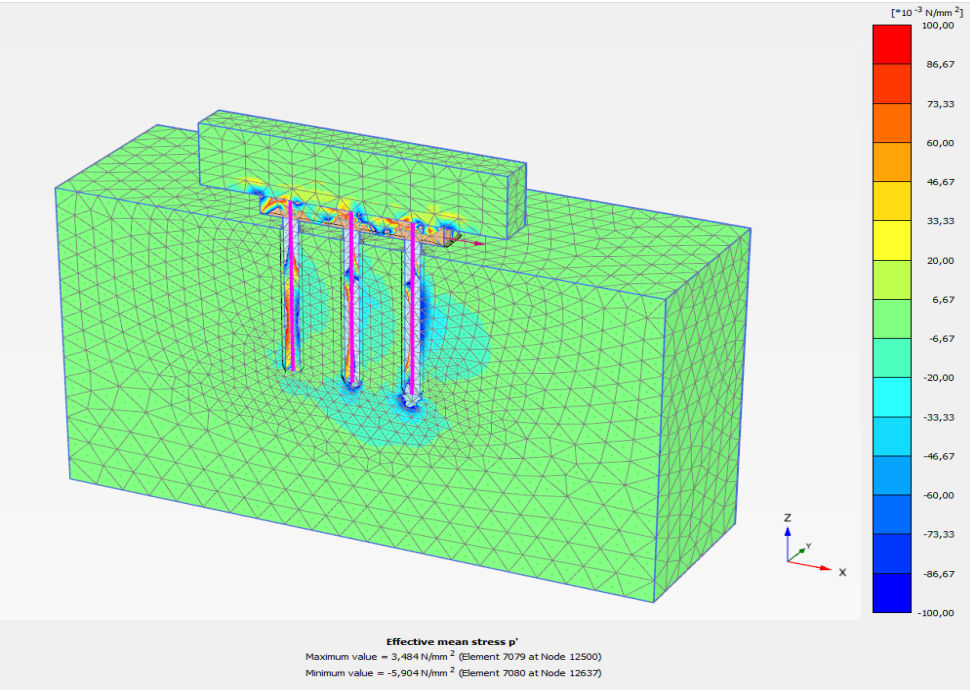

(b)

Figure 5.27 (continued).

Figure 5.28 shows the change in the proportion of horizontal load carried by the raft against *u*/*D*. At the beginning of the horizontal load test, the horizontal load carried by the raft is about 85 %, and it decreases with increasing *u*/*D* and finally becomes constant around 30 %. The calculation simulates well the measured behavior qualitatively and quantitatively.

Proportion of vertical load carried by the raft versus *u*/*D* is given in Figure 5.29. In the experiment, the raft takes 25 % of the vertical load prior to horizontal loading. The proportion decreases with increasing *u*/*D* at early stage of horizontal loading, and then increases with increasing *u*/*D* and finally becomes constant at about 30 % when *u*/*D* reaches 0.12. The calculation result has a similar trend to the measured result, but the proportion of vertical load carried by the raft in the calculation is considerably larger compared to the measured result. According to the calculation, higher pressures are transmitted to the ground from the raft base.

Therefore, soils surrounding the piles are assigned higher stiffness parameters in the calculations resulting in larger strength, hence larger horizontal resistance. Note that, the reason for the scatter in the measurements of Figure 5.28 and Figure 5.29 is due to the manual application of horizontal loads by wooden rods.

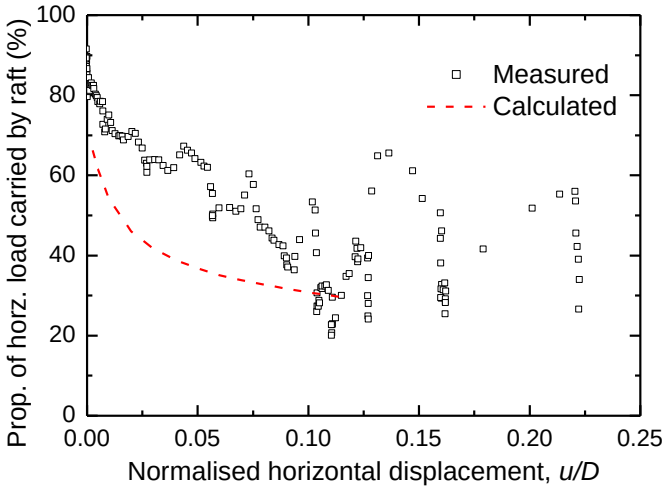

Figure 5.28 Proportion of horizontal load carried by the raft.

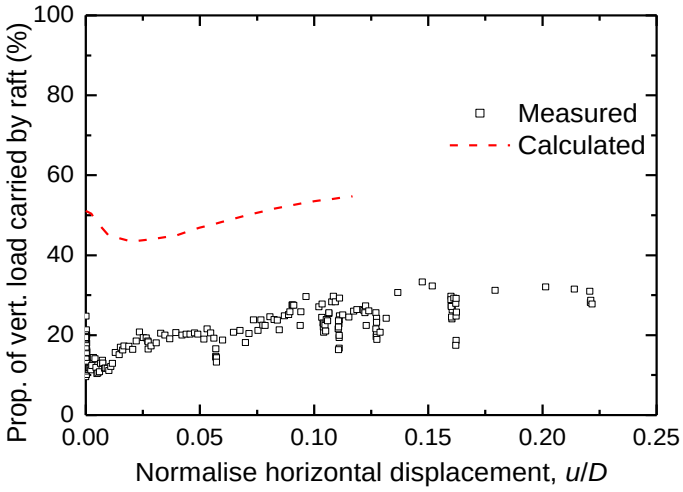

Figure 5.29 Proportion of vertical load carried by the raft.

The bending moments along the pile shaft for P1, P2 and P3 are given through Figure 5.30 (a) - (c) for piled raft model. In the experiment of piled raft, the maximum negative bending moment occurs at the top of each pile. Maximum positive bending moment occurs at depths of 0.55 - 0.60 of the pile length. It is seen from comparison of the figures that the magnitudes of bending moments generated in the front pile, P3 are the largest followed by those of the center pile, P2 and by the rear pile, P1. Similar behavior is observed in the experimental study of Horikoshi et al. (2003a). Although the calculation overestimates the measured bending moments considerably, the calculation simulates well the trends of measured distributions in all piles. As discussed earlier, the larger proportion of vertical load supported by the raft in the calculation and its effects on the stiffness and the strength of the soil surrounding the piles resulted in the overestimation of the bending moments of the piles.

Bending moment measurements and calculations for horizontal loading test of pile group for each pile member are shown in Figure 5.31 (a) - (c). Although, the total load carried by pile group is considerably smaller than that of piled raft, the bending moments along each pile are similar to that of piled raft for both measurements and calculations, which shows the advantage of piled raft over pile group.

When measured shear forces along each pile shaft is investigated for both piled raft (Figure 5.32 (a) - (c)) and pile group models (Figure 5.33 (a) - (c)), it is seen that they have largest value at top of the piles and they decrease gradually along the pile shaft. Moreover, front pile, P3 carries more shear load than other two piles, which is followed by the center pile, P2, and rear pile, P1. Negative calculated values at depth, z = 0 mm is due to the raft-pile connection. If these negative values are ignored, it is seen that calculation results have similar behavior with the measurements, although they are overestimated, which is also the case for bending moment distributions. Moreover, calculated and measured shear forces on piles have similar trends for piled raft and pile group, whereas

shear forces on piled raft are slightly larger than pile group case because of the stress increment in soil, which is due to the load transfer through the raft.

Axial forces along each pile during horizontal loading of piled raft are given in Figure 5.34 (a) - (c). In the experiment, the axial load carried by the rear pile, P1 decreases, whereas the axial load on the front pile, P3 increases with the increased applied load. The increment of the displacement has minor effect on the axial load along the center pile, P2. In pile group experiment, similar behavior is observed with the measured piled raft results of piles, P1 and P3 (Figure 5.35 (a) and (c)). Moreover, the measured axial load along the center pile is almost constant along the pile shaft and also it has minor changes during loading as in the center pile of piled raft model (Figure 5.35 (b)). In the calculations, the behaviors of the front pile and the rear pile are captured well, however decrement of the axial load along the middle pile is somehow overestimated.

Total displacement contours of piled raft and pile group are shown in Figure 5.36 (a) – (b). Since the loads are transmitted through the raft in piled raft analysis, the model ground has larger displacement in a wider area than that of pile group. However, the displacement at the pile tip of the front pile, P3 is larger at pile group analysis than that of piled raft analysis which indicates the advantage of the raft.

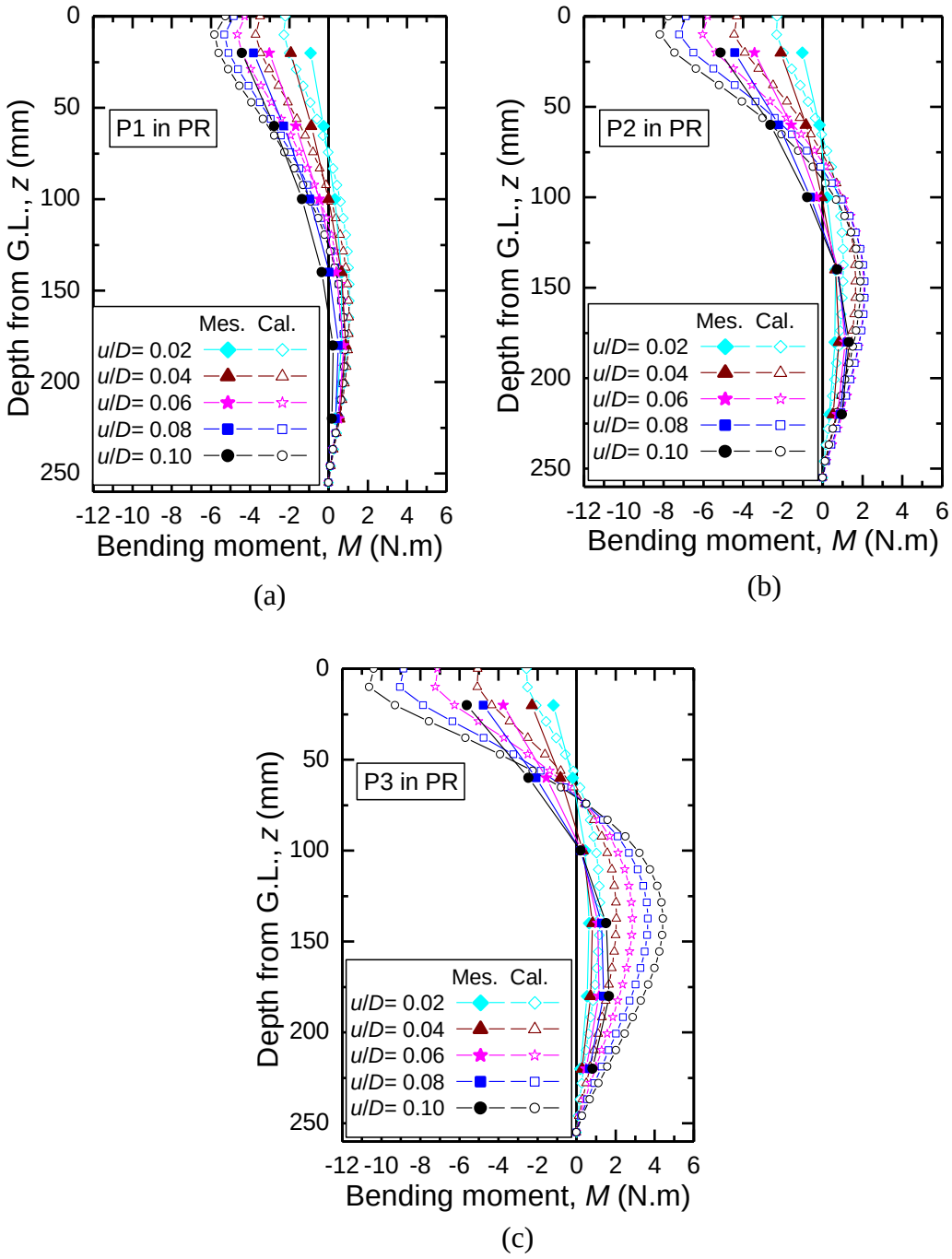

Figure 5.30 Bending moment distribution along each pile shaft (P1, P2 and P3) for piled raft.

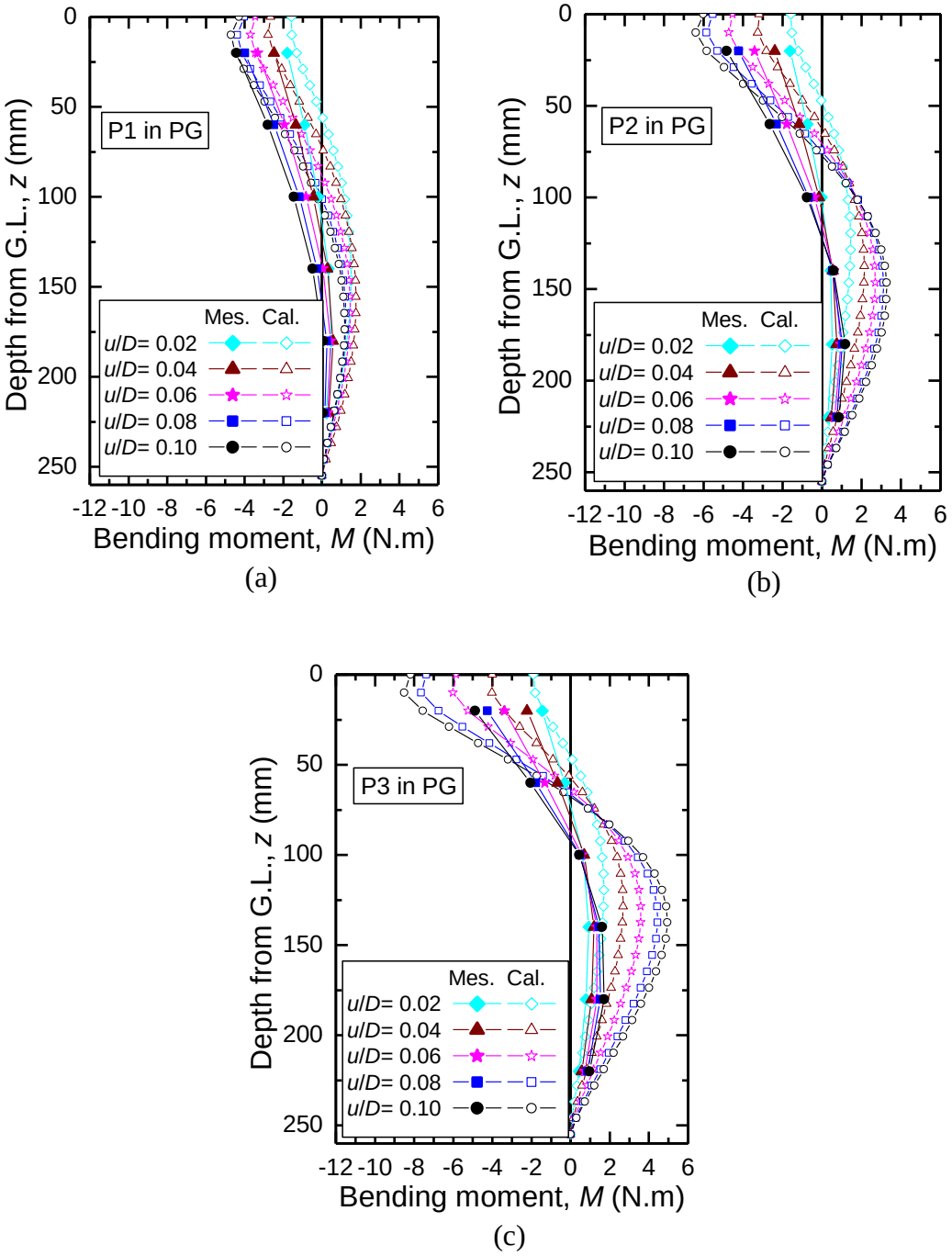

Figure 5.31 Bending moment distribution along each pile shaft (P1, P2 and P3) for pile group.

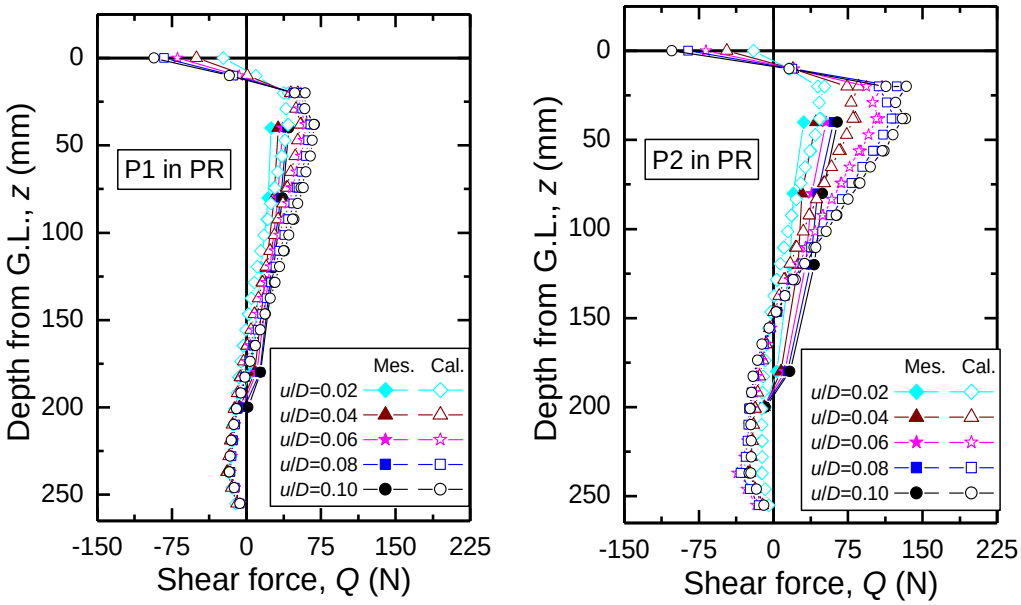

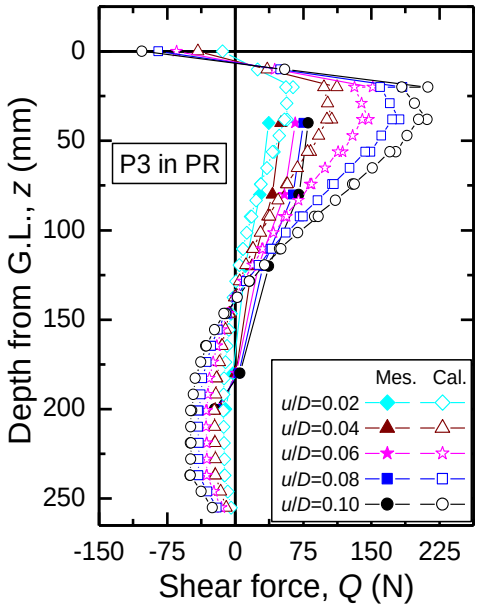

Figure 5.32 Shear force distribution along each pile shaft (P1, P2 and P3) for piled raft.

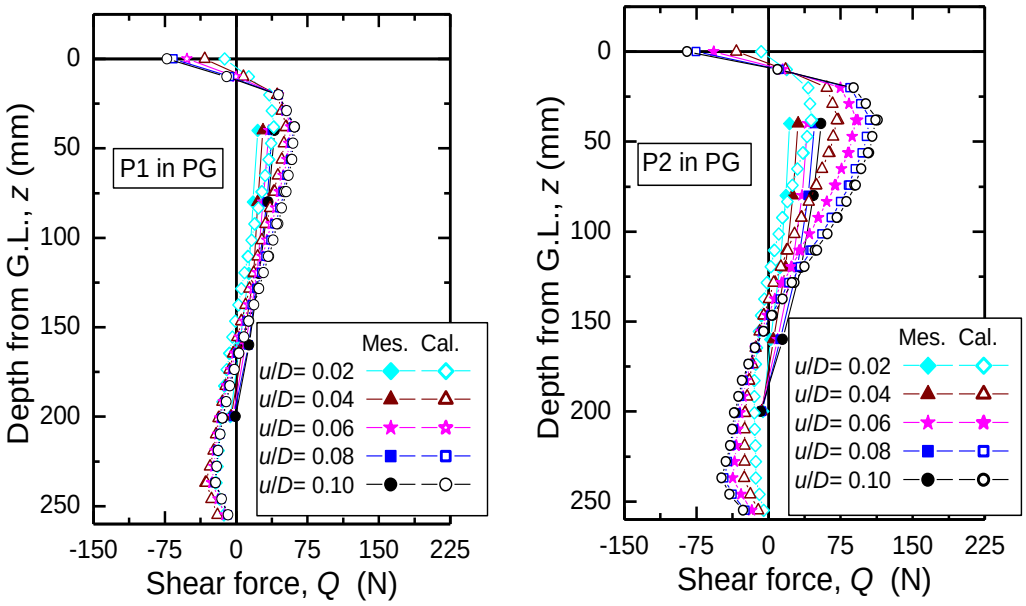

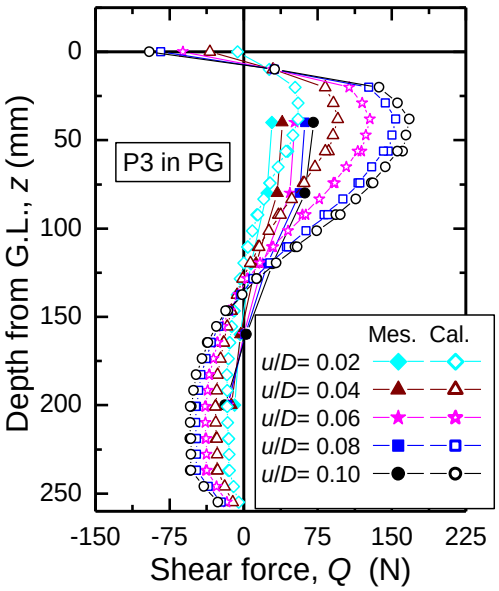

Figure 5.33 Shear force distribution along each pile shaft (P1, P2 and P3) for pile group.

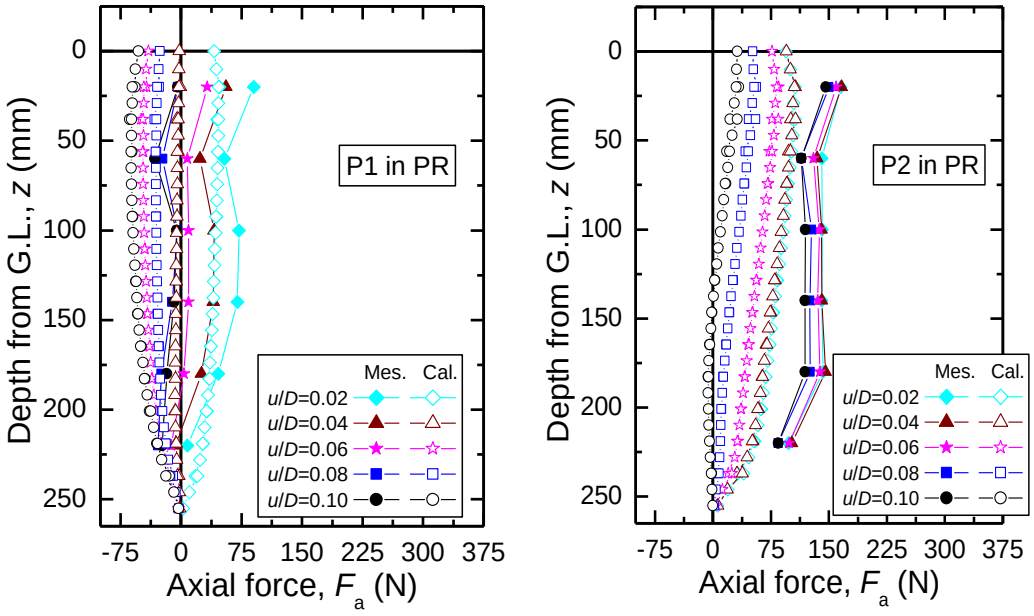

(a)

(b)

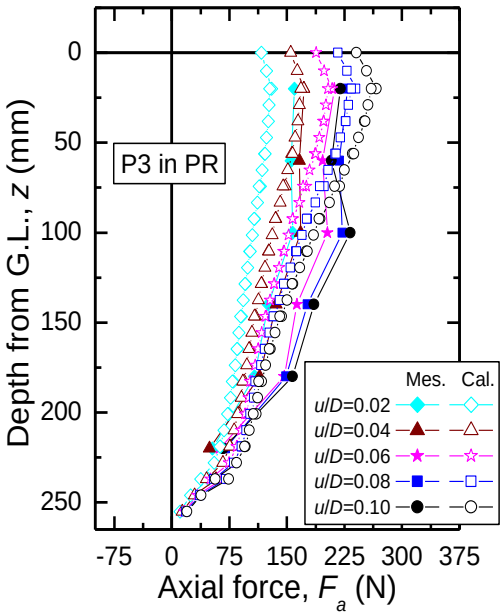

(c)

Figure 5.34 Axial force distribution along each pile shaft (P1, P2 and P3) for piled raft.

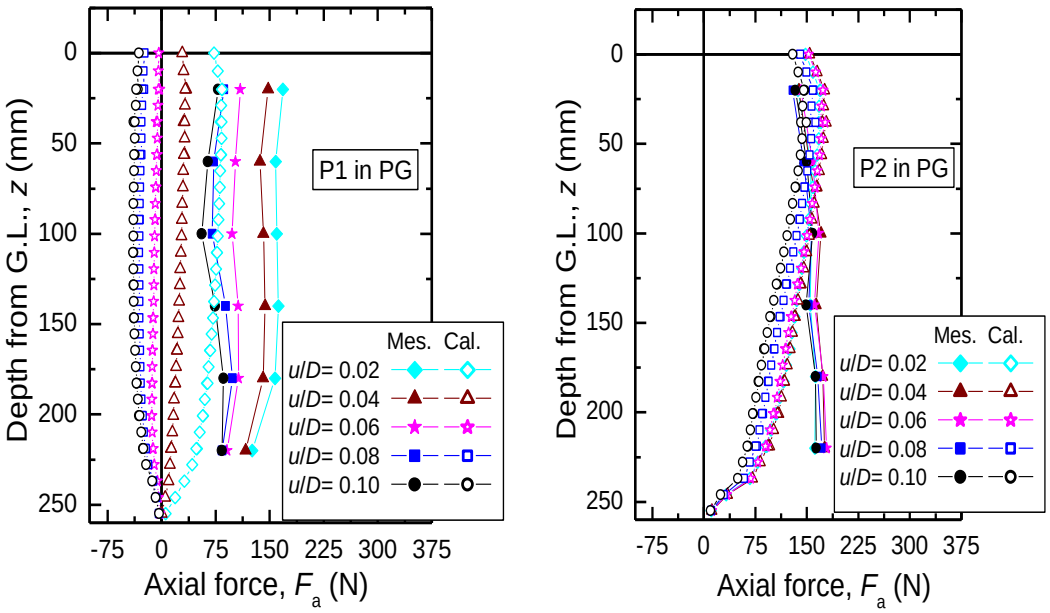

(a)

(b)

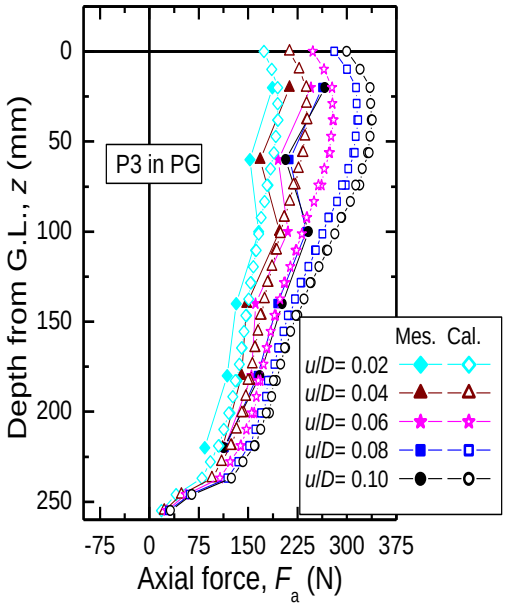

(c)

Figure 5.35 Axial force distribution along each pile shaft (P1, P2 and P3) for pile group.

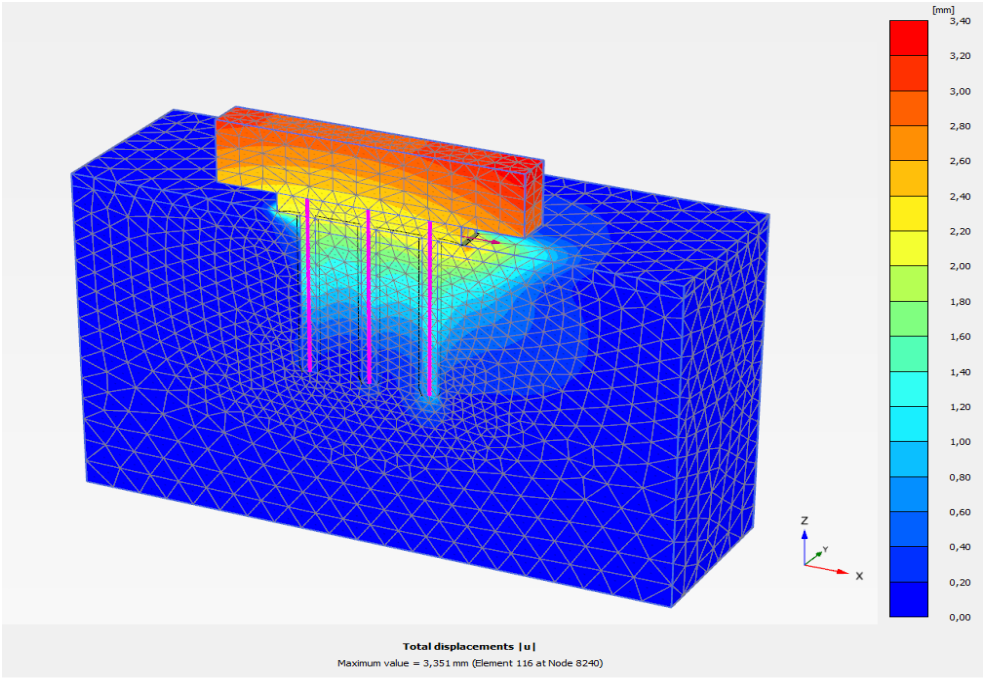

(a)

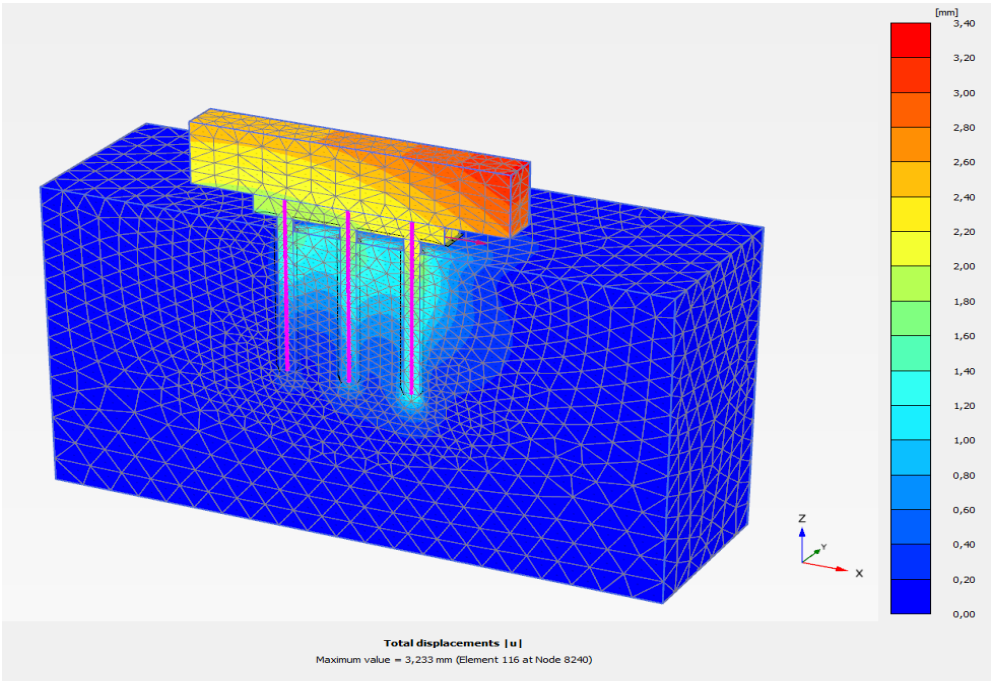

(b)

Figure 5.36 Total displacement contours under horizontal loading (a) PR (b) PG.

5.6 Conclusions

A series of vertical and cyclic horizontal loading tests on single pile, full raft, piled raft and pile group models were carried out in dry sand to investigate the resistance mechanisms of the piled raft. FEM modelling of the experiments were conducted to obtain more insight into the mechanisms and to explore a possible design approach. It should be noted that, only first step of cyclic horizontal load test is simulated in analyses due to the limitations of FEM.

The numerical calculations of the various experiments were carried out using a unique set of soil parameters of Hardening soil model estimated from the triaxial CD tests of the sand and its FEM analyses. The numerical calculations for vertical loading of the single pile, the full raft and the piled raft models simulate the experimental results reasonably well quantitatively and qualitatively. Although the numerical calculation of the horizontal loading of the piled raft does not yield an excellent simulation of the measured behaviors quantitatively, the numerical calculation simulates the trends of the experimental results reasonably well.

From the numerical calculation results as well as the experimental results in the range of this study, the following implications have been derived for the pile raft subjected to combination of vertical and horizontal loads:

The behavior of the piled raft is not mere summation of the components of raft and piles beneath the raft, but is largely influenced by the interaction of the components as well as the level of the applied load.

Raft has an important contribution on the behavior of piled raft, i.e., transmitting of vertical load through the raft which causes stress increment in the soil. The load carried by pile components varies during vertical and horizontal loading depending on this stress increment.

CHAPTER 6

SUMMARY, CONCLUSIONS AND RECOMMENDATIONS

6.1 Summary

In this study, results of physical model tests and numerical simulations on the static and dynamic behavior of piled raft foundations were presented. For this purpose, vertical load tests, cyclic horizontal load tests and shaking table tests were carried out on various model foundations; such as piled raft, pile group, full raft and single pile in dry sand condition to investigate the response of the foundations. Numerical analyses were performed using the finite element software, PLAXIS 3D, 2013.

Model piles were aluminum pipe piles having 255 mm effective length and 20 mm diameter with 1.1 mm wall thickness. Therefore, they can be considered as short piles. They were also friction piles since their tips were not fixed to the bottom of the soil box. Piled raft (or pile group) was composed of 3 friction piles and a raft having dimensions of 240 mm × 80 mm × 30 mm and the spacing between the piles was 4 times the diameter of the piles. The model ground was silica sand #6 which had a constant relative density of 70 % throughout the study. The properties of the model ground (silica sand) were determined by laboratory tests.

In both shaking table and static cyclic horizontal load tests, vertical load was applied to the models prior to the start of horizontal loading, in order to take into account the superstructure effect on the foundation behavior. All 1-g model tests were performed in a laminar container (having 800 mm length, 500 mm width and

530 mm height. In shaking table tests, sinusoidal waves having constant amplitude with 5 Hz and 20 Hz frequencies were applied as an input motion.

Static and dynamic behaviors of model foundations were discussed in terms of contribution of the raft contact, interaction of the piles and raft and generated accelerations in model ground and on model foundation under “low” and “high” frequencies. The behavior of the various model foundations under static monotonic horizontal loading and vertical loading were also compared with those calculated by finite element analyses.

6.2 Conclusions

Main findings from the experiments and implications for design of piled raft foundations based on the experimental and numerical results in this research are summarized in two parts.

6.2.1 Conclusions regarding static test results and finite element analyses

1) Vertical load test results of capped pile (CP) (composed of a single pile and a small raft), single pile (SP) and small raft (SR) (without pile) show that, the response of capped pile cannot be obtained by merely summing the response of small raft and single pile due to the interaction between the raft and the pile. When the response of single pile is compared to the pile component of capped pile, the resistance of the pile in capped pile is slightly larger than that of the single pile. It may be attributed to the fact that a part of the applied vertical load is transferred to the ground through the raft base, which results in an increase of stiffness and strength of the ground and also an increase of horizontal stresses acting on the pile shaft.

2) 3 × single pile, full raft and piled raft responses were examined under vertical loading. The interaction between the piles and the raft could be observed

largely in the piled raft than in capped pile-single pile case. Sharing of the applied load between 3 piles and the raft shows that although 3 piles carry most of the load until 0.8 mm settlement of the raft, the raft carries more load than the piles after that settlement due to the yielding of the piles. After that, 3 piles start to carry slightly larger load (60 % of the applied vertical load) than the raft (40 % of the applied vertical load).

Another important point is the axial forces along the center pile (P2) (carries 40 % of the sum of the total load carried by 3 piles) are larger than those of the edge piles (P1 and P3) (each of which carries 30 % of the total load carried by 3 piles), which may be due to the larger confining stresses around the center pile caused by the contact pressure of the raft. It may be reasonable to assume that the stress level in the soil surrounding P2 is higher than that surrounding P1 and P3.

3) The results of static cyclic horizontal load test of capped pile with and without vertical loading shows the effect of vertical loads simulating the superstructure effect, indicating that existence of vertical load increases the horizontal load carrying capacity of the model.

4) The horizontal loading tests on small raft and full raft indicates that, rafts may be considered as "horizontal displacement reducers" until slippage occurs. Initial horizontal stiffness, k_h, of both small and full rafts tends to increase as the contact pressure increases, which also may be attributed to the load transfer from raft to the ground.

5) The horizontal tests of piled raft and pile group were performed under a constant vertical load of 497 N. Horizontal resistance of the piled raft is found to be larger than that of the pile group as expected because of the contribution of the raft. In both cases, the front pile carries most of the horizontal load (60 % and 58 % of the total horizontal load for piled raft and pile group,

respectively), the rear pile carries the least (5 % and 10 % of the total horizontal load for piled raft and pile group, respectively) and the center pile carries almost the same amount of load under positive and negative loading (20 % and 32 % of the total horizontal load for piled raft and pile group, respectively). This result may be due to the changes in load transfer from the raft to the soil depending on the pile positions and due to the interaction among the members of the structure in the soil.

In literature, the first test on a pile group with two rows with 2*D* pile spacing was carried out at 1-g by Barton (1984), and it was stated that front row carries 60 % of the lateral load, and rear row carries 40 %. McVay et al. (1995) also studied on three row pile groups (3 × 3) with 3*D* and 5*D* spacing under lateral loading by centrifuge test (45*g*), it was indicated that group distribution varies 41 %, 32 %, 27 % for 3*D* spacing to 36 %, 33 %, 31 % for 5*D* spacing in medium dense sand ground. In this study, as it was stated pile lateral load sharing was found as 58 %, 32 %, 10 % for 4*D* spacing of pile group, which are in general agreement with the studies cited.

6) The settlement of the piled raft is half of the pile group settlement, which is advantage of the piled raft. For both of the models, inclination of the raft is linearly related with the horizontal displacement, in other words inclination increases with horizontal displacements.

7) Bending moments are maximum at the top of the pile, both for positive and negative loading of piled raft and pile group models. Larger bending moments are observed along the front pile rather than the rear pile. In case of center pile, bending moments and shear loads are equal for both positive and negative loadings. Bending moments of the piles in the piled raft is slightly larger than the piles in the pile group, thus the horizontal loading capacity of the piled raft increases without an increase of bending moments along the piles. Nevertheless, shear forces on piles of piled raft are about 50 % larger than the

piles of pile group, which is to say that the shear forces on piles are more critical than bending moments for piles in piled rafts.

8) For piled raft and pile group models, most of the axial forces are carried by the front piles (55 % and 65 % of the total axial load at u/D = 0.2 for piled raft and pile group, respectively) during static cyclic horizontal loading. Centre pile and rear pile carry 12 %, 8 % and 23 %, 12 % of the total axial load at u/D = 0.2 for piled raft and pile group, respectively. It can be stated that, the axial forces carried by piles of piled raft are smaller than that of pile group showing the contribution of the raft.

9) In Japan, many buildings were observed by field monitoring systems (Yamada et al., 2001, Yamashita et al., 2014, Yamashita et al., 2011a, Yamashita et al., 2012). Yamada et al. (2001) stated that 40 % - 45 % of the total axial load was carried by piles in a 12 stories building. Yamashita et al. (2011a) monitored many instrumented buildings with piled raft foundation in Japan nothing that piles carried about 54 % of the total vertical load after the end of construction and this value increases to 55 % - 65 % after water level increased. Yamashita et al. (2012) monitored a base isolated building on soft ground in Tokyo, where the axial load sharing of piles was measured as 66 % in average. Another study on piled raft showed that the ratios of the axial load carried by the piles to the effective stress were between 67 % - 85 % and 57 % - 82 % before and after the earthquake according to the position of the pile, respectively (Yamashita et al., 2014). In this study, it is found that 3 piles carry about 60 % of applied vertical load during vertical loading of piled raft, and 3 piles carry 60 % to 90 % of the applied vertical load during static cyclic horizontal loading of piled raft. Results of this study are compatible with the researches cited above, as given in conclusion (8).

10) The behavior of model foundations under vertical loading is estimated fairly well with finite element analyses. However, the calculated load-settlement

curves exhibit bi-linear responses for all model foundations. This may be primarily due to the dilatancy angle assumption made in finite element model. Unfortunately, the reduction of dilatancy angle under large stress levels couldn't be modelled by hardening soil model.

11) In numerical analyses of model foundations under horizontal loading, the initial state of loading in positive direction was focused. It is observed that the predictions of finite element analysis are relatively larger than the measured results of physical model tests. However, predictions are consistent with measurements in assessing the general trend.

6.2.2 Conclusions regarding dynamic test results

1) The resonant frequency of the model ground is estimated to be 20 Hz from the experiments on model ground alone. Hence, it was decided to conduct main part of the dynamic tests with 20 Hz frequency.

2) The results of shaking table tests on piled raft and pile group under 20 Hz frequency indicate that although the horizontal loads carried by piles are similar in both models, piled raft carries twice more load than the pile group due to the mobilization of the raft base resistance. During dynamic loading, most of the axial load is carried by the front pile in both models, as it was observed in static tests.

3) Horizontal displacement of piled raft is smaller than that of the pile group under similar excitations. Thus, it can be said that an advantage of piled raft over pile group is smaller settlements as compared with the pile group settlements. On the other hand, inclinations of the raft are similar for piled raft and the pile group tests.

4) Horizontal load - horizontal deflection relationship shows that initial stiffness of the piled raft is larger than that of the full raft (raft without piles). Also, it is seen that the horizontal displacement of the piled raft is smaller than the displacement of full raft. Therefore, the piles under the raft contribute to increase stiffness and decrease horizontal displacement under dynamic loading.

5) The measured acceleration amplitude of the piled raft is smaller than the amplitude of the input motion in 20 Hz test, whereas the measured acceleration amplitude on the piled raft is larger than that of the input acceleration at 5 Hz test. This may be due to the different natural frequencies of the superstructure – foundation – model ground system and model ground without foundation, which is estimated as 20 Hz.

6) The raft resistance prevents the sudden failure of the foundation under 5 Hz frequency dynamic loading, despite the large deformation experienced and vertical and horizontal resistances of the piles are greatly reduced.

7) Dynamic test results under low frequency shaking (5 Hz) are comparable with the static cyclic load test results. Therefore, it is reasonable to accept that, inertial effect is predominant rather than kinematic effect on the foundation behavior. On the contrary to low frequency tests, the behavior of the model foundations under higher frequencies could not be conjectured from static cyclic load tests.

The purpose of this study is to have a deeper understanding of the behavior of the piled raft subjected to vertical and horizontal loading. It is difficult to apply the experimental results on small model directly to prototypes. However, it is suggested that an appropriate combination of soil tests and numerical analyses may be utilized in the design of prototype foundation structures.

The experimental work presented in this study on the pile-soil-pile, pile-soil-raft and raft-soil interactions and the contribution of the raft under vertical and horizontal loading, demonstrates that ignoring the raft resistance may cause uneconomical designs.

6.3 Recommendations for Future Studies

In the scope of this study, the testing conditions are limited due to the nature of the research. To have a deeper understanding of the soil response, more data and analysis are required to be carried out in different soil types such as saturated sand and cohesive soils. Greater configurations of model foundations such as longer piles having different pile spacing in a larger laminar box with various combinations of loads could be tested under static cyclic and dynamic loads having various frequencies and amplitudes. In order to validate the results and to adopt the results to the design procedures, full scale model tests on large group of piles and centrifuge tests on smaller scales may be conducted by measuring settlement, horizontal and vertical loads generated on the foundation. Also, further studies on the behavior of model foundations under dynamic loads could be performed by three dimensional finite element analyses will be helpful to improve our current knowledge.

REFERENCES

Barton YO. (1984) Response of pile groups to lateral loading in the centrifuge. *Application of Centrifuge Modelling to Geotechnical Design*, Rotterdam: Balkema, 457-474.

Baziar MH, Ghorbani A, Katzenbach R. (2009) Small-scale model test and three-dimensional analysis of piled-raft foundation on medium-dense sand. *Int. Journal of Civil Engineering*, 7 (3): 170-175.

Boulanger RW, Curras CJ, Kutter BL, Wilson DW, Abghari, A. (1999) Seismic soil-pile-structure interaction experiments and analyses. *Journal of Geotechnical and Geoenvironmental Engineering, ASCE*, 125 (9): 750-759.

Brown DA, Morrison C, Reese LC. (1988) Lateral load behavior of pile group in sand. Journal of Geotechnical Engineering, ASCE, 114 (11): 1261-1276.

Butterfield R, Banerjee PK. (1971) The problem of pile group-pile cap interaction. *Géotechnique,* 21 (2): 135-142.

Castelli F, Maugeri M. (2009) Simplified approach for the seismic response of a pile foundation. *Journal of Geotechnical and Geoenvironmental Engineering*, ASCE, 135 (10): 1440-1451.

Chang YL. (1937) Discussion of lateral pile loading tests. *Transactions of ASCE*, 102: 272-278.

Coduto DP. (1994) Foundation design principles and practices. *Published by Prentice-Hall*, New Jersey.

Cubrinovski M, Sugita H, Tokimatsu K, Sato M. Ishihara K., Tsukamoto Y, Kamata T. (2005) 3-D numerical simulation of shake-table tests on piles subjected to lateral spreading. *Proc. Geotechnical Earthquake Engineering Sattellite Conf.*, Osaka, 199-206.

Duncan JM, Chang CY (1970) Nonlinear analysis of stress and strain in soil. *Journal of Soil Mech. Found. Div. ASCE*, 96: 1629-1653.

Duncan JM, Byrne P, Wong KS, Mabry P. (1980) Strength, stress-strain and bulk modulus parameters for finite element analyses of stresses and movements in soil masses. *Report No. UCB/GT/80-01, Office of Research Services University of California*, Berkeley California, 20-49.

Duncan J, Bursey A (2013) Soil Modulus Correlations. *Foundation Engineering in the Face of Uncertainty, Published by ASCE*, 321-336.

El-Mossallamy, Y. (1999) Load settlement behavior of large diameter bored piles in over-consolidated clay. *Numerical Models in Geomechanics, NUMOG VII, 1999* Rotterdam: Balkema, 443-450.

Feng S, Wang J. (2006) Research on lateral resistance of pile in saturated sand under shake loading. *ASCE GeoShangai Int. Conference 2006*, Shangai, China, 490-497.

Finn WDL, Fujita N. (2002) Piles in liquefiable soils: seismic analysis and design issues. Soil Dynamics and Earthquake Engineering, 22: 731-742.

Finn WDL. (2005) A study of piles during earthquakes: Issues of design and analysis. *Bulletin of Earthquake Engineering*, 3 (2): 141-234.

Franke E, Lutz B, El-Mossallamy Y. (1994) Measurements and numerical modelling of high rise building foundations on Frankfurt clay. *Vertical and Horizontal Deformation of Foundations and Embankments, Geotechnical Special Publication*, 40: 1325-1336.

Gazetas G, Dobry R. (1984) Horizontal response of piles in layered soils. *Journal of Geotechnical Engineering, ASCE,* 110 (1): 20-40.

Hecht T, Dürwang R. (2001) Optimierung der Gründung der Reichenbachtalbrükemit der Kominierten Pfahl-Plattengrüdung. *Pfahl-Symposium 2001*, 21-34.

Horikoshi K, Matsumoto T, Hashizume Y, Watanabe T, Fukuyama H. (2003a) Performance of piled raft foundations subjected to static horizontal loads. *IJPMG-International Journal of Physical Modelling in Geotechnics*, 3 (2): 37-50.

Horikoshi K, Matsumoto T, Hashizume Y, Watanabe, T. (2003b) Performance of piled raft foundations subjected to dynamic loading. *Int. Journal of Physical Modelling in Geotechnics*, 3 (2): 51-62.

Hutchinson T, Chai YH, Boulanger RW. (2005) Simulation of full-scale cyclic lateral load tests on piles. *Journal of Geotechnical and Geoenvironmental Engineering, ASCE,* 131 (9): 1172-1175.

Iai S. (1989) Similitude for shaking table tests on soil-structure-fluid model in 1g gravitational field. *Soil and Foundations*, 29 (1): 105-118.

Idriss I, Sun J. (1992) User's Manual for Shake 91. *Center for Geotechnical Modelling, University of California*, Davis.

Irshad A, Akhtar NK. (2006) Kinematic seismic response of piles importance and modelling. *ASCE Geocongress 2006*, Atlanta, US, 187 (176): 1-6.

Ishizaki S, Tokimatsu K, Nagao T. (2012) Overview of semi-rigid pile head connection methods and their effect on buildings in liquefiable soil. *Proc. the 9th Int. Conf. on Testing and Design Methods for Deep Foundations: IS- Kanazawa 2012*, 13-24.

Kagawa T, Sato M, Minowa C, Abe A, Tazoh T. (2004) Centrifuge simulation of large-scale shaking table tests: Case studies. *Journal of Geotechnical and Geoenvironmental Engineering, ASCE*, 130 (7) 663-672.

Kasali G, Lemke J, Jabakhanji R, Mabsout M. (2006) Finite element model of dynamic pile test using embedded transducers. *ASCE Geocongress 2006*, Atlanta, US, 187 (179): 1-6.

Katzenbach R, Arslan U, Moorman C, Reul O. (1998) Piled raft foundation: Interaction between piles and raft. *Darmstadt Geotechnics, Darmstadt University of Technology*, (4): 279-296.

Katzenbach R, Leppla S. (2013) Economic solutions for geotechnical challenges like super high-rise buildings and urban tunneling. *Int. Conf. State of the art of pile foundation and pile case histories*, Indonesia, A1-1-A1-12.

Kaynia AM, Mahzooni S. (1996) Forces in pile foundations under seismic loading. *Journal of Engineering Mechanics, ASCE*, 122 (1): 46-53.

Kim Y, Jeong S. (2011) Analysis of soil resistance on laterally loaded piles based on 3D soil-pile interaction. *Computer and Geotechnics*, 38: 248-257.

Kimura M, Zhang F. (2000) Seismic evaluations of pile foundations with three different methods based on three-dimensional elasto-plastic finite element analysis. *Soils and Foundations*, 40 (5): 113-132.

Kitiyodom P, Matsumoto T. (2002) A simplified analysis method for raft and pile group foundations with batter piles. *Int. Journal for Numerical and Analytical Methods in Geomechanics*, (26): 1349-1369.

Kitiyodom P, Matsumoto T. (2003) A simplified analysis method for piled raft foundations in non-homogeneous soils. *Int. Journal for Numerical and Analytical Methods in Geomechanics*, 27: 85-109.

Konagai K, Ahsan R. (2002) Simulation of nonlinear soil-structure interaction on a shaking table. *Journal of Earthquake Engineering*, 06 (01): 31-51.

Matsumoto T, Fukumura K, Kitiyodom P, Oki A, Horikoshi K. (2004a) Experimental and analytical study on behaviour of model piled rafts in sand subjected to horizontal and moment loading. *Int. Journal of Physical Modelling in Geotechnics,* 4 (3): 1-19.

Matsumoto T, Fukumura K, Horikoshi K, Oki A. (2004b) Shaking table tests on model piled rafts in sand considering influence of superstructures. *Int. Journal of Physical Modelling in Geotechnics,* 4 (3): 21-38.

Matsumoto T, Fujita M, Mikami H, Yaegashi K, Arai T, Kitiyodom P. (2010) Load tests of piled raft models with different pile head connection conditions and their analyses. *Soils and Foundations,* 50 (1): 63-81.

Matsumoto T. (2013) Implications for design of piled raft foundations subjected lateral loading. *Proc. Int. Symp. on Advances in Foundation Engineering,* Singapore, 113-136.

McVay M, Casper R, Shang T. (1995) Lateral response of three-row groups in loose to dense sands at 3D and 5D pile spacing. *Journal of Geotechnical Engineering*. 121 (5) 436-441.

Meymand PJ, Riemer MF, Seed RB. (2000) Large scale shaking table tests of seismic soil-pile interaction in soft clay. *12th World Conference on Earthquake Engineering,* Auckland, New Zeland, 915.

Murono T, Nishumura A, Nagazuma M. (1997) Model test on a group-pile considering the vibration of ground in seismic evaluation. *Proc. of the 24th Symp. of Japan Earthquake Engrg.*, 625-628.

Oh EYN, Huang M, Surarak C, Adamec R, Balasurbamaniam AS. (2008) Finite element modelling for piled raft foundation in sand. *11th East Asia-Pacific Conference on Structural Eng. & Construction*, Taipei, Taiwan, 1-11.

Ordu E, Özkan MT. (2006) Kazıklı temellerin deprem performanslarının üç boyutlu sonlu elemanlar yöntemi ile incelenmesi. *İtü dergisi*, 5 (2): 27-34. *(in Turkish)*

Plaxis BV (2013) *Netherlands User Manuals,* Plaxis 3D.

Poulos HG, Davis EH. (1980) Pile foundation analysis and design. *Published by Rainbow-Bridge Book. Co.,* Canada.

Poulos HG, Davis EH. (2005) AJ Foundation design for the Emirates Twin Towers, Dubai. *Canadian Geotechnical Journal,* 2: 716-730.

Poulos HG, Small JC, Chow H. (2011) Piled raft foundations for tall buildings. *Geotech. Eng. Journal of SEAGS & AGSSEA*, 46 (2): 78-84.

Prakash S. (1981) Soil dynamics. *Published by McGraw-Hill*, United States of America.

Prakash S, Sharma HD. (1990) Pile foundations in engineering practice. *Published by John Wiley & Sons, Inc.,* United States of America.

Ramachandran J. (2005) Analysis of pile foundations under seismic loading. *CBE Institute: Final Report.*

Reese LC, Cox VR, Koop FD (1974) Analysis of laterally loaded piles in sand. *Proc. 6th Annual Offshore Technology Conf.*, Houston, Tex, (80).

Reul O, Randolph MF. (2003) Piled rafts in overconsolidated clay: comparison of in situ measurements and numerical analyses. *Géotechnique*, 53 (3), 301-315.

Reul O, Randolph MF. (2004) Design strategies for piled rafts subjected to nonuniform vertical loading. *Journal of Geotechnical and Geoenvironmental Engineering, ASCE,* 130 (1): 1-13.

Reul, O. (2004) Numerical study of the bearing behavior of the piled rafts. *International Journal of Geomechanics, ASCE,* 4 (2): 59-68.

Rollins K, Snyder JL, Broderick RD. (2005) Static and dynamic lateral response of a 15 pile group. *Procs. 16th International Conf. on Soil Mechanics and Geotech. Engineering, Millpress, Rotterdam,* The Netherlands, (4): 2035-2040.

Rollins KM, Olsen RJ, Egbert JJ, Jensen DH, Olsen KG, Garrett BH. (2006) Pile spacing effects on lateral pile group behavior: Load tests. *Journal of Geotechnical and Geoenvironmental Engineering, ASCE*, 132 (10): 1262-1271.

Romo MP, Mendoza MJ, Garcia SR. (2000) Geotechnical factors in seismic design of foundations state of the art report. *12th World Conference on Earthquake Engineering,* Auckland, New Zeland, 2832.

Roy DG, Bransby MF, Yun GJ. (2004) Centrifuge investigation of the lateral response of pile groups in sand. *Proceedings of the Fourteenth International Offshore and Polar Engineering Conference*, France, 451-458.

Schanz T, Vermeer PA, Bonnier PG. (1999) The hardening soil model: Formulation and verification. *In R.B.J. Brinkgreve., Beyond 2000 in Computational Geotechnics,* Rotterdam: Balkema, 281-290.

Shibata T, Yashima A, Kimura M. (1989) Model tests and analyses of laterally loaded pile groups. *Soils and Foundations*, 29 (1): 31-44.

Song E, Wu S. (2009) Seismic analysis of rigid pile composite ground. *US-China Workshop on Ground Improvement Technologies.* 189-197.

Specifications for Highway Bridges IV Substructures, Japan Road Association, (2012) (*in Japanese*).

Su D, Li XS. (2006) Effect of shaking intensity on seismic response of single-pile foundation in liquefiable soil. *ASCE GeoShangai Int. Conference 2006*, Shangai, China, 379-386.

Tamura S, Minowa C, Suzuki Y, Sugimoto M, Fujii S, Kagawa T. (1999) Dynamic response and failure mechanism of a pile foundation during soil liquefaction under shaking table test using a large-scale laminar shear box. 252-257.

Tokimatsu K, Suzuki H. (2004) Pore water pressure response around piles and its effects on p-y behavior during soil liquefaction. *Soils and Foundations*, 44 (6): 101-110.

Tokimatsu K, Suzuki H, Sato M. (2005) Effects of inertial and kinematic interaction on seismic behavior of pile with embedded foundation. *Soil Dynamics and Earthquake Engineering*, 25 (7-10): 753-762.

Uesugi M, Kishida H. (1986) Frictional resistance at yield between dry sand and mild steel. *Soils and Foundations*, 26 (4): 139-149.

Unsever YS, Kawamori M, Matsumoto T, and Shimono S. (2013) Cyclic horizontal load tests of single pile, pile group and piled raft in model dry sand. *Proc. of 18th Southeast Asian Geotechnical & Inaugural AGSSEA Conference*, Singapore, 891-896.

Unsever YS, Matsumoto T, Shimono S, Ozkan MY. (2014) Static cyclic load tests on model foundations in dry sand. *Geotech. Eng. Journal of SEAGS & AGSSEA*, 2014, 45 (2): 40-51.

Wood DM, Crewe A, Taylor C. (2002) Shaking table testing of geotechnical models. *International Journal of Physical Modelling in Geotechnics*, 1: 1-13.

Wood DM. (2004) Geotechnical Modelling. *Published by Spon Press*, London and New York.

Wu X, Sun L, Hu S, Fan L. (2002) Shaking table model tests on soil-pile-superstructure interaction by using a laminar shear box. *Seventh International Symposium on Structural Engineering for Young Experts.*

Yamada T, Yamashita K, Kakurai M, Tsukatani H. (2001) Long-term behaviour of tall building on raft foundation constructed by top-down method. *Proc. 5th Int. conference on deep foundation practice incorporating PILETALK international 2001,* Singapore, 411-417.

Yamashita K, Yamada T, Hamada J. (2011a) Investigation of settlement and load sharing on piled rafts by monitoring full-scale structures. *Soils & Foundations,* 51 (3): 513-532.

Yamashita K, Hamada J, Yamada T. (2011b) Field measurements on piled rafts with grid-form deep mixing walls on soft ground. *Geotechnical Engineering Journal of the SEAGS & AGSSEA,* 42 (2): 1-10.

Yamashita K, Hamada J, Onimaru S, Higashino M. (2012) Seismic behavior of piled raft with ground improvement supporting a base-isolated building on soft ground in Tokyo. *Soils and Foundations,* 52 (5): 1000-1015.

Yamashita K. (2012) Field measurements on piled raft foundations in Japan. *Proc. of Int. Conf. on Testing and Design Methods for Deep Foundations,* Kanazawa, 79-96.

Yamashita K, Hashiba T, Ito H, Tanikawa, T. (2014) Performance of piled raft foundation subjected to strong seismic motion. *Geotech. Eng. Journal of SEAGS & AGSSEA*, 2014, 45 (2): 33-39.

Zhang LM, McVay MC, Lai PW. (1999) Numerical analysis of laterally loaded 3x3 to 7x3 pile groups in sands. *Journal of Geotechnical and Geoenvironmental Engineering, ASCE,* 125 (11): 936-946.

Zhang F, Okawa K, Kimura M. (2008) Centrifuge model test on dynamic behavior of group-pile foundation with inclined piles and its numerical simulation. *Front. Archit. Civ. Eng.,* China, 2 (3): 233-241.

CURRICULUM VITAE

PERSONAL INFORMATION

Surname, Name: Yeşim Sema ÜNSEVER
Nationality: Turkish
Date and Place of Birth: 07 January 1981, Kayseri
Marital Status: Married
Phone: +90 312 2102416
e-mail: ysunsever@gmail.com

EDUCATION

Ph.D. (2015)	Civil Engineering, Middle East Technical University, Ankara, Turkey
M.Sc. (2007)	Civil Engineering, Middle East Technical University, Ankara, Turkey
B.Sc. (2004)	Civil Engineering, Middle East Technical University, Ankara, Turkey

PROFESSIONAL EXPERIENCE

April 2005- Present	Research Assistant at Middle East Technical University, Department of Civil Engineering, Division of Geotechnical Engineering, Ankara, Turkey
September 2012-August 2013	Researcher at Kanazawa University, Graduate School of Natural Science, Kanazawa, Japan

TEACHING EXPERIENCE

Soil Mechanics, Foundation Engineering I, Introduction to Soil Dynamics, Dam Behavior and Safety, Advanced Soil Mechanics I and II (descriptions of the courses are available at **www.ce.metu.edu.tr**).

FOREIGN LANGUAGES

Advanced English, Beginner Japanese

MEMBERSHIPS

2014 – Present	Soil Mechanics and Geotechnical Engineering Association of Turkey, Member
2012 – Present	American Society Civil Engineers, Member
2004 – Present	Turkish Chamber of Civil Engineers, Member

PUBLICATIONS

Unsever, Y.S., Matsumoto, T., Shimono, S., Ozkan, M.Y. (2014) Static Cyclic Load Tests on Model Foundations in Dry Sand, *Geotech. Eng. Journal of SEAGS & AGSSEA*, 45 (2), 40-51.

Unsever, Y.S., Matsumoto, T., Özkan M.Y. (2015) Numerical analyses of Load Tests on Model Foundations in Dry Sand. *Journal of Computer and Geotechnics*, 63, 255-266.

Ünsever, Y.S., Yıldız, S.G., Özkan M.Y. (2007) Behavior of Muratli Dam for End of Construction and Reservoir Filling Cases, *International Dam Safety Symposium and Exhibition (IDSS)*, Ankara, Turkey, May 2007.

Ünsever, Y.S., Yıldız, S.G., Özkan M.Y. (2007) Deformation Behavior Analysis of Muratlı Rockfill Dam, *Civil Engineers' Chamber 2. Geotechnical Symposium*, Adana, Turkey, November 2007.

Ünsever, Y.S., Yıldız, S.G., Özkan M.Y. (2009) Behavior of Rockfill Dams: Muratlı and Borçka Dams Case Study, *Civil Engineers' Chamber 3. Geotechnical Symposium*, Adana, Turkey, December 2009.

Ünsever, Y.S., Yıldız, S.G., Özkan M.Y. (2010) Placement and Utilization of Instrumentations at Rockfill and Earthfill Dams, *Yapı Dünyası*, October 2010.

Gülerce, Z., Yılmaz, M.T., Huvaj, N., Sağlam, S., Sandıkkaya, A., **Ünsever, Y.** (2011) Seismic and Structural Field Observations from 23 October 2011 Mw=7.2 Van Earthquake Part 2: Geotechnical Damage, *METU EERC Report*, November 2011.

Ünsever, Y.S., Özkan M.Y., Yıldız, S.G. (2012) The Deformation Behavior of Muratlı Asphalt Faced Rockfill Dam, *ASCE Geocongress,* Oakland, CA, March 2012.

Gülerce, Z., Çetin, K.Ö., Yılmaz, M.T., Sarıhan, N.H., **Ünsever, Y.S.,** Ünsal, S., Sağlam, S., Sandıkkaya, M.A. (2012) Geotechnical Field Observations from 23 October 2011 Van Earthquake (Mw=7.1), *SSA 2012 Annual Meeting*, San Diego, CA, April 2012.

Gülerce, Z., Çetin, K.Ö., Yılmaz, M.T., Sarihan, N.H., **Ünsever, Y.S.,** Ünsal, S., Sandıkkaya, A., Türkoğlu, M. (2012). 23 October 2011 Van-Tabanlı Earthquake (Mw=7.1) Geotechnical Field Observations, *10th International Congress on Advances in Civil Engineering,* Ankara, October 2012.

Unsever, Y.S., Kawamori, M., Matsumoto, T., Shimono, S. (2013) Cyclic Horizontal Load Tests of Single Pile, Pile Group and Piled Raft in Model Dry Sand, *18th Southeast Asian Geotechnical Conference*, Singapore, May 2013.

Kawamori, M., **Unsever, Y.S.,** Matsumoto, T., Kobayashi, S., Shimono, S. (2013) Cyclic Horizontal Load Experiments on Model Pile Foundations in Dry Sand Part1: Experiment Description, *48th Japan National Conference on Geotechnical Engineering*, Toyama, Japan, July 2013 (in Japanese).

Unsever, Y.S., Kawamori, M., Matsumoto, T., Kobayashi, S., Shimono, S. (2013) Cyclic Horizontal Load Experiments on Model Pile Foundations in Dry Sand Part 2: Experimental Results, *48th Japan National Conference on Geotechnical Engineering*, Toyama, Japan, July 2013.

Unsever, Y.S., Özkan, M.Y., Matsumoto, T., Shimono, S., Esashi, K. (2014) Physical and Numerical Modelling of Pile Foundations Subjected to Vertical and Horizontal Loading in Dry Sand, *14th IACMAG*, Kyoto, Japan, September 2014.

Unsever, Y.S., Matsumoto, T., Shimono, S. (2015) Shaking Table Tests of Piled Raft and Pile Group Foundations in Dry Sand, *6th ICEGE*, Christchurch, New Zeland, November 2015 (*Accepted*).